Strathclyde University

A Generic Evaluation of Loads in Horizontal Axis Wind Turbines

Romans Kazacoks

A thesis presented in fulfilment of the requirements
for the degree of Doctor of Philosophy

Centre for Doctoral Training in Wind Energy Systems
Department of Electronic and Electrical Engineering
University of Strathclyde
Glasgow G1 1XW
Scotland, UK

May 2017

This thesis is the result of the author`s original research. It has been composed by the author and has not been previously submitted for examination which has led to the award of a degree.

Acknowledgement:

At first I would like to express my appreciation and thanks to my supervisors, Peter Jamieson, Professor William Leithead, for their support, patience and advice they have given me. It would be very difficult to finish the PhD without their guidance.

Secondly I would like to thank guys from DNV GL, Graeme McCann, Robert Emrys Harries, William Collier and Alec Beardsell, for support in general guidance and use of GH Bladed software.

The last 4.5 years I was a part of the Centre for Doctoral Teaching in Wind Energy system within the University of Strathclyde. So, I would like to thank Drew Smith, David Infield, Alasdair McDonald and Olimpo Anaya-Lara for their help along these 4.5 years. Additionally, the author would like to thank the EPSRC for their financial support as the PhD was funded by EPSRC

Abstract:

Thousands of load calculations for wind turbine design have been calculated by manufactures, consultants and certification bodies. These have been done as required to develop and validate specific designs. However, there has not been a general systematic study of trends in loads related to key wind turbine design parameters and external operating conditions. The aim of this thesis is parameterise and quantify trends of extreme and fatigue loads based on systematic modifications of wind turbine characteristics.

This thesis is in two main parts. The first part provides an overview of loads calculation methods, flow modelling and approach adopted also considering scaling rules, comparing scaling with similarity and the scaling evident in from commercial world turbines data.

The second part presents and evaluates loading trends for extreme and fatigue loads related to systematic alterations of key wind turbine parameters. Three chapters of results investigate the load impacts of blade structural properties, rotor solidity and up-scaling respectively. The chapter on blade structural properties demonstrates that the self-weight of blades is a major component influencing loads of the blade root and hub. The chapter on rotor solidity shows that significant load reduction can result for blade root, shaft and yaw bearing in reducing the solidity of rotor. However, the aerodynamic damping reduces with reducing solidity, which is crucial for tower base fore-aft loads; therefore the reducing rotor solidity has an adverse impact on the tower base fore-aft loads. The chapter on up-scale demonstrates that up-scaling with similarity method can give good prediction of loads with an error of ±10% and ±15% for extreme and fatigue loads of large wind turbines (up to 10MW) at the mean wind speed within power production range. Additional, the chapter of up-scaling showed that the up-scaled wind turbines reduce the sensitivity to turbulence with the size of rotor.

1. Introduction

1.1. Inspiration and aims

The majority of the public associate wind energy with an upwind, three bladed wind turbine, which is commonly used around the world. The first machines were fixed speed, stall regulated with an induction generator in the drive train [1]. A comparison of characteristics between early and modern units shows significant development of technologies and innovations. This progress is a result of the continuous work to improve efficiency, power production and to minimise the cost of energy. This process of optimisation is endless, because every day innovations push the technology forward to a new level and almost every component of a wind turbine will be further optimised. Many innovations modify the loads experienced by wind turbines, and although thousands of load calculations for new turbine designs have been performed, there still lacks a systematic parameterised and quantitative characterisation of the trends in wind turbine loads and a lack of a systematic understanding of the impact that these loads have. It is common to see studies which declare, for example, “blade root flap-wise bending loading has been reduced by 10%”, but which fail to make any connection to the significance of this reduction in terms of fatigue and extreme loads.

This research tries to answer the question:

- *How do fatigue and extreme loads change due to modification of wind turbine parameters?*

The above question leads to an enquiry, what these parameters are. The list of these parameters is depicted in Figure 1.1. This work covers structural parameters, operational parameters (solidity) and scaling as these are the most important ones, however additional parameters could also be looked at in the future. The scope of this research is displayed in Figure 1.2.

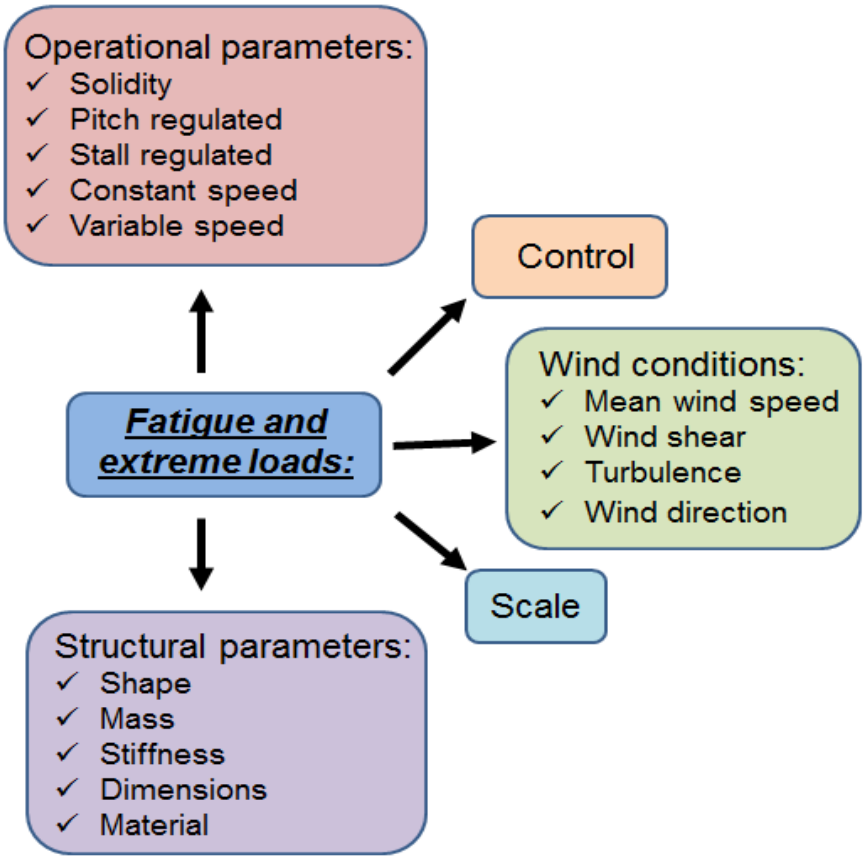

Figure 1.1: The parameters which influence fatigue and extreme loads.

Figure 1.2 shows a graphical representation of the main aim of this study, which is a sensitivity analysis of wind turbine extreme and fatigue loads to the selected wind turbine parameters (structural parameters, rotor solidity and scaling). Consequently, this research includes three main investigations relating to the selected parameters. Additionally, this research tries to answer a second question, which is:

- *Is it possible to identify fatigue and extreme loads trends as a function of the selected parameters?*

In the sensitivity analysis for fatigue loads, each of the three main investigations focuses on two types of material: steel and composites. The main focus of this study is the change in fatigue and extreme loads, which are considered the design drivers for wind turbines [2].

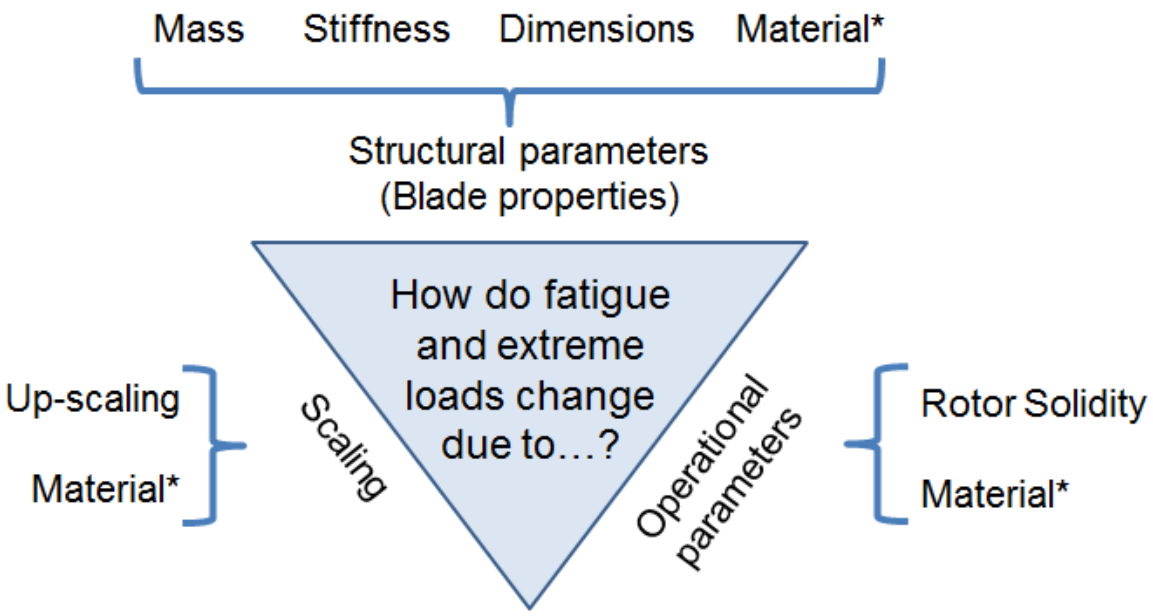

Figure 1.2: Graphical representation of the research

1.2. Key areas of the investigation:

The loads on a wind turbine depend on several factors or parameters. Each of these parameters is modified separately in order to investigate the changes in the loads. The study is divided into different areas, which investigate changes in loads due to the applied modifications. The following bullet points demonstrate the key areas of the investigation in the study as shown in Figure 1.2:

- Structural properties of blades**:** It is recognised that the amount of energy produced depends on the rotor diameter. As a result, there is a desire to increase rotor diameter as much as possible. However, there are many issues with the increasing blade length, concerning self-weight effects and dynamics of the blades. The wind turbine blades are connected to a steel hub or pitch bearing at the root while the rest of blade is made of composite materials. The weight of the blades has to be carried by other parts of wind turbine (hub, tower and foundation). Any increase in blade weight affects other parts of the wind turbine, which usually bear the additional loads. In this case one solution is to introduce lighter and more robust materials. These will generally have different properties: density, stiffness and etc. Therefore, this part of the research focuses on the dependency of the extreme and fatigue loads from the mass, stiffness and dimensions of blades.

- Rotor solidity: Rotor solidity is considered in two parts. Firstly the impact of tip speed on the loads is evaluated considering that the optimum rotor solidity varies inversely as the square of design tip speed [3] if the original aerofoils are maintained. Increase in design tip speed is relevant to offshore wind turbines as there are less severe acoustic restrictions offshore compared to onshore. In this way, at any given rated power level, the rated torque can be reduced since power is the product of the angular velocity and torque. This can lead to cost reduction as mass and cost of much of the drive train is related to rated torque levels.

  Secondly an optimum rotor design has a unique lift distribution. Lift is proportional to the product of chord width and design lift coefficient (approximately the lift coefficient associated with maximum lift to drag ratio of the chosen aerofoil). Thus without changing rotor design speed, optimum rotors of varying solidity may be developed by choosing aerofoils with different design lift values. The loading implications of changing solidity in this way are also explored.

- Up-scaling: Up-scaling can be defined as the transformation of a turbine design at a smaller scale to a larger scale so that the new turbine has a larger power rating. This typically leads to changes in dimensions and affects quantities such as loads. Offshore especially has driven the up-scaling of wind turbine units. Increase in unit size reduces cost of energy (£/MWh) by reducing the total cost of infrastructure, operation and maintenance for a large wind farm [4]. The up-scaling of wind turbines is investigated primarily based on up-scaling with similarity. The method of up-scaling with similarities is explained in section 3.1. Although commercial design will often depart from this, especially to reduce the impact of self-weight loading on very large units, scaling with similarity is considered the best way to clarify underlying trends in loads and explain loading impacts. As it was mentioned at the previous bullet point the generated power is a function of rotor swept area and wind speed. In this case the up-scaling is applied to the entire wind turbine to enlarge the energy output. Additionally, the up-scaled wind turbine experience higher wind speeds due to the increased tower height and wind shear (see section 3.1.6). Furthermore, the up-scaling effect on turbulence is investigated as there is a common belief that larger wind turbines are less sensitive to turbulence.

1.3. Outline of thesis

This section provides a brief summary of the chapters in this thesis.

Chapter 2: Loads

The chapter provides an overview of different types of loads and the causes of these loads. It also provides a brief description of the different standards for wind turbine design. As the IEC 61400-1 standard is employed in this study, the design load cases of the IEC standard are investigated to select the most severe cases for the calculation of the extreme and fatigue loads. At the end of this chapter the methods for the determination of extreme and fatigue damage equivalent loads are explained.

Chapter 3: Scaling

The classical scaling with similarity and up-scaled commercial data are explained and compared in this chapter. Moreover, the dependency of wind turbine components on scaling is outlined. Additionally, the size limits of wind turbines are highlighted.

Chapter 4: Software for designing wind turbines

Different software tools for design load calculations of wind turbines are examined to select one for this research. The GL coordinate systems are used in the GH Bladed software tool and are employed as GH Bladed has been chosen for this study. The GH Bladed built-in controller is generally used in this research with tuning adjustments to deal with specific dynamic effects.

Chapter 5: Methodology

This chapter consists of two parts. The first parts outlined the method of steady loads assessment and a technique of separation into deterministic and stochastic loads to perform the post processing calculations separately. Furthermore, the procedure of calculation is included for extreme loads extrapolation and lifetime damage equivalent loads of deterministic part of loads.

The second part of chapter models the wind flow and considers and compares the Kaimal and the Mann wind models. It also outlines the parameters, which are employed to generate the wind inflow. Moreover, wind classes, normal turbulence models, extreme turbulence model and extreme wind speed model of IEC standard are overviewed.

Chapter 6: Base model of wind turbine

This chapter provides an overview of publicly available wind turbine models in order to choose the most suitable wind turbine model for this research. Additionally, this chapter includes the validation of the reference model, which was selected from the publicly available wind turbine models.

Chapter 7: Blade structural properties

The main focus of this chapter is the effect of blade modifications on extreme and fatigue loads. Therefore, modifications are applied only to the blades, with other components of the wind turbine unchanged. There are four different scenarios of modifications, which cover the changes of mass, stiffness and dimensions of blades. The 2^{nd} and 4^{th} scenarios modify the structural parameters in such way to maintain the natural frequency of reference model. Power trend lines are employed to parameterise the changes of extreme and fatigue loads due to the modification of blades.

Chapter 8: Impact of rotor solidity

In chapter 8 the impact of rotor solidity on extreme and fatigue loads is investigated. There are two ways to alter the rotor solidity. The first method assumes no changes of aerofoil properties and deals with the changes of the tip speed and chord length of blades. The second method is based on the changing the chord length and replacing old aerofoils with new ones with different aerodynamic coefficients. Both these methods are discussed in chapter 8. Additionally, the aerodynamic damping dependency on rotor solidity is considered.

Chapter 9: Up-scaling

This chapter examines the effect of up-scaling on loads. The reference model, which has a rated power of 3MW, is up-scaled to 4, 5, 6, 7, 8, 9 and 10 MW by using up-scaling with similarity. Trend lines from the loads data determine the up-scaling exponent of extreme and fatigue loads in order to compare with the predicted up-scaling factor of steady loads, which was estimated by the technique of up-scaling with similarity.

Chapter 10: Conclusions and Recommendations

The chapter is the final chapter of this thesis, which summarises the work done throughout this research, highlights the limitations of the performed calculations and provides some ideas about work that can be performed in the future.

2. Loads

Loads play a dominant role in wind turbine design because the loads are acting on the wind turbine continuously throughout their lifespan. Moreover, the wind turbine is a dynamic system responding to continuously varying wind conditions, which means the wind turbine loads are varying constantly. Whether idling or maintaining stable power production, the wind turbine has to withstand all loads throughout their lifetime.

This chapter outlines the different types of loads, which the wind turbine experiences throughout their lifespan. The causes of these loads are highlighted and also described. There is the overview of different wind turbine standards and especially IEC Standards [5], which is used in this study. Moreover, the chapter provides details of the most severe design load cases from the IEC Standards [5] for extreme and fatigue loads. The procedure of calculating extreme and lifetime damage equivalent (fatigue) loads is shown in the last section of this chapter.

2.1. Types of loads on a wind turbine

As mentioned before the main focus of this research is to investigate the changes in loads of a wind turbine associated with specific design modifications. A wind turbine is a dynamic system, which is under constantly varying loads during its life. This section gives an overview of the different types of loads, which act on the wind turbine.

- Steady loads: these are types of loads that do not change for a long interval of time.

- Cyclic loads: these are repeatable loads. An example of cyclic loads is the blade root loading from the blades self-weight, which repeat with each rotation (cycle) of the rotor.

- Resonance loads are cyclic loads. The resonance loads often occur when the natural frequency of structural components coincides with the rotational frequency of unbalanced rotor blades passing a tower, and its harmonics. The resonance loads have to be avoided whenever possible as they are characterised by high magnitude and lead to rapid failure [1], [6], [7].

- Transient loads: these are types of loads which arise for the short period of time. Transient loads are typically caused by gust, brake or rapid acceleration of rotor.

- Stochastic loads: are from turbulence. This loading changes in time, but there is no well-defined pattern of load changes as the turbulence changes randomly.

The above mentioned types of loads have different sources, which can be divided into three basic categories:

- **Gravity loading**: This is due to the earth's gravitational attraction which is the source of weight of all bodies. The most sensitive gravity or self-weight induced loads are the edge-wise blade root cyclic loads, because of the rotational motion of rotor. If the blade position is horizontal the blade root can be split into two segments: leading and trailing edge. In one angular position of a blade, the leading edge segment is under compression and the trailing segment is under tension stress. As the rotor rotates by 180 degrees from this position, the stresses reverse putting the leading and trailing blade segments in tension and compression respectively.

- **Aerodynamic Loads**: They are caused by the wind flow acting on the wind turbine. The wind flow generates the perpendicular force (thrust) to the rotor plane and tangential force (torque) along the rotor plane. The wind flow is not constant across the rotor plane as it varies in time and space due to wind shear and turbulence (see Figure 2.1). Furthermore, most of time the wind flow direction is not perpendicular to the rotor axis plane because wind direction varies all the time and the rotor axis cannot follow these changes of the wind direction. Thus the wind turbine operates under some degree of yawed flow conditions most of the time. The efficiency of the rotor decreases and cyclic loadings increase as the yaw angle increases.

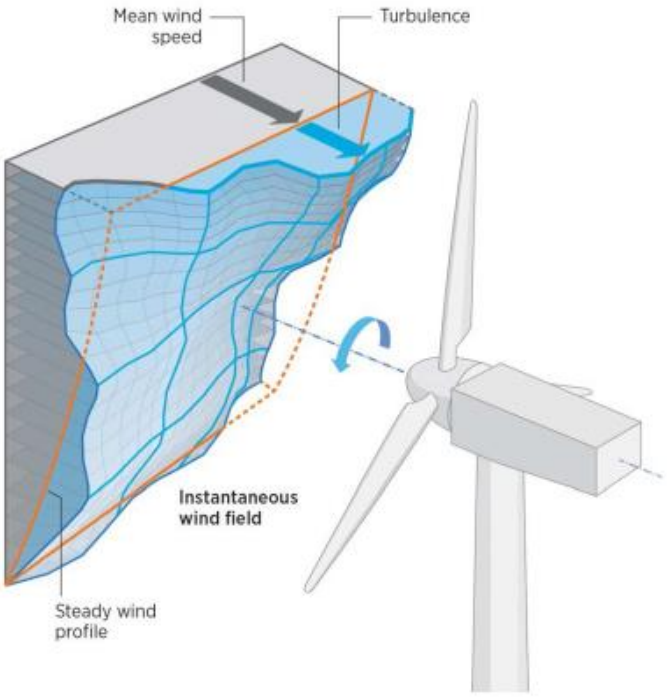

Figure 2.1: Instantaneous wind profile which is seen by a wind turbine [8].

- **Inertia:** This especially impacts on transient loads. For example, the blade root experiences transient loading when the brake is applied to stop the wind turbine (see Figure 2.2). The figure illustrates that the transient force *(dF)* is acting on the blade element due to the inertia of rotor motion when brake torque *(T)* is employed to stop the rotor. The same rule applies for the starting of the rotor from the standstill condition.

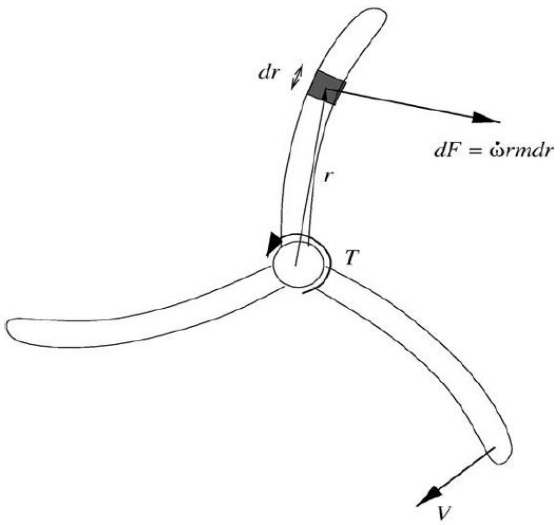

Figure 2.2: Braking causes the inertia loads [2]

The above mentioned information about the types and sources of loads can be summarised by Figure 2.3 which links the five different load types with the sources which cause these loads.

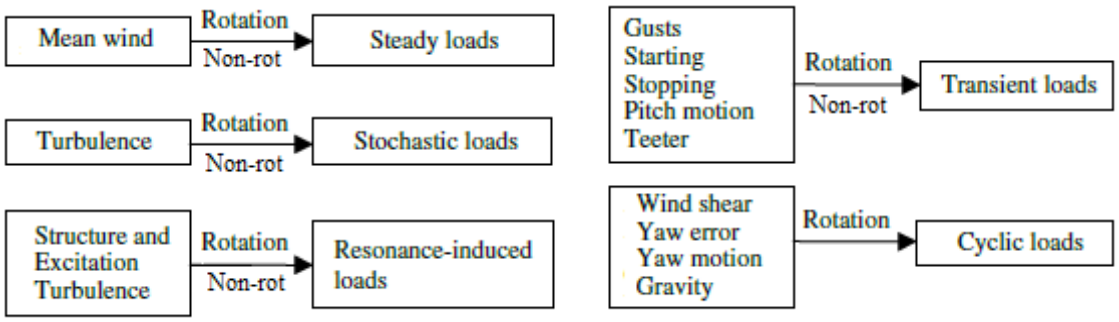

Figure 2.3: Sources and types of wind turbine loads [6].

It is necessary for a wind turbine to be able to withstand the fatigue and extreme loads throughout its life. The fatigue loads are the summation and accumulation of continuously varying above mentioned loads during the entire design life (20 years) of the wind turbine. Extreme loads are peak loadings associated with particular operational states and extreme weather conditions (e.g. storm, hurricane and so on.) when the rotor may be idling. The extreme and fatigue loads are described in the following sections of this chapter.

2.2. Wind turbine standards

It is necessary to have a procedure to check that the wind turbine is well designed and is able to withstand loads and specific environmental conditions of the site. Thus, standards have been developed to regulate the procedure of examination of machine design from the 1980s [1]. At the moment there are several well-known wind turbine standards, which can be employed to check the wind turbine's design [6]:

- Germanisher Lloyd (GL)
- Det Norske Veritas (DNV)
- International Electrotechnical Commission (IEC)
- Danish Energy Agency DS-472

The IEC standards were chosen as the procedure to check the design requirements of the wind turbines in this research, because the IEC standards are more commonly used by industrial

companies for the design requirements of wind turbines. The IEC standards are divided into different divisions as it depicted by Table 2.1. For this research IEC 61400-1 will be used to check design requirements [5].

Source/Number:	Title :
IEC WT01	IEC System for Conformity Testing and Certification of Wind Turbines Rules and Procedures
IEC 61400-1	Wind Turbines – Part 1: Design Requirements, edition 2
IEC 61400-2	Wind Turbines – Part 2: Safety Requirements for Small Wind Turbines
IEC 61400-3	Wind Turbines – Part 3: Design Requirements for Offshore Wind Turbines
ISO/IEC 81400-4	Wind Turbines – Part 4: Gearboxes for Turbines from 40 kW to 2MW
IEC 61400-11	Wind Turbines – Part 11: Acoustic Emission Measurements Technique
IEC 61400-12	Wind Turbines – Part 12: Power Performance Measurements of Electricity Producing Wind Turbines
IEC 61400-13	Wind Turbines – Part 13: Measurement Mechanical Loads
IEC 61400-14	Wind Turbines – Part 14: Declaration of Apparent Sound Power Levels and Tonality Value of Wind Turbines
IEC 61400-21	Wind Turbines – Part 21: Power Quality Measurements
IEC 61400-22	Wind Turbines – Part 22: Conformity Testing and Certification of Wind Turbines
IEC 61400-23	Wind Turbines – Part 23: Full-scale Structural Testing of Rotor Blades
IEC 61400-24	Wind Turbines – Part 24: Lightning Protection
IEC 61400-25	Communication for Monitoring and Control of Wind Turbines

Table 2.1: Standards of the IEC for wind turbines [6]

2.3. Design load cases

As it was mentioned in the previous sections the fatigue and extreme loads will be calculated by using the procedure from IEC 61400-1 standards [5]. There are 22 different design load cases in total, with 17 and 5 design load cases for the extreme and fatigue loads, respectively. A combination of various wind turbine state and wind condition is described by each design load case. The minimum requirement of a machine is to withstand the design load cases to prove that the machine has the adequate design. The design load cases are divided into 8 groups, which are summarised below:

- **Power production:** where a machine operates at normal condition and generates electricity as it has been designed. The power production considers the normal and extreme wind conditions.
- **Power production with fault:** different types of fault are considered during the power production such as: control system, disconnection from electrical network, protection system, etc.

- **Start up:** investigate the transient condition of the wind turbine when the machine state changes to power production from the standstill or idling conditions.
- **Normal shut down:** include investigation of the transient conditions of wind turbine due to changing the wind turbine state from power production to idling or standstill conditions.
- **Emergency shutdown:** transient condition from emergency stop.
- **Parked (stand still or idling):** The energy is not generated by the machine as the wind turbine is at idling or standstill conditions.
- **Parked with fault conditions:** The condition of the wind turbine is the same as in the previous design load case, but a fault has to be considered. The type of error can be either with the machine or grid connection.
- **Transporting, assembling, maintenance and repair.**

The more detailed explanation of design load cases can be found in the IEC 6400-1 standards [5]. Rather than using all of the design load cases. The most important or severe ones are selected, which produce the highest load. The selection of design load cases is explained in the following sections.

2.4. Extreme loads

Extreme loads refer to loads caused by extreme conditions such as high wind speed with a parked regime, high turbulence, a gust at low wind speed or significant yaw misalignment [9]. However, the extreme loads consider the event of the largest load, which would occur once 50 years. The extrapolation approach is used to determine the 50-year load from the load calculation at normal wind conditions. Additionally, the extreme conditions consider a fault with the combination of the extreme or normal conditions [1]. In this case the extreme loads can be divided into two groups, which are illustrated by Figure 2.4. Each group demonstrates the combination of the wind turbine state with the type of wind condition.

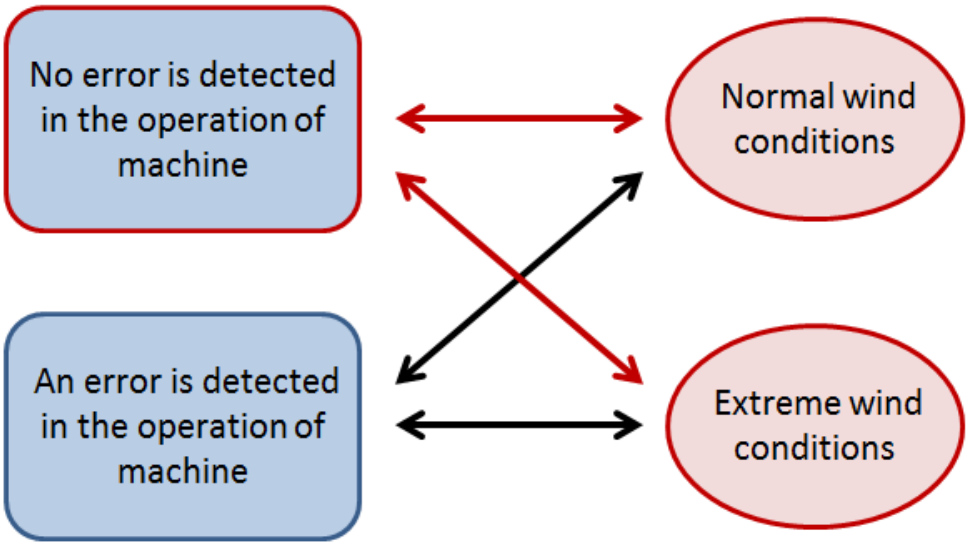

Figure 2.4: Key areas of investigation for extreme loads.

The focus of the research is normal machine states with different wind conditions. Hereby the study assumes that a unit operates without any error. The investigation of the combination of any fault in wind turbines with the different wind conditions is beyond the scope of research, because turbines will automatically shut-down depending on the severity of the fault. Testing fault cases is testing that the safety system works and can cope with the transient loads. Figure 2.4 depicts the focus of research by highlighting the border line of rounded rectangular and ellipses by red colour.

The aim in extreme load calculations is to calculate the maximum and minimum loading which can be withstood by the wind turbine. However, the calculating procedure of extreme loads involves three further complications, which are described briefly below [10].

- Assign a safety factor to a load type. It depends on the design load case according to IEC 61400 standards [5].
- Take into account uncertainties raised from stochastic phenomena, which is turbulence. These uncertainties can be reduced by using an appropriate number of seeds of wind speeds. Different seeds are a result of different realisations of a wind speed pattern over the simulated time. The wind pattern with different seeds represents the same stochastic model, meaning that the realised average wind speed and turbulence level match this model, so are close to the theoretical values. The required minimum of seeds is six for most load design cases according IEC 61400-1 standards to make the extreme load assessment more accurate.

- An area of interest is contemporaneous loads [10], [11], which are close to the mean value of the maximum loads. So if there are six seeds for each wind speed, the maximum loads appear at some specific wind speed from the range of wind speeds for the six seeds. The contemporaneous load from the six seeds is the load of the seed which has the nearest value to the mean value of these six seeds for this specific wind speed.

In IEC 61400-1 standards there are 17 design load cases (DLCs) as mentioned previously. The next step is to select a reduced set of design load cases (DLCs) from the seventeen in order to restrict overall scope of the project to a manageable scale. In his thesis Bergami [12] has compared outputs of DLC in terms of bending moment of the 5MW NREL wind turbine. There are the six bending moments considered, these are: edge-wise and flap-wise blade root, tower base fore-aft and side-to-side, yaw (or tower torsional) and drive train torsion of the low shaft. If a reader is not familiar with such moments, the explanation of these moments can be found in chapter 4. The comparison is shown in Figure 2.5, which has the six graphs corresponding to the mentioned bending moments. Each graph shows ten design load cases, which are commonly used to evaluate wind turbine design requirements in industrial practice. A brief explanation of these DLCs is below:

- **DLC 1.1.** This case covers the power production range (4-25 m/s mean wind speed) with a normal turbulence model (NTM) wind field, and a mean yaw misalignment of ±8°. The wind turbine is connected to an electrical load without any faults.
- **DLC 1.3.** This case covers some specific wind speeds (9.2, 11.2, 13.2, 20, 25 m/s) of production range without any fault at extreme turbulence model (ETM). A machine is connected to the electrical load.
- **DLC 1.4.** This case relates a specific transient case which is extreme coherent gust with direction change at rated wind speed. A machine is connected to the electrical load.
- **DLC 1.5.** This case characterises a specific transient case which is extreme wind shear occurring in the power production range of wind speeds. The machine is connected to the electrical load.
- **DLC 2.1.** This case corresponds to the power production range (4-25 m/s mean wind speed) with a control system fault or a loss of electrical network connection. The NTM wind field with a mean yaw misalignment of ±8°is used.
- **DLC 2.3.** This case describes the combination between extreme operating gust with an internal or external electrical system fault, which is the loss of electrical network connection, at the rated wind speed of a wind turbine.

- **DLC 3.2 & 3.3.** These two DLCs define a transient situation of switching to power production conditions from standstill or idling.
- **DLC 6.1.** This case corresponds to an idling condition of 50 m/s wind speed with a mean yaw misalignment of ±8° using the turbulent extreme wind model (EWM).
- **DLC 6.3.** This case relates to idling conditions with 40 m/s wind speed with extreme yaw misalignment using the turbulent extreme wind model (EWM).

Note a more detailed explanation of the DLCs can be found in the IEC Standard [5]. The turbulence models will be discussed in chapter 6, which overviews the wind conditions.

Figure 2.5 demonstrates that the highest loads are most often produced by design load cases related to operation in power production range (DLC 1.1-1.4). However, in Figure 2.5 graphs of flap-wise blade root and tower base fore-aft bending moments have the highest loads from DLC 2.3, which simulates power production with an electrical fault as a result of network loss. Note that electrical network faults are not considered in this study, meaning that there is an assumption of no faults with the machine or network. Moreover, in Figure 2.5 the graph of tower base side-to-side bending moment does not follow the common pattern of Figure 2.5, because the maximum loads are from DLCs 6.1-6.3, which examine the loads at standstill and idling conditions of the wind turbine during the 50-year extreme wind speed.

The regular power production conditions are defined by three design load cases (1.1, 1.3 and 1.4) in Figure 2.5. Design load cases 1.1 and 1.3 have more severe loads than DLC 1.4 in four graphs out of six at Figure 2.4. The exception is graphs of flap-wise blade root and fore-aft tower base bending moment, where load of DLC 1.4 is marginally higher than loads of DLC 1.1 and 1.3 for tower base fore-aft bending moment. Overall, DLC 1.1 and 1.3 are considered more valuable than DLC 1.4.

According to the examination of DLC of extreme loads from Figure 2.5, the extreme loads will be investigated by the four design load cases: DLC 1.1, DLC 1.3, DLC 6.1 and DLC 6.3.

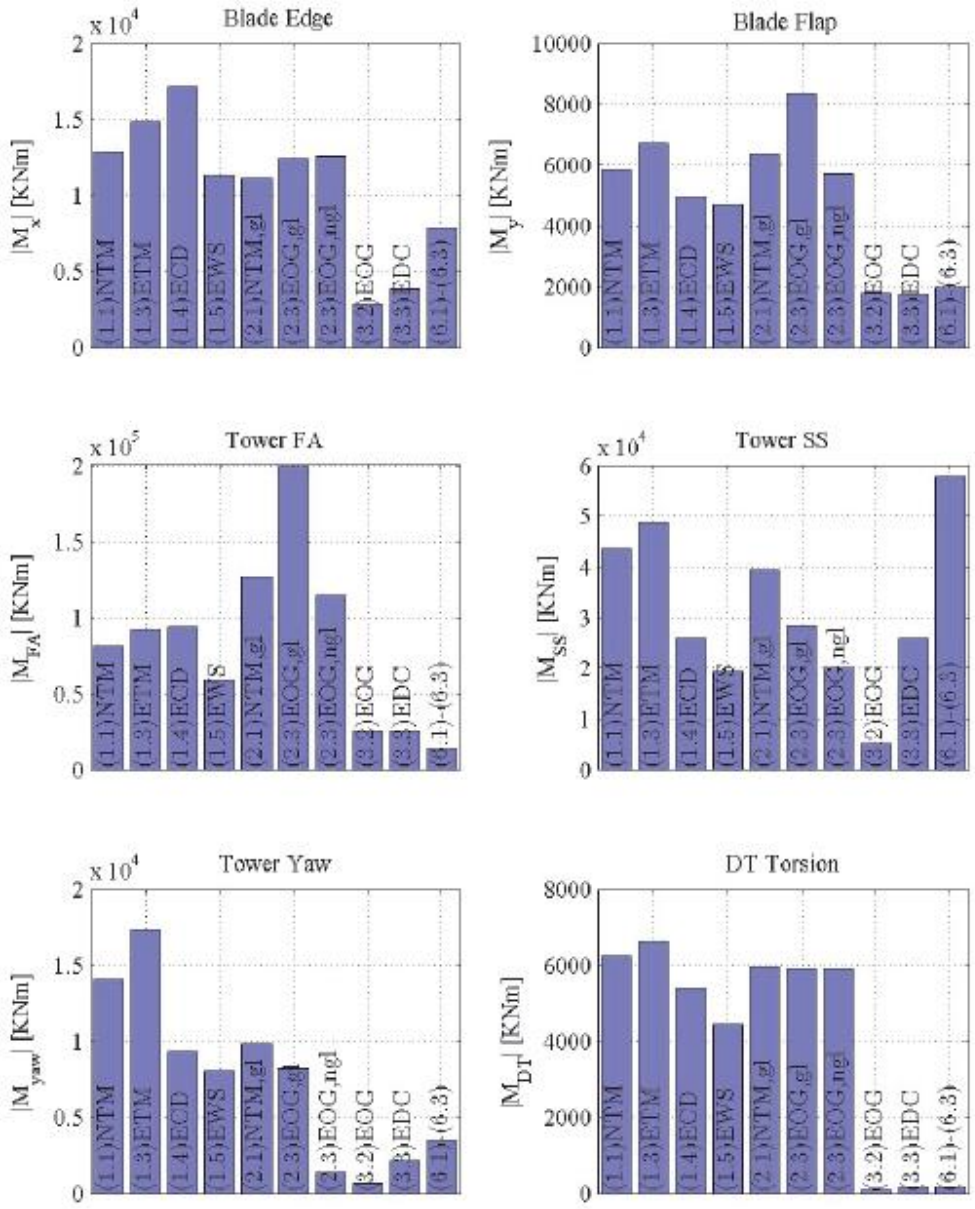

Figure 2.5: Relative distribution among DLC of extreme loads based on IEC standards [12]. Where:

- M_x –edge-wise blade rood moment, My - flap-wise blade rood moment,
- M_{FA} –fore-and-aft tower moment, M_{SS} - side-to-side tower moment
- M_{yaw} - tower torsional or yaw moment, M_{DT} – low shaft moment

2.5. Fatigue Loads

As it was mentioned previously, the fatigue loads are a key part of design driving loads for any wind turbine, because the wind turbine is a dynamic system, which is in operation for most of its lifespan. The default lifespan of a wind turbine is 20 years. The combination of hours per year and

theoretical Weibull distribution of wind speed of class I is depicted in Figure 2.9. If a wind turbine operates in the wind speed range between 4 and 25 m/s, the wind turbine will operate 18.5 years out of 20 with 8.9 m/s annual average wind speed, which was calculated from Weibull distribution. Consequently, the wind turbine will produce revolutions of rotor according to the rough estimation based on Figure 2.9. However, it is unlikely that the wind flow exactly follows the Weibull distribution for 20 years. Therefore, it is assumed that a wind turbine produces approximately revolutions of a rotor per lifespan as 2 MW machine [2]. The number of revolutions per lifespan is going to be used to calculate the reference frequency in equation (2.6 to calculate damage equivalent loads (DELs).

As it was written previously there are five DLCs in IEC 61400-1 standards to check the resistance of wind turbines to fatigue loads. Figure 2.6 depicts a specific example of DEL contribution among the DLCs for the different parts of the 5MW NREL wind turbine.

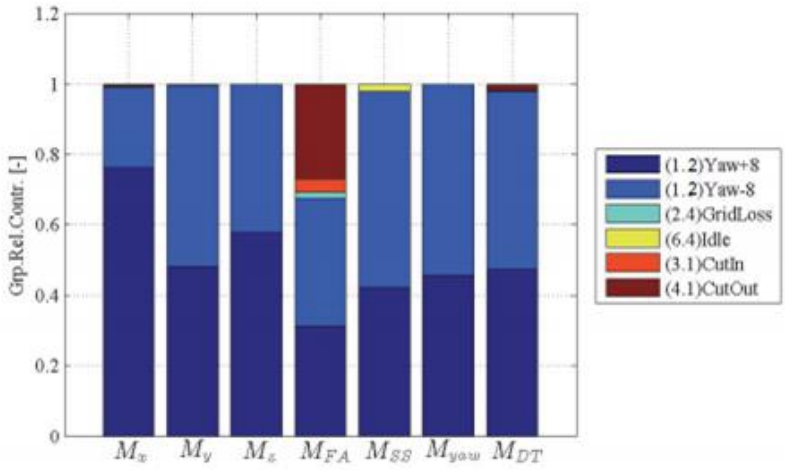

Figure 2.6: Relative contributions of fatigue DELs by DLC for 5MW NREL wind turbine [12].

- M_x – edge-wise, M_y - flap-wise, M_z - torsional blade moment
- M_{FA} – fore-and-aft, M_{SS} - side-to-side tower moment
- M_{yaw} - tower torsional or yaw moment
- M_{DT} – low shaft moment

Figure 2.6 demonstrates that for the 5MW NREL machine in each specified moment DLC 1.2 has the largest DEL impact from all five DLCs. The contribution of four DLCs (2.4, 3.1, 4.1 and 6.4) is not significant compared with DLC 1.2. However, DLC 4.1 has a significant impact to DEL contribution of the fore-and-aft tower moment. Four DLCs (1.2, 3.1, 4.1 and 6.4) out of five will be used to check the fatigue loads in this research, because these four DELs cover four operation conditions such as: power production, start-ups, shut downs and idling since DLC 2.4 (grid loss)

has only a minor impact on fatigue damage (Figure 2.6), it is excluded from the determination of DELs employed in this study. The brief explanation of the four DLCs is given below:

- DLC 1.2 is the power production range (4-25 m/s mean wind speed) with a normal turbulence model (NTM) wind field, and a mean yaw misalignment of ±8°. The wind turbine is connected to an electrical load without any faults.
- DLC 3.1 is the start-up of a wind turbine from idling or standstill to power production conditions at steady wind.
- DLC 4.1 is the normal shut down from the power production or idling to standstill condition at steady wind.
- DLC 6.4 is an idling condition (3, 30, 35 m/s) with a yaw misalignment of ±8 ° using a NTM wind field.

2.5.1. Lifetime Damage Equivalent Load (DEL):

Methods of predicting fatigue damage have been long established. The essence of the problem is to replace a complicated signal of stress-time history at some location in a structure with a number of cyclic stress repetitions of fixed amplitude that will consume the same proportion of total fatigue life [13]. To be applied quantitatively to materials, it is essential to work with stress at specific locations. However, for comparative purposes, especially in the evolution of design, the same methodology may be applied to moments. This will provide an indication of how design changes or operational changes may affect fatigue life and whether certain component designs appear to be driven primarily by fatigue or extreme loads.

Damage equivalent loads (DELs) are employed to represent the fatigue damage. DELs are based on Palmgren-Miner linear cumulative damage theory [14], which assumes that fatigue damage increases linearly as a function of number of cycles, until it reaches the prescribed life exhausted of material [15]. Additionally, it assumes that only cycle load range contributes to fatigue damage, i.e. there is no contribution to fatigue damage from the mean value of cycles. Figure 2.7 shows a diagram of Palmgren-Miner linear cumulative damage. The vertical and horizontal axes of the diagram represent stress and cycles to failure, respectively. The diagonal line is the S-N curve which is a boundary between failures and safe zone of a material. The slope gradient of S-N curve represents the type of material. According to cumulative damage theory at constant stress (σ_1) the failure of material occurs when the amount of cycles (n_1) reaches the maximum possible amount cycles (N_1) of σ_1 or $n_1/N_1 = 1$. If there are low-cycle constant stress (σ_1) and high-

cycle constant stress (σ_2) in a test and it goes from σ_1 to σ_2. The maximum amount of cycles (N_2) of σ_2 reduces by a part which corresponds to an amount of life exhausted or damage (D_1) at σ_1 according to the linear manner of fatigue damage accumulation. Using other words σ_2 is going to have a different S-N curve, which depicts by dash dot line in Figure 2.6. It is caused by the life exhausted (D_1) at σ_1. Palmgren-Miner linear cumulative damage law is expressed in equation 2.1.

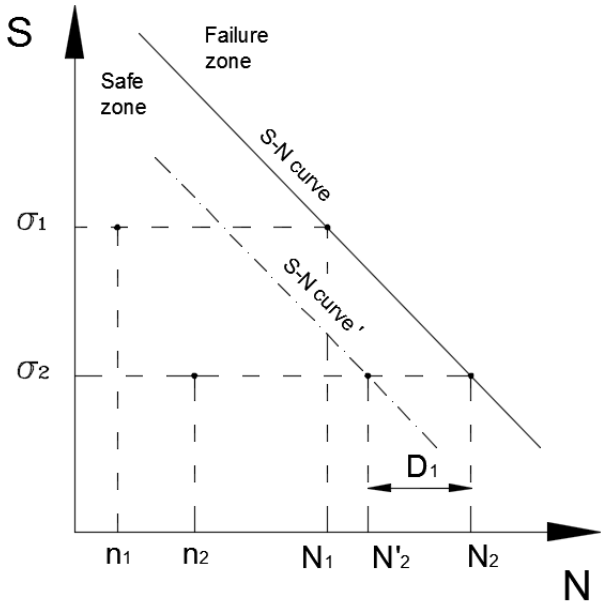

Figure 2.7: Diagram of linear cumulative damage at high to low loading sequence [16], [17]

The Rain flow counting (RFC) technique [18]–[20] method is applied to count range, mean (peaks, nadirs) and amount of cycles in a time series. The output of RFC is presented in the format of a Markov matrix, and depicts the counted means, ranges and cycles as shown in Figure 2.8.

$$D_{ip} = \sum_{i}^{k} \frac{n_i}{N_i} \tag{2.1}$$

Where n_i is counted cycles for the specific range, N_i is maximum amount of cycle or fatigue life for the specific amplitude, *k* is total number of amplitude.

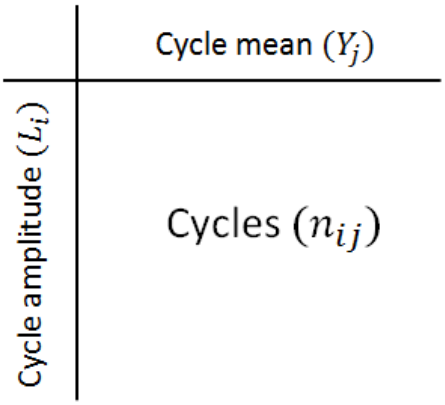

Figure 2.8: The output of RFC algorithm per each simulation.

Palmgren-Miner linear cumulative damage method assumes that cycles mean values of load do not contribute to fatigue damage as it was mention above. In this case Markov matrix of RFC outputs has to be reordered to sum up the cycles with different mean values for the specific range (see equation 2.2).

$$n_i = \sum_j n_{ij} \tag{2.2}$$

Equation 2.3 expresses the maximum amount of cycles or fatigue life variable from equation 2.1.

$$N_i = \left(\frac{L_0}{L_i}\right)^m \tag{2.3}$$

where L_i is the amplitude of cycle, L_0 is fatigue endurance or limit and m is the Wohler coefficient or exponent, which is the slope of the S-N curves. Different materials have different values for the Wohler coefficient. Steel and composite materials are typically expressed by Wohler coefficients 4 and 10 respectively. The substitution of equation 2.2 into 2.1 gives the fatigue damage per each simulation of time, which is shown in equation 2.4.

$$D_{ip} = {L_0}^{-m} \sum_i^k n_i \, L_i^m \tag{2.4}$$

The total fatigue damage of all wind speed simulations can be calculated by summation of the fatigue damage of each wind speed simulation as shown by equation 2.5

$$D_{TSim} = {L_0}^{-m} \sum_{ip} D_{ip} = {L_0}^{-m} \sum_{ip} \left(\sum_{i}^{k} n_i \, L_i^m \right) \tag{2.5}$$

Equation 2.6 depicts that the fatigue damage can be expressed in term of DELs.

$$D_{TSim} = {L_0}^{-m} n_{DEL} \, L_{DEL}^m \Rightarrow L_{DEL} = \left(\frac{D_{TSim} \, {L_0}^m}{n_{DEL}} \right)^{\frac{1}{m}} = \left(\frac{\sum_{ip} \left(\sum_i^k n_i \, L_i^m \right)}{t_{sim} \, f} \right)^{\frac{1}{m}} \tag{2.6}$$

Where, t_{sim} is 600s as simulation time, f is the reference frequency, which is $f = n_{DEL}/t_{20\,years}$. As it was mention previously Lifetime DELs are calculated by combination DELs of 10 minutes time series with wind speed probability per year. The probability of mean wind speeds is determined by the Weibull distribution, which is used to estimate the wind distribution over a year. Figure 2.9 depicts the Weibull distribution, which describes wind distribution of a site for DLC 1.1, 1.2.

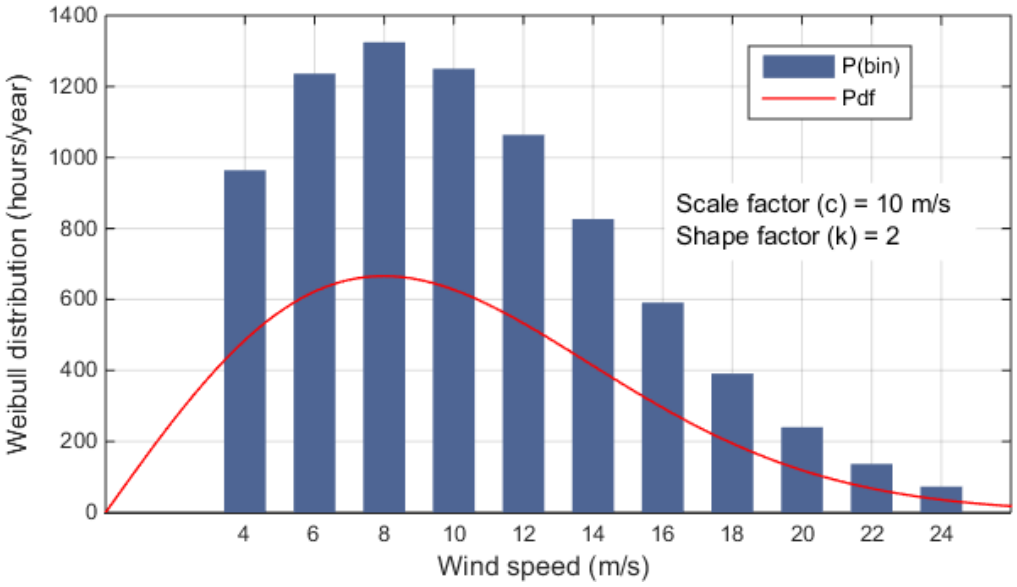

Figure 2.9: Weibull distribution for DLC 1.1 1.2 and 6.4

Equation 2.7 shows the calculation to estimate Lifetime DELs for the particular wind speed per lifespan for specific Wohler coefficient.

$$L_{DEL\,weighted} = \sqrt[m]{L_{DEL}^m \, P(v)} \tag{2.7}$$

$P(v)$ is probability of a wind speed calculated from Weibull distribution.

The Lifetime DELs of particular Wohler coefficient can be calculated from equation 2.8.

$$L_{Lifetime\ DEL} = \sqrt[m]{\sum L_{DEL_{weighted}}{}^{m}} \tag{2.8}$$

2.6. Summary

This first section of this chapter is an overview of the different types of load and what causes these loads. Section 2.2 highlights different design standards for wind turbines. IEC standards were selected for use in this study. Section 2.3 outlines the different types of design load cases (DLCs) in IEC 61400-1 standards. The DLCs characterise the minimum requirements for a wind turbine to withstand different situations, which can happen during their lifetime. Section 2.4 and 2.5 cover the most crucial DLCs of extreme and fatigue loads for a wind turbine. DLC 1.1, 1.3, 6.1 and 6.3 were selected to examine the extreme loads in this study. DLC 1.2, 3.1, 4.1 and 6.4 were chosen for fatigue loads. Additionally, the procedure of calculating extreme loads and lifetime DELs (fatigue loads) were discussed in section 2.4 and 2.5.

3. Scaling

A key research interest of this thesis is to investigate systematically the changes of wind turbine loads due to up-scaling. It is very important to note that much of the scaling in this thesis involves scaling with similarity, sometimes called "linear scaling" where all the corresponding dimensions vary linearly and in consequence, associated areas vary quadratically and masses vary cubically. Commercial designs especially at the largest scales tries to avoid the weight and associated cost penalties of such scaling and this often involves changes to blade materials and to structure and system concepts. While this is fully recognised, the reason for adhering generally to scaling with similarity is that this is most likely to reveal clear trends while the complexity in comparing essentially dissimilar commercial designs of varying scale will obscure such trends. Scaling rules are developed in other topics of this study, which include blade modifications and rotor solidity impact. This aims to suitably adjust the properties of blades to the dimensional changes. More details about these changes can be found in chapters 7, 8 and 9. Additionally, there are many works which suggest the reduction of energy cost as a result of the up-scaling wind turbine [21], [22]. In this case the chapter provides the overview of scaling with similarity method and scaling of existing commercial trend of wind turbines. Afterwards these methods are compared. Moreover, the scale effect on the cost of wind turbine components is outlined to improve understanding of how the cost changes with the scale. In the penultimate section of this chapter the size limits of wind turbines is overviewed to estimate the boundaries of wind turbine size.

3.1. Scaling with similarity technique

Scaling with similarity provides rules for changes in geometry and physical properties of a wind turbine with variation of the rotor diameter or rated power. Similarity scaling is required to maintain the original aerodynamic properties of a reference model [3], [6], [7]. The rules are

- The geometry of a wind turbine scales linearly and the material properties of the machine are preserved.
- Rated power is scaled to maintain power density (rated power/ swept area).
- The tip speed ratio remains (TSR) constant. As a consequence, a rotor angular velocity changes inversely to the size of diameter, i.e. if a wind turbine increases in size the rotor angular velocity will decrease.

Maintaining the original value of TSR of the scaled models does not preserve the same aerodynamic properties of the reference model for the scaled wind turbines, because Reynolds number modifies along with the scale of wind turbine as shown by equation 3.1. In this case the scaled turbines will naturally be experiencing different wind fields - as they are different sizes.

$$Re = \frac{\rho w c}{\mu} \qquad 3.1$$

Re is Reynolds number, ρ is density, *w* is relative velocity, *c* is a chord of blade and is the kinetic viscosity.

The difference in the aerodynamic characteristics as a function of Re is not significant as it is shown by Figure 3.1 and 3.2. Figure 3.1 depicts lift coefficient against the angle of attack for three different Reynolds number. The three curves overlap each other up until the angle of attack reaches 8 degrees. For the higher angles divergence occurs among the three Reynolds numbers. Nevertheless, the divergence among the curves is too minor to cause the significant changes for lift coefficient.

Figure 3.2 shows lift coefficient against drag coefficient for the same three Reynolds numbers as Figure 3.1. The three curves do not overlap each other but they are fairly close to each other. Figure 3.1 and 3.2 have confirmed that there are no significant changes of lift and drag coefficients due to different values of Reynolds number. Therefore, the variation of aerodynamic properties of the flows due to varying Reynolds number is minor and can be neglected for the up-scaled wind turbine [23].

- In commercial designs, geared drive trains are rarely scaled with similarity. Generator speeds related to choice of pole number and grid frequency define a limited number of specific speeds that are suitable. Thus gear ratios usually change with up-scaling, but would not if strict similarity were observed.

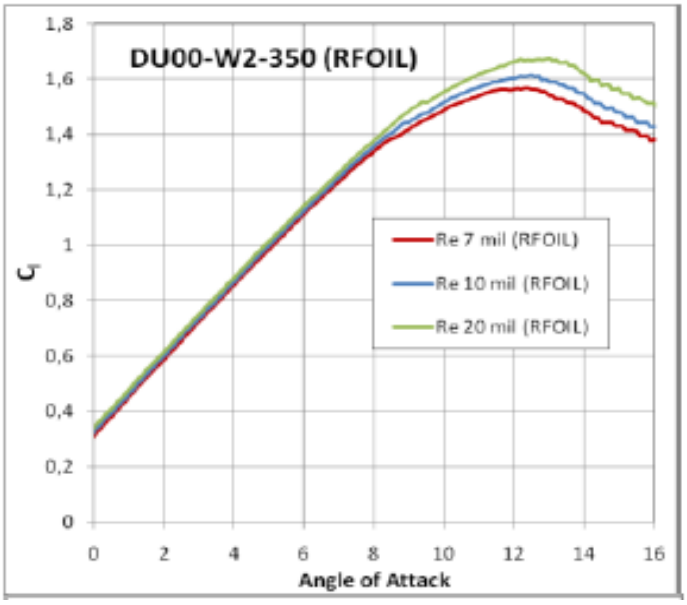

Figure 3.1: Cl against angle of attack graph [23].

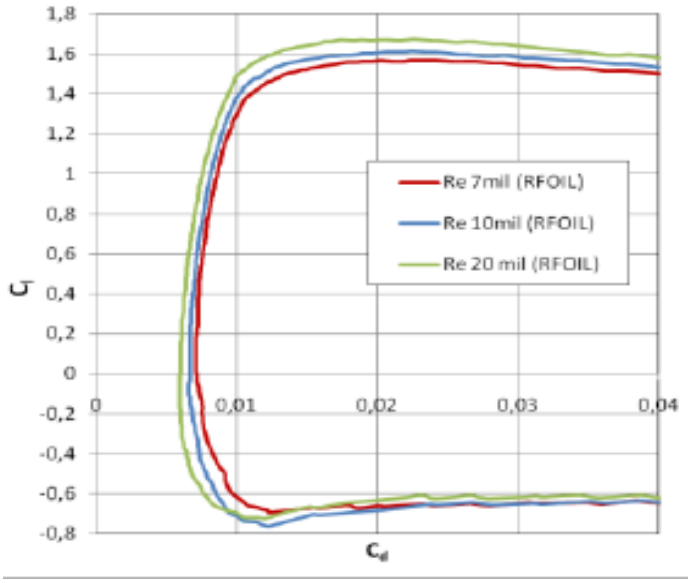

Figure 3.2: Cl against Cd graph [23].

In the past several research works were done to investigate the similarity scaling technique for wind turbines. The biggest and most valuable research from these works was the UPWIND project, which examines the influence of up-scaling onto wind turbine loading and performance [24]. However, the UPWIND project did not include the aerodynamic changes relating to wind shear from the up-scaling. Section 3.1.6 demonstrates the effect of wind shear on up-scaled wind turbines in this study. Table 3.1 demonstrates the scaling key parameters of wind turbine as function of wind turbine radius which scales linearly.

Quantity	*Symbol*	*Relation*	*Scale dependence*
Power, forces and moments			
Power	P	$\frac{P_1}{P_2} = \left(\frac{R_1}{R_2}\right)^2$	$\sim R^2$
Torque	Q	$\frac{Q_1}{Q_2} = \left(\frac{R_1}{R_2}\right)^3$	$\sim R^3$
Thrust	T	$\frac{T_1}{T_2} = \left(\frac{R_1}{R_2}\right)^2$	$\sim R^2$
Rotational Speed	Ω	$\frac{\Omega_1}{\Omega_2} = \left(\frac{R_1}{R_2}\right)^1$	$\sim R^{-1}$
Weight	W	$\frac{W_1}{W_2} = \left(\frac{R_1}{R_2}\right)^3$	$\sim R^3$
Aerodynamic moments	M_A	$\frac{M_{A_1}}{M_{A_2}} = \left(\frac{R_1}{R_2}\right)^3$	$\sim R^3$
Centrifugal forces	F_C	$\frac{F_{C_1}}{F_{C_2}} = \left(\frac{R_1}{R_2}\right)^2$	$\sim R^2$
Stresses			
Gravitational	σ_g	$\frac{\sigma_{g_1}}{\sigma_{g_2}} = \left(\frac{R_1}{R_2}\right)^1$	$\sim R^1$
Aerodynamic	σ_A	$\frac{\sigma_{A_1}}{\sigma_{A_2}} = \left(\frac{R_1}{R_2}\right)^0 = 1$	$\sim R^0$
Centrifugal	σ_c	$\frac{\sigma_{c_1}}{\sigma_{c_2}} = \left(\frac{R_1}{R_2}\right)^0 = 1$	$\sim R^0$
Resonance:			
Natural frequency	ω	$\frac{\omega_1}{\omega_2} = \left(\frac{R_1}{R_2}\right)^1$	$\sim R^1$
Excitation	Ω/ω	$\frac{\Omega_1/\omega_2}{\Omega_2/\omega_2} = \left(\frac{R_1}{R_2}\right)^0 = 1$	$\sim R^0$

Table 3.1: Scaling of key parameters of wind turbine [6]**.**

The following sections provide the overview of the scaling of specific wind turbine components. The information is extracted from "Similarity rules for wind turbine upscaling" report [24].

3.1.1. Blades

The first highlighted component of a wind turbine is the blades as they play a vital role in extracting energy from the wind flow [1]. According to the scaling with similarity the geometry of blades changes linearly. Nevertheless, the other parameters of blades scale differently such as: tip speed, mass, moments and so on. Table 3.2 highlights changes of blade parameters in terms of wind turbine radius due to the scaling with similarity. Table 3.2 shows that the energy capture increases by power of 2, but the blade mass and flap-wise moment increases cubically and edge-wise moment increases quadratically. Hence, there is a trade-off between increased energy production and loading.

Quantity	Symbol	Size dependency
Blade length	L	$\sim R$
Rotor rotational speed	w_{rot}	$\sim R^{-1}$
Tip speed	$w_{rot}\, L$	$\sim I$
Blade Chord distribution	$c_{bld}(x)$	$\sim R$
Blade thickness distribution	$t_{bld}(x)$	$\sim R$
Bladed twist distribution	$\theta_{bld}(x)$	$\sim I$
Flap-wise moment	M_{flp}	$\sim R^3$
Edge-wise moment	M_{edg}	$\sim R^4$
Rotor power	P_{rot}	$\sim R^2$
Rotor torque	T_{rot}	$\sim R^3$
Blade section area	$A_{bld}(x)$	$\sim R^2$
Area moment of inertia	$I_{are}(x)$	$\sim R^4$
Mass moment of inertia	$I_{mas}(x)$	$\sim R^5$
Blade mass	M_{bld}	$\sim R^3$
R: Linear dependency, I: Size independency		

Table 3.2: Generic similarity scaling of wind turbine blade [24].

3.1.2. Low speed shaft

Table 3.3 demonstrates the changes of low speed shaft because of scaling with similarity. The geometry of low speed shaft varies linearly same as the geometry of blade.

Quantity	Symbol	Size dependency
Shaft length	L_{lss}	$\sim R$
Shaft thickness	t_{lss}	$\sim R$
Shaft sectional area	A_{lss}	$\sim R^2$
Shaft area moment of inertia	$I_{are-lss}$	$\sim R^4$
Shaft bending moment due to weight	$M_{bnd-wgt}$	$\sim R^3$
Shaft bending moment due to tilt and yaw	$M_{bnd-yaw}$	$\sim R^3$
Shaft torsional moment	$M_{trs-lss}$	$\sim R^3$
Low speed shaft mass	M_{lss}	$\sim R^3$

Table 3.3: Generic similarity scaling of low speed shaft [24].

3.1.3. Gearbox

The changes of gearbox properties due to similarity scaling are presented by Table 3.4. As a result of gearbox complexity the gearbox mass cannot be obtained as a proportion of gearbox size. In this case the assumption was made that gearbox mass depends on the rotor torque. Consequently, this assumption can give the rough estimation gearbox mass dependency from the scaling.

Quantity	Symbol	Size dependency
Rotor rotational speed	ω_{rot}	$\sim R^{-1}$
Generator rotational speed	ω_{gen}	$\sim I$
Gearbox ratio	N_{gb}	$\sim I$
Gearbox torque	T_{gb}	$\sim R^3$
Gearbox mass	M_{gb}	$\sim R^3$

Table 3.4: Scaling of gearbox parameters [24].

3.1.4. Generator

The generator geometry or dimensions scale with similarity. In this case the generator mass was assumed to be proportional to the generator torque as shown by Table 3.5.

Quantity	Symbol	Size dependency
Generator torque	Q_{gen}	$\sim R^3$
Generator mass	M_{gen}	$\sim R^3$

Table 3.5: Generic similarity scaling of generator [24].

3.1.5. Tower

Table 3.6 shows the scaling with similarity for a tapered tubular wind tower. The parameters scale in same way as the wind turbine blades.

Quantity	Symbol	Size dependency
Tower length	L_{tow}	$\sim R$
Tower thickness distribution	$t_{tow}(x)$	$\sim R$
Tower sectional area	$A_{tow}(x)$	$\sim R^2$
Area moment of inertia	$I_{are}(x)$	$\sim R^4$
Mass moment of inertia	$I_{mas}(x)$	$\sim R^5$
Fore-aft bending moment	$M_{for-aft}$	$\sim R^3$
Side-to-side bending moment	$M_{sid-sid}$	$\sim R^3$
Torsional moment	M_{trs}	$\sim R^3$
Tower mass	M_{tow}	$\sim R^3$

Table 3.6: Similarity scaling of wind turbine tower [24].

3.1.6. Effect of wind shear

The effect of wind shear has to be taken into account because the wind shear interacts with the scaling. Using other words an up-scaled wind turbine is experiencing stronger wind flow than the reference wind turbine because the rotor of the up-scaled model is higher than the rotor of the reference model. Figure 3.3 depicts the effect of wind shear on two different size wind turbines. Wind turbine 1 is the reference model and wind turbine 2 is the up-scaled wind turbine from the reference. The up-scaled wind turbine is experiencing higher wind speeds than the reference or wind turbine 1 as shown in Figure 3.3. Therefore, it is necessary to consider the effect of wind shear in scaling method.

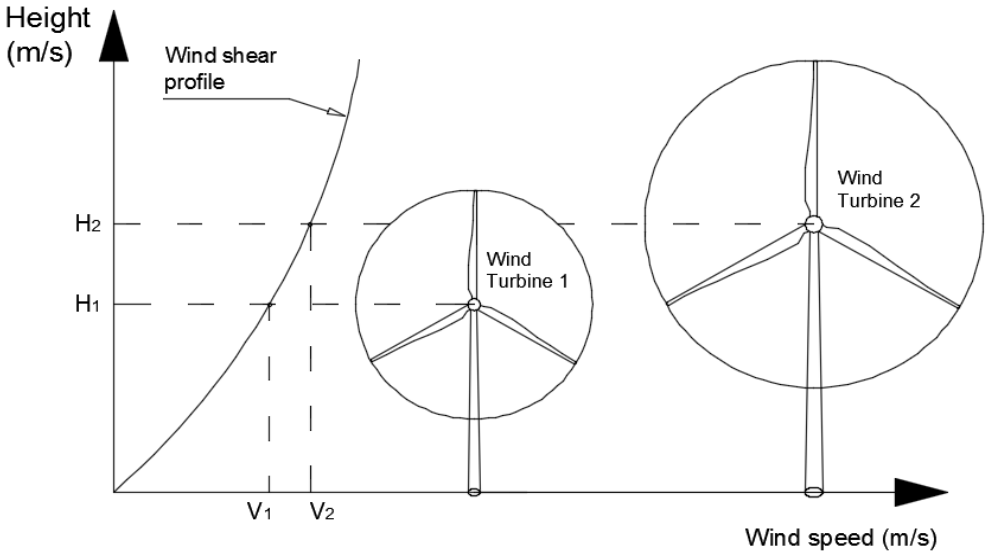

Figure 3.3: Effect of wind shear on two different sizes of wind turbines.

The power production formula is presented by equation 3.2. According to the scaling with similarity method the power increases by power two [3], [6], [7]. Moreover, the height of rotor

becomes higher as a result of the up-scaling. In this case the rotor will see the higher wind speed profile as a consequence of wind shear. Subsequently the rotor will experience higher aerodynamic loads.

$$P = \frac{1}{2}\rho\pi R^2 U^3 C_p \qquad 3.2$$

Regarding the similarity scaling, the geometry changes linearly and the original value of TSR is preserved. As a result of the assumption of the similarity scaling, the original power coefficient of reference is preserved in the scaled models. Therefore, the power production is proportional to radius and velocity [3] as shown in equation 3.3.

$$P \propto U^3 R^2 \qquad 3.3$$

The wind velocity (U) is a function of rotor height, because the wind flow speed varies with the height due to wind shear law as shown in Figure 3.3. The rotor height is proportional to the rotor radius and tower dimensions change linearly. Therefore, velocity (U) can be substituted by R^{α}, because the height is proportional to radius as it was mentioned before [3]. Alpha (α) is the wind shear exponent. Consequently, the power production can be shown as a function of radius and wind shear exponent as depicted by equation 3.4.

$$P \propto R^{2+3\alpha} \qquad 3.4$$

Equation 3.5 depicts the blade root flap-wise moment [6]

$$M_{flp} = \frac{2}{3}\frac{T}{B}R = \frac{2}{3}\frac{(0.5\rho\pi R^2 U^2 C_T)}{B}R \qquad 3.5$$

where, *B* is number of blades, *T* is thrust force and is rotor radius. Equation 3.5 showed that the flap-wise blade root bending moment is proportional to velocity and rotor radius. Applying the identical analysis of the generated power for the flap-wise blade root bending moment, it can be stated that the flap-wise blade moment is a function of radius and wind shear exponent as demonstrated by equation 3.6.

$$M_{flp} \propto R^{3+2\alpha} \qquad 3.6$$

3.2. Scaling issues affecting commercial data

This section provides an overview of the load trends of wind turbines, which are generated from commercial wind turbines. The load trends are represented as a function of rotor diameter. Commercial designs often deviate from similarity in respect of:

- operational strategy
- stage of development
- environmental condition of sites (wind class and turbulence level).

This leads to greater scatter in data and less clarity in revealing trends. However, it is still possible to notice general patterns. A more detailed explanation of load trends of commercial existing wind turbine data can be found in these works [3], [25].

3.2.1. Loading trends

This section presents the extraction of work from [3], [25] which was done by P. Jamieson. In his work forty-two pitch regulated wind turbines were employed to develop the loading trend. Stall regulated wind turbines are excluded from data as having significant different loading characteristics. Nevertheless, all these wind turbines have various operational strategies and are designed for different environmental conditions (wind class and turbulence level). In this case the data is more scattered, but a general trend is still visible. Only trend lines are shown in Figures 3.4 to 3.5 due to confidentiality of the commercial data. The loading trend lines are presented in terms of power law equations with correlation coefficient, Q^2, which indicates the goodness of fit of the trend lines to the data, i.e. $Q^2 = 0$ is no fit and $Q^2 = 1$ is perfect fit.

Figure 3.4 and 3.5 show the blade root flap-wise and edge-wise bending moment of commercial wind turbines respectively. The X axis and Y axis of Figure 3.4 and 3.5 denote rotor diameter and blade root bending moment respectively. Moreover, only trend lines are shown in Figure 3.4 and 3.5 due to confidentiality of the commercial data. The power law exponent of trend line flap-wise moment is $R^{2.86}$ and the exponent of trend line edge-wise moment scales $R^{3.25}$. The exponent of edge-wise bending moment is more severe than the exponent of flap-wise moment because the blade root edge-wise bending moment is a function of gravity loads while the flap-wise bending moment depends on aerodynamic loads. The scaling with similarity predicts that flap-wise and edge-wise blade root moment up-scales by R^3 and R^4. Hence the exponents of flap-wise and

edge-wise blade root bending moment of commercial wind turbines are not far away from the predicted values estimated by the scaling with similarity. Consequently, it demonstrates that the method of scaling with similarity can provide a good approximation of loads for the blades at the design stage of a project.

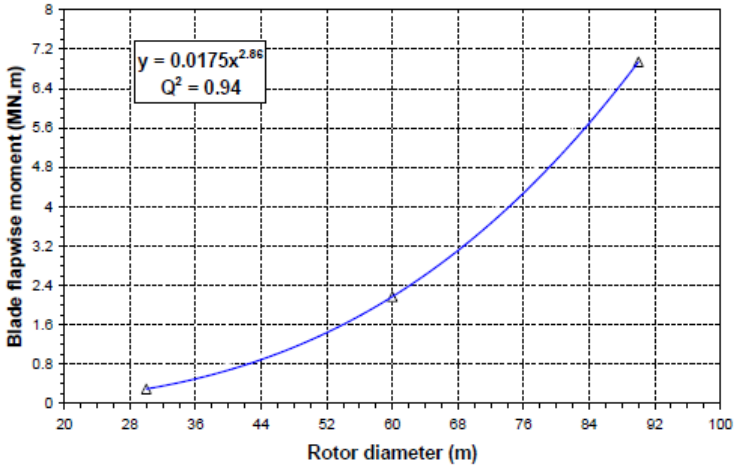

Figure 3.4: Blade flap-wise bending moment [25].

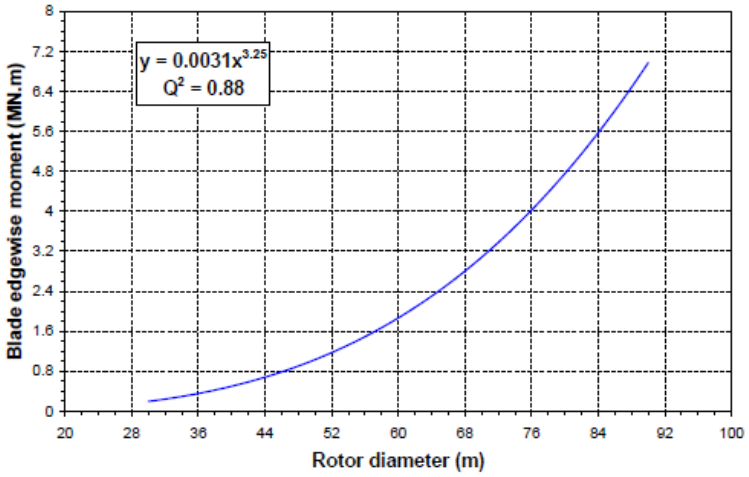

Figure 3.5: Blade edge-wise bending moment [25].

The rest of load trends are going to depict by power law formulas in Table 3.7. Additionally, the correlation coefficient of each power law equation will be included in Table 3.7.

Variables	Power law equations	
Tower fore-aft moment	$M_{f-a} = 1.7891x^{2.33}$	0.71
Tower side-side moment	$M_{s-s} = 0.0348x^{3.23}$	0.74
Tower torsional moment	$M_{tsr} = 8E-5x^{4.05}$	0.76
Shaft mass	$m_{lss} = 0.0463x^{2.76}$	0.99
Low speed shaft bending moment	$M_{wgt-lss} = 0.004x^{3.01}$	0.99
Low speed shaft torsional moment	$M_{trs-lss} = 0.004x^{3.03}$	0.99

Table 3.7: Power law equations of commercial wind turbines [3], [25], [26]

Table 3.7 depicts that commercial trend line exponents of fore-aft, side-to-side and torsional tower base moment are 2.33, 3.23 and 4.05, respectively. However, the values of Q^2, which represent statistical correlation number and illustrates the accuracy of trend lines as regard to the output data, are 71%, 74% and 76% for tower-aft, side-side and torsional tower base moment respectively. The low correlation coefficient value can be caused by the scattered data, which is a result of various operational strategies and different environmental conditions of the sites among the 42 wind turbines [25] as mentioned before. Therefore, the obtained commercial exponents are not very precise, but they show the general trend. The similarity scaling predicts that exponents of fore-aft, side-to-side and torsional tower base are equal to R^3 as shown in Table 3.6. In this case the commercial exponent of fore-aft tower base moment is smaller by 22% than the predicted exponent, but the commercial exponent of side-to-side and torsional tower base moment is larger by 8% and 35% respectively.

In the work of Peter Jamieson [3], [25] there is no load trends for shaft moments, but there is the trend of shaft mass for Enercon machines in his work. The commercial exponent of shaft mass for Enercon units is slightly lower than the predicted exponent, R^3, from Table 3.3. The mass of the shaft is proportional to the torsional bending moment of shaft, because the moment arm does not change with the scaling with similarity. Additionally, the research work of scaling trend for prospective offshore wind turbines [26], which has designed the three optimised offshore wind turbines were designed with rated power 5MW, 10 MW and 20 MW, is employed to examine how the low speed shaft bending moment scales. $M_{wgt-lss}$ and $M_{trs-lss}$ exponents of these three optimised machines are around 3, which matches perfectly with the predicted exponents of low speed shaft moments (see Table 3.3) estimated by the scaling with similarity. Moreover Q^2 is 0.99, which shows almost perfect correlation between trend line and data, for exponents of $M_{wgt-lss}$ and $M_{trs-lss}$.

3.2.2. Rated power trend

This section investigates the trend in the rated power of wind turbines. In works [3], [25], [27] there is no graph that shows the trend of rated power for the commercial data. In this case the generated rated power of wind turbines has been collected from the web sites of major manufactures such as: Siemens, Vestas, Gamesa and so on. Overall 71 onshore and offshore wind turbines have been selected to generate the trend of power production scaling. Figure 3.6 demonstrates the up-scaling of rated power of commercial wind turbines, where the rated power is presented as a function of rotor diameter. The exponent of power law equation is 2.36 approximately, which is larger than the prescribed exponent scale factor (R^2) by square-cube law or scaling with similarity. Probably, it is the consequence of the wind shear effect, which was mentioned in section 3.1.6. However, the elimination of small wind turbines, diameter less than 40 m, from data minimise the exponent.

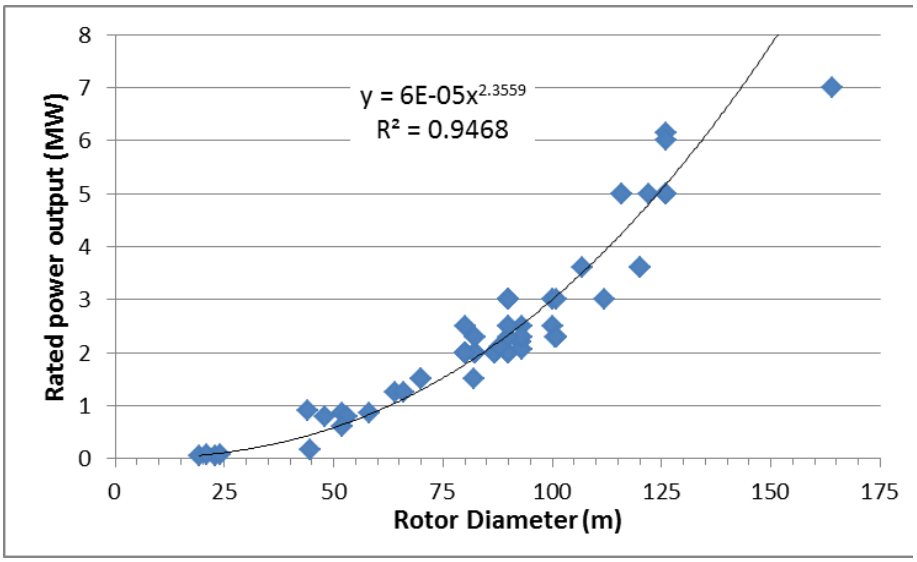

Figure 3.6: Power production scaling of commercial wind turbines.

Figure 3.7 shows the trend of rated power without small wind turbines, which are smaller than 40m. The exponent of the optimised trend is equal to 1.93, which is closer to the foreseen exponent value, which is equal to 2. To sum up this section, the production power of commercial wind turbines scale by almost the same value as that predicted by the scaling with similarity.

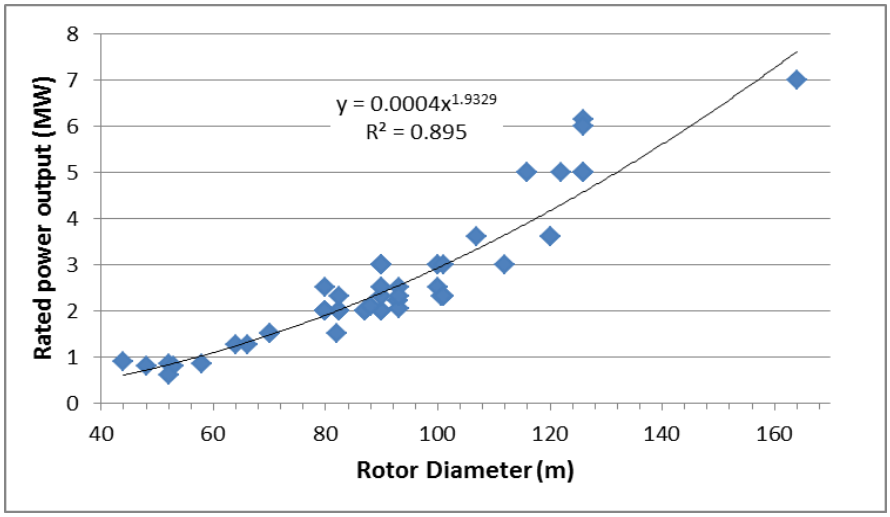

Figure 3.7: Power production scaling of medium and large commercial wind turbines.

3.3. Comparison of similarity scaling with commercial data

This section compares the calculated exponents of commercial wind turbines with the theoretical exponents of scaling with similarity rule. Table 3.8 depicts the commercial and theoretical exponents extracted from section 3.1 and 3.2. Additionally, Table 3.8 includes Q^2 of the commercial power law trends.

Variables	Exponent of commercial wind data		Exponent of scaling with similarity
Flap-wise blade root moment	2.86	0.94	R^3
Edge-wise blade root moment	3.25	0.88	R^4
Tower fore-aft moment	2.33	0.71	R^3
Tower side-side moment	3.23	0.74	R^3
Tower torsional moment	4.05	0.76	R^3
Shaft mass	2.76	0.99	R^3
Low speed shaft bending moment	3.01	0.99	R^3
Low speed shaft torsional moment	3.03	0.99	R^3
Electrical power output	2.36	0.95	$R^{2+3\alpha}$

Table 3.8: Comparison between the calculated exponents of commercial wind turbine and theoretical exponents of scaling with similarity method [3], [24]–[26].

The correlation coefficients of tower base moments are not relatively high compared with the rest values of Q^2 for different variables in Table 3.8.

The commercial exponents of flap-wise and edge-wise blade root moment are 2.86 and 3.25, respectively. Scaling with similarity predicts that the exponents of flap-wise and edge-wise blade

root moment are 3 and 4, respectively. The deviation between the predicted and commercial exponents is 5% and 19% for flap-wise and edge-wise blade root moments. The comparison of flap-wise blade root moment showed a good match, but for edge-wise blade root moment there is significant difference. Possibly, the difference at edge-wise blade root moment is a consequence as the scaling with similarity preserve the technology of the reference model, but the commercial wind turbines are updated in terms of technology and design in order to reduce the blade mass as it leads the reduction in cost of other wind turbine components [28].

For tower base moments the comparison showed more major difference than in the blade root moments apart from tower side-to-side base moment, where the exponent of commercial wind turbines is larger by 8% than predicted one. For the fore-aft tower base moment the commercial exponent is smaller by 22% than the foreseen exponent, but for tower torsional moment the commercial exponent is larger by 35%. However, *Q*-squared values of three tower commercial trends are not high enough to rely much on the calculated exponent. Probably, the significant difference between the commercial and predicted exponents is a result of the uncertainties of the commercial data, which are operational strategy and environmental condition of sites, as was mentioned before.

The shaft mass scales slightly smaller than the rule of scaling with similarity predicted. The difference between the exponent of commercial data and scaling rule is 8%. The exponents of low speed shaft bending moments almost match the theoretical exponents as shown in Table 3.8.

The electrical power output of commercial wind turbines scales by 2.36 exponent, which is higher than the predicted exponent by scaling with similarities [24]. It is a result that the method of scaling with similarities does not consider the effect of wind shear in scaling. According to the effect of wind shear in the scaling the power scales up by $2 + 3\alpha$ as shown in section 3.1.6 and by the commercial wind turbines in Figure 3.6.

The comparison between exponents of commercial data and those predicted by the scaling with similarity demonstrated a good ability to predict the loads, especially for blades and shaft. The scaling with similarity technique cannot provide very high accuracy of load prediction because of its assumption, which preserves the original shape and technology of the wind turbine. Hence, the technology progress and improvement of design are not considered by the method of scaling with similarity. However, this technique can provide a reasonable approximate insight of loads changes and physical parameters in the primary phases of design studies.

3.4. Size limits of wind turbines

There are certain boundaries to wind turbine size, which illuminate the possible minimum and maximum size for wind turbines. This section goes through the requirements, which have to be met to allow wind turbines to operate.

3.4.1. The lower limit of wind turbine size

The rotor of a horizontal axis wind turbine rotates because of torque generated by lift and drag force, which depend on Reynolds number, which is a function of the relative velocity as shown in equation 3.1.

Reynolds number is vital for the generating the lift and drag force. In low Reynolds number (*Re < 50 000*), which characterises the small wind turbines (diameter < 5m), there is the increase of drag that limits the efficiency of small wind turbines [29].

3.4.2. The upper limit of wind turbine size

The maximum size of a wind turbine depends on the gravity loads, which come from the weight of material. The square-cube law and linear scaling technique state that if the generated power increases by the square because of the expanding of the radius of rotor, the mass of rotor or blades increases by power three. The growing of mass has a significant affect for fatigue loads contribution, especially for the edge-wise blade root moment, which is mainly a function of the gravity. Equation 3.7 expresses the edge-wise blade root bending moment of a blade [7].

$$M_{edg} = mgl \tag{3.7}$$

where, m is mass of a single blade, g is acceleration due to gravity, l is distance between the blade root and point of centre gravity mass.

Therefore, the self-weight of the structure material sets boundaries for the maximum available size of a wind turbine. According to UPWIND report [30] there are suitable technologies and materials to build a 20 MW wind turbine. However, the limit is determined by economics, which are challenging for the large three bladed up-wind wind turbines.

3.5. Summary

The first section of this chapter showed the overview of the scaling with similarity method. It also included the prescribed changes of blade, low speed shaft, gearbox, generator and tower in terms of the scaling with similarity. Moreover, the effect of wind shear on up-scaled wind turbines was included. Section 3.2 highlighted the scaling of existing commercial data for loads and power production. The comparison between the existing commercial data and the scaling with similarity was shown by section 3.3, which declared that the similarity scaling can provide adequate prediction of wind turbine properties due to scaling scale. In section 3.4 limits to scaling were reviewed.

4. Numerical model

Nowadays there are a vast number of software tools and computer codes, which can be used to design or examine specific components of wind turbines or the entire machine. Unfortunately, numerical models cannot simulate all circumstances that a unit goes through during its lifespan. However, the numerical models can predict fairly accurately the behaviour of wind turbines during the most severe circumstances (weather conditions or any fault), which must be withstood by wind turbines according to design requirements. This chapter focuses to highlight the commonly used wind turbine simulation software simulations or numerical models for design of wind turbines. Advantages and disadvantages of the simulation software are overviewed in order to choose the appropriate software for this study. Algorithms, which are used in the selected wind turbine simulation software, will be briefly highlighted to familirise a reader. Section 4.3 highlights the reference coordinate systems of this study to minimise any uncertainties of reading graphs or data. Section 4.4 describes briefly the simple PI controller as the applied modification of the reference wind turbine model requires this new controller.

4.1. Simulation software

This section highlights software and codes, which were developed to perform an analysis for wind turbine models.

4.1.1. FAST

Fatigue, Aerodynamics, Structures and Turbulence (FAST) is an open source code, which is used for the aerodynamic and dynamic analysis of horizontal axis wind turbines. FAST is a summation of three codes [31], which are the code for two-bladed units (FAST2), the code for three-bladed machines (FAST3) and AeroDyn, a code to calculate the aerodynamics of wind turbine blades [32]. The FAST code is certified to perform the design load calculation for onshore machines by Germanisher Lloyd WindEnergie [33]. The more detailed explanation of FAST can be found in theory and user manuals [31], [34].

4.1.2. HAWC

HAWC stands for Horizontal Axis Wind Converter, which was developed by Riso National Laboratory. This code was developed to compute loads of horizontal axis wind turbines [35]. Finite element method (FEM) is applied to implement structural calculations. HAWC code has several restrictions. There is no high accuracy in the representation of large deflections. This is an outcome of the structural model of the machine, which consists of three sub-structures (i.e. rotor, nacelle and tower) with local coordinate systems for each sub-structure. The code calculates the deflection of any sub-structures in a linear manner[36].

4.1.3. Garrad Hassan Bladed

GH Bladed is commercial software, which obtains loads and full range performance of a wind turbine. This software is applied for designing entire and specific components of a wind turbine. BEM theory is employed to do aerodynamic calculations in Bladed.

In GH Bladed software the structural calculations are performed by modal analysis, which uses modals to express the dynamics of a wind turbine. The modal analysis is based on the same approach used in the investigation of the dynamics of helicopters, which is a very dependable method, because it requires few degrees of freedom to provide a decent dynamic model of the wind turbine. The detailed discussion to the background theory of Bladed can be found in Bladed Theory manual [10].

4.2. Selection of numerical model

The previous section provides the brief overview of three different numerical models, which are implemented to design and analyse wind turbine modes.

GH Bladed software package was chosen to use in the research as a numerical model for the analysis of wind turbines, because it is the most common used software by commercial companies in the industry. Onshore and offshore wind turbines can be certificated by GH Bladed software because the accuracy of GH Bladed generated results has been validated by a comparison between the numerical calculated data and the measured data from a variety of

existing wind turbines [10]. GH Bladed is based on the blade element moment momentum theory, which is going to outline in section 4.2.1. Moreover, GH Bladed includes the dynamic stall, which is overviewed in section 4.2.2.

4.2.1. Classical blade element momentum theory (BEM)

The BEM theory is based on the combination of two theories: blade element and momentum [1], [6], [7], [37]. According to the assumption of blade element theory the blade of a wind turbine can be separated into minor segments, which are discrete to the adjacent segments. The two dimensional aerofoil characterises of each segment are applied to obtain the aerodynamic forces from the local aerofoil flow. The total forces acting on the blade is the summation of the local forces of each segment. According to the momentum theory the pressure drop in the vicinity of the rotor plane is a result of work done. In this case the axial and tangential induced velocities acting on the aerofoil can be calculated from the pressure drop in wind flow next to the rotor plain. The local flow velocities of aerofoil of each segment are amended by the induced velocities. Therefore, the aerodynamic forces calculated by blade element theory depend on induced axial and tangential velocities obtained by momentum theory.

The advantage of BEM theory is the simplicity of method, which applies the two dimensional aerofoil to determine the aerodynamic forces from the inflow speed with the combination of induced velocities. The aerodynamic forces are employed to calculate the torque and thrust, which are important forces to design a wind turbine.

However, there are restrictions to BEM theory, which are briefly highlighted below.

- As it was mentioned before the aerodynamic calculations are based on the two-dimensional independent aerofoil for each segment. As a consequence, span-wise flow is ignored, which leads to small variations of pressure along the blade length. In practise, there is a significant pressure variation, especially for heavily loaded rotors.

- The BEM theory assumes that the aerofoil circulation of each segment is under the conditions of static inflow. In this case the speed of passing flow of aerofoil varies immediately to avoid time spending to build the circulation around the aerofoil to adjust to the alterations of wake vortices. In reality, the building of circulation around aerofoil requires time to adjusts to the alterations of wake vortices due to the changes of inflow [38].

- The BEM theory fails when there is large out of plane deflection of the blades. The momentum theory assumes the pressure drops occur in the vertical plane, which is parallel to the rotor plane. Any large deflection of blades leads to the distortion in the rotor plane from the vertical position. Consequently, errors develop.

- There are additional limitations such as: tip loss, hub loss and skewed wake correction. Prandtl model and Glauert correction [39] are applied to improve these limitations.

The detailed explanation about the BEM theory can be found in books and reports [1], [6], [7], [32], [37].

4.2.2. Dynamic stall

In GH Bladed the dynamic stall model is based on semi-empirical Beddoes-Leishman model [40]–[42], which was developed to analyse helicopter rotors, with the applied modifications [10]. The stall characterises the detached flow from the upper surface of the aerofoil. The stall occurs at high angle of attack. The dynamic stall provides the approximation of a fluctuating aerofoil, which describes the unsteady flow (turbulence, wind shear, gust and yaw misalignment) behaviour around the fluctuating aerofoil. In dynamic stall there is the delay of the stall occurring due to the above mentioned unsteady condition. Consequently, the lift coefficient goes beyond the maximum value of lift coefficient compared to the static case. The dynamic stall expresses the appearing the vortex at vicinity to the leading edge of the suction side of aerofoil [43]. During the period of time when the vortex travels with the flow along the suction side of aerofoil to the trailing edge and the angle of attack keeps rising, the lift coefficient keeps rising higher than the maximum static value. The circulation around aerofoil maintains up to the traveling vortex leaves the trailing edge. After the flow separates from the suction side of aerofoil and the lift force falls. The stall conditions remain as long as the angle of attack reaches the requirement minimum to attached flow to the aerofoil for the developing the circulation around the aerofoil.

4.3. Coordinate system of GH Bladed

There is a possibility of variation of coordinate system among the different numerical models. To avoid confusion, the reference coordinate system of this study is provided here section 4.3.

Based on Germanischer Lloyd standards [44], [45] GH Bladed uses four different coordinate systems to express outputs of aerodynamic loads and blade. The principal axis type was selected as the reference coordinates system of this study for the blade. Figure 4.1 demonstrates the principal axis, where the Z-axis follows along the span-wise or deflected neutral (pitch) axis. The Y-axis is tangential to a rotor plane, fixed to blade root and does not rotate with pitch. The X-axis follows same direction as a wind flow and is orthogonal to the Y and Z axis.

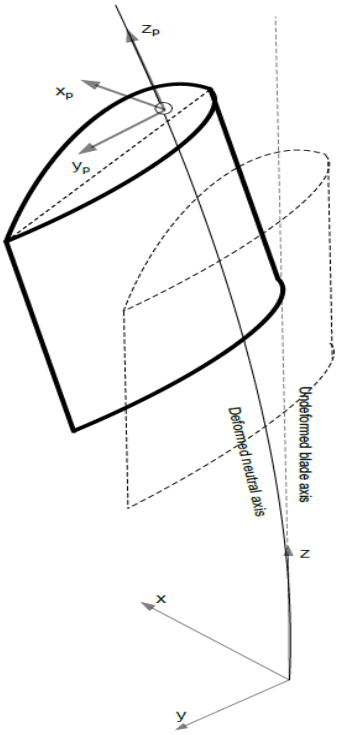

Figure 4.1: Diagram of blade principle axis [11].

The reference coordinate systems for hub, rotor, yaw bearing and tower, of the wind turbine are shown in Figure 4.2.

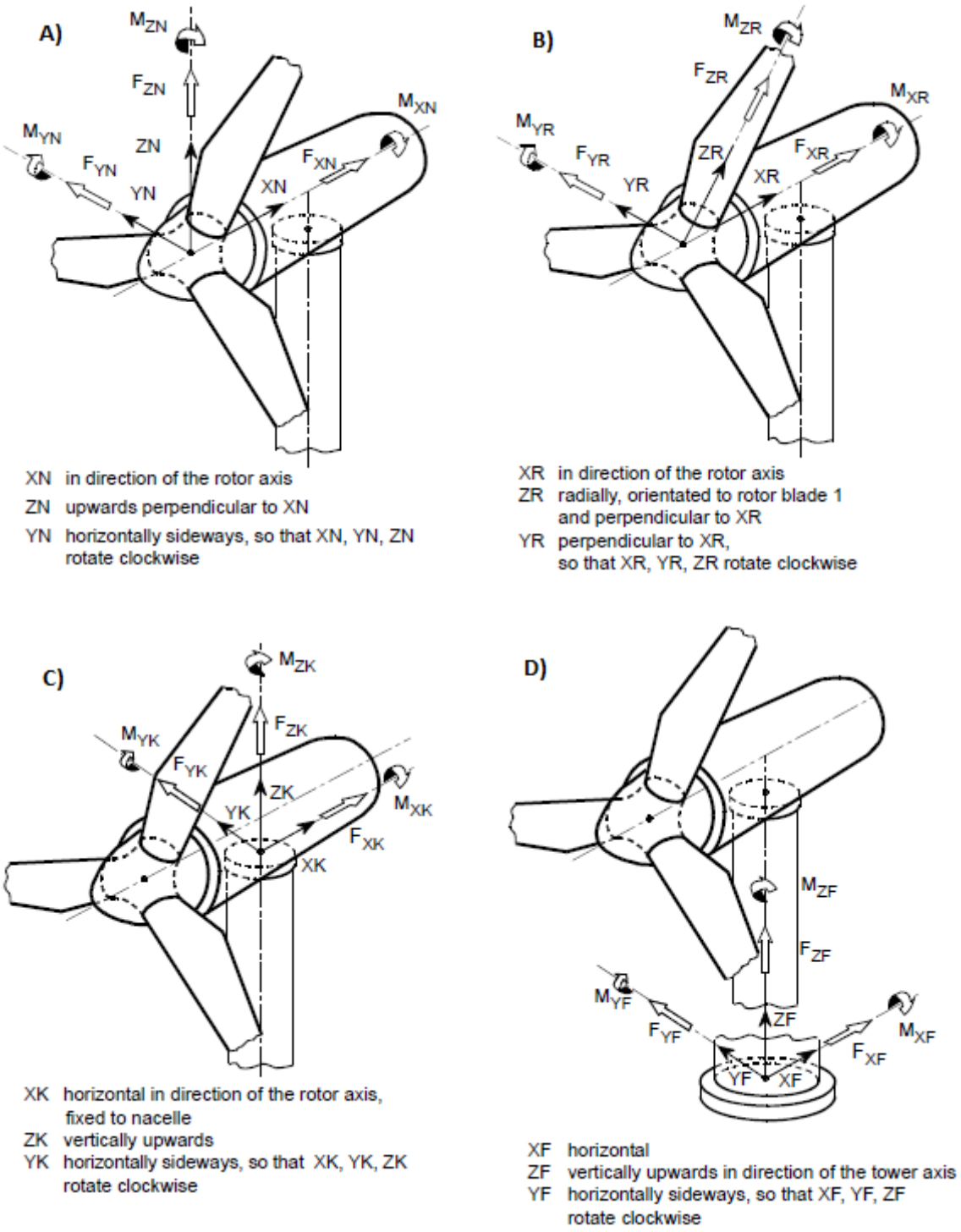

Figure 4.2: Reference coordinate systems for hub (A) , rotor (B), yaw bearing (C) and tower (D) [44], [45].

4.4. PI simple controller

In this section a brief explanation of the wind turbine controller is presented A simple PI controller is chosen for use with the modified models to provide a clear picture of the generic trends in loading. As although more sophisticated controllers could be used to better alleviate loads, these would actually mask some of the trends that this work is trying to identify.

Every wind turbine has a control system, which makes sure the wind turbine operates in an automatic and safe way to provide stable energy production without fluctuation and minimise the operational loads. The original controller of reference model is designed for the reference model and its properties. The applied modifications to the reference wind turbine model changes the properties of the reference model. In this case the modified reference model requires the new controller, which matches the properties of the modified reference model. Figure 4.3 depicts the block diagram of the simple controller, which is built in GH Bladed software, for the variable generator speed and pitch regulated wind turbine.

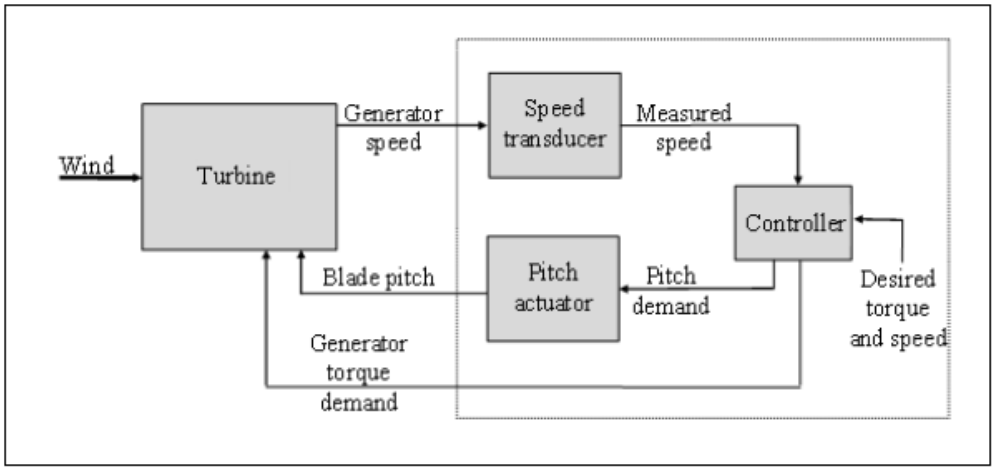

Figure 4.3: Scheme of the simple controller algorithm for a variable speed pitch regulated wind turbine [10].

The variable speed provides the variation of rotor speed, which is done by decoupling the frequency of the generator from the grid frequency by the converter. In this case the reaction or load torque can be controlled by the generator in the below rated region [1], [10], [46]. Equation 4.1 shows that the extracted power from wind is a product of aerodynamic torque and rotor speed.

$$P_a = \Omega \, T_a \qquad 4.1$$

Maintain the maximum value of power coefficient by the setting optimal tip speed ratio increases energy capture at the below rated region as shown in equation 4.2.

$$T_a = 0.5\,\rho\pi R^3 U^2 \frac{C_p}{\lambda} = 0.5\,\rho\pi R^5 \Omega^2 \frac{C_p}{\lambda^2} \qquad 4.2$$

Bossanyi *et al*. [46] declares that the optimum TSR can be retained if the generator torque is a function of the generator speed square as in equation 4.3.

$$T_g = T_a - T_L = 0.5\,\rho\pi R^5 \omega_g^2 \frac{C_p}{\lambda^3 G^3} - T_L = K_{opt}\,\omega_g^2 - T_L \qquad 4.3$$

K_{opt} is optimal gain which maintains the optimal tip speed ratio, *G* is gear box ratio, $\omega_g\ (= G\Omega)$ is generator speed, $\lambda\ (= \Omega \mathrm{R/U})$ is tip speed ratio, T_a is aerodynamic torque and T_L is mechanical losses.

Figure 4.4 depicts the work strategy of a variable speed and pitch control wind turbine at steady state. The operating curve is divided into several sectors. S1 is the first constant speed section and shows 'cut in', where the minimum rotor speed is specified along with the minimum operating wind speed of the wind turbine. There is the gap in the operating curve between S2 and S3 to avoid a resonance with the tower, because 3P harmonics of rotor frequency passes through the first tower structural bending mode. The second constant speed section is presented by S4, where the maximum generator speed is set. Sector S5 is an optional choice and it is not very common. This sector is applied to introduce a boundary between the two control strategies to avoid unnecessary swapping between below and above rated control strategies due to a wind gust. Usually there is no sector S5. As a result, H and L points are commonly coincident.

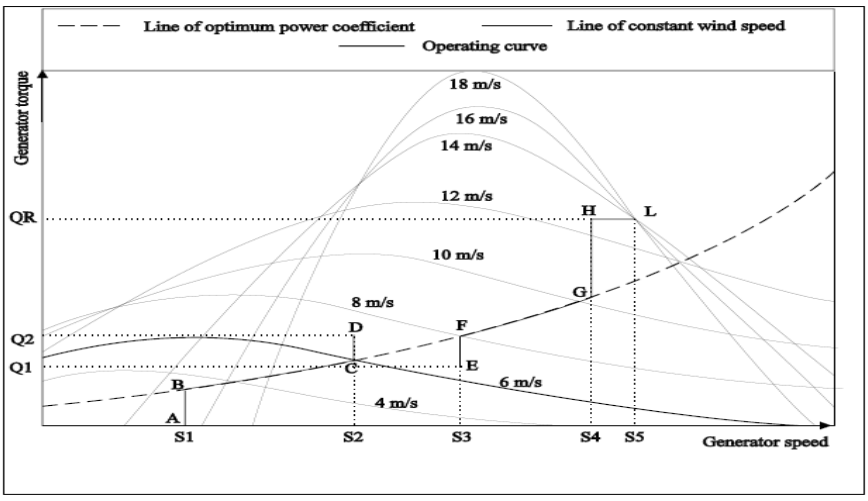

Figure 4.4: Strategy of variable speed and pitch regulated wind turbine [10].

The region between S1 and S4 or the trajectory A-B-G-H depicts the below rated region. BG segment of curve corresponds to maximum power coefficient, which is maintained by optimal gain (K_{opt}) , which is expressed in by equation 4.4 [3], [46].

$$K_{opt} = \frac{\pi \rho R^5 C_p}{2\lambda^3 G^3} \quad 4.4$$

The torque control strategy is employed to operate at the below rated region. Therefore, the pitch control is not active and the pitch angle is constant in the below rated region. When the wind speed reaches the above rated region, the torque controller becomes inactive by the setting the constant rated value for the torque demand. The pitch control system starts to operate to maintain constant torque and generator speed. In the built-in controller there is a switch to choose a control strategy for the below or above rated region as shown in Figure 4.5. The switching procedure is activated by the generator speed as the minimum and maximum generator speeds are set. If the generator speed is located at range between the minimum and maximum generator speeds, the below rated strategy is chosen. If the generator speed is equal or more than the maximum value, the switch selects the above rated strategy. Additionally, there will also be a torque ratchet or similar, otherwise when the wind speed dips above rated and the rotor speed drops it will suddenly be "below rated" despite having a positive pitch angle.

This procedure for generating maximum energy in the below rated region is based on in the steady state condition. In reality the maximum *Cp* value cannot be tracked perfectly because the wind speed varies continuously and rapidly. The high inertia of the wind turbine rotor precludes the fast changes of rotor speed limiting capability to follow the changing velocity of the wind [1], [46].

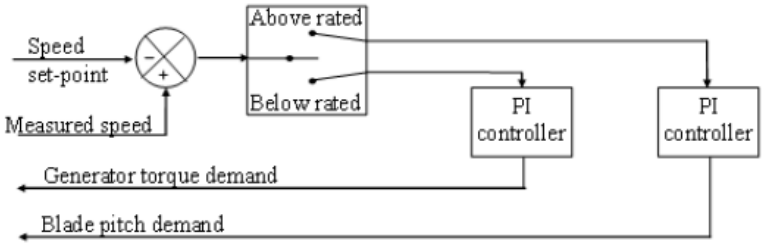

Figure 4.5: Simple controller of the variable speed and pitch regulated wind turbine [10].

4.5. Summary

This chapter highlighted and briefly overviewed three numerical models, which are commonly used for wind turbine calculations, in order to choose the base numerical model to perform calculations for this research. The GH Bladed software tool was selected for this study to perform the analysis because it is most commonly used software in the industry and certified by Germanischer Lloyd. The reference coordinate system is defined for different components such as: blade, hub, rotor, yaw bearing and tower. An overview was provided about GH Bladed built-in simple PI controller, which is used for the modified reference wind turbine models.

5. Methodology

This chapter consists of two parts which are the approach procedure of investigation (for the changes of extreme and fatigue loads) and wind flow modelling. Section 5.1 of the chapter provides the overview of wind modelling based on the IEC 61400-1 standards [5] in order to perform simulations. According to the IEC standards Kaimal or Mann can be used to generate the wind flow. Both of these models and parameters of wind flow are reviewed to choose the most relevant for this study. Additionally, section 5.1 includes the description of the normal turbulence model, extreme turbulence model, extreme wind speed model and wind classes, which are used in this study.

Section 5.2 describes the calculation methods, which are applied to investigate the changes of wind turbine loads as a consequence of the modification of the reference models. The instantaneous loads are examined by basic statistics and spectral analysis. The post processing calculations are applied to calculate the lifetime damage equivalent loads and extreme loads.

5.1. Modelling of wind flow

Following the IEC standard, Design Load Cases (DLCs) are employed to calculate the extreme and fatigue loads of the modified reference wind turbine models. In chapter 2, DLC 1.1, 1.3, 6.1 and 6.3 are selected to perform the calculation for extreme loads, and DLC 1.2, 3.1, 4.1 and 6.4 for fatigue loads.

In order to perform any simulation of DLCs the wind profile has to be generated for the wind speeds specified by the requirements of DLCs in the IEC standard [5].

5.1.1. Selection of wind flow model

In GH Bladed software there are three approved models: Kaimal [47], Von Karman [48], [49] and Mann [50], [51], which can be used to generate the wind flow. However, the Von Karman wind flow model is not presented in IEC 61400-1 standards [5] (it was removed from the third edition of IEC standards in 2005 [52]), because the von Karman wind flow model is not accurate for the prediction of atmospheric turbulence below 150 meters altitude [1]. However, the detailed explanation of the von Karman model can be found in Wind Energy Handbook [1]. The hub

height of current and prospective wind turbines is lower than 150 meters. Thus, the Von Karman wind flow model is not applicable.

According to IEC standards, the wind flow can be generated by either Kaimal or Mann model. In order to choose the right model for the wind flow, the power spectral density (PSD) analysis must be used to investigate the Kaimal and Mann model, because each model has to provide the sufficient approximation of real wind flow conditions. To obtain an adequate approximation of wind flow the spectrum of each model has to approach the asymptotic limit proportional to at high frequencies based on Kolmogorov's law, which characterises the energy distribution of turbulence in the wind flow [1], [53].

Figure 5.1 depicts the wind speed spectrums of Kaimal and Mann models at the hub height with the asymptotic limit. At the higher frequencies the spectrum of Mann model goes away from the asymptotic limit, which shows that the accuracy of the approximation is deficient. The effect of Mann model spectrum distancing away from the asymptotic limit is caused by an insufficient amount of FFT points for lateral and vertical directions wavelengths [10]. The accuracy of the Mann model can be improved by increasing the number of FFT points, but the increased amount of FFT points has an impact on the computer memory required, limiting use. Therefore, the Kaimal model is selected to generate the wind flow for this project, because it is more consistent, provides better approximation of wind flow and requires less computer capacity compared to the Mann wind flow model.

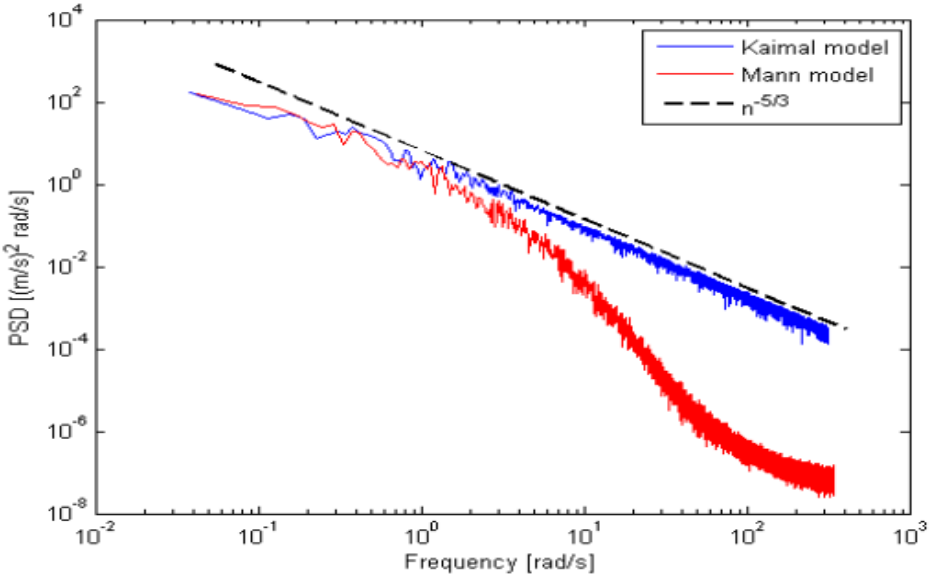

Figure 5.1: The PSD of Kaimal and Mann wind flow models at the hub height [54]

5.1.2. Generation of the wind flow

The Kaimal model has been selected to generate the wind flow as explained in section 5.1.1. In order to generate the wind flow the parameters of the Kaimal model and wind profile characteristics must be specified as shown by Table 5.1 and 5.2.

Axis components	$\boldsymbol{XLu}$	$\boldsymbol{XLv}$	$\boldsymbol{XLw}$
Standard deviation	σ	$0.8\,\sigma$	$0.5\,\sigma$
Length scale	$8.1\,\beta$	$2.7\,\beta$	$0.66\,\beta$
Coherence decay constant	12		
Coherence scale parameter	$8.1\,\beta$		

Table 5.1: Parameters of Kaimal model turbulence spectrum [5].

β is longitudinal scale parameter $\beta = 0.7z$ if $z = \leq 60m$ or $\beta = 42$ m if $z > 60m$

- *XLu* is longitudinal direction or along wind flow
- *XLv* is lateral or perpendicular to the longitudinal direction
- *XLw* is vertical direction or perpendicular to both above mentions directions.

Note, the values of standard deviation of the three components are invariant with height. The power spectral density of the three perpendicular turbulence components asymptotically $S_1(f)$, $S_2(f)$, $S_3(f)$ approach the following forms as the frequency in the inertial sub range increases:

$$S_1(f) = 0.05\sigma_1^2 \left(\frac{\beta_1}{V_{hub}}\right)^{-\frac{2}{3}} f^{-\frac{5}{3}} \quad 5.1$$

$$S_2(f) = S_3(f) = \frac{4}{3} S_1(f) \quad 5.2$$

Wind profile parameters	Units	Value
Number of points along Y axis	-	40
Number of points along Z axis	-	50
Volume width Y	m	200
Volume height Z	m	250
Duration of wind file	s	600
Frequency along X	Hz	13.6533
Mean wind Speed	m/s	4-25
Turbulence Seeds	-	1-999
Time Step	s	0.02

Table 5.2: Characteristics of wind inflow

The number of points along Y and Z axis represents the grid resolution of wind flow, which influences the accuracy of synthetic wind flow compared to the real wind flow. However, the simulation time of generating a wind profile is a function of the grid resolution or number of points raised to the power 4 [10]. Hence, it is often necessary to choose the smallest number of points to produce sufficiently accurate results. The GL guide advises to use less than 10 m spacing for the grid [44], [45]. For this research it was selected to use 5 m for the grid spacing.

Turbulence seeds are a random number, which is varied from 1 up to 999 to characterise the specific turbulence profile based on a fixed method and fixed statistical parameters [11]. In order to achieve sufficient results, each mean wind speed requires at least six 10-minute simulations with the different numbers of turbulence seeds [5]. Uncertainty in results can be reduced by increasing the number of 10-minute simulations with a dissimilar turbulence profile per each mean wind speed [13].

5.1.3. Turbulence models

As was mentioned in chapter 2, the selected design load cases are applied to perform the calculation for the extreme and fatigue loads. According to IEC Standards a specific turbulence model is assigned for each DLC. In this research there are three turbulence models, these are: normal turbulence model (NTM), extreme turbulence model (ETM) and turbulent extreme wind model (EWM). A brief explanation about the turbulence models is extracted from the IEC 61400-1 standard [5] and located in subsection 5.1.3.1, 5.1.3.2 and 5.1.3.3 . Each of the turbulence models depends on wind turbine classes, which are characterised by the mean wind speed and level of

turbulence intensity as shown in Table 5.3. The wind turbine class is representative of the most severe category wind conditions that a turbine has been designed for.

Wind turbine class		I	II	III	S
V_{ref}	(m/s)	50	42,5	37,5	Values
A	I_{ref} (-)	0,16			specified
B	I_{ref} (-)	0,14			by the
C	I_{ref} (-)	0,12			designer

V_{ref} is the reference wind speed average over 10 min,
A designates the category for higher turbulence characteristics,
B designates the category for medium turbulence characteristics,
C designates the category for lower turbulence characteristics and
I_{ref} is the expected value of the turbulence intensity[3] at 15 m/s.

Table 5.3: Properties of wind turbine classes

5.1.3.1. Normal turbulence model

For the normal wind conditions, the shear coefficient is assumed to be equal to 0.2. The mean velocity of the inflow across the rotor defines the wind profile, which is a function of the vertical distance from the hub and wind shear coefficient as shown by equation 5.3.

$$V(z) = V_{hub}\left(\frac{Z}{Z_{hub}}\right)^{0.2} \quad 5.3$$

The wind profile is applied to represent the average wind shear across the swept area of rotor. At the hub height the turbulence standard deviation of the wind speed is defined by equation 5.4 for the normal turbulence model.

$$\sigma_1 = I_{ref}(0.75V_{hub} + b)\,; \quad b = 5.6\,m/s \quad 5.4$$

Equation 5.5 shows the way to calculate the turbulence intensity.

$$I = \frac{\sigma_1}{V_{hub}} \quad 5.5$$

5.1.3.2. Extreme turbulence model

The extreme turbulence model (ETM) employs the same wind shear profile as in the NTM (see equation 5.3). The standard deviation of longitudinal turbulence component of ETM can be calculated by equation 5.6.

$$\sigma_1 = c\, I_{ref} \left(0.072 \left(\frac{V_{ave}}{c} + 3\right) \left(\frac{V_{hub}}{c} - 4\right) + 10\right); \quad c = 2\, m/s \tag{5.6}$$

Where, $V_{ave} = 0.2\, V_{ref}$; $V_{ref} = 15m/s$

5.1.3.3. Extreme wind speed model

There are two different wind profiles for the EWM, which have 50 years and 1 year recurrence period, which are presented by equation 5.7 and 5.8 respectively.

$$V_{50}(z) = V_{ref} \left(\frac{Z}{Z_{hub}}\right)^{0.11} \tag{5.7}$$

$$V_1(z) = 0.8\, V_{50}(z) \tag{5.8}$$

In the EWM there is a fixed standard deviation of longitudinal turbulence component, which is shown in equation 5.9.

$$\sigma_1 = 0.11\, V_{hub} \tag{5.9}$$

5.1.4. Selection of wind conditions

Section 5.1.2 highlighted the wind classes, which represent the wind conditions of the majority of sites (see Table 5.3). The aerodynamic loads depend on the wind conditions. Therefore, the aerodynamic loads vary throughout the wind classes. In this case it is necessary to specify the certain wind classes for the research in order to reduce the number of unnecessary calculations, which simply add time to the process.

According to the investigation of the sensitivity of extreme and fatigue loads to the turbulence reference intensity and inflow wind speed [55]–[58], the IA wind class is selected for this study. Where the reference velocity is 50 m/s and turbulence reference intensity is 0.16. This was chosen as this type of wind class provides the highest loads for wind turbines.

5.2. Approach

In chapter 1 it was mentioned that the focus of the project is to investigate the dependency of wind turbine fatigue and extreme loads from several factors such as: blade properties, rotor solidity and scaling. The information gained from this can then be applied to develop general load trends for the areas focused on in this investigation. These trends can give more understanding to the variation of extreme and fatigue loads due to applied modifications.

The fatigue loads are calculated by using lifetime DELs. The procedure of calculating extreme loads and lifetime DELs is explained in section 2.4 and 2.5. However, before calculating fatigue and extreme loads, the basic statistic and spectral analyses are examined to detect any uncertainties in the calculated steady loads of the modified model.

5.2.1. Basic statistics analysis

The spread sheet of basic statistics analysis is used to calculate the minimum, mean, maximum and standard deviation value of the specific parameter for each simulation. The calculated values are plotted to find signs of any inappropriate behaviour of wind turbine at the specific mean wind speed. Any irregular output of basic statistics analysis is a result of errors in the applied modifications or operational condition of the control system.

5.2.2. Spectral analysis

The spectral analysis includes the calculation of power spectral density, which distributes the energy in the frequency domain [10], [11], [59]. Consequently, frequency values associated with high energy levels, which relate to damage caused by the loads, can be determined. The spectral analysis is used to check that that a wind turbine avoids operation in the vicinity of the resonant frequency of wind turbine components (drive train, structural modes of blades and tower), which can be a source of excessive loading that may even lead to the failure of the machine. In chapter 6 the spectral analysis is applied to investigate the operating condition of the reference wind turbine in the dynamic state.

5.2.3. Extrapolation of extreme load

Usually a limited amount of 10 minutes simulations is applied to calculate the extreme loads of the wind turbine model according to IEC standards [5]. Each of these 10 minutes simulations is characterised by the specific mean wind speed with the turbulence conditions. So the evaluation of a wind turbine is restricted by the level of accuracy of simulations in relation to the real wind flow conditions of a site [60]. Moreover, the full range of wind conditions is not covered by the simulations. Thus the accuracy of calculated extreme loads is restricted by the amount and accuracy of simulations. The possible solution is to use long simulations with large variations in turbulence conditions. However, long simulations with large variations in turbulence conditions demand a lot of time and computation power, which make these simulations very time consuming and expensive [61]. As a consequence, long simulations are not widely used.

The IEC 61400-1 standard [5] though provides a solution for accuracy issues in extreme loads. It demands using the statistical extrapolation technique based on long-term (50-year period) exceedance probability for the calculation of extreme loads. According to the GH Bladed software manual, fifteen simulations for each mean wind speed are necessary to be performed for the extreme load extrapolation to deliver a good level of accuracy [10]. According to the IEC 61400-1 standard, the procedure to calculate the extreme load extrapolation for a 50-year period is:

I. Specify a threshold for the extreme load values, which is equal to the mean plus 1.4 times the standard deviation. This value of threshold minimises the statistical uncertainties at the low level of turbulence and increases accuracy of the generated trend of extreme loads [62]. Select the extreme load values, which are larger than the threshold, in each wind speed (V_j).

II. Calculate the short-term probability distribution of extreme loads, $P(F|V_j)$, for each wind conditions by using Gumbel methods.

III. Evaluate the long-term exceedance distribution probability by the using equation 5.10.

$$P_e(F) = \sum_j \left(1 - \left(1 - P(F|V_j)\right)^{n_j}\right) \left(e^{-\pi\left(\frac{V_j - \frac{\Delta V_j}{2}}{2V_{ave}}\right)^2} - e^{-\pi\left(\frac{V_j + \frac{\Delta V_j}{2}}{2V_{ave}}\right)^2} \right) \qquad 5.10$$

Where, V_j is the centre of the bins, ΔV_j is the width of bin.

IV. Obtain the extremes from the 50-year exceedance probability by using the value 50 year recurrence value $P(F_k) = 3.8 * 10^{-7}$ of the reference 10 minute period.

The MATLAB script of calculating the extremes from the 50-year exceedance probability can be found in Appendix C.

5.2.4. Deterministic lifetime DELs

Chapter 2 mentioned that the load signal consists of deterministic and stochastic parts. The deterministic load is predictable, e.g. gravity loads, wind shear, tower shadow etc., which depend on the azimuth position of rotor. The stochastic loads are random caused by turbulence, which may have overall statistics but no instantaneously predictable pattern. As a result, edge-wise blade loads can be divided into deterministic and stochastic components, because edge-wise blade loads are mainly due to self-weight. Therefore, the deterministic component of load can be investigated separately for a better understanding of the effect of blade properties, rotor solidity and scaling. Fourier transforms are employed to perform the separation of deterministic and stochastic loads [63], [64]. Figure 5.2 and 5.3 depict the separated deterministic and stochastic loads of edge-wise blade root bending moment, respectively.

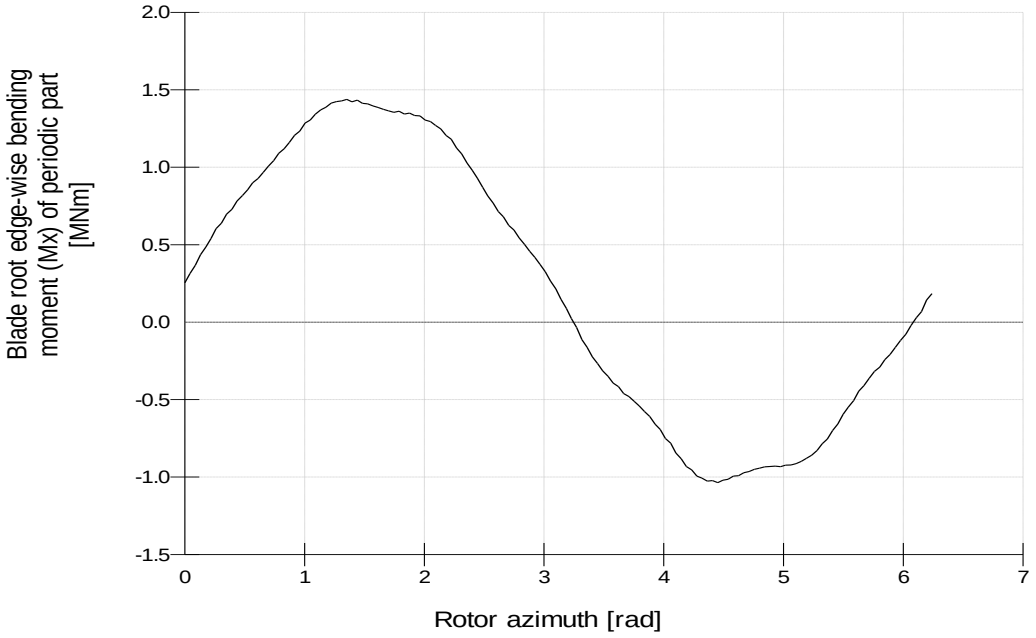

Figure 5.2: Deterministic part of edge-wise blade root bending moment of the reference wind turbine model at 10 m/s wind speed.

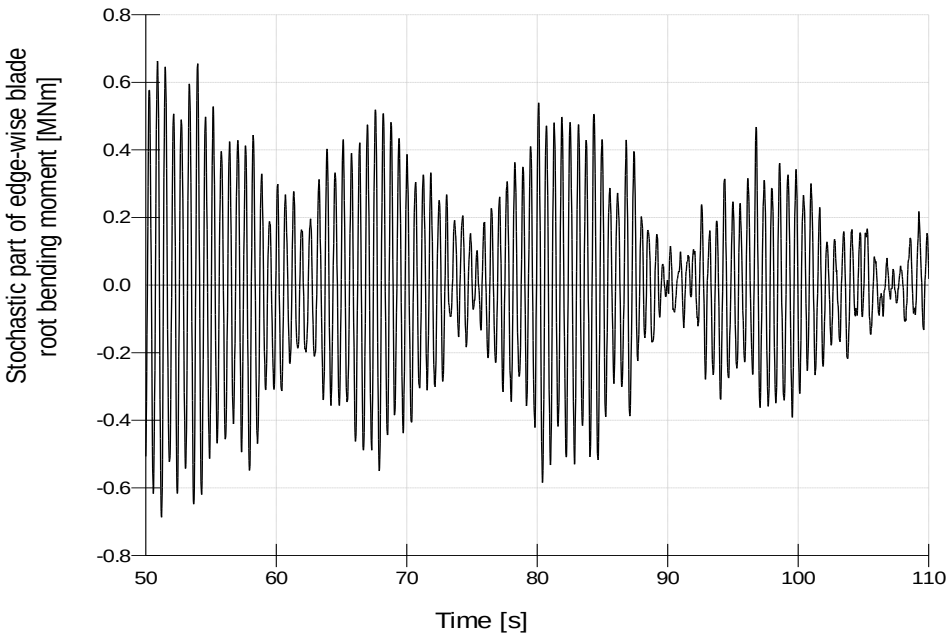

Figure 5.3: Stochastic part 60 seconds extraction of edge-wise blade root bending moment of the reference wind turbine model at 10 m/s wind speed in

The calculation procedure of DELs from the deterministic component of loads does not require the Rain flow counting (RFC) method to count the number and range of cycles, because the deterministic loads component is represented by a sinusoidal shaped curve. Hence, the amplitude and number of rotor revolutions can be calculated straight forwardly without using the RFC method. The procedure of the calculating deterministic Lifetime DELs is as follows:

I. Obtain the amplitude of deterministic load component per one revolution. The amplitude is equal to the amount of load produced per one revolution.
II. Determine the average rotor rotational frequency of each simulation.
III. Calculate the amount of rotor revolutions per each 10-minute simulation by using the average value of rotor frequency. As one revolution is equal to one cycle.
IV. Calculate the DELs for each mean wind speed simulation by using equation 2.6.
V. Use the Weibull distribution to determine a mean wind speed probability distribution.
VI. Combine the calculated DELs of each mean speed with the Weibull distribution of mean wind speed to calculate Lifetime DELs by using equation 2.7 and 2.8.

The MATLAB code of the calculation of deterministic Lifetime DELs calculation can be found in Appendix C.

5.3. Summary

This chapter was divided into two sections: wind modelling and approach. The wind modelling reviewed the modelling of wind flow based on IEC and GL standards. The two wind models: Kaimal and Mann were considered for use in this study. The Kailmal wind model was selected, because it provides a better approximation of wind flow and requires less computer capacity for the calculations. Furthermore, the general parameters of the wind profile were highlighted such as: the height, width, frequency and grid resolution of the wind profile. The grid spacing was chosen to be 5 m based on GL standards. Additionally, the wind classes and turbulence models (NTM, ETM and EWM) were reviewed. As a result, IA wind class was selected to use for this study, because it is the source of highest loads compared with other wind classes.

The second part of this chapter describes the approach method highlighting the loads calculation performed in this study. The main focus of research is extreme and fatigue loads (lifetime DELs). Basic statistics and power spectral analyses are employed in order to inspect the changes wind turbine parameters and instantaneous loads due to applied modifications.

6. Base model of wind turbine

This chapter provides an overview of the wind turbine model, which is used as the reference model for this research. Section 6.1 highlights possible options for the reference wind turbines. Moreover, it explains the reason for selecting the reference model. The description of the reference model is shown in section 6.2. The examination of the reference model is demonstrated in section 6.3 in order to ensure that the selected model for the reference wind turbine for this study operates correctly.

6.1. Reference model selection

Nowadays the most commonly used wind turbines are horizontal, up-wind and three-bladed machines. Hence, the research requires a model of the wind turbine with such characteristics: three bladed, up-wind, horizontal axis, pitch regulated and variable speed. There are several models of wind turbines with such characteristics which are available for public use. The most common wind turbine models are highlighted below:

- 1.5 MW WindPact [65]
- 5MW NREL [66]
- 6MW DOWEC [67]
- 10MW DTU [68]

The 1.5 MW WindPACT wind turbine model is not suitable for the role of reference wind turbine model, because the 1.5 MW WindPact model is relatively old, having been developed in the early 2000s.

One of the objectives of the project is to investigate the scaling effect on the loads. Accordingly, the 10MW DTU model is not practical as the reference model, since the rating of the 10MW DTU exceeds the size of any commercially available wind turbine.

Both the 5MW NREL and 6 MW DOWEC wind turbine models were considered for use as the reference model for this project. However, neither the 5 MW NREL nor 6 MW DOWEC models were selected as the reference model. One reason for this is that the NREL and DOWEC design involve a twist flap coupling which may unhelpfully complicate the general overview of loading trends that is being sought in this study. The second was that the reference model has to be similar to commercial wind turbines. Therefore, a new 3MW generic design, which is based on commercial designs of around 3MW rating and has been evolved from work of DNV GL and

University of Strathclyde, has been selected as the reference model. Section 6.2 provides the description of selected 3MW generic wind turbine.

6.2. Description of the reference model

In this section the key parameters of the 3MW generic wind turbine model are highlighted. The more detailed characteristics of the reference model can be found in the appendices, which are divided into two categories:

- Appendix A The general and structural parameters.
- Appendix B Aerodynamic characteristics of aerofoil.

Table 6.1 shows the key characteristic parameters of reference model of this research.

Rated power	3MW
Number of blades	3 blades,
Rotor position	Up-wind
Control	Collective pitch
Speed type	Variable
Transmission gearbox ratio	46.667
Rotor diameter	100 m
Hub height	81.11 m
Cut-in wind speed	4 m/s
Rated wind speed	11.5 m/s
Cut-out wind speed	25 m/s
Design tip speed ratio	9
Rated tip speed	75 m/s
Blade mass	8221 kg
Rotor mass	69932 kg

Table 6.1: The key parameters of reference wind turbine model

There are seven aerofoils profiles along each blade of the 3MW generic wind turbine. The aerofoil profile next to the hub has a cylindrical shape. The rest of the six aerofoil profiles are defined as NACA 634XX aerofoils. The drag, lift and pitching coefficients of each aerofoil can be found in Appendix B. Table 6.2 shows the distribution of chord, aerodynamic twist and aerofoil profile along the blade, which is extracted from Appendix A.

Frequency (Hz)	Damping ratio	Type of mode
0.82	0.005	Blade flap-wise normal mode
1.591	0.005	Blade edge-wise normal mode
2.243	0.005	Blade flap-wise normal mode
4.67	0.005	Blade edge-wise normal mode
0.289	0.005	Tower side-side translational attachment mode
0.29	0.005	Tower fore-aft translational attachment mode
1.83	0.005	Tower side-side rotational attachment mode
1.893	0.005	Tower side-side normal mode
1.893	0.005	Tower fore-aft normal mode
1.979	0.005	Tower fore-aft rotational attachment mode
5.532	0.005	Tower fore-aft normal mode

Table 6.2: Natural frequency and damping ratio of blades and tower

Figure 6.1 shows the rotor characteristics of the reference wind turbine model. In Figure 6.1 there are four curves corresponding to the chord, twist, lift and drag coefficients distribution along the blade of the reference model.

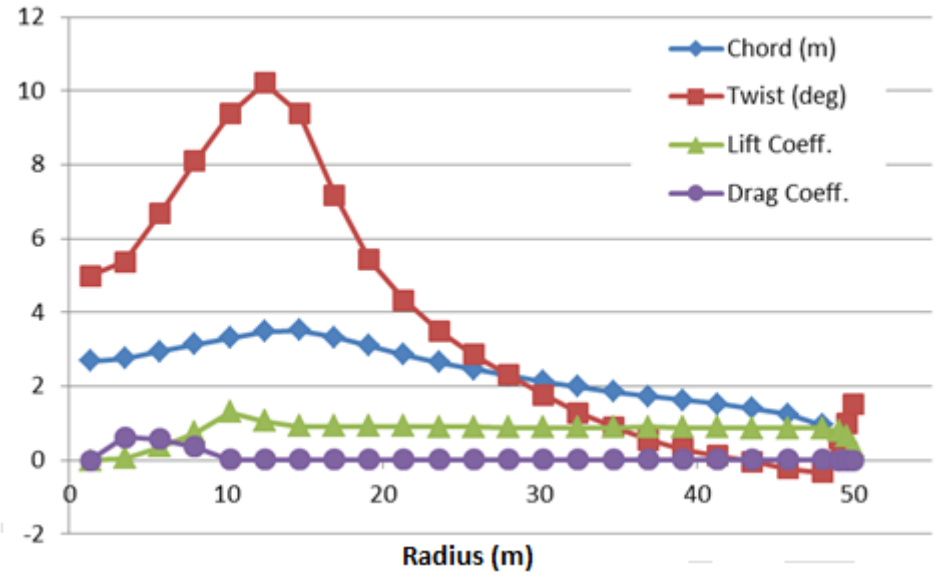

Figure 6.1: Rotor characteristics of reference wind turbine model

6.3. Validation of reference model

This section focuses on the validation of the 3MW reference wind turbine, which was selected as the reference model for this study. Therefore, it has to be checked for the accuracy of the performance before the implementation of any modification of the reference model and analysis

according to the objectives of the project. There are two conditions to perform the examination for accuracy of design and operation: steady state and dynamic state.

6.3.1. Steady state conditions

The two following figures depict the key parameters of the reference model in steady state conditions. Figure 6.2 depicts the rotor speed, electrical power; rotor thrust force and aerodynamic torque against wind speed. Figure 6.3 demonstrates the rotor speed, tip speed ratio and pitch angle against wind speed. Both figures do not reveal any unusual behaviour of the specified key parameters of the 3MW generic wind turbine. Thus the reference model is designed suitably in terms of steady state conditions.

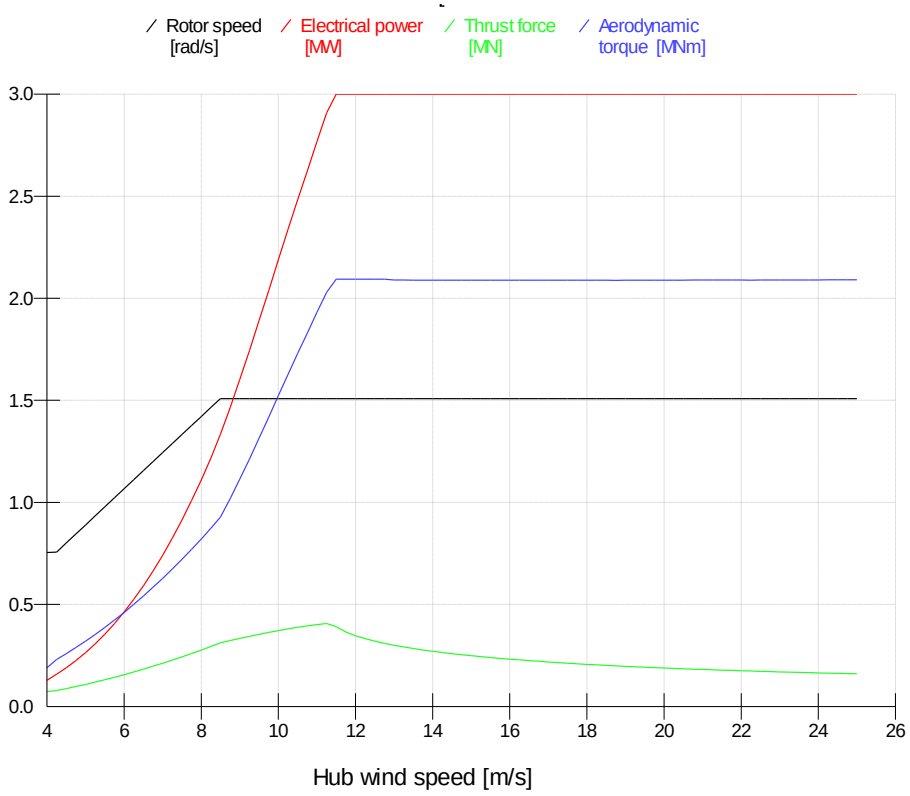

Figure 6.2: General parameters of the reference model against wind speed

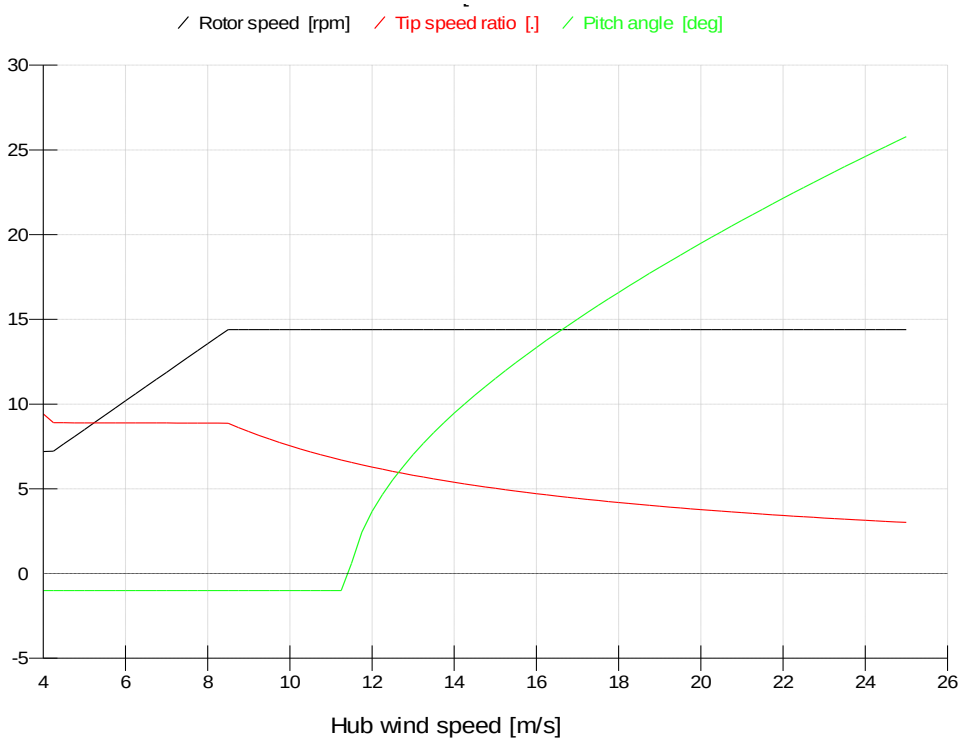

Figure 6.3: General parameters of the reference model against wind speed

Additionally, Figure 6.4 demonstrates the rotor speed-torque diagram of the reference wind turbine model, which depicts the operational strategy of the reference model.

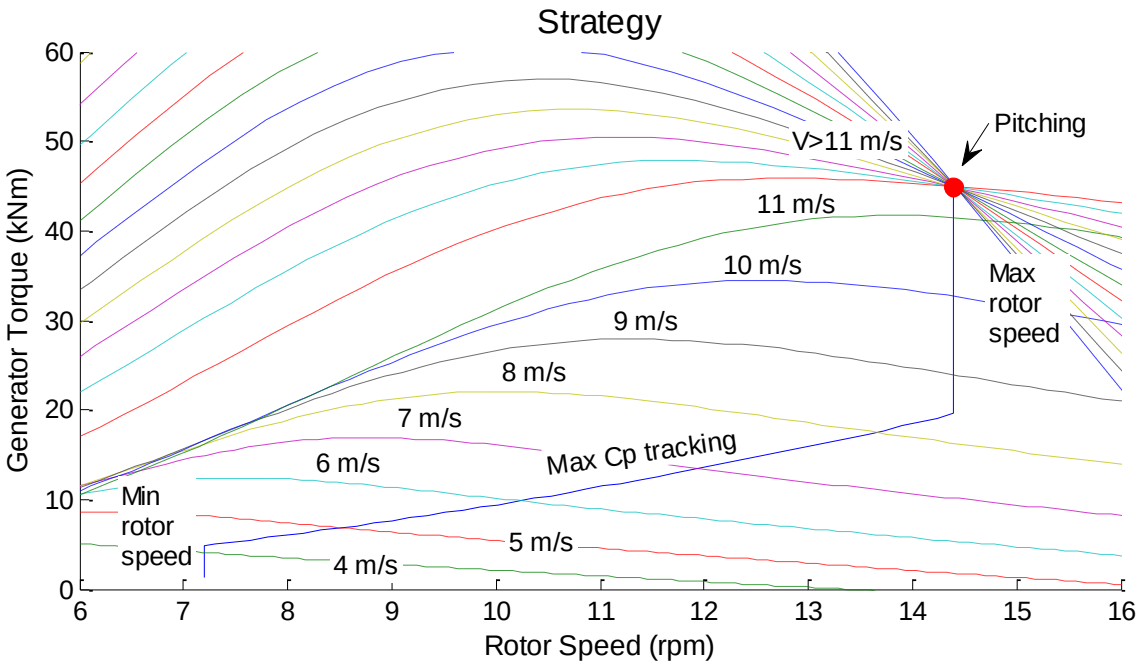

Figure 6.4: Rotor speed and torque diagram of reference wind turbine model

6.3.2. Dynamic state conditions

Figure 6.5, 6.6 and 6.7 demonstrate the general components (such as: wind speed at the hub height, rotation speed of rotor, mean pitch angle, bladed demanded pitch angle and electrical power) of the wind turbine model against a short period of time (60 seconds) at the three different wind speeds, which represent the different operating regions of the wind turbine. Figure 6.5 depicts the below rated region at 8 m/s wind speed. Figure 6.6 shows the intermediate state between below and above rated region, which is characterised by 12 m/s mean speed as the rated wind speed is 11.5 m/s. The above rated region at 16 m/s wind speed is depicted by Figure 6.7.

In Figure 6.4 and 6.5 there is the very small difference or lag between the mean demanded pitch angle and mean pitch angle curve. As a result, it can be assumed that these two lines are identical.

Furthermore, the rotor speed and electrical power curves look like straight lines without any steep rises and falls in the all three figures (6.5, 6.6 and 6.7). The straight lines of both variables indicate that there are only small variations, which can be neglected due to the minor size of these variations. Hence, Figure 6.5, 6.6 and 6.7 do not show any concerning behaviour of the reference wind turbine model.

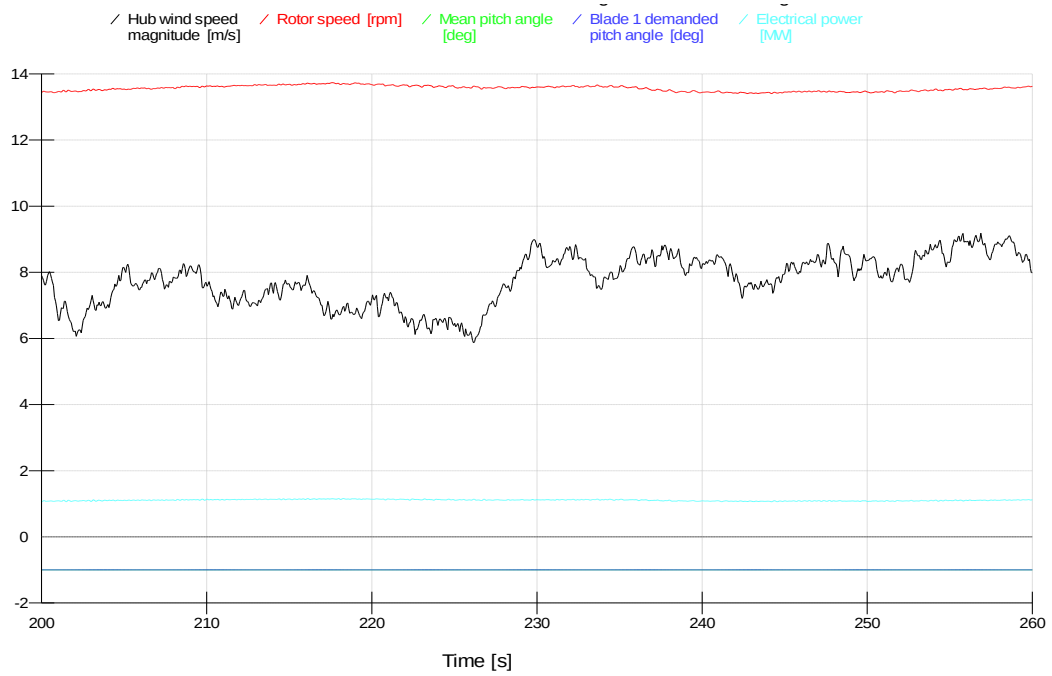

Figure 6.5: Outputs of reference wind turbine model at 8 m/s wind speed.

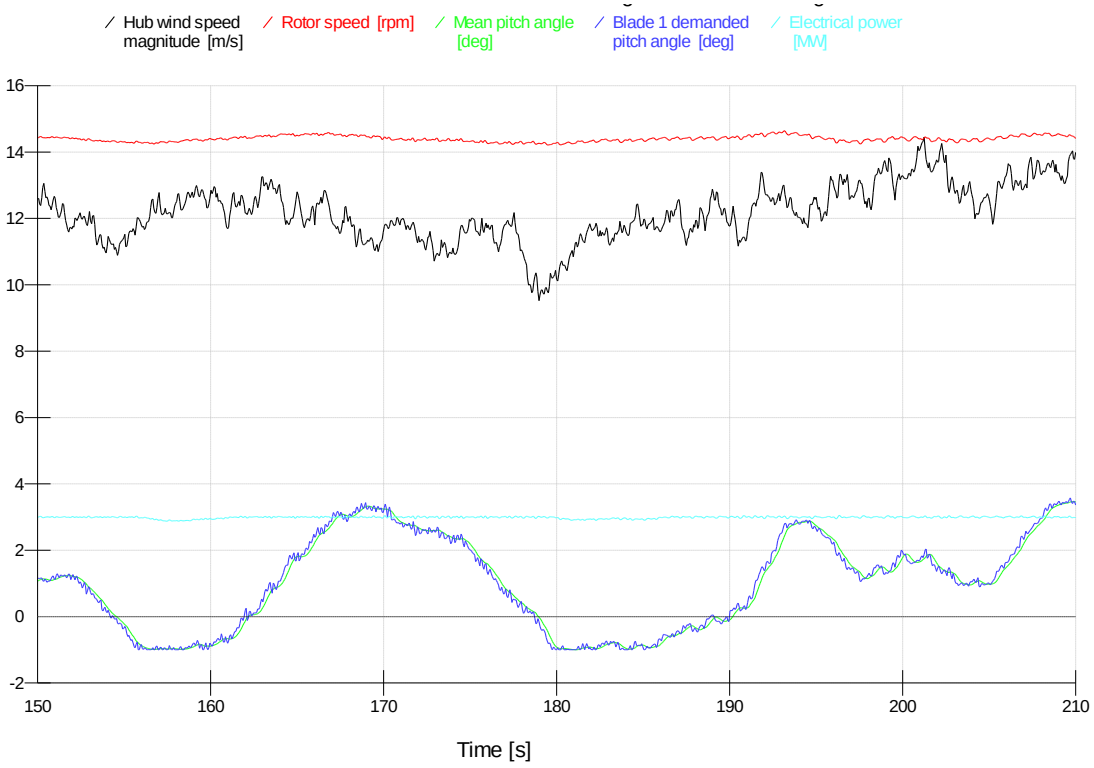

Figure 6.6: Outputs of reference wind turbine model at 12 m/s wind speed.

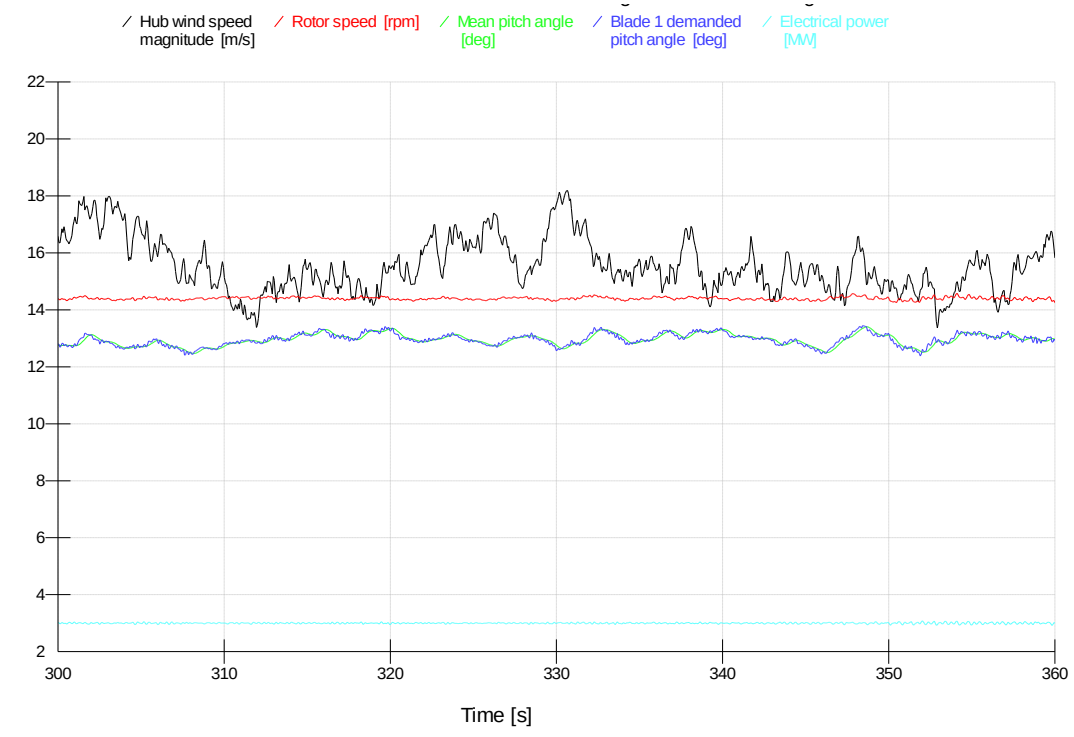

Figure 6.7: Outputs of reference wind turbine model at 16 m/s wind speed.

However, it is difficult to examine the dynamic conditions of the wind turbine in the time domain. It is much better to investigate the dynamic conditions of the wind turbine in the frequency domain.

Dynamic analysis of the wind turbine is better to perform in the frequency domain because the rotating blades and other components of a wind turbine are experiencing periodic loads. This periodic load causes the vibration of wind turbine components in one or more discrete geometric patterns, called mode shapes, with different modal frequencies among the mode shapes. The mode shape and its frequency depend mainly on mass and stiffness of the structure. However, the modal frequencies of wind turbine components can be changed due to the rotation movements, because the stiffness is affected by Coriolis and centrifugal forces [69].

Dynamic analysis in the frequency domain can highlight the possible dangerous resonant regions, which represent the conditions when natural frequencies of the wind turbine components are equal or nearly equal to the frequency of the periodic loading. In a hinge-less (wind turbine) rotor the frequency of periodic loading is equal to the rotor frequency. Generally, resonance describes a significant rise of displacement and internal loads [70], which leads to excessive loads of the structure. Figure 6.8 depicts a Campbell diagram of the reference wind turbine model, which points out the potential harmful resonant regions by plotting natural frequencies of structure components against the rotor frequency and its harmonics. The black dashed lines correspond to the rotor frequency *(1P)* and its harmonics *(nP)* as these lines are labelled in Figure 6.8. The natural frequencies of wind turbine components are represented by almost horizontal lines, which have a small inclination due to the rotation. The dangerous resonant regions are shown by the intersections between the black dashed lines and almost horizontal lines. Figure 6.8 shows that the rotor frequency and its harmonics coincide with the natural frequencies of blade and tower. The coincidence of natural frequencies has to be avoided in order to have a robust wind turbine design. The following subsections ensure the above mentioned matches of natural frequencies are avoided in the reference wind turbine model.

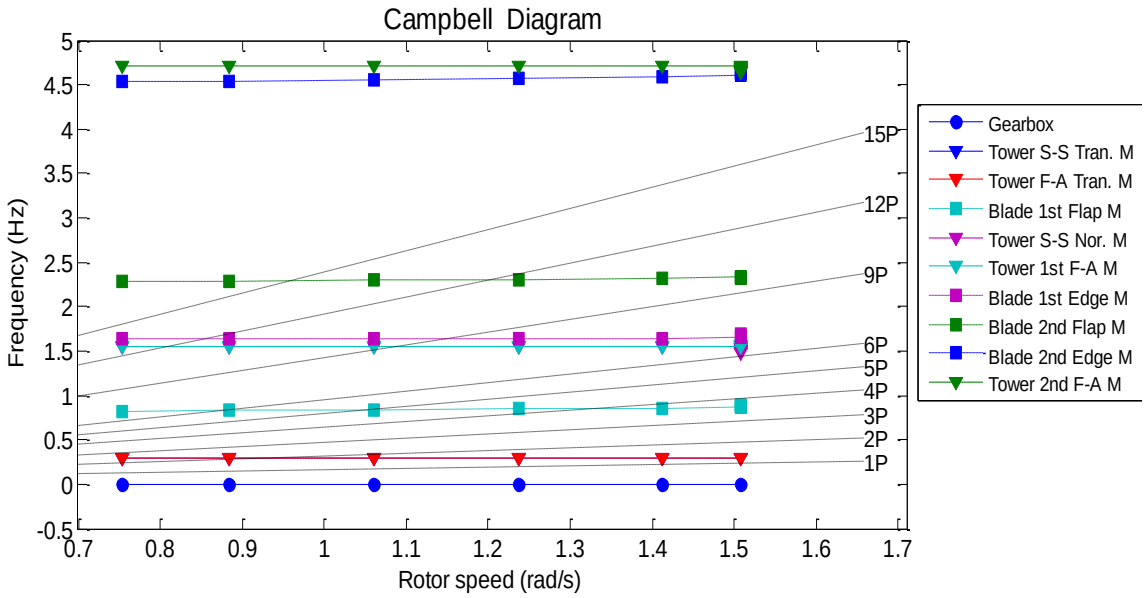

Figure 6.8: Campbell diagram of reference wind turbine.

6.3.2.1. Blade roots

The inspection of the reference model in the frequency domain starts with the blades because they play a crucial role in energy production. The blade root moments are the focus of this investigation as the highest moments occur at the blade root. The bending moment data is first developed in the time domain, which restricts interpretations. Hence, power spectral density (PSD) is applied to show the bending moment signal of time series in the frequency domain by employing Fourier analysis [59], [63], [64].

Figure 6.9 depicts the PSD of the edge-wise bending moment of the blade root for 14 m/s wind speed. In Figure 6.9 there are four curves of the edge-wise bending moment, which have the same wind speed, but different seeds of turbulence. It is noticeable that the four curves overlap each other and look very similar, but there is some small dissimilarity among these four curves with some peaks a bit higher and wider. It is a consequence of the different seed number of turbulence for each curve.

In Figure 6.9 the largest and first peak is *1P*, which corresponds to the largest load cycle amplitudes because of the asymmetric or unbalance load on the blade. The unbalance blade loading is caused by the tower shadow and vertical wind shear [71]. Therefore, *1P* on edge-wise is almost certainly due to gravity. Flap-wise would be due to shear and tower shadow, as the gravity loading is perpendicular/normal to the flap-wise moment. The frequency of 1P represents the rotor frequency, which is around 0.24 Hz. The following peaks (such as: *2P, 3P, 4P* and etc.) are

the harmonics of the rotor speed frequency. Each subsequent harmonic peak should not be higher than the previous peak. Otherwise there is a problem with the control system, which can lead to the failure of a unit. However, there are exceptions like the harmonic peaks which are located next to a structural mode. In Figure 6.6 harmonic peaks *5P, 6P* and *7P* are located in the vicinity of the first blade edgewise dynamic mode. The first blade edgewise mode is defined by a very wide triangle due to damped energy. Besides there is another high peak, which relates to the combination the *12P* harmonic and the second blade edgewise dynamic mode, which follows the same exception that was mentioned above.

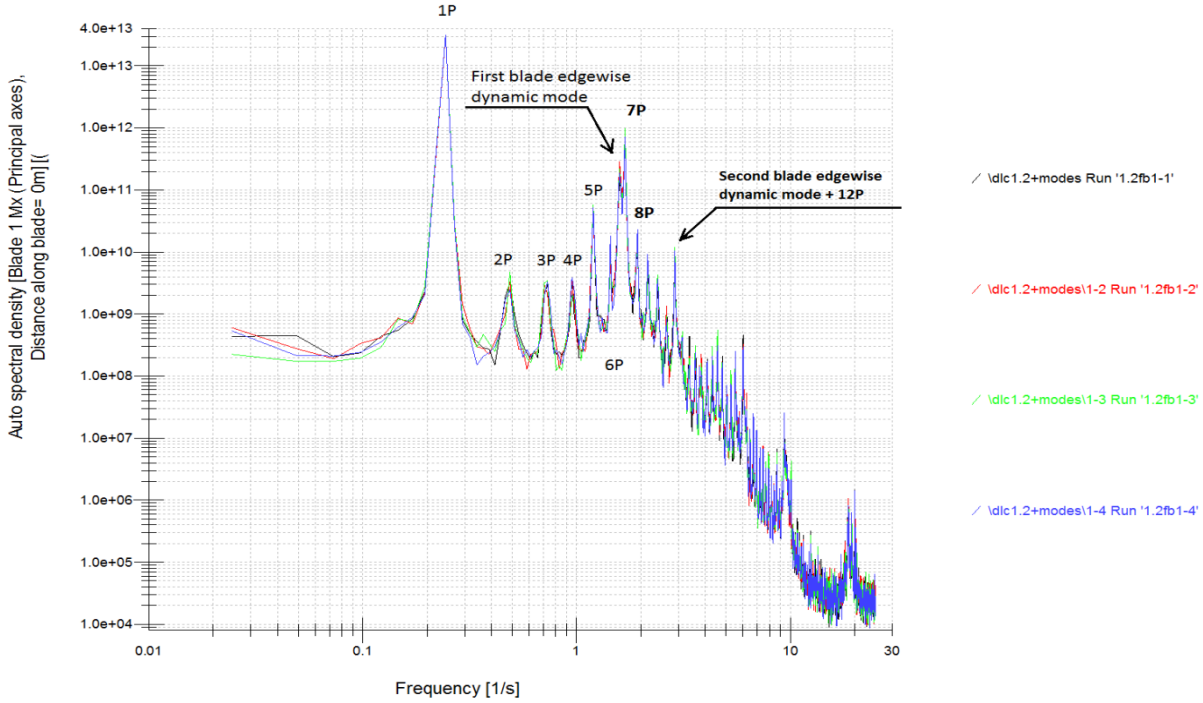

Figure 6.9: Edge-wise root bending moment of four different seeds at 14 m/s

Figure 6.10 shows the PSD of flap-wise moment of blade root for the four different seeds at 12 m/s mean wind speed.

In Figure 6.10 the harmonic peaks of rotor frequency and structural modes follow the same rule as for the edge-wise blade root moment, which is shown by Figure 6.9. The second and third blade flap-wise structural modes are easily spotted due to the wide triangle shape apart from the first flap-wise structural mode, which is almost completely damped as it denotes by the small swelling under 4P harmonic peak.

The next step is to compare the frequencies of the first blade flap-wise and edge-wise structural modes as this is one of the conditions, which shows the correctness of wind turbine design. In the robust design of a wind turbine, the frequency of first blade flap-wise mode has to be lower

than the frequency of first edge-wise mode due to the shape of blades. It is clearly visible from Figure 6.9 and 6.10 that the first blade edge-wise mode has a higher frequency than the first blade flap-wise mode. It shows that the blades are designed correctly. Additionally, both Figure 6.9 and 6.10 demonstrate that the controller does not operate in the vicinity of the natural frequencies of the blades as there are not any high and narrow peaks, which are higher than the *1P* harmonic.

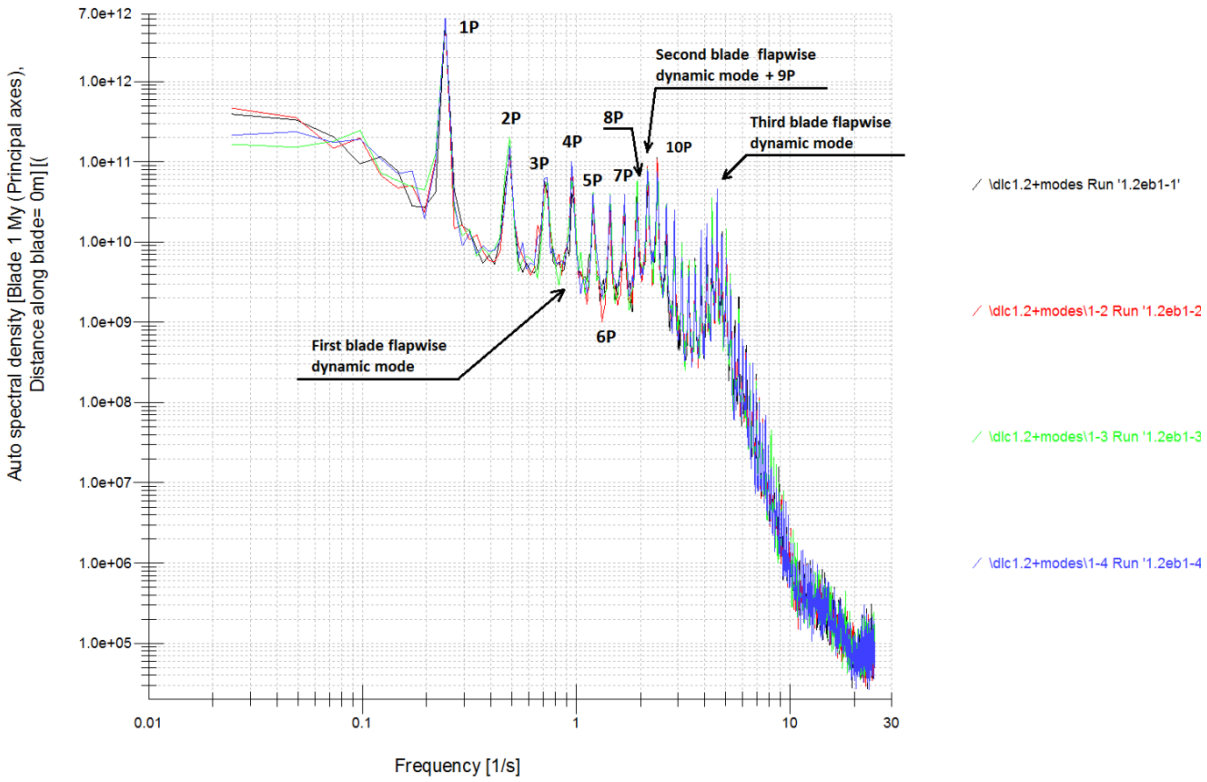

Figure 6.10: Flap-wise root bending moment of four different seeds at 12m/s

6.3.2.2. Drive-train

The kinetic energy is converted into mechanical power, where a generator produces the electrical energy from the mechanical power [72]. Generally the drive-train consists of structural components such as: hub, low speed shaft, gearbox, high speed shaft and generator [73], [74]. Each of these components has an individual dynamic response. The summation of all these individual dynamic responses generates the drive-train dynamic response, which can be represented by dynamic modes. The key dynamic mode is the first drive train mode because it is at low frequency and may possibly coincide with *3P, 6P*, or higher harmonic peaks. The frequency

match of the first drive train and harmonic peaks has significant effect on the load of drive train components and the operation conditions of the wind turbine control system. The asymmetrical distributed aerodynamic loads among the three blades of the rotor represents by *3P, 6P, 9P*, etc. harmonic peaks [71]. The asymmetric aerodynamic load distribution over the rotor plane is caused by turbulence, wind shear and tower shadow.

Figure 6.11 depicts the PSD and cumulative PSD of generator torque. The cumulative PSD is applied to determine the amount of energy carried by the PSD peaks. The first drive train mode is damped and does not have a significant effect on the load, seen as only a minor increase in the cumulative PSD curve above the first drive train peak. However, there is a significant impact on the load from the combination of *12P* and *15P* harmonic peaks and second drive train mode as shown by the rise of cumulative PSD curve.

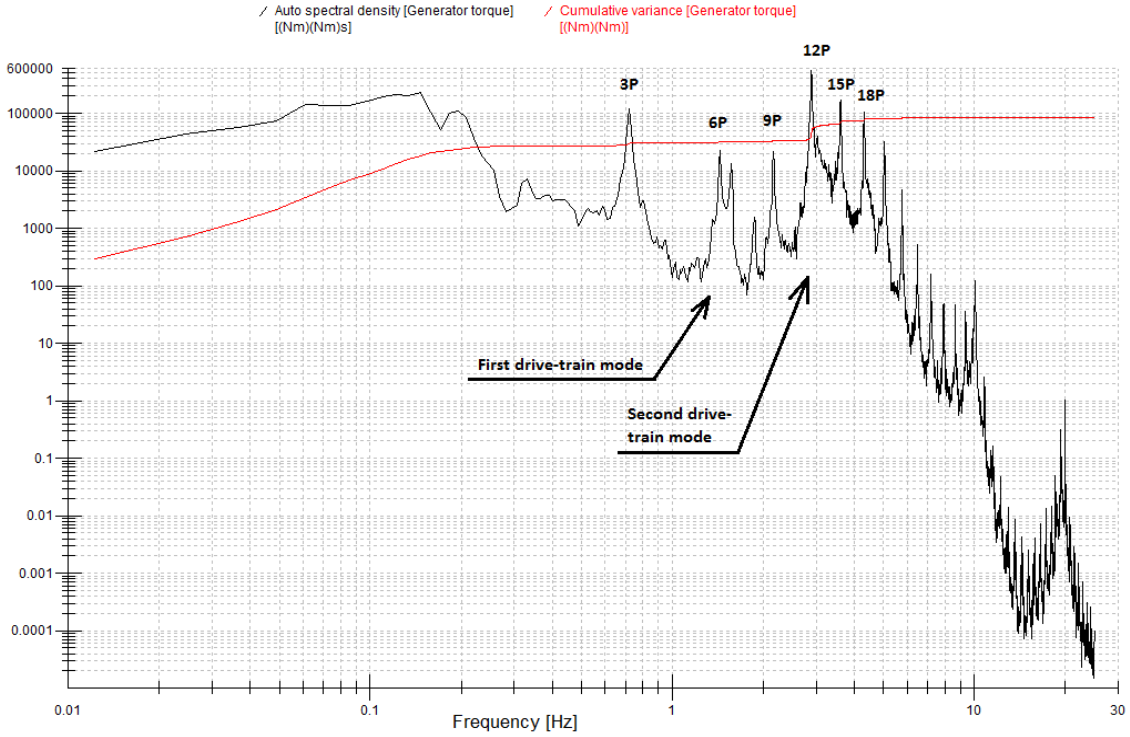

Figure 6.11: PSD and cumulative PSD of generator torque at 14 m/s mean wind speed.

6.3.2.3. Yaw bearing

This section examines the yaw bearing of the reference wind turbine model. Figure 6.12 shows the PSD and cumulative PSD of yaw bearing bending moment at 14m/s mean wind speed. The loading of yaw bearing is a function of the harmonics peaks (*3P, 6P, 9P, 12P,* etc.) as shown by significant rises at the cumulative PSD curve due to these harmonic peaks. Moreover, the

frequency of harmonic peaks of 6P and 9P coincides with the frequency of edge-wise and flap-wise blades modes. Where *6P* and the first edge-wise mode is dampened well, but the coupling of *6P* harmonic with the second flap-wise structural mode is not damped enough as the coupling peak is narrow and higher than *3P* harmonic peak. Therefore, it is possible to state that the coupling of *9P* and the second flap-wise structural mode should be dampened by improving the controller.

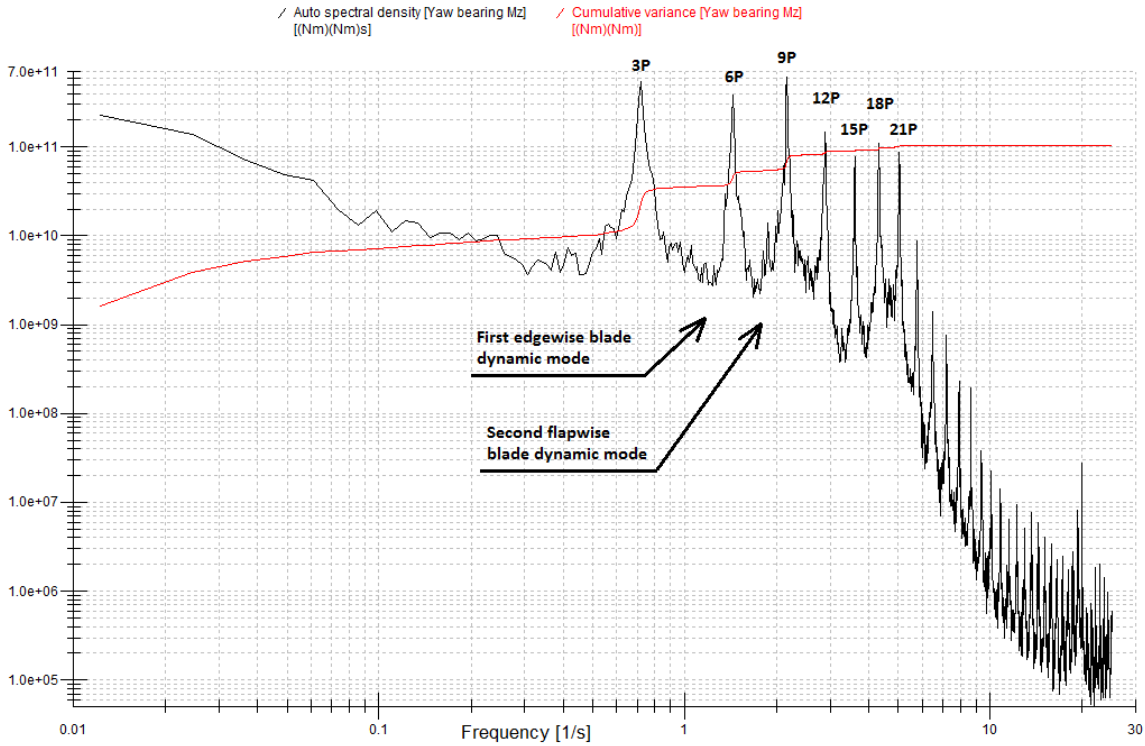

Figure 6.12: PSD and cumulative PSD of yaw bearing moment at 14 m/s mean wind speed.

6.3.2.4. Tower

This section represents the dynamic response of the tower base side-side and fore-aft bending moments. The PSD and cumulative PSD graphs of side-side and fore-aft tower base bending moment are shown by Figure 6.13 and 6.14.

In Figure 6.13 there is not a combination of any tower modes and the rotor rotational frequency harmonics, which would be observable by high and narrow peaks. However, there are harmonic peaks at *18P* and *21P*, which are located next to the 3rd tower side-side rotational and normal modes. The above mentioned harmonics and tower structural modes do not generate a

significant effect, as shown by the cumulative PSD curve. The largest impact on loads is caused by the tower side-side translational attachment mode, which is located at low frequency.

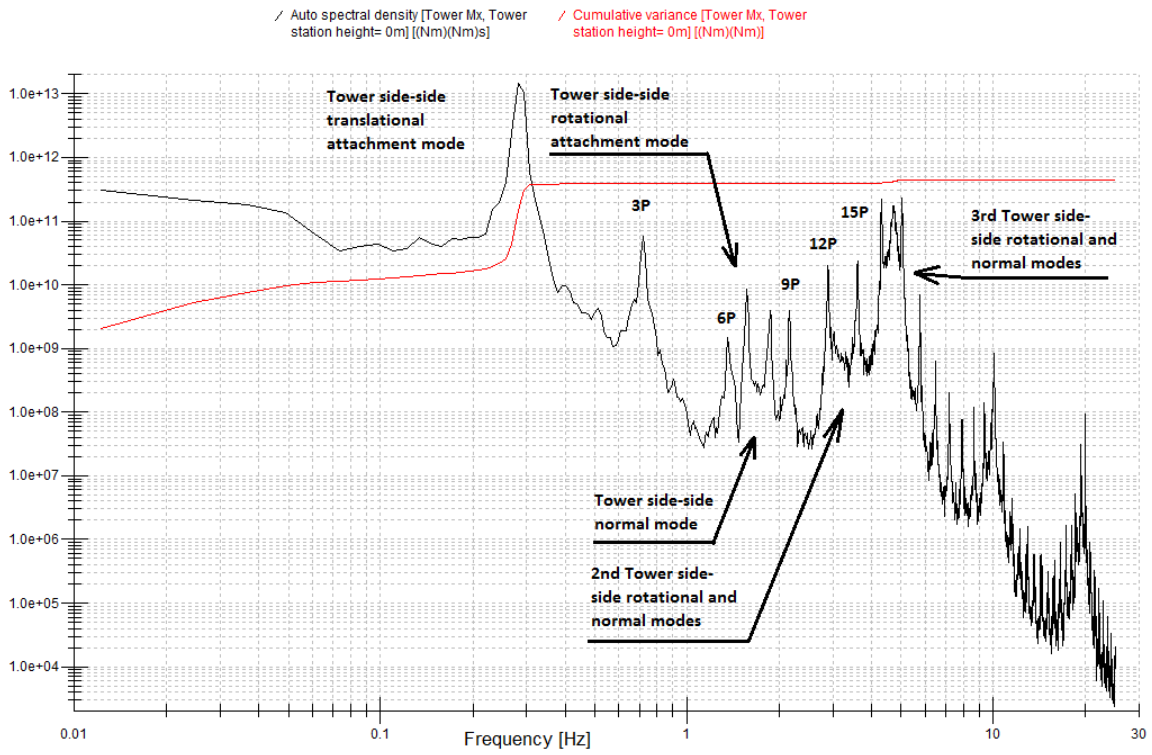

Figure 6.13: PSD and cumulative PSD of Side-side tower base bending moment at 14 m/s mean speed

In Figure 6.14 the fore-aft translational attachment tower mode is a result of the significant load for tower base fore-aft motion. There is small effect on tower load from the combination of harmonics peaks with the 3rd tower fore-aft rotational and normal modes as there is a tiny rise in the cumulative PSD curve. Furthermore, there are harmonics peaks of *6P, 9P, 12P, 15P* and 18*P* located within the vicinity of the frequency of tower structural modes, but it does not have any effect on the tower loading as there is not an increase in the cumulative PSD curve. In this case the fore-aft tower bending moment depends on mainly the fore-aft translational attachment tower mode.

Both above mentioned Figure 6.13 and 6.14 of tower base bending moment shows that the control system dampens the peaks, which correspond to the frequency coupling between harmonics and tower modes.

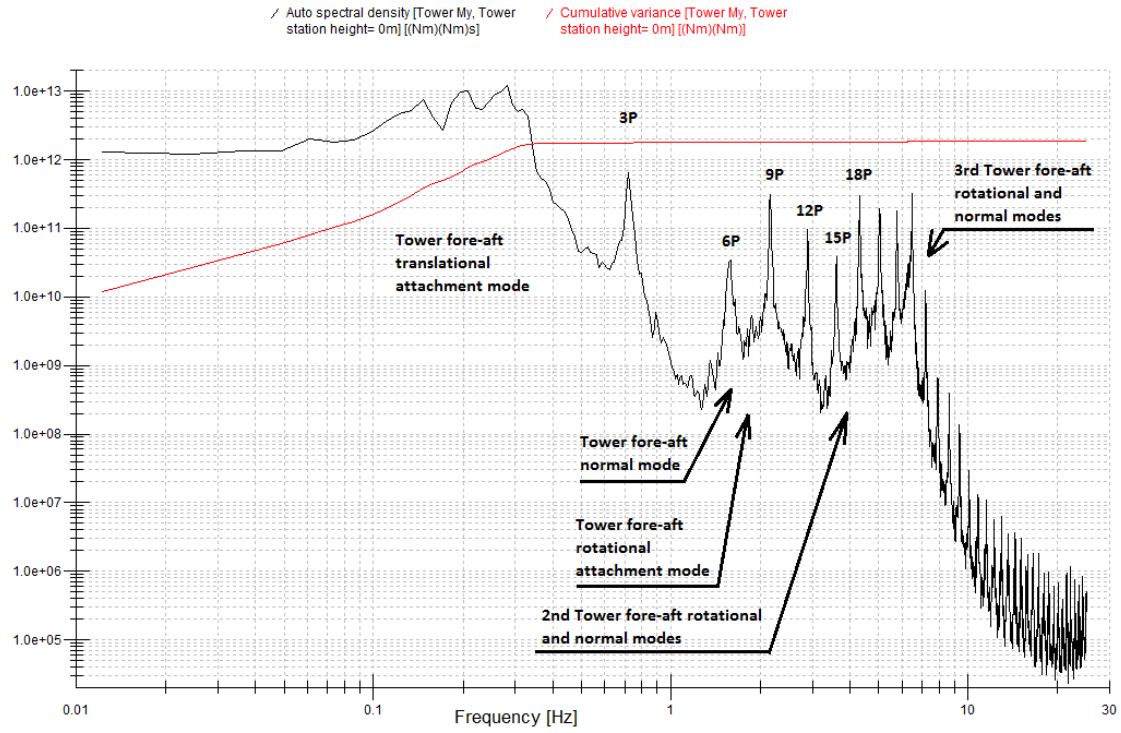

Figure 6.14: PSD and cumulative PSD of fore-aft tower base bending moment at 14 m/s mean speed

6.3.3. Discussion of validation

A 3MW generic wind turbine model was examined in the steady and dynamic state conditions. The demonstrated graphs do not show any unusual behaviour of the wind turbine model. It demonstrates that the wind turbine is robustly designed. Additionally, the control system has been tuned accurately to avoid the operation of the wind turbine in the vicinity of the resonance frequencies as it was shown by spectral analysis for wind turbine components such as: blade, drive-train, yaw bearing and tower. However, it is small issue with the controller to dampen the coupling between harmonic peaks and structural modes in terms of the yaw bearing, which can be neglected. In this case this 3MW generic wind turbine is validated to use as the reference model for this project.

6.4. Summary

This chapter was divided into three sections. Section 6.1 provided the information about the wind turbines, which can be used as the reference model. It is also explained the reason for selecting

the 3MW generic wind turbine as the reference model for this study. The properties of the reference model were briefly highlighted in section 6.2. Section 6.3 provided the examination of the generic wind turbine in steady and dynamic conditions to ensure that the 3MW generic wind turbine model has the sufficient design and is valid for this project as the reference model. The investigation showed that the generic wind turbine model is completely applicable to be used as the reference model. The evaluation of system dynamics revealed a few areas where the control system design may be improved. However, for a generic design that is to be up-scaled or have parameters varied at a fixed scale, there is no need for the design to have a very refined control.

7. Blade structural properties

The investigation of wind turbine loads starts from this chapter, which examines how the structural parameters of blades affect the loads especially extreme and fatigue loads. The idea of this chapter is to answer the questions, which were asked at the beginning of this thesis. However, these questions are going to be highlighted below to remind the reader.

I. *How do fatigue and extreme loads change due to modifications of parameters?*
II. *Is it possible to develop fatigue and extreme loads trends of the gained data of sensitivity analysis as a function of the modified parameters?*

This chapter includes the four different scenarios of blades modifications. However, the blade mass changes in the same way in the four scenarios in order to give a possibility to compare the changes of the loads among the four scenarios. Additionally, for the 3rd and 4th scenarios the modifications of blade dimensions are proportional to blade mass according to the linear scaling rule [3], [6], [7], [24]. The detailed explanation of proportion and blade properties modifications can be found in section 7.1. In section 7.2, spectral analysis is used to examine the modified models for any unrepresentative effects, which may be due to specific dynamic interactions with the control system for example. The analysis of fatigue loads as affected by the blade modifications are provided in section 7.3. Section 7.4 examines the changes in fatigue loads for edge-wise blade root in terms of the deterministic part of the load. The analysis of extreme loads is located in section 7.5. The last section of this chapter provides the summary, discussion and conclusion of the impact of blade proprieties onto the extreme and fatigue loads.

Note the modifications in the four scenarios do not involve large variations in design parameters. Thus, the original controller of the reference model can be used among the modified wind turbine models for these four scenarios. As parameter variations are evaluated checks on control system performance are routinely conducted.

7.1. Modification of blade structural properties

As was mentioned previously, there are the four scenarios of modifications of wind turbine blades, which are described below:

1. Only blade mass is modified in the 1st scenario**.** The blade of wind turbine may be considered as a single degree of freedom system, where a single coordinate system describes the motion of system [6], [75], [76]. According to the single coordinate system, the natural frequency of blade depends on mass and stiffness of blade as it shown by equation 7.1.

$$\omega = \sqrt{\frac{k}{m}} \qquad 7.1$$

Where: ω is natural frequency; k is stiffness; m is mass

2. The 2nd scenario alters the blade mass and stiffness, which are modified by same factor to preserve the natural frequency of the blade for the modified models, which is based on the assumption of the first scenario as shown equation 7.1.

3. Mass, stiffness as represented by the second moment of area and dimensions of blades are modified in the 3rd scenario. The specified modifications are performed in terms of the linear scaling rule, which states that the mass and stiffness of blades are proportional to dimensions of blades as shown by equation 7.2 and 7.3.

$$m \propto L^3 \qquad 7.2$$

$$I \propto L^4 \qquad 7.3$$

Note, the twist distribution angle along the blade does not change.

The natural frequency of the blade alters because of the applied modification of the 3rd scenario. According to simplicity, the structural model of the wind turbine rotor blade is assumed as a cantilever beam with such properties: rectangular, untwisted and homogeneous in terms of material. Therefore, the natural frequency of the cantilever beam is presented in equation 7.4 as stated in many books: [6], [7], [77].

$$\omega = \Lambda^2 \sqrt{\frac{EI}{mL^4}} \qquad 7.4$$

Where: *E* is the Young modulus; *I* is the second moment of area; *L* is the length of the blade, and Λ is the eigenvalue of the cantilever beam.

4. The fourth scenario changes the blade mass, stiffness and dimensions but in such manner to preserve the natural frequency of the reference model. Hence, the mass and dimensions change in the same way as these variables in the 3rd scenario based on the linear scaling rule. In order to maintain the original natural frequency of the modified models the bending stiffness (EI) or second moment of area changes in such a way to match the changes of denominator of equation 7.4. Therefore, equation 7.5 shows how the bending stiffness has to change to maintain the frequency of reference model.

$$EI \propto L^7 \qquad 7.5$$

Each scenario is divided by 9 cases, which are related blade mass modifications in a range from -20% to +20%. Each step is 5% compared to the original model. The blade structural properties depend on blade mass based on linear scaling rule. So if the blade mass rises by 20% the blade dimensions rise by 2.714% (see equation 7.2) because of scale with similarity. In this case, the rotor diameter increases or decrease by 2.7% for utmost cases of scenarios 3 and 4. As a result, the rotor varies by 7.37% for the utmost cases of the 3rd and 4th scenarios. The energy output and flap-wise blade root moment are proportional to the swept area of wind turbine as shown in equation 3.2 and 3.5. Therefore, if the radius rises by 2.7%, the power output and flap-wise moment increase by 7.37% and 20% respectively in the utmost cases of scenario 3 and 4 and vice versa.

7.2. Validation of changes

In this chapter, the modified reference models of the four scenarios are investigated by spectral analysis to make sure that the applied modifications are not causing instability of the system or unduly large loadings due to resonance between rotor harmonics and structural modes.

The following sub section demonstrates the comparison between the four scenarios and the reference model for specific components. Each of the scenarios is presented by the cases which are related to the outermost modifications of blades. Hence the cases of -20% and +20% of blade mass modifications are applied in the following subsections.

A single spectral analysis graph includes two scenarios out of four with the reference model in order to more easily read the graphs, because it is difficult to read a spectral graph when more than three models are included.

7.2.1. Blade root edge-wise moment

Figure 7.1 and 7.2 depict the PSD and the cumulative PSD of the blade root edge-wise moment in the comparison between the four scenarios and the reference model. In Figure 7.1 the first and second scenarios are represented by the outermost modification cases, which correspond to -20% of mass for both scenarios. In Figure 7.2 the third and fourth scenarios are represented by the cases, which relate to +20 % to blade mass for both scenarios.

The applied modification of the first scenario changes the natural frequency of blades. As a result the first blade edge-wise structural mode is shifted to the high frequency as shown by Figure 7.1. In Figure 7.2 there is no shift at the curve of the 2nd scenario because the mass and stiffness were modified by the same factor to preserve the natural frequency. The cumulative PSD curves of scenario one and two are identical as the blade mass in both scenarios was modified by the same value. Therefore, the cumulative curves of the 1st and 2nd scenarios overlap because the blade root edge-wise moment is affected by gravity loading. Additionally, the dependency of blade root edge-wise loads from the weight of blades explains a reason why the cumulative PSD curve of original model is higher the curves of the 1st and 2nd.

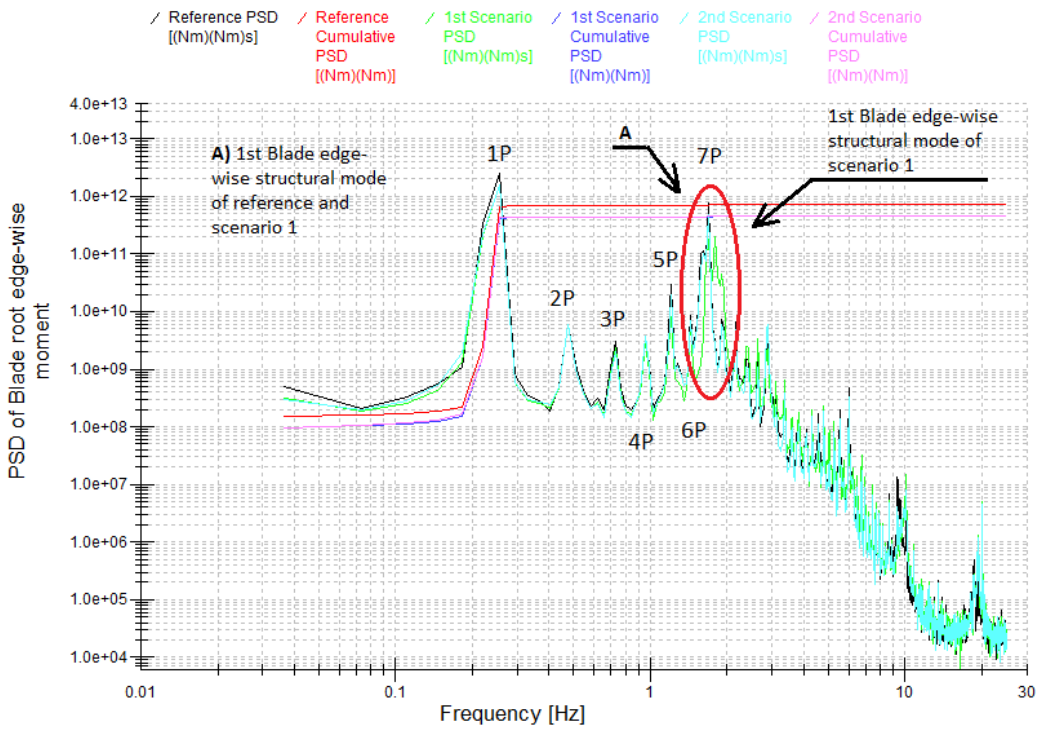

Figure 7.1: PSD of blade root edge-wise moment of reference model, 1st and 2nd of scenario at 14 m/s

In Figure 7.2 there is a similar situation as at Figure 7.1 since the applied modifications amend blades natural frequency of the 3rd scenario and do not alter natural frequency of the 4th scenario.

The difference between the 1st and 3rd scenarios is the direction of shifting of blade natural frequency because both these scenarios use the opposite utmost cases of modifications. Therefore, the 3rd and 4th scenarios are presented by the cases of modification which add +20 % to blade mass. It leads the 1st blade root edge-wise structural mode of the 3rd scenario to shift to lower frequency as stated by equation 7.4. Furthermore, it leads to the cumulative PSD curves of the last pair of scenarios being higher than the cumulative PSD curve of the reference model.

In both Figure 7.1 and Figure 7.2, there are no other shifts among the other peaks apart from the structural modes, which are based on the natural frequency of the blades. The other peaks are harmonic peaks of *1P*, which is characterised by the rotor frequency. The heights of the peaks vary among the reference and scenarios because edge-wise moment depends on gravity loads, which are a function of mass. Moreover, there is not any un-damped peak (combination of harmonics and structural mode) which is higher than the peak of *1P*. Thus, both Figure 7.1 and Figure 7.2 demonstrate that the applied modifications do not cause any control system instability to the reference model in terms blade root edge-wise moment.

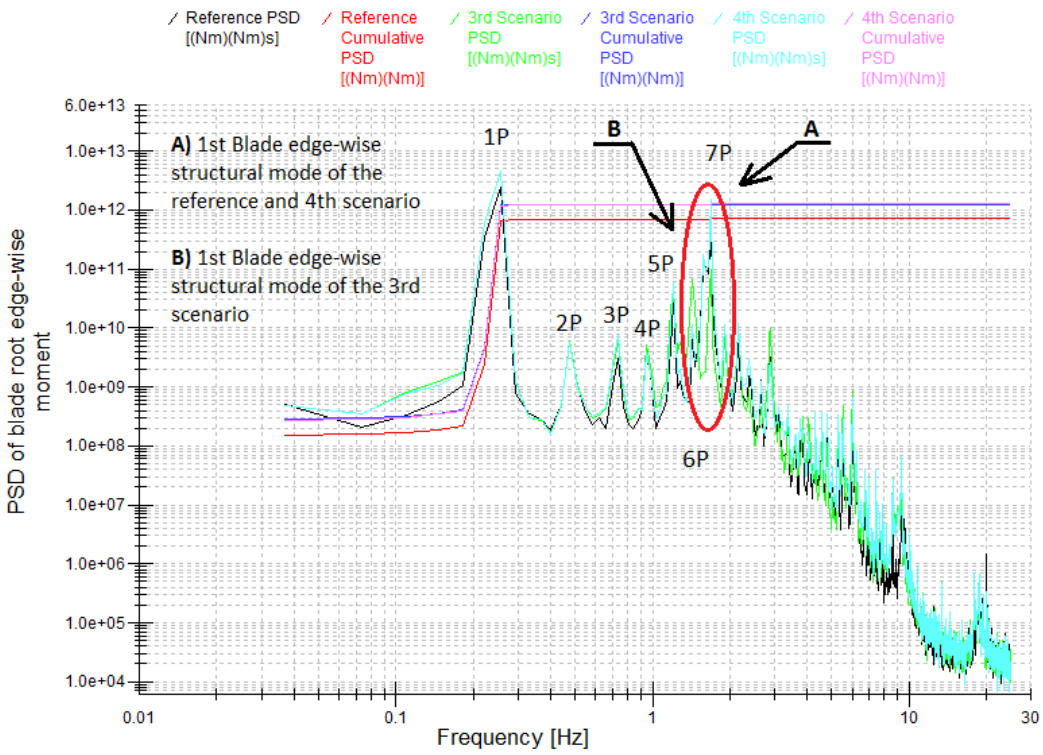

Figure 7.2: PSD of blade root edge-wise moment of reference model, 3rd and 4th of scenario at 14 m/s

7.2.2. Blade root flap-wise moment

The spectral analysis of blade root flap-wise moment of the four scenarios is shown in Figure 7.3 and 7.4. The four scenarios are divided by two pairs in the same way as in the previous subsection of edge-wise blade root to make sure that the data can be easy to read from the graphs. In Figure 7.3 there is not much difference among the 1st and 2nd scenarios and the reference model because the curves of models coincide or overlap. This is a result of the minor effect on the flap-wise loads from the applied modifications for both scenarios as the flap-wise blade moment depends on mostly aerodynamics loads, which are neutral to modifications of blade mass, and stiffness. However, there is frequency shifting of the 2nd and 3rd structural blade modes in the 2nd scenario because of the applied modifications. The frequency alteration of the 2nd scenario does not have a negative effect on the model as the frequency of rotor harmonics are not located in the vicinity of the resonant frequency of the blade structural modes.

In Figure 7.4 the variation is more visible between the second pair of scenarios (3rd and 4th) and the reference model compared to the curves of Figure 7.3. The difference of peaks height between the modified models and reference model is a consequence of the modified dimensions

at the second pair of scenarios. As it was mentioned previously the flap-wise loads are a function of aerodynamics loads, which act on the wind turbine blades. Therefore, any changes of shape and dimensions of blades lead to alteration of the flap-wise blade moments. The modification of blades mass and stiffness of blades has the insignificant effect on the flap-wise blade root moment. The curve of the 3rd scenario demonstrates the frequency changes of the blade structural modes, but there is no an adverse impact for the model caused by the change of frequency.

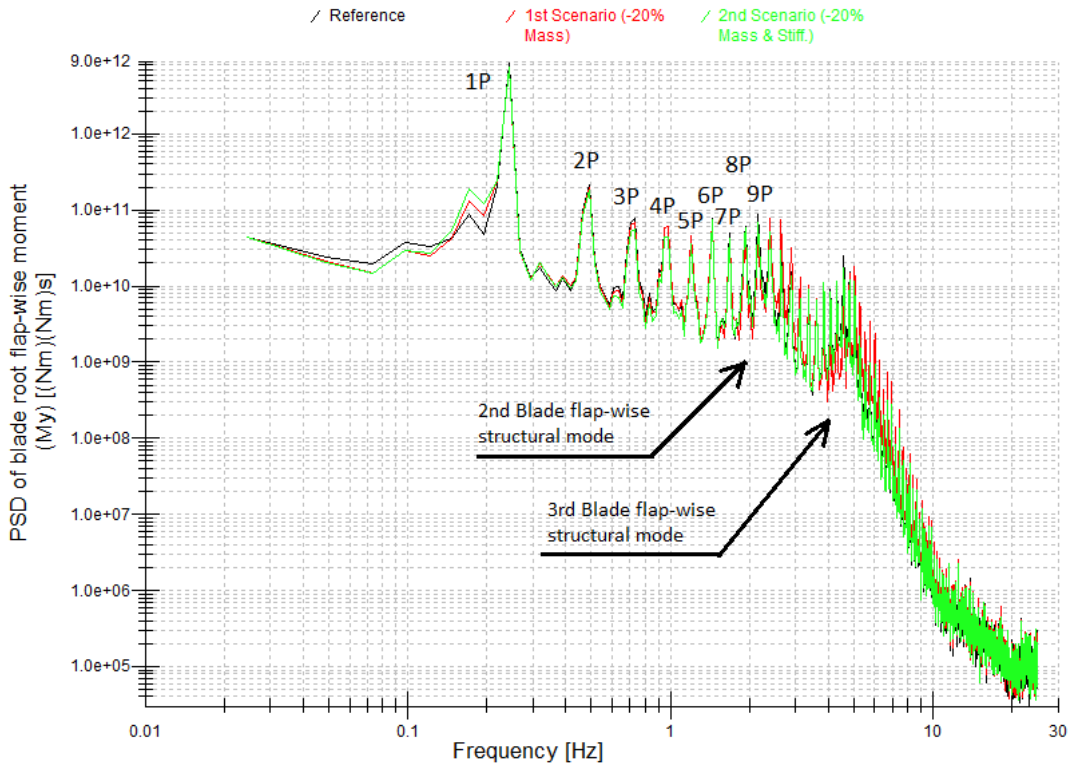

Figure 7.3: PSD of blade root flap-wise moment of reference model, 1st and 2nd of scenario at 14 m/s

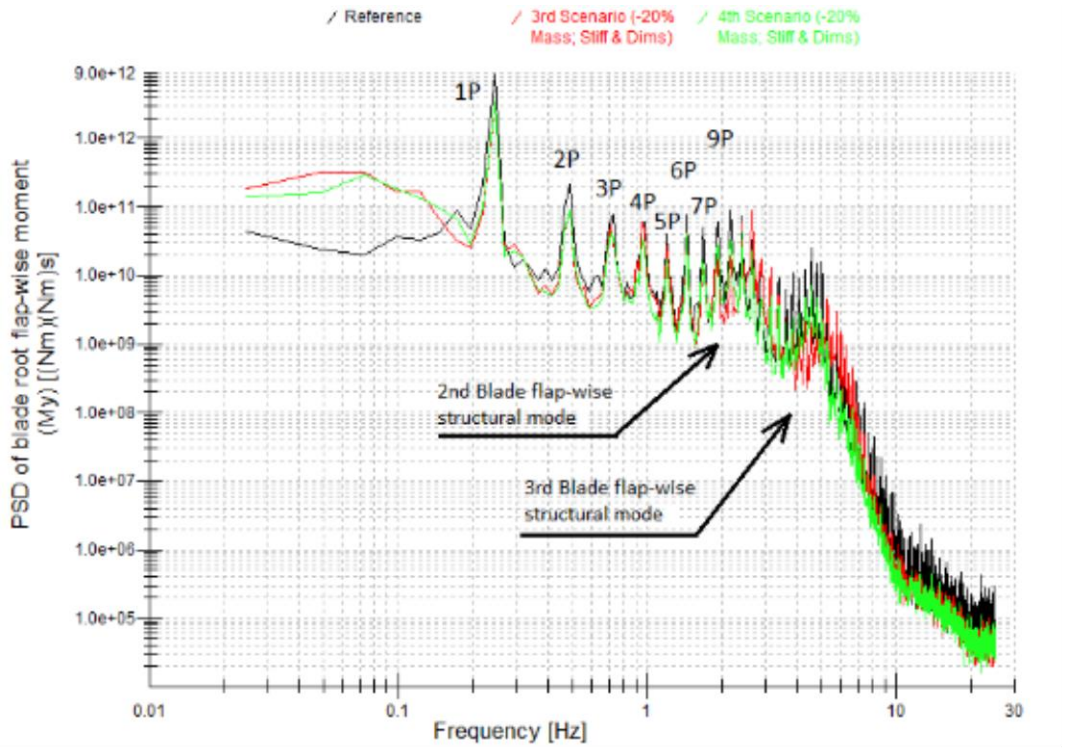

Figure 7.4: PSD of blade root flap-wise moment of reference model, 3rd and 4th of scenario at 14 m/s

Both Figure 7.3 and Figure 7.4 of flap-wise blade root moment demonstrate the applied modifications of the four scenarios do not lead to control system problems or unrepresentative dynamic effects.

7.3. Fatigue loads analysis

This section provides an answer to the two questions, which were posed at the beginning of this chapter, in terms of fatigue loads. According to IEC standards, the fatigue loads are demonstrated by damage equivalent loads (DELs). The bending moments are used to represent the changes of Lifetime DELs as a result of the applied modifications because stresses do not scale according the linear scaling rule [3], [6], [7], [24].

This section is divided into the two subsections, which correspond to the area of interests of this chapter: blade root edge-wise and flap-wise moments. Each of these two subsections demonstrates fatigue load changes for different design load cases (DLCs) which relate to different operational conditions of the wind turbine: normal power production (DLC 1.2), number of start-ups and shut downs (DLC 3.1/4.1) and idling (DLC 6.4).

7.3.1. Blade root edge-wise moment

Figure 7.5 shows the two graphs of the lifetime DELs of blade root edge-wise bending moments for Wohler coefficients four and ten, which typically represent steel and composite material, respectively. The Wohler coefficient represents the slope of the S-N curve [78], [79] , which shows the relation between the cycles until failure and stresses. The left and right graph corresponds to the changes of lifetime DELs for Wohler coefficient four and ten, respectively. Figure 7.5 depicts only DLC 1.2 as the trends of DLC 3.1/4.1 and 6.4 are similar to the trends of DLC 1.2. Nevertheless, the generated power trend equations of DLC 3.1/4.1 and 6.4 are going to be highlighted in Table 7.1. If a reader is curious about the graphs of DLC 3.1/4.1 and 6.4, these graphs can be found in Appendix D. Note DLC 3.1/4.1 represents the combination of 3.1 and 4.1 DLCs.

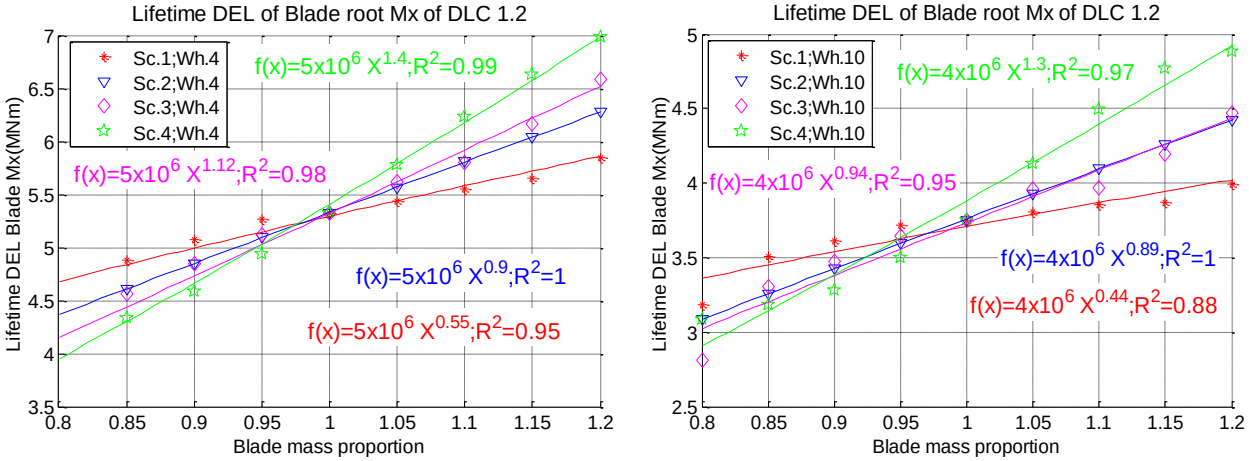

Figure 7.5: Edge-wise blade root moment lifetime DELs of DLC 1.2 for four scenarios of different blade modifications (the left graph - Wohler coefficient 4 and the right graph - Wohler coefficient 10).

Each graph of Figure 7.5 contains four curves, which represent the output data of the four scenarios of modifications, which were discussed in the beginning of this chapter. The trend line of power law is generated for each scenario to examine the changes of lifetime DELs due to the modification of blades.

Both graphs of Figure 7.5 show well defined trends in the four scenarios. However, there is a variation among the exponents of the trend lines of the four scenarios. Possibly, it is a result of the stochastic part of the load as the edge-wise blade root moment depends on self-weight of the

blades. The mass of blades changes in the same manner among the four scenarios. Additionally, in the graph with Wohler coefficient 10 the exponents of the trend lines are smaller the exponents of the trend lines for Wohler coefficient 4. It is a consequence of the material properties, as Wohler coefficient 4 and 10 characterise steel and composite materials. The composite materials have better resistance to tensile loads due to different types of fiber. In this case the resistance of composite materials improves the fatigue performance.

Design load case	Scenarios	Wohler Coefficients	
		4	***10***
3.1/4.1	***1***	$f(x) = 10 * 10^5 x^{0.9}; R^2 = 1$	$f(x) = 2 * 10^6 x^{0.55}; R^2 = 0.96$
	2	$f(x) = 10 * 10^5 x^{0.94}; R^2 = 1$	$f(x) = 2 * 10^6 x^{0.7}; R^2 = 1$
	3	$f(x) = 10 * 10^5 x^{1.58}; R^2 = 1$	$f(x) = 2 * 10^6 x^{1.33}; R^2 = 1$
	4	$f(x) = 10 * 10^5 x^{1.59}; R^2 = 1$	$f(x) = 2 * 10^6 x^{1.38}; R^2 = 1$
6.4	***1***	$f(x) = 6 * 10^5 x^{0.32}; R^2 = 0.97$	$f(x) = 6 * 10^5 x^{0.37}; R^2 = 0.97$
	2	$f(x) = 6 * 10^5 x^{0.24}; R^2 = 0.99$	$f(x) = 6 * 10^5 x^{0.22}; R^2 = 0.95$
	3	$f(x) = 6 * 10^5 x^{1.07}; R^2 = 0.99$	$f(x) = 6 * 10^5 x^{1.12}; R^2 = 0.99$
	4	$f(x) = 6 * 10^5 x^{1.01}; R^2 = 1$	$f(x) = 6 * 10^5 x^{1.01}; R^2 = 1$

Table 7.1: Equations of power law trend lines of DLC 3.1/4.1 and 6.4 for edge-wise blade root moment

7.3.2. Blade root flap-wise moment

Figure 7.6 depicts the changes of lifetime DELs of flap-wise blade root moment for DLC 1.2 of Wohler coefficient 4 and 10. The left and right graph characterises Wohler coefficient 4 and 10 respectively. In both graphs, the flap-wise blade root moments of the 1st and 2nd scenarios have minor changes as shown by low value exponents because the applied modifications to the above mentioned scenarios were not associated with any alteration of the blade dimensions. The changes of mass and stiffness do not affect the 1st and 2nd scenarios as shown by low value exponents. Additionally, equation 3.5 shows that flap-wise blade root depends on blade dimensions. Possibly, the low inclination of trend line of scenario 1 and 2 is a consequence of turbulence and wind shear as the trend lines of the 1st and 2nd scenarios are horizontal in DLC 3.1/4.1 (see Table 7.2), which correspond to steady flow without turbulence. The trend lines of the 3rd and 4th scenarios are similar as they have almost identical exponents in the power law equations. The dimensions of scenario 3 and 4 have been modified identically.

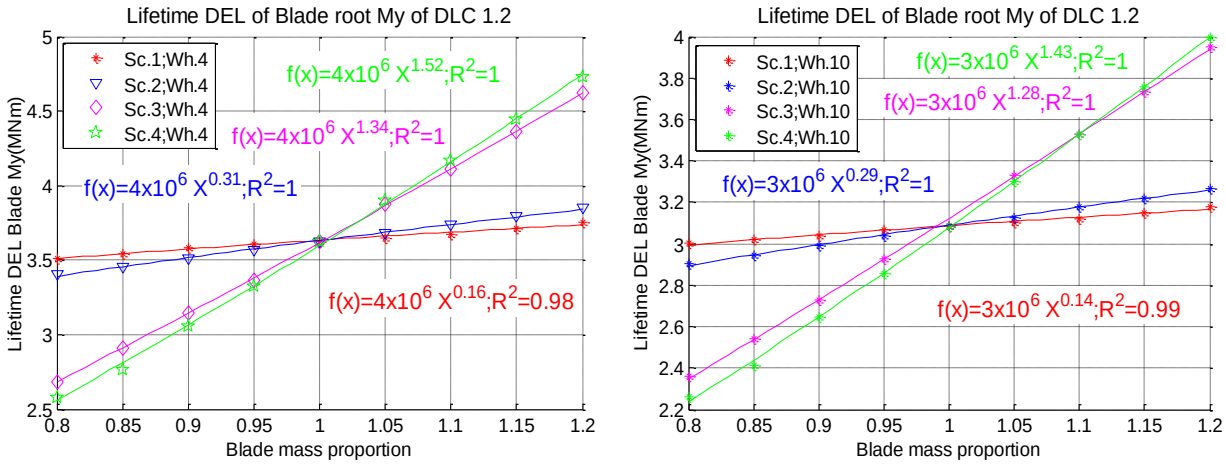

Figure 7.6: Flap-wise blade root moment lifetime DELs of DLC 1.2 for four scenarios of different blade modifications (the left graph - Wohler coefficient 4 and the right graph - Wohler coefficient 10).

The power trend line equations of lifetime DELs for DLC3.1/4.1 and 6.4 are shown in Table 7.2 because the trend line of DLC 3.1/4.1 and 6.4 of flap-wise blade root moment follow the similar pattern as the trend lines of DLC 1.2 for flap-wise blade root moment. However, the graphs of DLC 3.1/4.1 and 6.4 can be found in Appendix D.

Design load case	Scenarios	Wohler Coefficients	
		4	***10***
3.1/4.1	***1***	$f(x) = 10 * 10^5 x^{-0.01}; R^2 = 0.25$	$f(x) = 3 * 10^6 x^{-0.03}; R^2 = 0.37$
	2	$f(x) = 10 * 10^5 x^{0.03}; R^2 = 0.87$	$f(x) = 3 * 10^6 x^{0}; R^2 = -$
	3	$f(x) = 10 * 10^5 x^{0.93}; R^2 = 0.94$	$f(x) = 3 * 10^6 x^{0.88}; R^2 = 0.9$
	4	$f(x) = 10 * 10^5 x^{0.99}; R^2 = 0.94$	$f(x) = 3 * 10^6 x^{0.94}; R^2 = 0.9$
6.4	***1***	$f(x) = 1 * 10^6 x^{0.32}; R^2 = 0.99$	$f(x) = 2 * 10^6 x^{0.19}; R^2 = 0.98$
	2	$f(x) = 1 * 10^6 x^{0.37}; R^2 = 0.99$	$f(x) = 2 * 10^6 x^{0.25}; R^2 = 0.98$
	3	$f(x) = 1 * 10^6 x^{1.02}; R^2 = 1$	$f(x) = 2 * 10^6 x^{1.05}; R^2 = 1$
	4	$f(x) = 1 * 10^6 x^{1.07}; R^2 = 1$	$f(x) = 2 * 10^6 x^{1.1}; R^2 = 1$

Table 7.2: Equations of power law trend lines of DLC 3.1/4.1 and 6.4 for flap-wise blade root moment

7.4. Deterministic fatigue loads analysis

This section provides an overview of the fatigue analysis of the deterministic load part in terms of lifetime DELs. In section 7.3.1 there is statement, which says that the variations of exponent in edge-wise blade root moment is a result of the stochastic part of the loads, because the deterministic part of the load relates to blade self-weight loads. The masses have been changed identically among the four scenarios and the edge-wise blade root moment is a function of cyclic

loads due to gravity. Thus, there was an expectation to have the same inclinations or exponents of trend lines among the four scenarios.

In this case the deterministic part of the edge-wise blade root bending moment of DLC 1.2 is going to be investigated in order to verify the statement that the stochastic part of the load causes the variation of the trend lines among the four scenarios.

The flap-wise blade root moment is not presented in this section, because aerodynamic loads contribute the major part to flap-wise moments, and are not deterministic loads.

Figure 7.7 shows the two graphs, which express the deterministic part of edge-wise blade root bending moment of the four scenarios for Wohler coefficient 4 and 10, respectively. Both graphs show that the output data from the four scenarios overlaps, which shows the deterministic load part is identical among the four scenarios. The above-mentioned overlapping among the trend lines proves that the deterministic part of the edge-wise loads is mainly a function of blade mass and the variation of the trend lines in section 7.3.1 is caused by the stochastic part of the load, which corresponds mainly to turbulence and wind shear.

Additionally, the exponent value of the power law equation of the trend line of the four scenarios is roughly equal to one for Wohler coefficient 4 and 10. It demonstrates the deterministic lifetime DELs moment of the blade root changes linearly to the mass of blades.

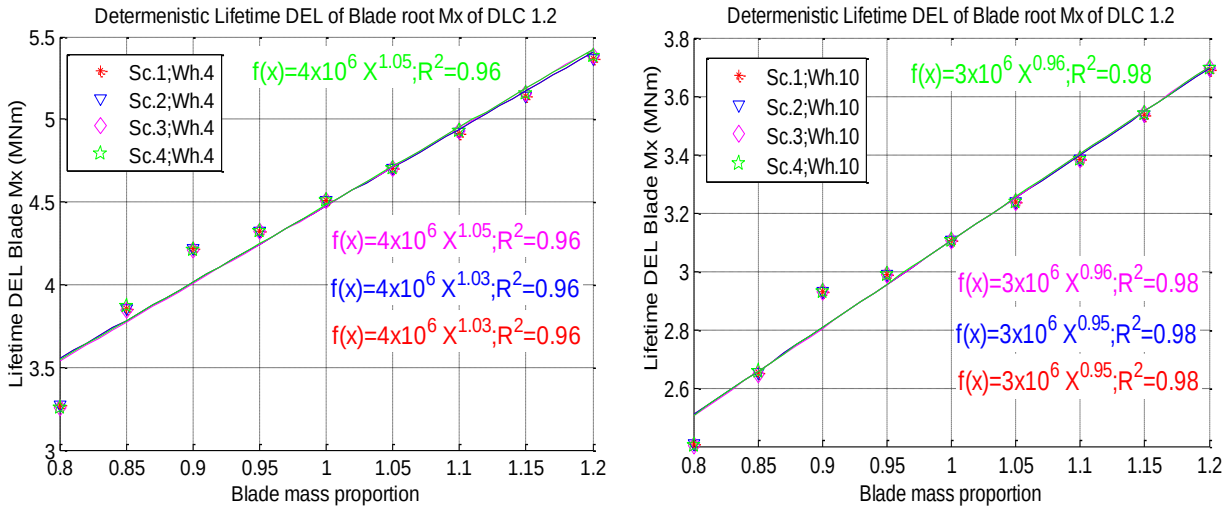

Figure 7.7: DLC 1.2 deterministic lifetime DELs of edge-wise blade root bending moment of four scenarios for Wohler coefficient 4 and 10.

7.5. Extreme loads analysis

This section depicts the changes in extreme loads of the edge-wise and flap-wise blade root moment among the four scenarios. The power law trend line was generated for each scenario in order to quantify the changes of extreme loads. This research focusses on the four DLCs (1.1, 1.3. 6.1 and 6.3) of extreme loads as it was stated in chapter 2. However, only DLC 1.1 will be presented in this chapter because the rest of DLCs follow the same pattern as DLC 1.1. Results from DLC 1.3, 6.1 and 6.3 can be found in Appendix D.

7.5.1. Design load case (DLC) 1.1

DLC 1.1 uses a statistical extrapolation technique based on long-term (50-year period) exceedance probability for the calculation of extreme loads in a wind flow with normal turbulence model (NTM). The explanation of DLC 1.1 and the procedure of calculating extreme loads for a 50 year period can be found in chapters 2 and 5.

Figure 7.8 includes the two graphs, which represent the calculated extreme load values of 50-year periods of edge-wise and flap-wise blade root moments. In the graph of edge-wise blade root moment there is only the 2nd scenario trend line with sufficient value of correlation coefficient, or "*R*-squared", which indicates the level of correlation between output data and the generated power trend line from the output data. The data of the 1st, 3rd and 4th scenarios is scatter and does not show the general pattern or trend. This is demonstrated by the very low value of *R*-squared in the 1st, 3rd and 4th scenarios.

The chaotic distribution of output data is a result of the applied modifications to the wind turbine blades being minor in terms of their influence on extreme loads. The introduced modifications change the natural dynamic of wind turbine, which has an influence on the performance of the controller to alleviate loads. Therefore, any modifications of the wind turbine model require the retuning of the controller in order to have the maximum performance from the controller, e.g. loads alleviation.

The second graph of Figure 7.8, which represents the extreme loads of flap-wise blade root moment, depicts a similar pattern of trend lines to the pattern of lifetime DELs of flap-wise blade root moments.

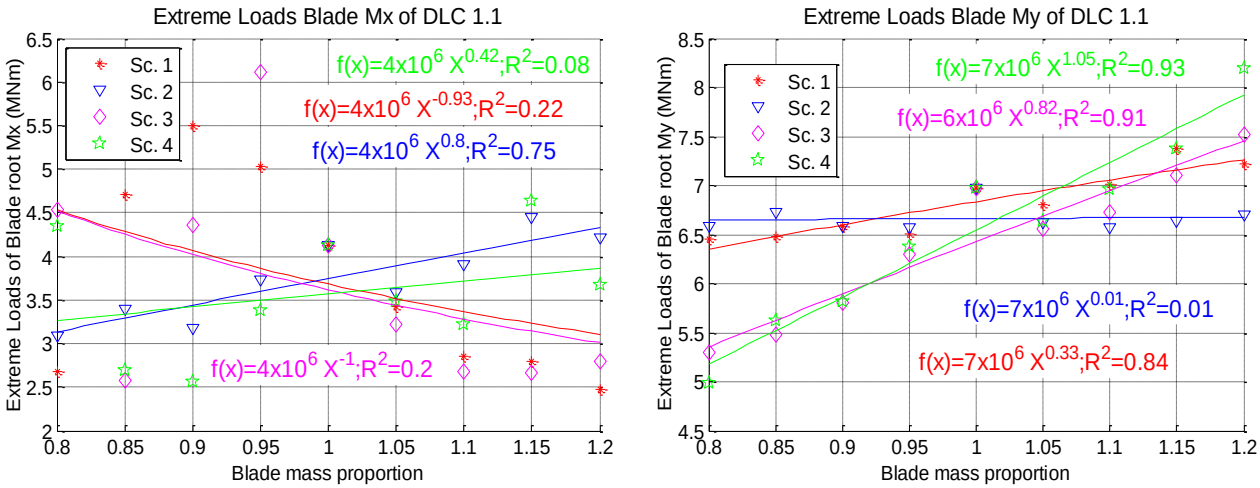

Figure 7.8: DLC 1.1 extreme loads of edge-wise and flap-wise blade root moment of four scenarios.

7.6. Summary and discussion

This chapter has provided an overview of the dependency of blade loads to the structural parameters of the blades. There are four different scenarios of blade modifications, which were investigated in this chapter.

The power spectral analysis of edge-wise and flap-wise blade root moment was used to validate the accuracy of the applied modifications. The power spectral analysis shows the shifting of the blade natural frequency in the modified models of scenario 1 and 3. However, the shifted natural frequencies of blades do not coincide with the rotor frequency and its harmonics, which leads to resonance. The modifications of scenario 2 and 4 preserve the original frequency of the blades. Therefore, the PSD curves of the 2nd and 4th scenarios match the PSD curves of reference model. The cumulative power spectral density graphs demonstrate that all peaks of structural blade modes and harmonics of rotor frequency are well damped and do not cause any severe loads which could lead to a failure of the wind turbine.

Fatigue load analysis was used for design load cases based on the IEC standards [5], where fatigue loads were calculated in terms of lifetime DELs. It demonstrates the well-developed pattern of the changes lifetime DELs in the output data among the four scenarios for edge-wise and flap-wise blade root moments. The exponents of the generated trend lines vary slightly among the four scenarios (in DLC 1.2) and different DLCs, which characterise the different operating conditions of a wind turbine. However, fatigue load analysis of the deterministic part of the edge-wise moment shows that the output data of the four scenarios is identical. Therefore, the

stochastic part of the loads is responsible for the variation of exponents among the four scenarios for edge-wise blade root moments in DLC 1.2.

Extreme loads analysis has depicted that the extreme moments of the flap-wise blade root has produced more or less the same trend as the trend lines of lifetime DELs for most of the scenarios in extreme loads. But for edge-wise blade root moment the applied modifications were not significant enough to produce the changes of extreme loads in order to develop well defined trend lines. Instead of the well-defined trend lines the output data of extreme edge-wise blade root moment is scattered randomly. Possibly, this is a result of the control system, because the original controller of reference model was implemented for the modified models wind turbine models (4 scenarios) without adjusting to the modified models.

At the beginning of this chapter two questions have been asked. These two questions are below:

I. *How do fatigue and extreme loads change due to modifications of blade parameters?*
II. *Is it possible to develop fatigue and extreme loads trends of the gained data of sensitivity analysis as a function of the modified parameters?*

This chapter proves and demonstrates the possibility to generate the trend lines of fatigue and extreme (flap-wise blade root only) loads as a function of the specific property of a wind turbine, which was the mass of blades in this chapter, as shown in Figure 7.5, Figure 7.6, Table 7.1, Table 7.2, Figure 7.8 and Appendix D. These trend lines can be used to investigate the changes of fatigue and extreme loads and develop an algorithm for calculating the fatigue and extreme loads for the prospective wind turbine models. This chapter highlighted that the controller of wind turbine requires tuning to adjust to any modifications of the base model in order to have maximum efficiency in performance of the controller for alleviation of loads.

8. Effect of rotor solidity on loads

This chapter investigates the impact of rotor solidity on wind turbine loads especially on extreme and fatigue (lifetime DELs) loads. There are two ways to change the rotor solidity. The first way is based on the modification of TSR or tip speed and chord length of aerofoils. The second method maintains the original TSR by varying the chord length and using aerofoils with a different design lift coefficient. The modifications related to both methods require adjusting the aerodynamic (inflow and twist angle) and structural properties (chord, mass and stiffness) of the wind turbine blades.

Blonk *et al.* [80] states that the reduction of rotor solidity mitigates the tower top loads and blade and generator mass. The reduction of blade and generator mass decreases the cost of a wind turbine and energy. This chapter tries to check the hypothesis of Blonk *et al*. [80] for the reduction of extreme and fatigue tower top loads from rotor solidity. In this case the main goal or question of this chapter is:

- *How does the rotor solid affect the extreme and fatigue loads of wind a turbine?*

The second goal of this chapter is to develop the trends of the extreme and fatigue loads as function of rotor solidity or a parameter related to the rotor solidity.

According to these two methods this chapter is split into two parts. Section 8.1 investigates the impact onto extreme and fatigue loads based on the first method of changing of rotor solidity, and the influence of the second method on loads is examined in section 8.2.

Both sections of each method consist of subsections, which provide the overview of the necessary alterations of aerodynamic and structural parameters, the changes of rotor aerodynamic damping (as it depends on the rotor solidity), and steady state and spectral analysis to inspect the accuracy and any negative side effects of the applied modifications. The last three subsections present the changes of fatigue, the deterministic part of fatigue and the extreme loads due to the modification of rotor solidity.

This chapter is finished by section 8.3, which provides the summary and discussion of the gained results of each method.

8.1. Tip speed ratio impact

The solidity of the rotor is the ratio of blade total planform area to the swept area of rotor [3]. However, there are some uncertainties with the term of solidity as to whether it includes or excludes the inactive aerodynamic part of the rotor in the area around the hub. The definition of rotor solidity used in the present study follows.

The rotor solidity depends on the chord length, radius length and number of blades as defined by the following equation [3]:

$$\sigma = \frac{B \int_0^R c(\lambda, r) dr}{\pi R^2} \quad 8.1$$

Where, B is the number of blades, $c$is the chord width, λ is the tip speed ratio (TSR) and r is the local radius. Equation 8.1 demonstrates that the chord length is a function of TSR and local radius. Equation 8.2 shows a simplified formula for the chord.

$$c(\lambda, r) = \frac{16\pi R^2}{9BCl_d\lambda^2 r} \quad 8.2$$

Cl_d is the design lift coefficient which represents the value of lift coefficient at the maximum lift/drag ratio.

The simplified equation of chord length is based on BEM theory for the optimum rotor conditions, which assumes that:

- The axial induction factor is $a = \frac{1}{3}$ and tangential factor is $a' = \frac{a(1-a)}{\lambda^2\mu^2}$
- There is no aerodynamic drag
- There is no hub and tip losses

A detailed explanation and derivation of equation 8.2 can be found in chapters of the books [1], [3], [6], which discuss the rotor solidity and geometry or shape of blades.

Equation 8.2 shows the dependency between the chord length and tip speed ratio. Any changes in the TSR lead to changes of blade chord. Additionally, the alterations of TSR have an influence

on the inflow angle, which is the angle between the resultant flow vector and the net tangential flow vector, as shown by in equation 8.3.

$$tan\phi = \frac{1-a}{\lambda\mu(1+a')} \tag{8.3}$$

The modification of inflow angle affects the twist angle of the blades as defined by equation 8.4.

$$\theta = \phi - \alpha \tag{8.4}$$

The angle of attack is represented by α. A design value of α is selected corresponding to the maximum lift/drag ratio.

8.1.1. Blade properties

Changes in chord length affect the structural properties of blades such as the mass and bending stiffness of the blades. Mostly the blade mass depends on spar caps, shear web and shell of blade. The size and mass of the three above mentioned components are proportional to the dimensions of blade. Consequently, it is possible to assume that the blade mass is a function of the dimensions of blade, which are length, chord and thickness. The variation of solidity affects only the chord of blade, which has the influence on the thickness of blade because the thickness is a function of the chord as stated in the lecture notes of Area and Bending Inertia of Aerofoil Sections [81]. The length of the blades does not change with the rotor solidity. Hence, it is assumed that the mass of the blades is a square function of the chord length as shown in equation 8.5.

$$m = \rho * Lc^2 = m\,c^2 \tag{8.5}$$

Moreover the bending stiffness of the blades alters with the chord because the second moment of area depends on the length of chord as demonstrated by equation 8.6, which is extracted from [81].

$$I \cong K_I ct(t^2 + h^2); = I\,c^4 \tag{8.6}$$

Where, $K_I(\cong 0.036)$ is the proportional coefficient of the second moment of area, *t* is maximum thickness and *h* is the maximum camber.

8.1.2. Aerodynamic damping

The wind turbine is affected by two types of damping, which are aerodynamic and structural. The structural damping depends on the properties of the mechanical system such as: size, shape and material. The detailed explanation of structural damping can be found in these works [82], [83]. The goal of this subsection is to see the changes of the aerodynamic damping as a consequence of the changes in rotor solidity.

The following equation is given as an approximation of aerodynamic damping per unit length for a blade in terms of the flap-wise direction [1], [84].

$$c_{Aero}(r) = 0.5\rho\Omega r c(r) C_{L\sigma} \tag{8.7}$$

$C_{L\sigma}(d\,C_L/d\alpha)$ is rate of change of lift coefficient in terms of the angle of attack. If the air flow is attached to the aerofoil, the rate of change of lift coefficient is constant and equal to 2π [1]. It is noticeable from equation 8.7 that the aerodynamic damping of the blade varies along the span as it is proportional to the blade element size which depends on the length of chord. Thus the changes of rotor solidity have an impact on the aerodynamic damping based on equation 8.7. Figure 8.1 demonstrates the distribution of aerodynamic damping along the blades for the wind turbine models with different solidity.

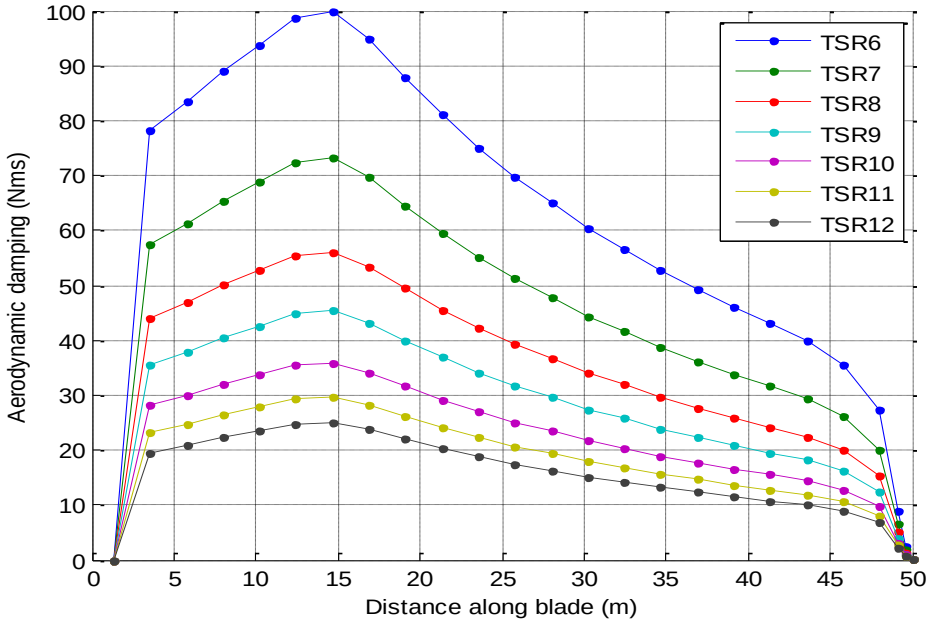

Figure 8.1: Aerodynamic damping of blade for different tip speed ratios at 16 m/s average wind speed and 1.51 rad/s average angular rotor speed

Figure 8.1 shows that aerodynamic damping has an inverse relation to tip speed ratio. In this case the increasing TSR leads to a reduction of aerodynamic damping, which can have an adverse effect on the support structure of the wind turbine, because the aerodynamic damping is proportional to the chord length as shown in equation 8.7. The reduction of aerodynamic damping leads to a decrease in the fatigue life for the tower. So Figure 8.1 reveals that the decreasing of TSR from 9 to 6 can double the aerodynamic damping generated by the blade and vice versa for increasing the TSR to 12. The effect of damping modifications on extreme and lifetime DELs are shown in section 8.1.4 and 8.1.6, respectively.

It is obvious that the rotor damping has an inverse relationship to TSR but a question can be asked, does the rotor aerodynamic damping alter by the same proportion to TSR as the aerodynamic damping of the blade? The aerodynamic damping ratio provides a relative measure for damping, which can be assessed in terms of the severity of the consequences on the loads. The subsequent equation [1] shows the approximation of theoretical aerodynamic damping ratio of the i^{th} mode for the rotor.

$$\xi_{Aeroi} = \frac{c_{Aeroi}}{2m_i w_i} = \frac{0.5\rho\Omega C_{L\sigma}\int_0^R rc(r)\mu_i^2(r)dr}{2w_i\int_0^R m(r)\mu_i^2(r)dr} \qquad 8.8$$

Equation 8.8 can be simplified to provide a constant value of the aerodynamic damping ratio [84] as shown by equation 8.9.

$$\xi_{Aero}(V_o) = \Omega(V_o)\frac{N_b \rho C_{L\sigma} m_{1b}}{4 M_o w_n} \quad 8.9$$

Where, N_b is number of blades, M_o is modal mass, w_n is natural frequency and m_{1b} is the first order moment of the blade area span wise as defined in equation.

$$m_{1b} = \int_0^R c(r) r dr \quad 8.10$$

Figure 8.2 demonstrates the theoretical aerodynamic damping of the entire rotor for the wind turbine models with different TSR, which were calculated by using equation 8.9. In Figure 8.2 there is the same pattern as at Figure 8.1 of aerodynamic damping along the blade as expected. Figure 8.1 and Figure 8.2 depict that increasing of TSR reduces aerodynamic damping. The theoretical aerodynamic damping of the rotor of the reference model with TSR of 9 is 4.5 % as demonstrated in Figure 8.2. Increasing the TSR from 9 to 12 reduces the aerodynamic damping ratio to 2.5 %, which is almost a half of original value. The decreasing of TSR from 9 to 6 increases the aerodynamic damping from 4.5 % up to 10 %, which is more than double the original value. This subsection indicated that the aerodynamic damping is a function of the chord length of the blade, which is inversely proportional to the TSR. Furthermore, the additional information about the advantages and disadvantages of increasing TSR are provided below.

Benefits of increasing of tip speed are:

- Reduced solidity which leads to the reduction of mass and cost of blades.
- Reduced torque as the power production is a function of torque and rotor angular velocity and the weight and cost of generator and gearbox depend on torque.

Drawbacks of the increasing of tip speed:

- Increased acoustic noise emission as 80 m/s tip speed is an aerodynamic acoustic restriction [3].
- Increased leading edge erosion of the blades.
- Reduction of aerodynamic damping.

Offshore acoustic noise restrictions may exist but are usually much less strict so design tip speeds are generally higher [3], [85]. Hence, the selection of TSR is a trade-off between the advantages

and disadvantages. The following subsections investigate the changes in loads due to changes of TSR.

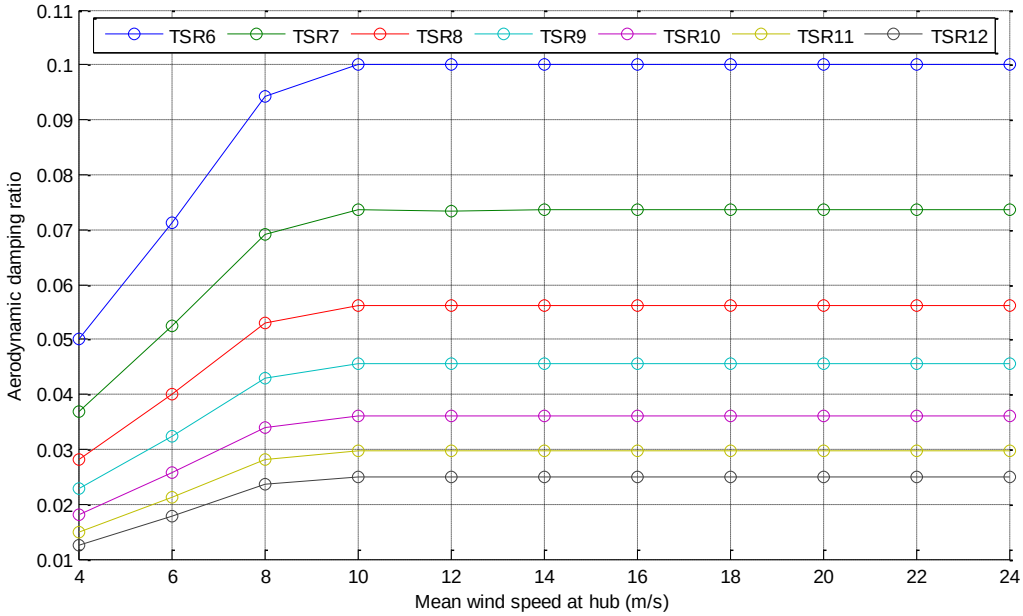

Figure 8.2: Theoretical aerodynamic damping ratio of the entire rotor for the wind turbine models with modified TSR.

8.1.3. Validation of performed changes

This section examines the accuracy of applied modifications in order to change the rotor solidity. This section is divided into two subsections: steady state analysis (8.1.3.1) and spectral analysis (8.1.3.2). Section 8.1.3.1 examines the accuracy of the change in a steady state, while section 8.1.3.2 inspects in a dynamic state.

8.1.3.1. Steady state analysis

The steady state analysis provides an overview of changes of rotor solidity to validate the accuracy of the applied modifications to the reference model in the steady state conditions. The aim of Section 8.1 is to alter the rotor solidity by performing the modification of TSR to the base model. Therefore, Figure 8.3 shows the TSR of the models, which are the six curves of the

modified machines (TSR 6, 7, 8, 10, 11, 12) and the curve of the reference model (TSR 9), against mean wind speed. Each of the seven curves matches the specified its label.

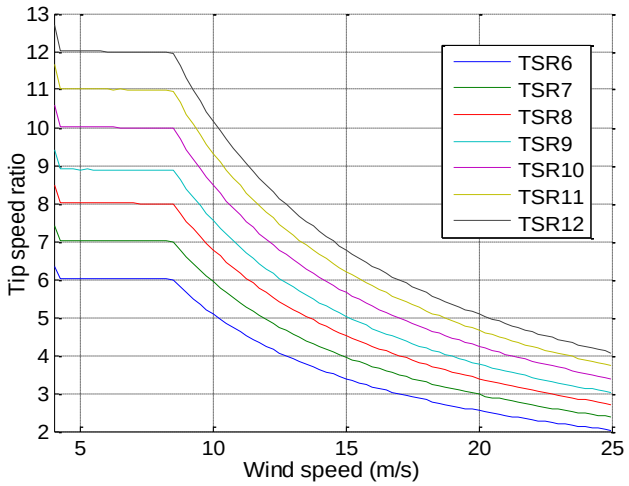

Figure 8.3: Tip-speed ratio of the reference and modified models.

The next step is to inspect the accuracy of adjusting the aerodynamic and structural properties due to the modification of TSR value. Hence, Figure 8.4 and 8.5 compares between the modified models and the base one for power coefficient and ideal power production, respectively. Figure 8.4 shows that max *Cp* values are shifted for the curves of modified models to adapt the new values of TSR, as it was anticipated as a consequence of the modifications. There is also the tiny reduction of the maximum *Cp* in the modified models compared to the maximum *Cp* value of the reference model. The highest reduction occurred for the model of TSR 6, which the maximum *Cp* equals to 0.4793. The maximum *Cp* value of the base model equals to 0.4874. So the maximum difference of max *Cp* values between TSR 6 and 9 models is <2%, which is very small and can be neglected.

Figure 8.5 demonstrate the power production curves of altered models overlap the curve of the reference model apart from in the below rated region at the vicinity of the switching point between the below and rated regions, because there is very small variation among the power curves. However, this variation is insignificant and can be neglected. Hence, the power curves of the reference and modified models can be assumed identical.

The steady state analysis confirms that the applied modifications of changing rotor solidity and adjusting blade properties were executed correctly in terms of steady conditions. The following section reviews the accuracy of modifications and adjusting procedure in terms of dynamic conditions.

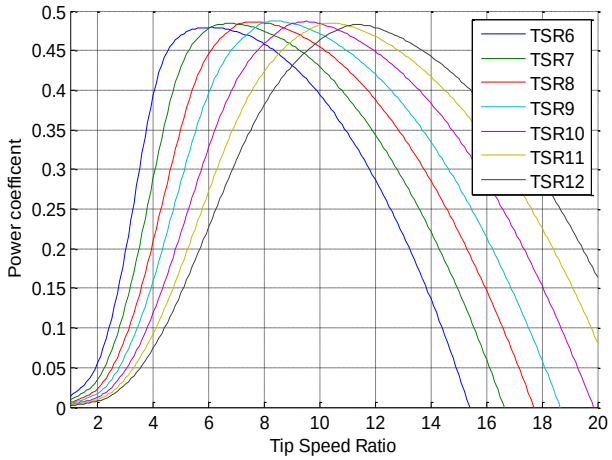

Figure 8.4: Power coefficient of the reference and modified models.

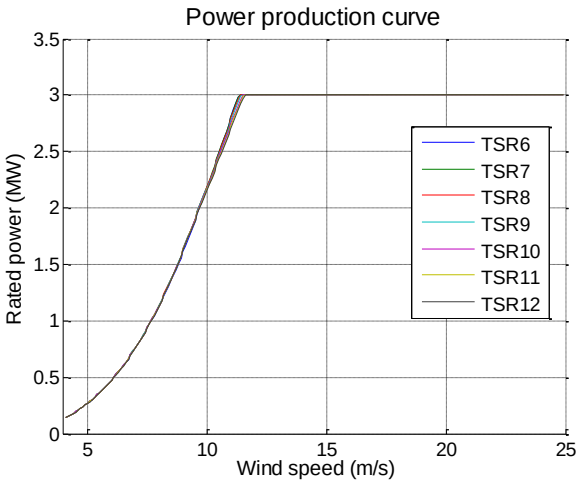

Figure 8.5: The power production output of the reference and modified models.

8.1.3.2. Spectral analysis

The spectral analysis inspects the changes in instantaneous loads of wind turbines for adverse impact due to the modifications of rotor solidity in terms of dynamic conditions.

As it was stated before each figure of the spectral analysis includes three models, which are TSR 6, TSR 9 (reference model) and TSR 11, to compare the modified models with the reference model for any changes occurred in the altered models.

8.1.3.3. Blade root edge-wise moment

Figure 8.6 includes the six curves, which correspond to PSD and cumulative PSD of blade root edge-wise moment of three models (TSR 6, TSR 9 and TSR 11).

It is noticeable that the applied modifications have changed the rotational frequency of rotor *(1P)* because *1P* of TSR 6 reduced or shifted to the left from 1P of original model and 1P of TSR 11 increased or shifted to the right. These changes of rotor frequency were expected for the altered models because the rotor rotational speed is proportional to the TSR.

The frequency of the blade structural mode altered in the reverse direction compared the rotor frequency because the natural frequency of blade is a function of blade stiffness and mass as shown in equation 7.4. The blade mass and stiffness are related to the chord length as stated by equation 8.5 and 8.6, but the length of chord is inversely proportional to the tip speed ratio (TSR) according to equation 8.2. Therefore, the decreasing of TSR leads to the increasing of the chord

length, blade mass, stiffness and natural frequency of structural modes and vice versa. According to Figure 8.6, the above mentioned changes do not have any negative impact because there are not any un-damped peaks, which have the matched frequency of harmonics of 1P and structural blade modes, and higher than *1P* peaks, in each curve. Additionally, the curves of cumulative PSD do not have a significant rise apart from *1P*. Therefore, the spectral analysis of edge-wise blade loads did not reveal any adverse impacts.

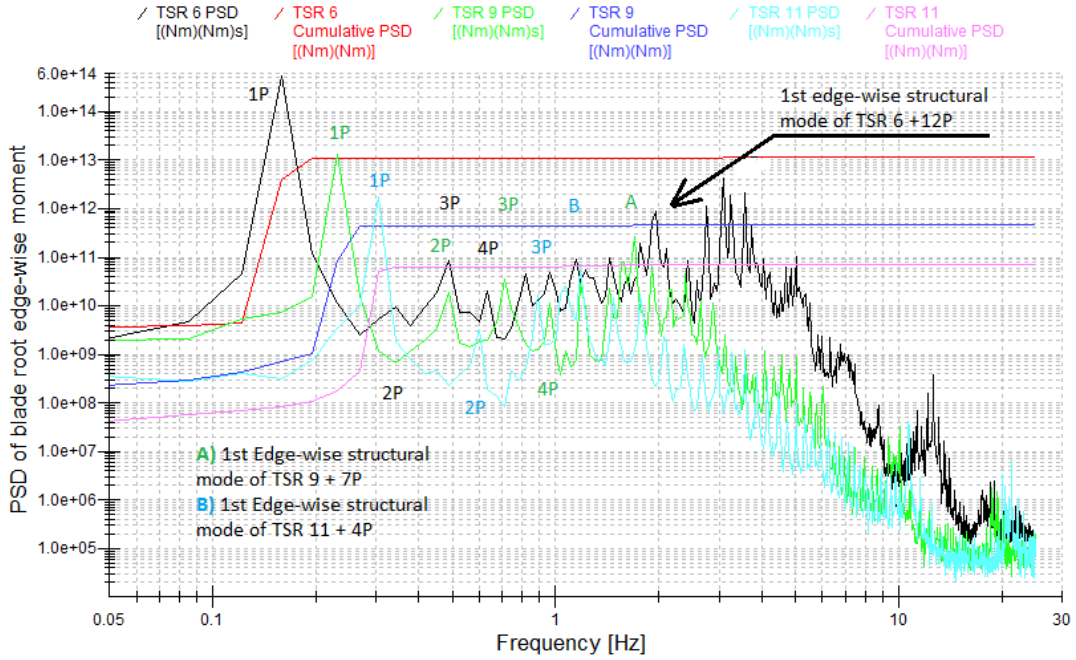

Figure 8.6: PSD and cumulative PSD of blade root edge-wise moment of TSR 6, 9 and 11 at 16 m/s mean wind speed.

The PSD graphs of blade root flap-wise, low-speed shaft and yaw bearing moments do not reveal any negative behaviour of the modified models. In this case these graphs are not going be presented in the main body of thesis. However, these graphs can be found in Appendix E.

8.1.3.4. Tower base moment

The fore-aft tower base moment is illustrated in Figure 8.7, which includes the two graphs of the PSD and cumulative PSD graphs for fore-aft tower base moment, respectively. Figure 8.7 demonstrates that the three modes A, B and C, are damped because the cumulative PSD curves do not have significant rises apart from tower fore-aft translational attachment mode. There is a high peak, which is labelled as *12P* + B, on the PSD curve of the reference model. It is not higher

than the peak of the tower fore-aft translational attachment mode. However, it is not well damped because it is narrow (e.g. has a shape of spike). In the cumulative PSD curve the *12P* + B responds to a rise as shown in Figure 8.7a. The *12P* + B peak characterises the coupling of the coincident frequency between the tower flap-wise structural mode and *12P* harmonic of rotor frequency.

Note the cumulative PSD curve of the TSR 6 model is lower than both curves of TSR 9 and 11 in Figure 8.7b. It means the magnitude of TSR 6 of fore-aft tower base moment is lower than the magnitude of TSR 9 and 11 as a consequence of the increasing of aerodynamic damping in TSR 6, which mitigates tower base loads, from the changes of rotor solidity as shown in Figure 8.2.

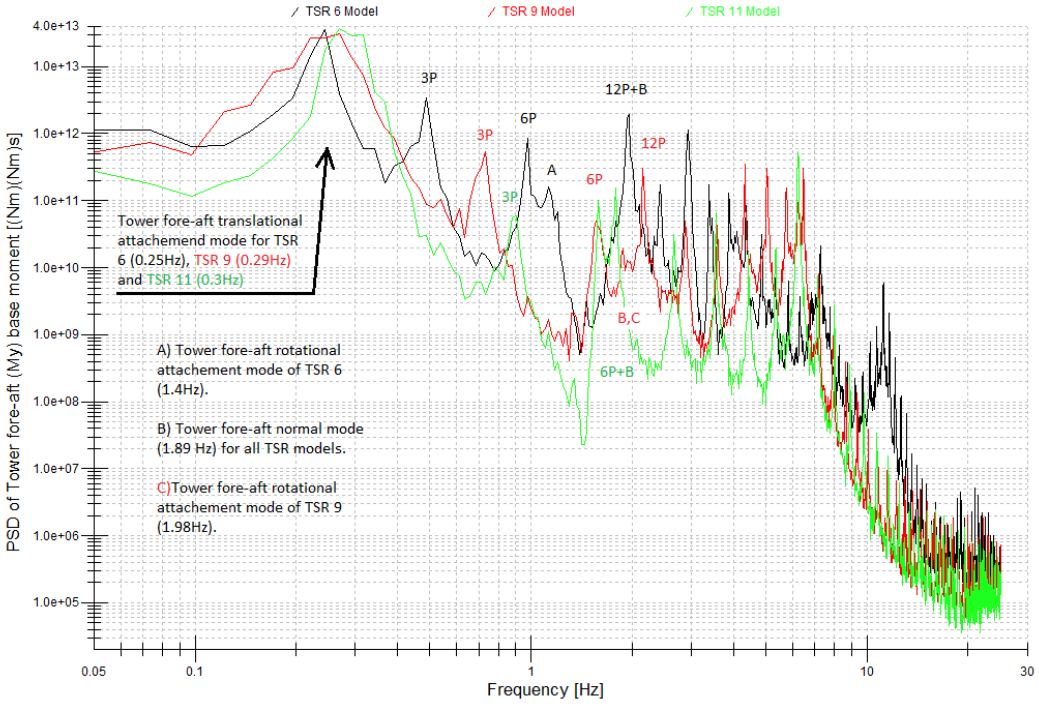

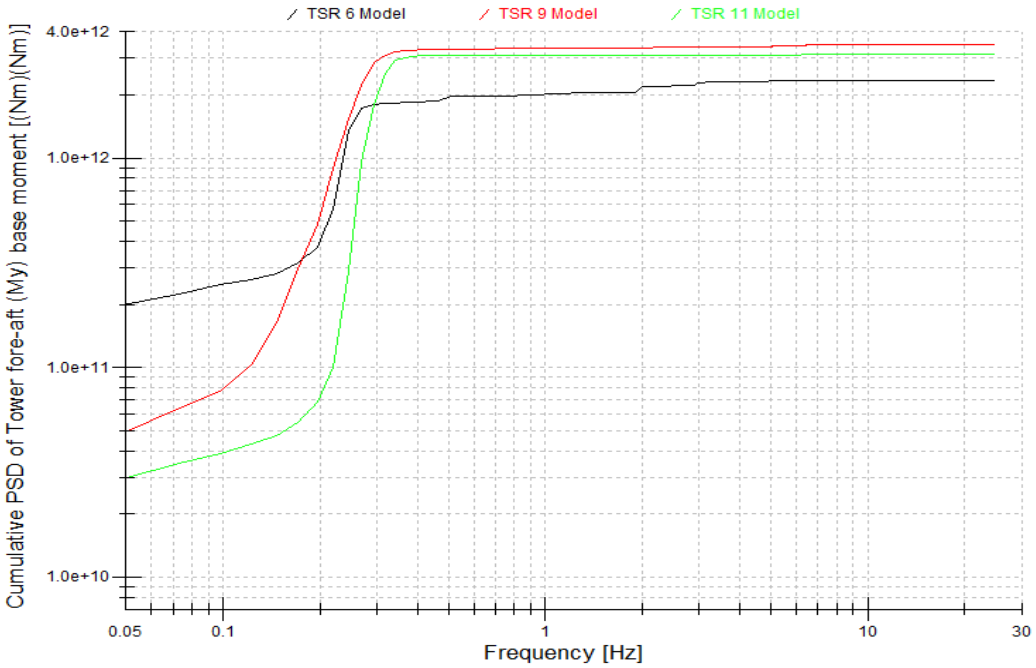

Figure 8.7: PSD and cumulative PSD of tower base fore-aft (My) moment of TSR 6, 9 and 11 at 16 m/s mean wind speed, respectively.

8.1.4. Fatigue loads analysis

This section looks through the changes of fatigue loads, which are presented by lifetime DELs, as a consequence of the modifications to rotor solidity. This section is divided into subsections, which correspond to the zones of interest: blade root, low-speed shaft, yaw bearing and tower base moments. Each of these subsections shows the changes of fatigue loads in the three different DLCs (1.2, 3.1/4.1 and 6.4), which relate to operational conditions of the wind turbine such as: power production range, summation of the number of start-ups and shut-downs and idling conditions. The lifetime DELs are plot against the chord modification factor in all the figures of fatigue loads analysis because the chord is a function of TSR as shown by equation 8.2.

8.1.4.1. Blade root edge-wise and flap-wise moments

Figure 8.8 demonstrates the six graphs of the three DLCs for edge-wise and flap-wise blade root moment. The first, second and third horizontal pair of graphs shows lifetime DELs changes of DLC 1.2, 3.1/4.1 and 6.4, respectively. In each graph the developed trend lines of output data depict the general pattern, which indicates that the fatigue loads increase with the increasing of chord.

For edge-wise moments it is a result of increasing of blade mass, which is a function of chord length squared as stated by equation 8.5. The variation of flap-wise moment is a consequence of the changes of rotor solidity because the thrust force is proportional to the chord length as demonstrated by equation 8.11 of the thrust in blade element theory, which was extracted from reference [6].

$$dT = \frac{1}{2} B \rho U_{rel}^2 (C_l cos\varphi + C_d sin\varphi) c dr \qquad 8.11$$

The exponents of power law equation of DLC 1.2, which are illustrated by the first pair of graphs in Figure 8.8, have the similar values of calculated exponents to predicted exponent values estimated by the method of scaling with similarity [3], [6], [7], [24], which are x^2 and x^1 for edge-wise and flap-wise blade root moments, respectively. Manwell and Gasch [6], [7] state that the blade root edge-wise moment is a product of mass, gravity and distance from blade root to centre of blade mass as shown by equation 3.7. According to the rotor solidity modification, the rotor speed and blade mass have changed and that will change will change number of loads cycles and so DELs, because the blade mass is a function of the chord as written before. The calculated exponents of edge-wise moment are smaller by 10 % than the predicted exponents due to dynamic conditions in simulations. In terms of flap-wise blade root moment the predicted exponent equals to x^1 because the flap-wise moment is a function of thrust force on the blade and distance from the blade root to point, where the resultant thrust acts at the blade. The modifications of rotor solidity affect only the thrust force, which depends on chord as shown by equation 8.11, the original length of the blades was preserved. The calculated exponents of flap-wise moments are not close to the predicted values compared to the edge-wise moment of DLC 1.2. Possibly, the dissimilarity between the calculated and predicted exponents is caused by the dynamic state conditions, especially turbulence and wind shear.

DLC 3.1/4.1 graphs of Figure 8.8 depict the variation of exponent values between Wohler coefficient 4 and 10. Therefore, the exponent of Wohler coefficient 4 of flap-wise moment is close to the exponent of DLC 1.2 of Wohler coefficient 4. The calculated exponent of Wohler coefficient 10 is lower than exponent of Wohler coefficient 10 for DLC 1.2. In terms of flap-wise moment the calculated exponents of both Wohler coefficients are located close to x^1.The comparison between the exponent of DLC 1.2 and DLC 3.1/4.1 shows that the values of exponents of Wohler coefficient 4 are not so different. But there is variation between the exponents of Wohler coefficient 10. The difference between DLC 1.2 and DLC 3.1/4.1 is dynamic wind flow (with turbulence) and steady wind (without turbulence). In this case the composite materials, which

characterises by Wohler coefficient 10, are sensitive to the small cycles caused by turbulence, because the composite materials either have low level of endurance limit or do not have it compared to steel. Therefore, for steel the small cycles do not contribute to damage, if these small cycles are lower than endurance limit.

In Figure 8.8 the last horizontal pair of graphs demonstrates that the obtained exponents of DLC 6.4 are significantly larger than the predicted values because the lifetime DELs of the two last wind turbine models, which correspond to 1.6 and 2.2 chord modification factor, are much higher than the values of the rest of models. Probably, it is a consequence of the amplified blades weight at high values of chord modification factors for edge-wise moment, but for the flap-wise moment it is a result of the extreme weather conditions and the increased chord length due to the modifications of rotor solidity.

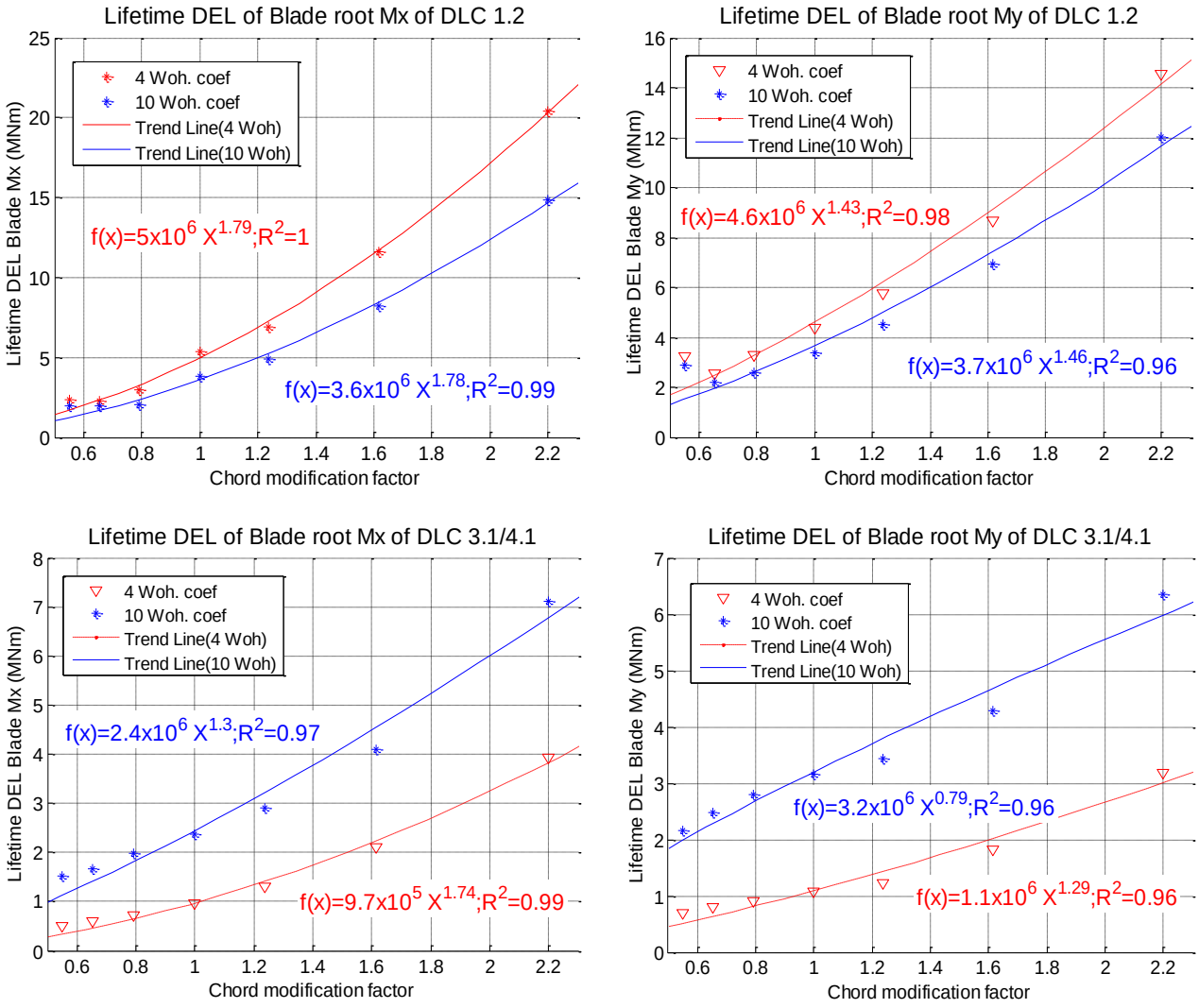

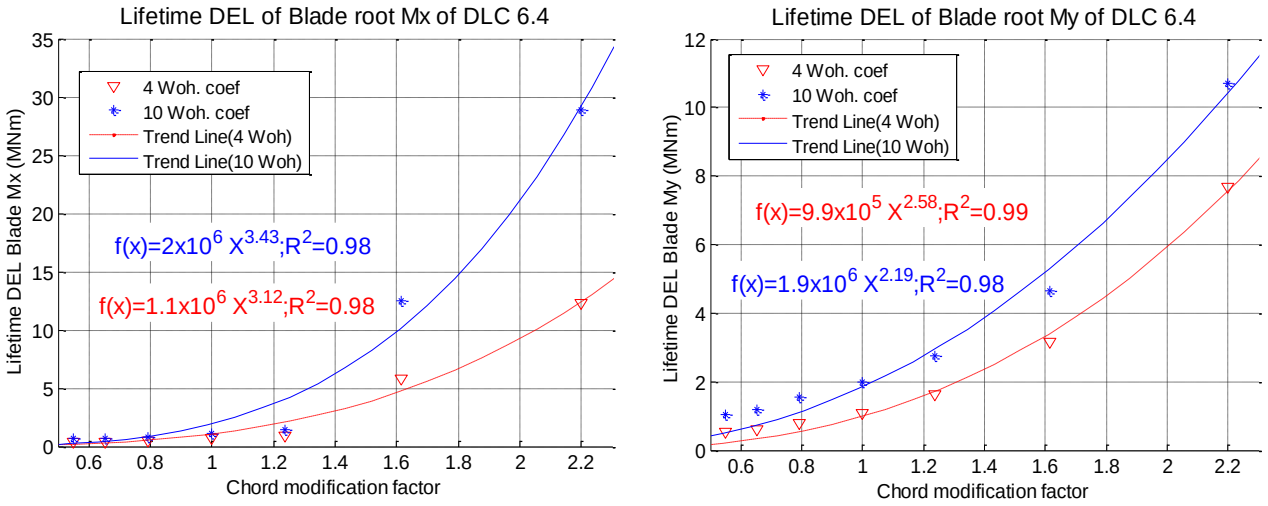

Figure 8.8: DLC 1.2, 3.1/4.1 and 6.4 lifetime DELs of edge-wise and flap-wise blade root bending moments for Wohler coefficient 4 and 10.

8.1.4.2. Low-speed shaft and yaw bearing moment

This section shows the equations of the trend lines for the low-speed shaft and yaw bearing moment, see Table 8.1. Because the changes to lifetime DELs of the low-speed shaft and yaw bearing moment have a similar pattern to the lifetime DELs of blade root moments, which were discussed in section 8.1.4.1, the graphs are not shown. If the reader is interested in the graphs of low-speed shaft and yaw bearing moment the graphs can be found in Appendix E.

Design load case	Moment	Wohler Coefficients	
		4	***10***
1.2	***Low – speed shaft***	$f(x) = 4.4 * 10^6 x^{1.25}; R^2 = 1$	$f(x) = 3.7 * 10^6 x^{1.23}; R^2 = 0.99$
3.1/4.1		$f(x) = 4.5 * 10^5 x^{0.76}; R^2 = 0.92$	$f(x) = 1.1 * 10^6 x^{0.84}; R^2 = 0.92$
6.4		$f(x) = 5.4 * 10^6 x^{3.37}; R^2 = 0.96$	$f(x) = 1 * 10^7 x^{3.81}; R^2 = 0.98$
1.2	***Yaw bearing***	$f(x) = 3.3 * 10^6 x^{1.66}; R^2 = 1$	$f(x) = 2.5 * 10^6 x^{1.62}; R^2 = 1$
3.1/4.1		$f(x) = 1.5 * 10^5 x^{1.55}; R^2 = 0.95$	$f(x) = 4.2 * 10^5 x^{1.27}; R^2 = 0.94$
6.4		$f(x) = 3.5 * 10^6 x^{3.82}; R^2 = 0.98$	$f(x) = 6.5 * 10^6 x^{4.24}; R^2 = 0.99$

Table 8.1: Equations of power law trend lines of DLC 1.2 ,3.1/4.1 and 6.4 for low-speed shaft and yaw bearing moments

8.1.4.3. Tower fore-aft base moment

This section illustrates the changes to fore-aft tower base fatigue moments among the modified rotor solidity models. Figure 8.9 contains two graphs, which express the changes for DCL 1.2 and 6.4, respectively. The changes of DLC 3.1/4.1 are depicted by Figure 8.10, which includes two graphs, where each graph relates to Wohler coefficient 4 and 10. DLC 3.1/4.1 output data of Wohler coefficient 4 and 10 is not shown as a single graph because there is huge difference between the outputs of Wohler coefficient four and ten. As a result, both curves are expressed as almost straight lines in the single graph. The output data of each Wohler coefficient has to be displayed in a separate graph in order to see the shape of each curve.

The DLC 1.2 graph of Figure 8.9 demonstrates that the output data of lifetime DELs generates curves, which have a similar shape to quadratic for both Wohler coefficients. The power trend lines do not follow the output value. In this case the quadratic trend line was used instead of the power trend line.

The quadratic shape is a result of the increasing blade mass due to increasing of chord length and the reduction of aerodynamic damping due to decreasing of chord. As it was mentioned above the blade mass is a function of chord squared. The increased blade mass has an effect on the fore-aft tower base moment because it has effect of the total weight of tower top, which includes the weight of nacelle, drive train and rotor. In operation of the wind turbine, the tower top experiences fore-aft oscillations due to the acting wind flow on the tower and rotor. When the tower top centre of mass is moved away from the original vertical tower axis, the tower top weight creates an additional moment on the tower base. Figure 8.11 depicts the additional moment from nacelle weight, which acts on the tower base, for better understanding.

On the other hand, increasing TSR leads to a reduction of chord length and blade mass. However, the aerodynamic damping is a function of the chord length as shown by equations 8.7, 8.8 and 8.9. As a consequence of the reduction of chord length the aerodynamic damping ratio of the rotor drops from 4.7 % to 2.5% as demonstrated in Figure 8.2. This is the reason for the augmentation of tower fore-aft fatigue loads at lower values of chord length compared to the fatigue loads of the reference model.

The graph of DLC 6.4 illustrates the tower fore-aft base fatigue loads in the idling conditions. The outputs of lifetime DELs are proportional to the length of chord for both Wohler coefficients. The

large values of lifetime DELs at the high values of chord is a result of the additional tower base moment from the weight of nacelle as it was mentioned for DLC 1.2 for the tower base moment.

The small values of lifetime DELs at the low values of chord are a consequence of the idling conditions, where the blades are pitched by 90 degrees to feather, which means that the leading edge of blades points into wind flow. At this position of the blades, the angle of attack is reduced to –2 degrees to minimise as much as possible the rotation and thrust force of the rotor, which depends on lift and drag [1], [6]. When the angle of attack equals -2 degrees, the lift and drag coefficients are equal to zero [1]. The angle of attack, when the lift coefficient equals to zero, can vary among different aerofoils. In this case there is no thrust force on the rotor, but the incoming wind generates a force at the tower, which produces a tower base moment and deflects tower. However, the blade mass is reduced to generate the significant additional tower base moment at tower base, which was mentioned before.

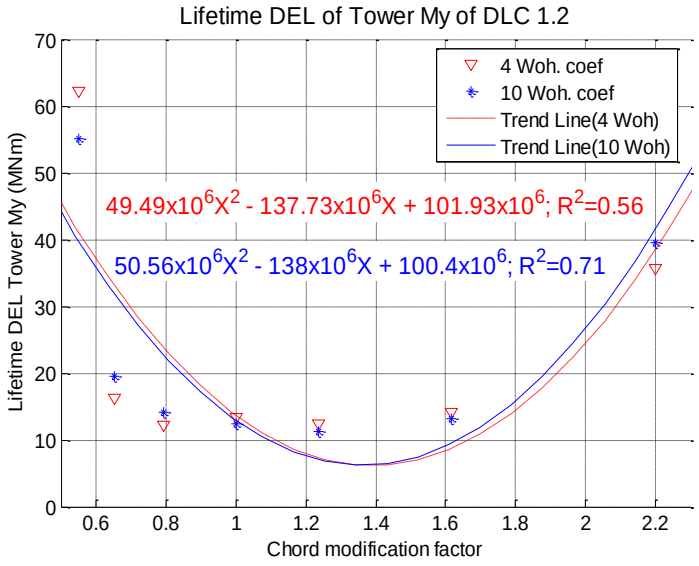

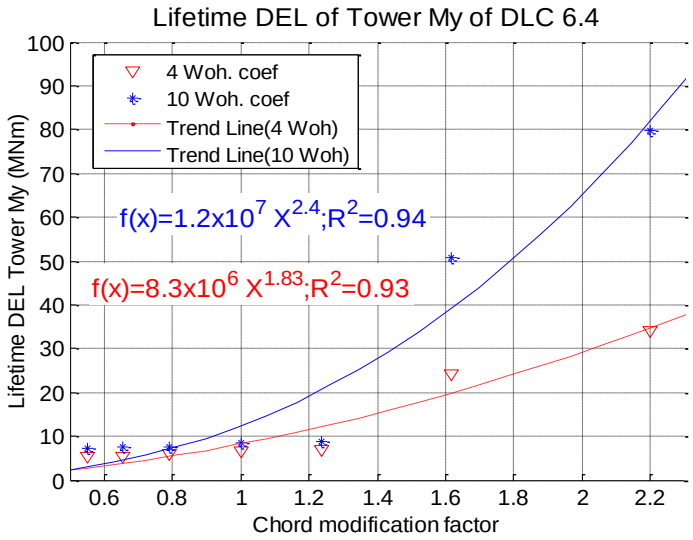

Figure 8.9: DLC 1.2 and 6.4 lifetime DELs of tower fore-aft base moments for Wohler coefficient 4 and 10.

At Figure 8.10 the two graphs of DLC 3.1/4.1 demonstrate the calculated output data of lifetime DELs produce curve shapes, which have some similarity to a quadratic curve. The power trend line was substituted by the quadratic trend lines because the power trend lines do not correlate to the output data of DLC 3.1/4.1. The generated output data of DLC3.1/4.1 repeats the characteristics of DLC 1.2 outputs, which was discussed in the beginning of this subsection.

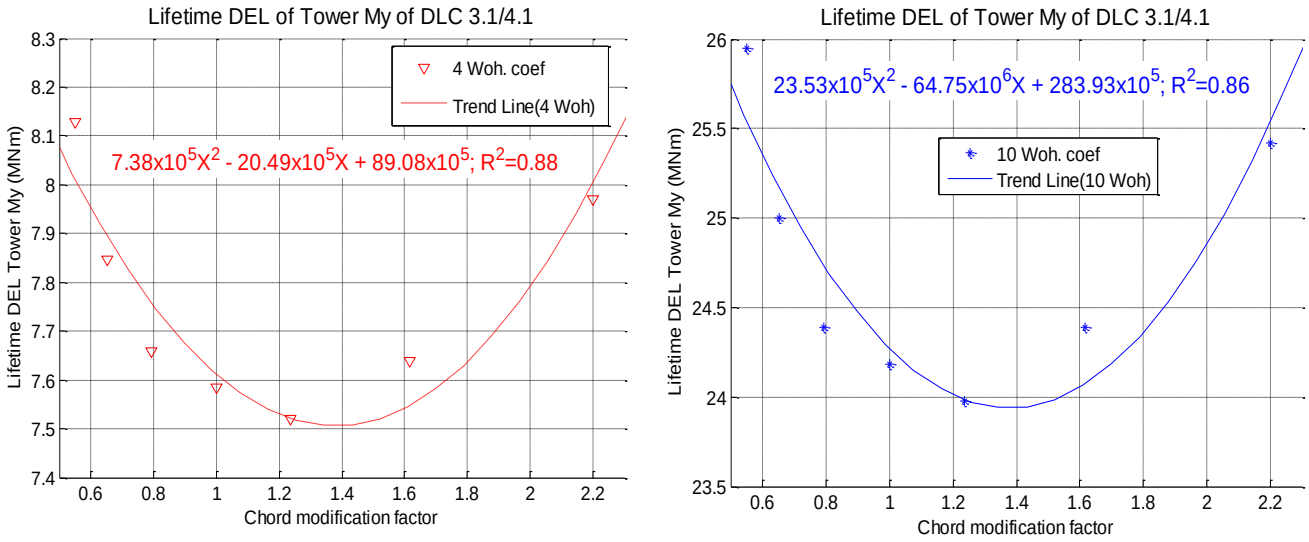

Figure 8.10: DLC 1.2, 3.1/4.1 and 6.4 lifetime DELs of tower fore-aft base moments for Wohler coefficient 4 and 10.

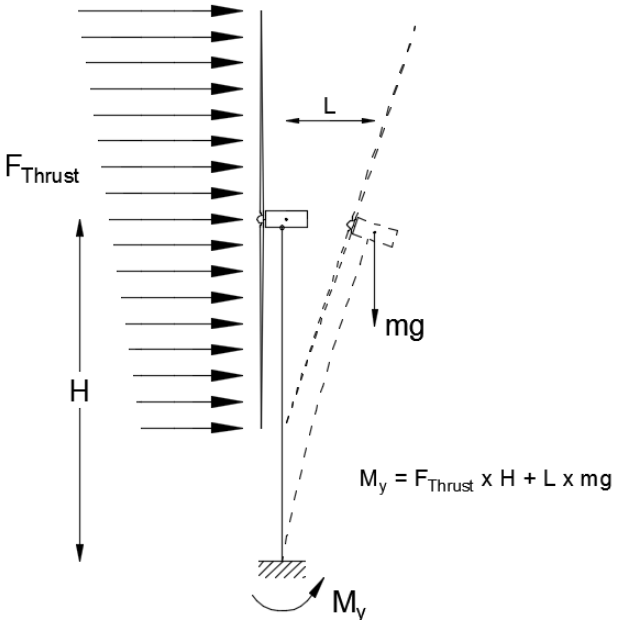

Figure 8.11: Additional moment of tower top for the fore-aft tower base moment.

8.1.5. Deterministic fatigue loads analysis

This section provides an overview of the changes in fatigue loads, which derived from the deterministic part of the loads. This section presents the edge-wise blade root loads of DLC 1.2 as the edge-wise blade root loads are primarily repeatable loads, which depend on the gravity loads as it was mentioned in chapter 7.

Figure 8.12 demonstrates the lifetime DELs of deterministic part of edge-wise blade root moment for Wohler coefficient four and ten. The power trend lines repeat the curve shape of trend lines of DLC 1.2 Lifetime DELs edge-wise blade root moment of Figure 8.8. However, the curves of deterministic moment are slightly shifted down compared to the curves of total load, because the deterministic part excludes the stochastic part of load. It is worth noticing that the value of deterministic exponents is a bit smaller than the exponents of original curves, which include the deterministic and stochastic parts of load. Therefore, the stochastic part of the load has an adverse effect, as the absolute values of the exponents are higher than exponents of the deterministic part of the load, but the discrepancy between absolute and deterministic exponents is very small to produce any significant difference in outputs. Nevertheless, it shows that the deterministic part plays a significant role in lifetime DELs of edge-wise blade root moments.

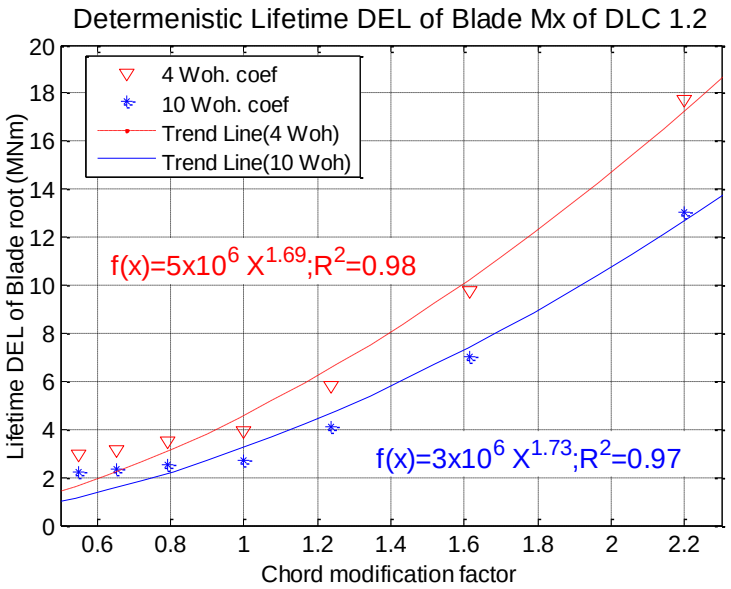

Figure 8.12: DLC 1.2 deterministic lifetime DELs of edge-wise blade root bending moment for Wohler coefficient 4 and 10.

8.1.6. Extreme loads analysis

This section exhibits changes of extreme moments (such as: edge-wise and flap-wise blade root, low speed shaft, yaw bearing and fore-aft tower base) due to the modifications of rotor solidity in terms of the alterations of TSR and blade dimensions. This section is split into two subsections, which relate to DLC 1.1 and DLC 1.3, 6.1 and 6.3 respectively.

8.1.6.1. Design load case (DLC) 1.1

The first subsection represents DLC 1.1 associated with the statistical extrapolation technique based on long-term (50 year period) exceedance probability for the calculation of extreme loads at a wind flow with NTM [60]–[62], [86]. This subsection consists of two parts, where the first part provides the overview of changes for the blade root extreme moments. The second part exhibits the alteration for the rotor idling extreme moments.

8.1.6.1.1. Blade root moments

The two graphs of Figure 8.13 demonstrate the outputs of DLC 1.1 for the edge-wise and flap-wise blade root extreme moments. In both graphs of Figure 8.13 the calculated exponents of trend lines are smaller by 25% approximately than the prognosticated exponents (x^2 and x^1 for

edge-wise and flap-wise blade root moments, respectively). But DLC 1.2 exponents of edge-wise blade root moment are smaller by roughly 10 % than the estimated value of the exponent for edge-wise blade root moment. Nonetheless, the DLC 1.1 exponent of flap-wise blade root moment is closer to the predicted value of flap-wise exponent than the DLC 1.2 exponent, which is equal to 1.45.

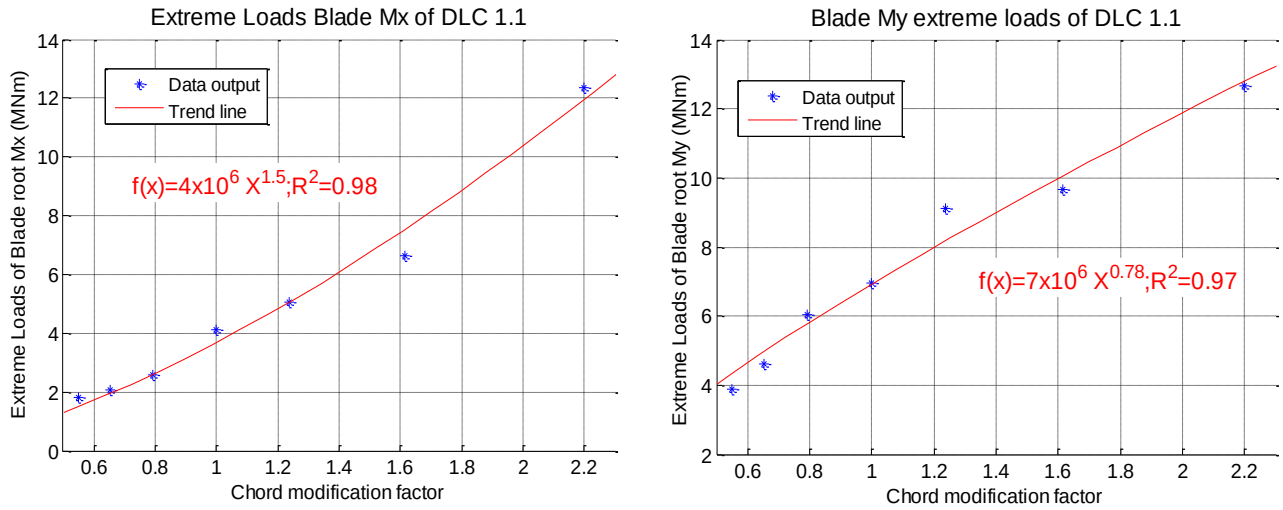

Figure 8.13: DLC 1.1 extreme loads of edge-wise and flap-wise blade root moments.

8.1.6.1.2. Low speed shaft, yaw bearing, fore-aft tower base moments

Figure 8.14 includes the three graphs, which shows the extreme moments of DLC 1.1 for the low speed shaft, yaw bearing moment and fore-aft tower base, respectively.

The first graph of Figure 8.14 shows that the output value of 1.23 chord modification factor or TSR 8 model is out of the general pattern. Therefore, the *R*-squared value equals to 0.88. Nevertheless, the *R*-squared value is still high enough to state that the power trend has a decent correlation with the output data. The generated exponent of the low speed shaft has almost a perfect match to the forecast exponent, which is equal to x^1 and identical to the predicted exponent of the flap-wise blade root moment.

The second graph of Figure 8.14 depicts the output data and the generated power trend line with *R*-squared equal to 0.99. The calculated exponent of DLC 1.1 is smaller by 23% than the exponent for the steady moment of yaw bearing, which is equal to x^2. The yaw bearing moment scales by power 2, because the mass of the yaw actuator scales with the torque as written in [24]. Where, the rotor torque is proportional to the rotor in-plane loads according to [1]. Moreover, the DLC

1.1 exponent of yaw bearing moment is slightly smaller than both exponents of DLC 1.2, which relate to lifetime DELs of the yaw bearing moment.

The last graph of Figure 8.14 corresponds to the fore-aft tower base extreme moment. The output data of the reference and modified models produces a curve, approximately following a square law. The explanation for what causes the so-called square law curve can be found in subsection 8.1.4.3. The power trend line cannot follow the outputs as shown by the low value of *R*-squared for the graph.

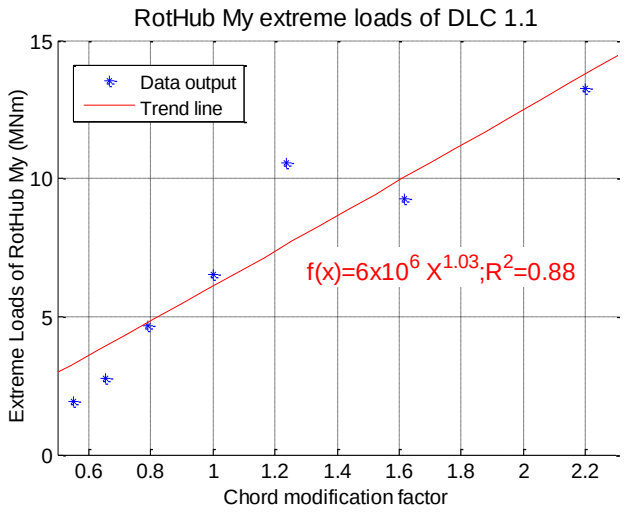

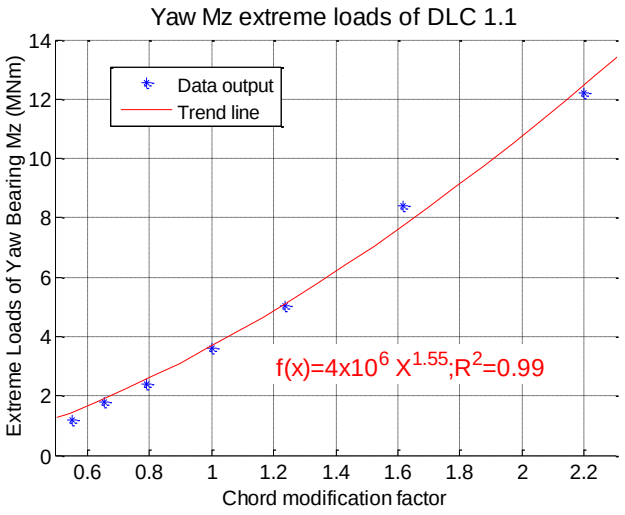

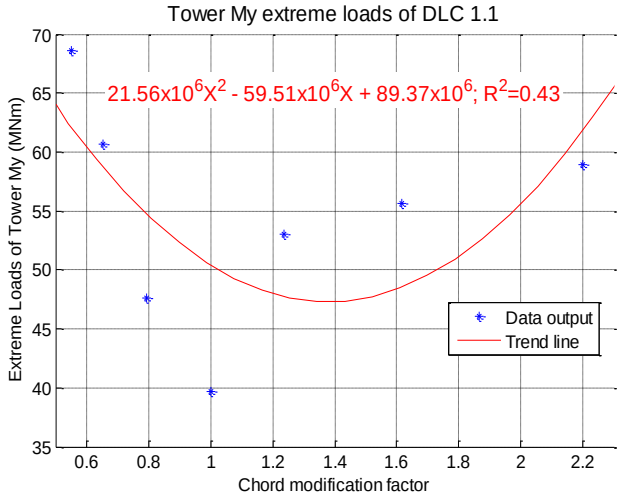

Figure 8.14: DLC 1.1 extreme loads of low speed shaft, yaw bearing and fore-aft tower base moment.

8.1.6.2. Design load case (DLC) 1.3, 6.1 6.3:

This subsection only shows the equations of power trend lines for DLC 1.3. 6.1 and 6.4, because the power trend lines repeat the pattern of trend lines of lifetime DELs (DLC 1.2, 3.1/4.1 and 6.4) and the extrapolated extreme loads (DLC 1.1), where DLC 1.3 relates the power production condition of wind turbine at ETM with $\pm$ 8 degree yaw misalignment, DLC 6.1 associates to idling conditions at 50 m/s wind speed with ETW and $\pm$ 8 degree yaw misalignment, DLC 6.3 corresponds with idling conditions at 40 m/s wind speed with ETW and $\pm$20 degree yaw misalignment. Table 8.2 shows the equations of the power trend lines for edge-wise and flap-wise blade root, low-speed shaft and yaw bearing moments. The equations of the power trend lines are presented in Table 8.3.

Design load case	Moment	Power trend line equation	Moment	Power trend line equation
1.3	***Edge-wise blade root***	$f(x) = 3 * 10^6 x^{1.56}; R^2 = 0.99$	***Flap-wise blade root***	$f(x) = 6 * 10^6 x^{1}; R^2 = 0.99$
6.1		$f(x) = 3 * 10^5 x^{5.66}; R^2 = 0.97$		$f(x) = 4 * 10^6 x^{1.2}; R^2 = 0.99$
6.3		$f(x) = 6 * 10^5 x^{4.08}; R^2 = 0.92$		$f(x) = 3 * 10^6 x^{1.44}; R^2 = 0.99$
1.3	***Low-speed shaft***	$f(x) = 3 * 10^6 x^{1.36}; R^2 = 0.99$	**Yaw Mz bearing**	$f(x) = 3 * 10^6 x^{1.59}; R^2 = 1$
6.1		$f(x) = 5 * 10^5 x^{4.73}; R^2 = 0.98$		$f(x) = 5 * 10^5 x^{4.51}; R^2 = 0.98$
6.3		$f(x) = 3 * 10^6 x^{2.27}; R^2 = 0.91$		$f(x) = 3 * 10^6 x^{2.37}; R^2 = 0.91$

Table 8.2: Equations of power law trend lines of DLC 1.3, 6.1 and 6.3 for edge-wise and flap-wise blade root, low-speed shaft and yaw bearing moments.

Design load case	Moment	Power trend line equation
1.3	***Tower fore-aft base***	$f(x) = 4 * 10^7 x^{-0.41}; R^2 = 0.66$
6.1		$f(x) = 3 * 10^7 x^{0.56}; R^2 = 0.74$
6.3		$f(x) = 2 * 10^7 x^{0.72}; R^2 = 0.73$

Table 8.3: Equations of power law trend lines of DLC 1.3, 6.1 and 6.3 for fore-aft tower base moment.

8.2. Chord impact

The second part of this chapter considers a different way in which rotor solidity may be altered. For any chosen design tip speed ratio an optimum rotor does not have a unique chord distribution but it does have a unique lift distribution. Lift is effectively determined by the product of lift coefficient (Cl) and chord width (c). Thus, at any chosen design TSR, the chord width and hence solidity may be altered by choosing aerofoils with different design lift coefficient (lift coefficient at maximum lift to drag ratio). The chord width,c, is then determined to maintain the product Cl at the required value for the chosen design TSR.

The aim of these modifications is to preserve the original aerodynamic performance of the base model by maintaining the same value of non-dimensional lift distribution as shown by equation 8.12. Therefore, if the chord length is reduced the aerofoil has to be replaced by a new aerofoil with higher lift coefficient value and vice versa.

$$\Lambda = \frac{c(\lambda, r) C_L}{R} \qquad 8.12$$

There are six modified models, which relate to alterations of chord (*0.85c, 0.9c, 0.95c, 1.05c, 1.1c* and *1.15c*). Figure 8.15 shows aerofoils used in the modified models to maintain the original non-dimensional lift distribution of the base wind turbine model. Furthermore, the design lift coefficient of each aerofoil is provided in Figure 8.15. However, the modified values of non-dimensional lift distribution vary slightly compared to the original values due to differences in the transitions between aerofoil types over the blade span. Note, NACA 63 4XX aerofoil types were used in the reference wind turbine model.

0.85c		0.9c		0.95c		1.05c		1.1c		1.15c	
Aerofoil	*Cl*	*Aerofoil*	*Cl*	*Aerofoil*	*Cl*	*Aerofoil*	*Cl*	*Aerofoil*	*Cl*	*Aerofoil*	*Cl*
NREL s818	1.405	NREL s826	1.340	NREL s826	1.251	NREL s826	1.146	NREL s818	1.086	NACA 63 421	1.04
NACA 63 421	1.04	NREL s816	0.978	DU25 A17	0.952	NACA 63 215	0.8133	NREL 19s817	0.793	NREL 17s816-s817	0.775
NACA 63 421	1.04	NREL s817	0.978	DU25 A17	0.952	NACA 63 215	0.8133	NREL 19s817	0.793	NREL 17s816-s817	0.775
NACA 63 421	1.04	NREL s818	0.978	DU25 A17	0.952	NACA 63 215	0.8133	NREL 19s817	0.793	NREL 17s816-s817	0.775
NACA 63 421	1.04	NREL s819	0.978	DU25 A17	0.952	NACA 63 215	0.8133	NREL 19s817	0.793	NREL 17s816-s817	0.775

Figure 8.15: Table of new aerofoil with lift coefficient for the modified models.

According to the above mentioned modifications the twist angle, blade mass and stiffness have to be adjusted in the same manner as mentioned in section 8.1 (when the rotor solidity was modified by TSR).

Also, there is an alternative way to amend the rotor solidity without changing TSR and aerofoils, which involves using the aerofoils of the reference model at a different angle of attack. The alternative method is based on the maintaining the non-dimensional lift distribution (see equation 8.12). The different angle of attack can be achieved by changing the twist angle of blades as shown in equation 8.4. This alternative method is beyond of the scope of this research. However, it can be done in the future work and the output data of the alternative method can be compared with data of this study.

8.2.1. Aerodynamic damping

The introduced modifications of rotor solidity have an effect on aerodynamic damping of the rotor. The changes of aerodynamic damping among the different models associated with the changes of rotor solidity can be found by using the same procedure which was employed to calculate the aerodynamic damping of the modified models, where the rotor solidity was a function of TSR and chord (see section 8.1.2). The changes of aerodynamic damping for the second method of rotor solidity modifications are illustrated in Figure 8.16, which demonstrates that theoretical aerodynamic damping varies approximately by ± 11 of nominal value between the reference model and models with the utmost blades modifications. The effect of the alternations in the aerodynamic damping will be investigated by changes of loads to the tower base in section 8.2.3.3.

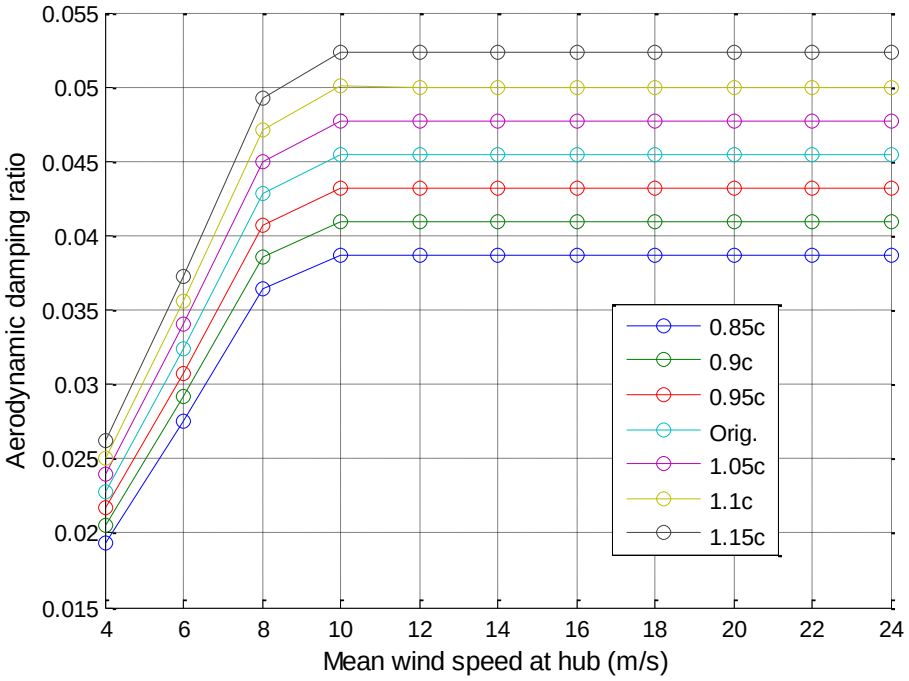

Figure 8.16: Theoretical aerodynamic damping ratio of the entire rotor for the wind turbine models with the preserved original TSR.

8.2.2. Validation of performed changes

This section examines the accuracy of the applied modifications in order to change the rotor solidity using the second method. This section consists of the subsections: steady and dynamic state analysis. The steady and dynamic state analysis is performed to validate the accuracy of the applied modifications in comparison to the reference wind turbine model.

8.2.2.1. Steady state analysis

The aim of the modifications was to change the rotor solidity without alterations to the TSR and to preserve the same power production curve. Figure 8.17 shows the pair of graphs, which corresponded to TSR against mean wind speed and power coefficient (Cp) against TSR, respectively. The first graph of Figure 8.17 shows the curves of the reference and modified models overlap at the horizontal segment of curves which corresponds to the Cp tracking region. However, a small variation between the models appears at the declining exponential segment of the curves. This is a consequence of the dissimilarity of non-dimensional lift distribution (see equation 8.12) between the modified models and the reference one and additional modifications

to maintain the original power production curve of the base model in the modified models. The second graph of Figure 8.17 displays the variation of power coefficient curves among the wind turbine models. Most of curves have a shifted maximum power coefficient due to the new aerofoils and have minor modifications to the rotor speed to maintain the original power production curve. There is also variation of Cp max but it is not major as the difference between the maximum and minimum is around 3.5%. Therefore, it is possible to state the aerodynamic performance of the modified models is broadly similar to the aerodynamics of the base model.

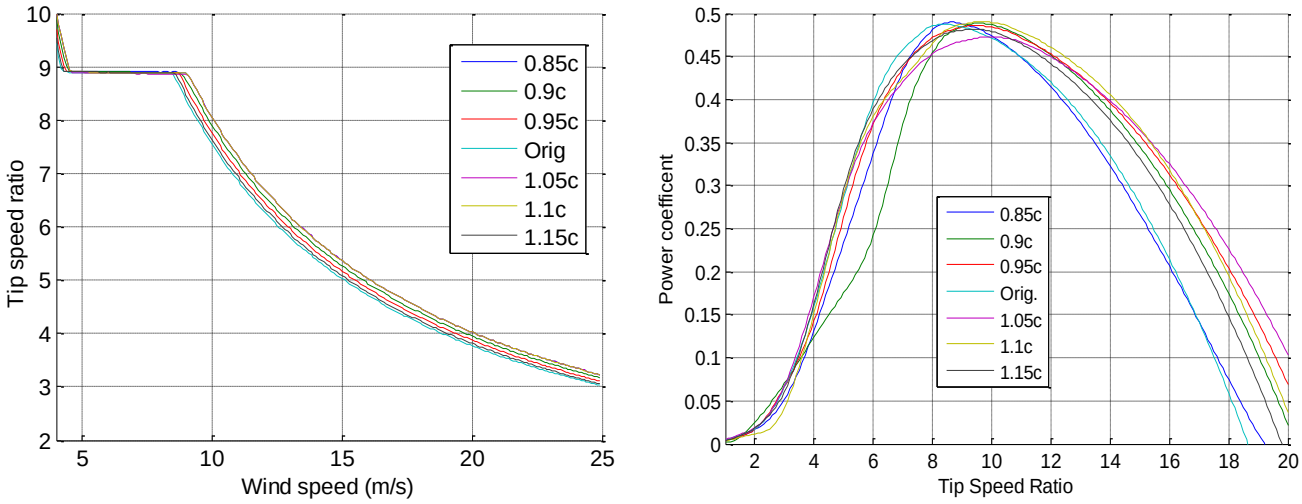

Figure 8.17: Comparison of reference and modified models with the preserved original TSR

a) Tip-speed ratio.
b) The power coefficient.

The next step is to compare the power curves of the modified models with the power curve of the base model to ensure the power curves of the modified models match to the curve of the reference model. Figure 8.18 shows the above mentioned comparison, where the curves overlay but there is a small variation between the power production curves in the below rated region in the vicinity of the transition region corresponding to the switch between the below and above rated control strategy. This variation is caused by the variation of rotor speed in the modified models to maintain the original TSR value. However, this variation is not very significant and may be neglected as a consequence of minor dissimilarities between the power curves.

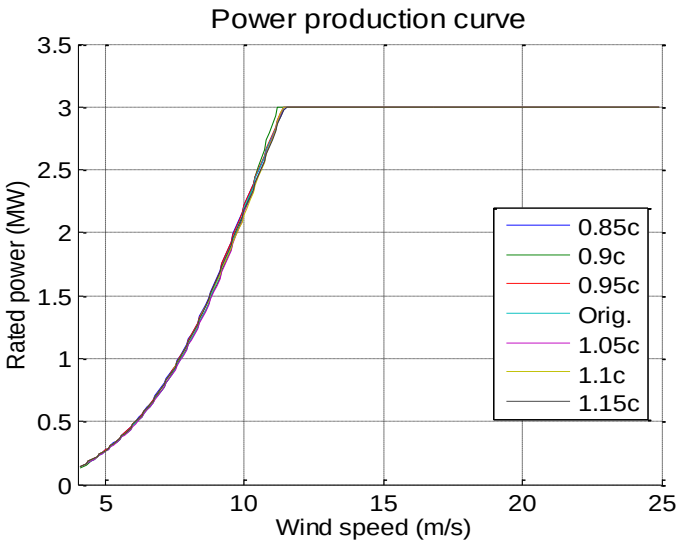

Figure 8.18: The power production curves of the reference and modified models with the preserved original TSR.

The two Figures, 8.17 and 8.18, of steady state analysis proved that the modifications were applied correctly. Hence, it is possible to proceed to the next stage, where the modified models are tested in the dynamic operation.

8.2.2.2. Dynamic state analysis:

Spectral analysis was used to perform the dynamic state analysis. The spectral analysis provides an overview of the instantaneous loads in the frequency domain as a result of changing the rotor solidity. The following figures of spectral analysis show the reference model and two models with greatest chord variation (0.85 chord and 1.15 chord) that will most clearly show the load changes in the altered models compared to the base model.

The dynamic state analysis subsection highlights the spectral analysis for the edge-wise blade root moment only, because the spectral analysis has not revealed any suspicious behaviour in the moments of interest due to modifications. Nevertheless, the graphs of spectral analysis for flap-wise blade root, low-speed shaft, yaw bearing and fore-aft tower base moments can be found in Appendix E.

8.2.2.2.1. Blade root edge-wise moment:

Figure 8.19 depicts two graphs of PSD and cumulative PSD of blade root edge-wise moment of the reference and two modified models. The majority of peaks are labelled in the PSD graph.

It is obvious that *1P* and its harmonic peaks of *0.85c* are slightly shifted compared to the peaks of the reference and *1.15c* models. This is a result of the alterations of rotor speed to adjust the applied modifications of rotor solidity in order to follow the power curve of the base model. Furthermore, the peaks of the edge-wise structural modes of the modified models are shifted because the changes of the chord have an effect on the blade mass and stiffness as shown by equations 8.5 and 8.6. The changes of edge-wise structural modes do not coincide with the harmonic peaks of *1P* for each modified models, because of this there are no un-damped, high and narrow peaks, which are higher than *1P* in the PSD graph of Figure 8.19. Additionally, in the cumulative PSD graph there is no significant rise in the curves of the modified models due to the alteration of the natural frequency of the blades apart from the rise at *1P*. Therefore, the applied modifications do not generate any negative effects.

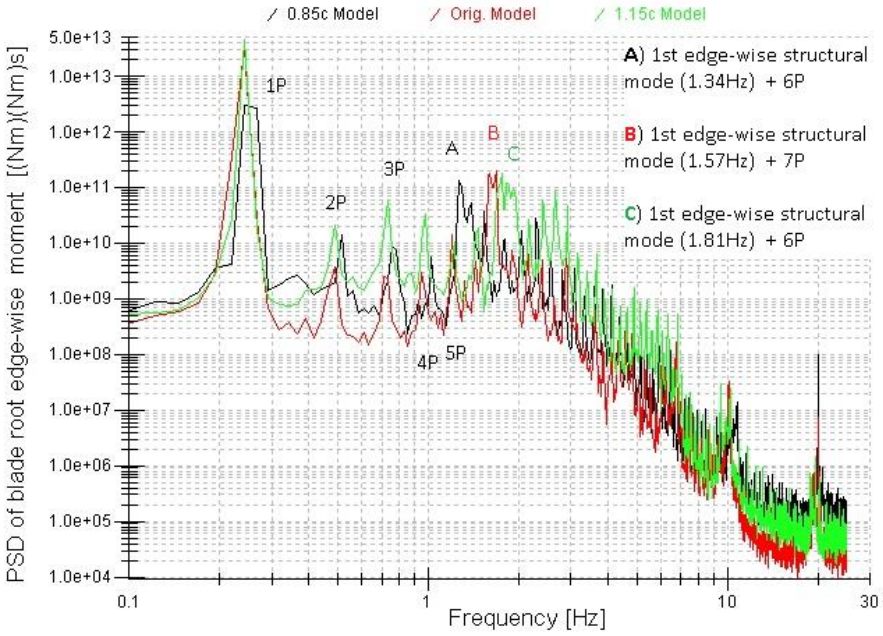

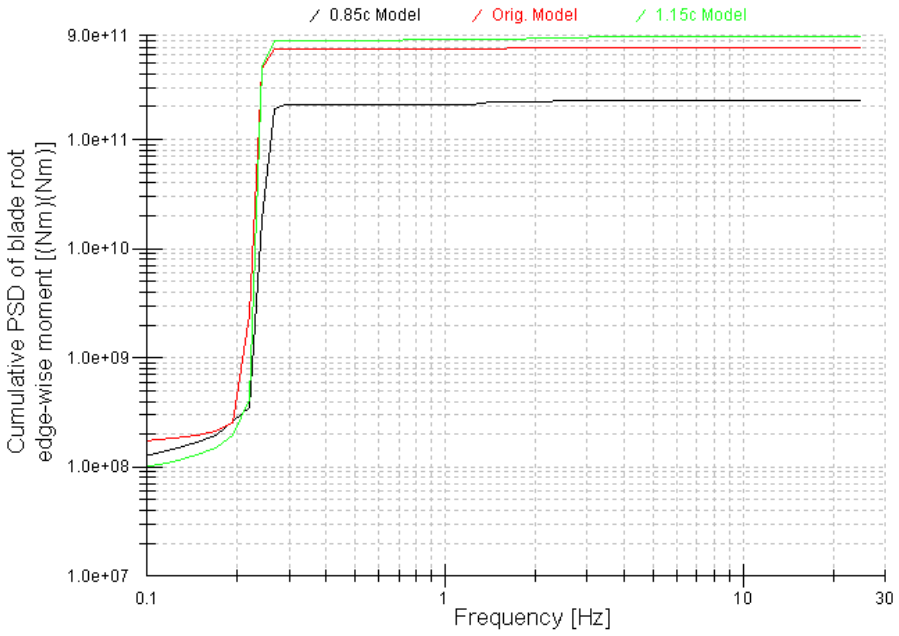

Figure 8.19: PSD and cumulative PSD of blade root edge-wise moment of 0.85c, original and 1.15c models at 16 m/s mean wind speed.

8.2.3. Fatigue loads analysis

This section provides the overview of changes of fatigue loads, which are represented by lifetime DELs against the modification coefficient of chord for Wohler coefficient 4 and 10, as a consequence of the modifications of rotor solidity. This section is divided into the subsections which correspond to the areas of interest: blade root, low-speed shaft, yaw bearing and tower base moment. Each of these subsections shows the changes of loads in the three different DLCs (1.2, 3.1/4.1 and 6.4), which relate to power production range, number of start-ups and shut-downs and idling conditions of a wind turbine.

8.2.3.1. Blade root edge-wise and flap-wise moments

Figure 8.20 demonstrates the DLCs of edge-wise and flap-wise blade root moments. In Figure 8.20 the first horizontal pair of graphs is related to DLC 1.2. The developed power trend lines from the output data depict the exponents of edge-wise blade root, which are equal to 2.13 for both Wohler coefficients. At the beginning of this chapter it was stated the blade mass is a function of the chord squared, which is shown by equation 8.5, because the blade mass is a product of

length, chord and thickness and density as stated in the up-scaling with similarity [3], [6], [7], [24]. According to the modification of rotor solidity, the original span length of the blades remains constant, but the chord and thickness of the blades alters, because the thickness depends on the chord length as declared in [81]. Therefore, the steady edge-wise blade root moment has to be scaled by the square as the edge-wise blade root moment is a function of the blade mass, gravity and distance from blade root to central of blade mass as written in books [6], [7]. The distance of the blade root to the centre of blade mass did not change, as the original blade span length was preserved. The lifetime DELs of edge-wise blade root moment scale slightly larger than it was predicted by the steady edge-wise blade root moment. The residual value of between the calculated and predicted can be caused by the dynamic state conditions especially turbulence and wind shear.

The exponents of flap-wise blade root moment of DLC 1.2 are around 1.25 for both Wohler coefficients. This value is slightly larger the predicted value than the steady flap-wise blade root moment at the power production steady state conditions. The value of predicted scale exponent is equal to x^1, because the blade root flap-wise moment depends on the force of wind flow, area of blades, which is experienced by the wind flow, and distance from the blade root to the resultant force [6], [7]. According to the modification of rotor solidity, the area of blades changes linearly in proportion to the chord length change, where the distance between the resultant thrust and root hub does not change because the original blade length was preserved. Therefore, the steady flap-wise blade root moment will scale linearly (x^1) with the chord. The difference between the calculated and predicted value of the exponent is a consequence of the dynamic state conditions of the simulations such as: wind shear and turbulence.

The second horizontal pair of graphs corresponds to the combination or summation of lifetime DELs of DLC 3.1 and 4.1, which are numbers start-ups and shut downs, respectively. Both graphs of Figure 8.20 show that the exponents of the trend lines are lower than the values of predicted exponents. Possibly, the reason of significant difference between the gained and expected exponent values is the conditions and calculations method of DLC 3.1/4.1. This design load case counts the number of start-ups and shut downs at steady wind flow of 3, 11.2 and 25 m/s.

In Figure 8.20 the last horizontal pair of the graphs characterises the changes of lifetime DELs of DLC 6.4, which corresponds to the idling conditions. For both graphs the exponents of both trend lines are equal approximately 1. For the edge-wise blade root moment the calculated exponents are lower by half than the expected one, but for the flap-wise moment there is almost a match between the predicted and calculated exponents. Probably, the difference between calculated

and expected exponents is a consequence of the operating conditions of the wind turbines at DLC 6.4.

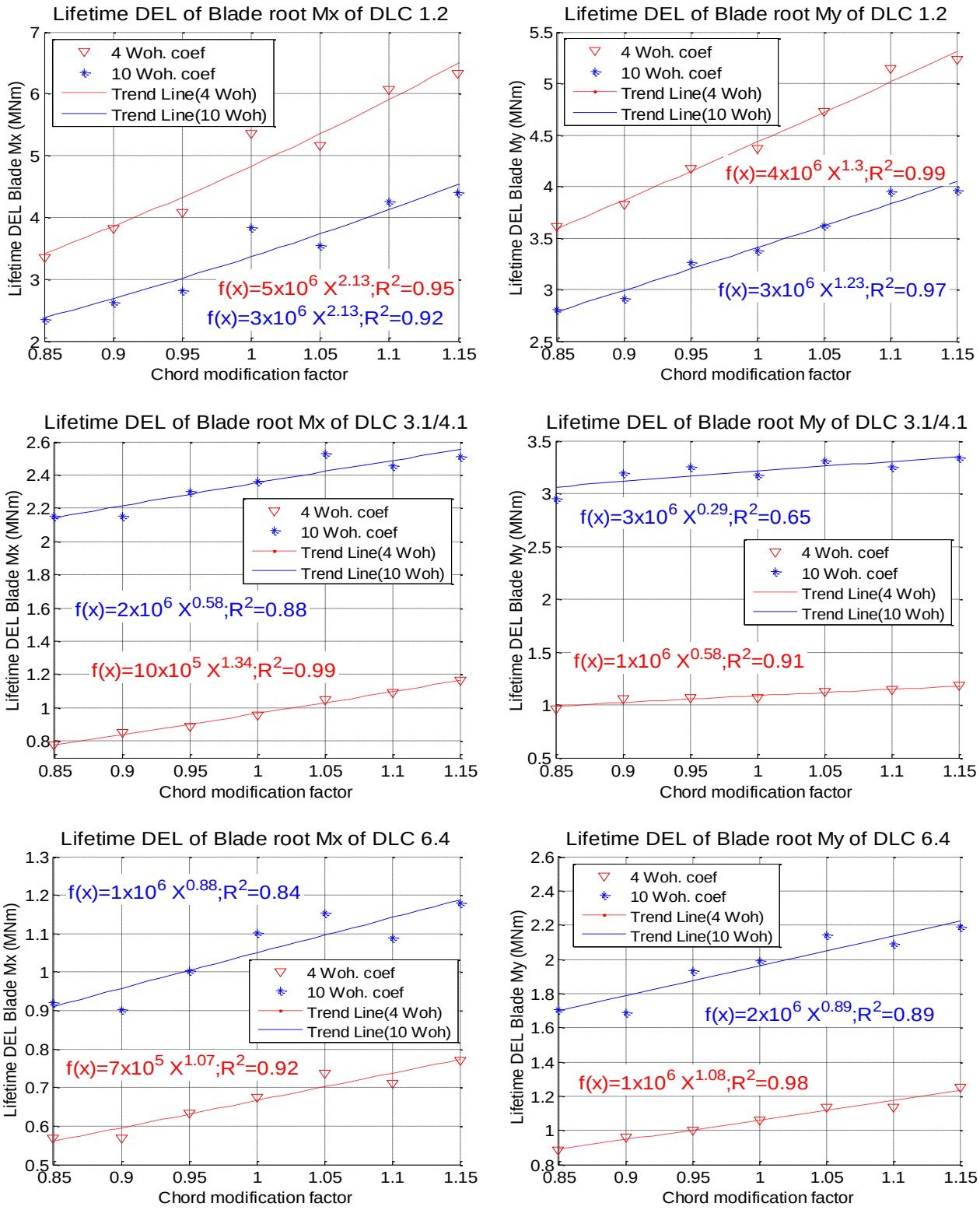

Figure 8.20: DLC 1.2, 3.1/4.1 and 6.4 lifetime DELs of edge-wise and flap-wise blade root bending moments for Wohler coefficient 4 and 10.

8.2.3.2. Low-speed shaft and yaw bearing moments

In this section Table 8.4 is used to present the equations of trend lines for low-speed shaft (M_y) and yaw bearing moments (M_z) instead of the graphs, because the power trend lines of low-speed shaft and yaw bearing moments are similar to the power trend lines of the flap-wise and edge-wise blade root moments. However, some trend lines in Table 8.4 have a low value of R^2, which shows that there is high diversity in the output data. Possibly, the reason of low values of R^2 is that insignificant blade modifications can produce major changes in loads.

The graphs of lifetime DELs of low-speed shaft and yaw bearing moments are located in Appendix E.

Design load case	Moment	Wohler Coefficients	
		4	***10***
1.2	***Low – speed shaft***	$f(x) = 5 * 10^6 x^{1.13}; R^2 = 0.97$	$f(x) = 4 * 10^6 x^{1.16}; R^2 = 0.94$
3.1/4.1		$f(x) = 5 * 10^5 x^{0.54}; R^2 = 0.62$	$f(x) = 1 * 10^6 x^{0.62}; R^2 = 0.59$
6.4		$f(x) = 7 * 10^5 x^{1.08}; R^2 = 0.81$	$f(x) = 9 * 10^5 x^{1.38}; R^2 = 0.98$
1.2	***Yaw bearing***	$f(x) = 3 * 10^6 x^{1.89}; R^2 = 0.98$	$f(x) = 3 * 10^6 x^{1.85}; R^2 = 0.99$
3.1/4.1		$f(x) = 5 * 10^5 x^{-0.98}; R^2 = 0.38$	$f(x) = 2 * 10^5 x^{-0.51}; R^2 = 0.19$
6.4		$f(x) = 8 * 10^5 x^{1.53}; R^2 = 0.78$	$f(x) = 1 * 10^6 x^{2.19}; R^2 = 0.43$

Table 8.4: Equations of power law trend lines of DLC 1.2 ,3.1/4.1 and 6.4 for low-speed shaft and yaw bearing moments

8.2.3.3. Tower fore-aft base moment

The lifetime DELs changes for tower fore-aft base moment is shown in Figure 8.21, which contains three graphs, corresponding to the three DLCs.

The DLC 1.2 graph of Figure 8.21 demonstrates that the exponents of the trend lines are negative. This is a consequence of the alteration of aerodynamic damping due to the applied modification of chord length. The aerodynamic damping depends on the chord length as it was highlighted in sections 8.1.2 and 8.2.1. The output data of Wohler coefficient 4 is scattered as seen by the low value of *R*-squared. Hence, the obtained exponent value of Wohler coefficient four cannot be used for any considerations. The low value of *R*-squared could be a result of small changes in the rotor solidity producing major alterations to the loads in the modified models. For Wohler coefficient 10 the coefficient of correlation is reasonably high to rely on the developed power trend line. The absolute value of calculated exponent is lower by 25% than estimated exponent, which equals to 1 as the tower fore-aft base moment is roughly a product of the thrust force and

distance from the tower base to the point where the resultant thrust force acts. According to the rotor solidity modification, the distance does not change, but the thrust force varies with rotor surface area, which depends on the blade chord. In terms of the prediction, the generated trend from the output data has to be proportional to the chord length, but the DLC 1.2 graph depicts the inverse proportion between the lifetime DELs of tower base moment and chord length. The inverse proportion is caused by the aerodynamic damping, which is a function of chord length, as was written at the beginning of this section.

The second graph of Figure 8.21, which corresponds to DLC 3.1/4.1, shows the same behaviour of trend lines with negative exponents as the trend lines of DLC 1.2. The exponents of both Wohler coefficients are almost identical and equal to the calculated exponent of Wohler coefficient 10 for fore-aft tower base moment of DLC 1.2, which is shown in the first graph of Figure 8.21.

The last graph of Figure 8.21 shows that there is a very small inclination of both trend lines as the output data of the modified models are scattered around the original value. Most likely it is a result of a minor modification, which cannot produce the significant changes in tower fore-aft base moment compared to the original output of loads from the reference model. Consequently, the correlation coefficients are very small for both trend lines due to the scattered output data to rely on the obtained exponents.

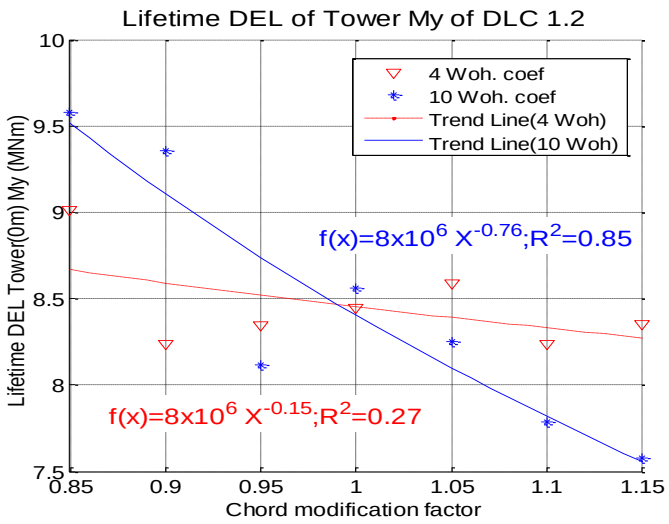

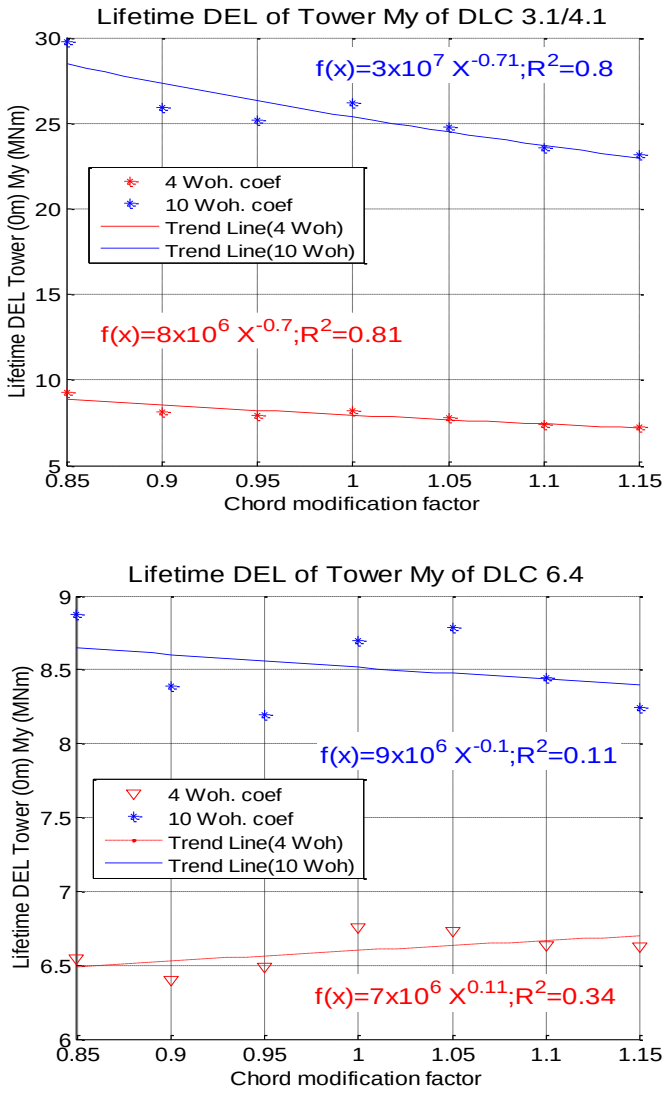

Figure 8.21: DLC 1.2, 3.1/4.1 and 6.4 lifetime DELs tower fore-aft base moments for Wohler coefficient 4 and 10.

8.2.4. Deterministic fatigue loads analysis

This section investigates the changes of the DLC 1.2 deterministic part of lifetime DELs for the edge-wise blade root moment of Wohler coefficient four and ten. Figure 8.22 shows the output data of the above mentioned deterministic lifetime DELs with the trend lines. The calculated exponents of both coefficients are slightly smaller than 2, which is the exponent for edge-wise blade root steady moment. The comparison between the exponents of the deterministic load part (Figure 8.22) and total load (Figure 8.20), which includes the deterministic and stochastic parts, demonstrates that the exponents of the deterministic load part is smaller by 11% for

Wohler coefficient four and ten respectively. Therefore, the difference between exponents is a result of the stochastic load part, which is turbulence and wind shear. Additionally, the small difference between exponents proves that the edge-wise blade loads depends mainly on gravity loads as mentioned before.

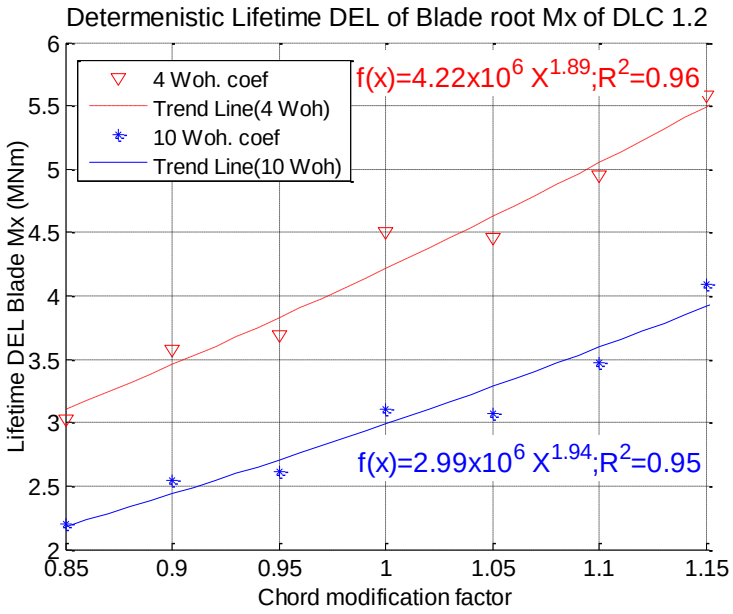

Figure 8.22: DLC 1.2 deterministic lifetime DELs of edge-wise blade root bending moment for Wohler coefficient 4 and 10.

8.2.5. Extreme loads analysis

In this section the changes of extreme loads are highlighted for edge-wise and flap-wise blade root, low speed shaft, yaw bearing and tower fore-aft base moments. The extreme loads are investigated by the four DLCs: 1.1, 1.3, 6.1 and 6.3 based on IEC standards [5]. This section consists of the two subsections, which correspond to the extrapolation of extreme moments (DLC 1.1) and the extreme moments at normal and extreme wind conditions (DLC 1.3, 6.1 and 6.3).

8.2.5.1. Design load case (DLC) 1.1

The first subsection represents DLC 1.1 associated with the statistical extrapolation technique based on long-term (50 year period) exceedance probability for the calculation of extreme loads for a wind flow with NTM [60]–[62], [86].

8.2.5.1.1. Blade root, low-speed shaft and yaw bearing moments

Table 8.5 shows the power trend line equation of edge-wise and flap-wise blade root, low-speed shaft and yaw bearing moments for DLC 1.1, because the output data of the above mentioned extreme moments does not show unusual behaviour. Generally, the trend lines of DLC 1.1 are similar to the trend lines of DLC 1.1 in section 8.1.6.1. The graphs of the above mention moments can be found in Appendix E.

Design load case	Moment	Power trend line equation
1.1	***Edge-wise blade root***	$f(x) = 4 * 10^6 x^{1.9}; R^2 = 0.81$
	Flap-wise blade root	$f(x) = 7 * 10^6 x^{0.61}; R^2 = 0.92$
	Low-speed shaft	$f(x) = 7 * 10^6 x^{1.12}; R^2 = 0.92$
	Yaw bearing	$f(x) = 4 * 10^6 x^{2.69}; R^2 = 0.9$

Table 8.5: Equations of power law trend lines of DLC 1.1 for edge-wise and flap-wise blade root, low-speed shaft and yaw bearing moments.

8.2.5.1.2. Fore-aft tower base moment

The output data of DLC 1.1 extreme moments for tower base fore-aft are illustrated in Figure 8.23.

Figure 8.23 depicts the extreme tower base fore-aft moment of DLC 1.1. The output data develops a curve which resembles similarities to a quadratic curve shape. The so-called quadratic curve of the output data is caused by the reduction of aerodynamic damping, which is a function of the chord length, and increased blade mass, which creates additional loads due to gravity when the nacelle of the wind turbine is moved from the nominal position. The detailed explanation about what causes the so-called quadratic shape curve of output data can be found in section 8.1.4.3.

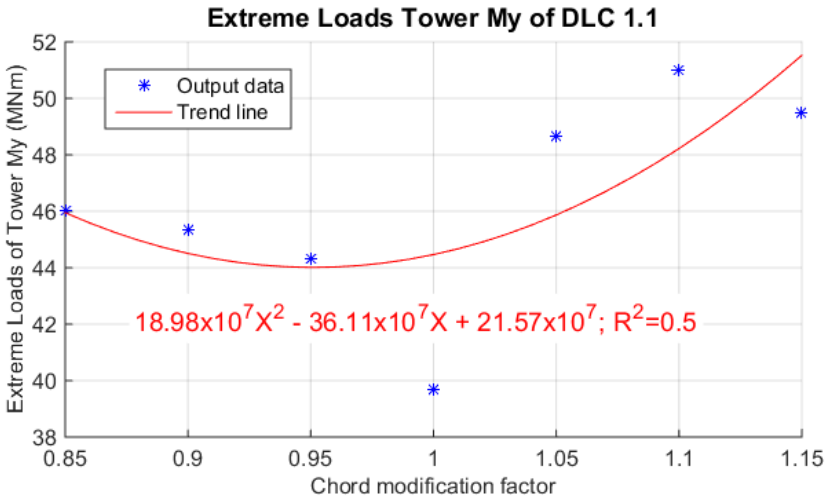

Figure 8.23: DLC 1.1 extreme loads of fore-aft tower base moment, when the original value of TSR is maintained.

8.2.5.2. Design load case (DLC) 1.3, 6.1 6.3

This subsection shows the changes of above mentioned extreme moments in terms of DLC 1.3, 6.1 and 6.3. The output data of three DLCs will be displayed as a single graph for the specific moment. The properties of aforementioned DLCs can be found in chapter 2, which provides the overview of loads.

8.2.5.2.1. Blade root moments

Figure 8.24 consists of the two graphs related to edge-wise and flap-wise blade root extreme moments, respectively

The first graph of Figure 8.24, which corresponds to edge-wise moments, illustrates that extreme moment of DLC 1.3 scales by a factor of 1.69, which is slightly lower than the predicted and DLC 1.1 exponents. The trend lines of DLC 6.1 and 6.3 are almost horizontal as the modifications do not have enough impact to produce the significant changes of extreme moments compared to the values of the reference model, because the output data of the modified models is scattered around the value of the extreme moment of the reference models as shown by the very low value of *R*-squared for DLC 6.1 and 6.3.

The flap-wise extreme moments are presented in the second graph of Figure 8.24, which shows that the exponent of DLC 1.3 is equal to 0.8. The obtained value is smaller by roughly 20% compared to the predicted exponent (x^1). Probably, the difference between the predicted and

calculated exponents is a consequence of extreme wind conditions. There is the similar situation of DLC 6.1 and 6.3 output data compared with the DCL 6.1 and 6.3 of the edge-wise extreme moment, because the extreme flap-wise moments of modified models are scattered around the values of the original model. Therefore, the changes of rotor solidity are not high enough to produce the significant changes in the extreme moments related to DLC 6.1 and 6.3.

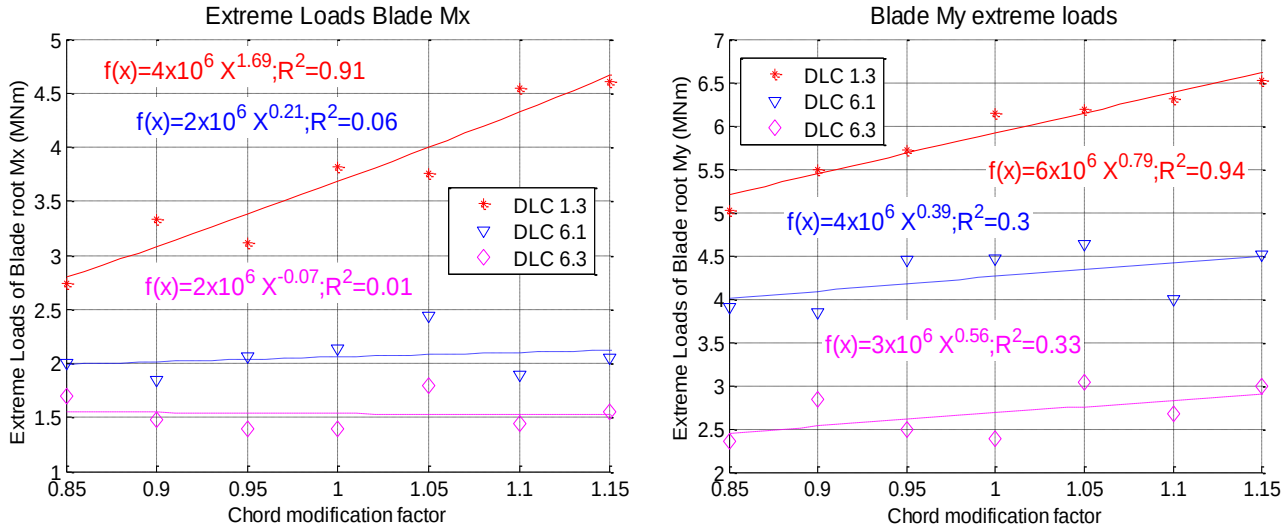

Figure 8.24: DLC 1.3, 6.1 and 6.3 extreme loads of edge-wise blade root moment, when the original TSR is maintained

8.2.5.2.2. Low speed shaft, yaw bearing, fore-aft tower base moments

Table 8.6 and Table 8.7 depicts the power trend line equation of DLC 1.3, 6.1 and 6.3 of the low speed shaft, yaw bearing and fore-aft tower base extreme moments. The graphs of output data and its trend lines of the above mentioned moments locate in Appendix E because the output data of the moments has similar pattern to the output data of edge-wise and flap-wise blade root moments of DLC 1.3, 6.1 and 6.3 (section 8.2.5.2.1).

Design load case	Moment	Power trend line equation	Moment	Power trend line equation
1.3	***Low-speed shaft***	$f(x) = 3 * 10^6 x^{1.42}; R^2 = 0.97$	**Yaw Mz bearing**	$f(x) = 3 * 10^6 x^{1.86}; R^2 = 0.97$
6.1		$f(x) = 2 * 10^6 x^{1.3}; R^2 = 0.69$		$f(x) = 2 * 10^6 x^{0.93}; R^2 = 0.44$
6.3		$f(x) = 1 * 10^6 x^{0.17}; R^2 = 0.01$		$f(x) = 1 * 10^6 x^{-0.42}; R^2 = 0.02$

Table 8.6: Equations of power law trend lines of DLC 1.3, 6.1 and 6.3 for low-speed shaft and yaw bearing moments.

Design load case	Moment	Power trend line equation
1.3	***Tower fore-aft base***	$f(x) = 4 * 10^7 x^{-0.09}; R^2 = 0.04$
6.1		$f(x) = 3 * 10^7 x^{0.15}; R^2 = 0.58$
6.3		$f(x) = 2 * 10^7 x^{0.31}; R^2 = 0.46$

Table 8.7: Equations of power law trend lines of DLC 1.3, 6.1 and 6.3 for fore-aft tower base moment.

8.3. Summary and discussion

This chapter investigated the changes of fatigue and extreme loads as a consequence of rotor solidity modifications. The chapter was divided into two scenarios because there are two ways to alter the rotor solidity. The first scenario applied the changes of TSR or tip speed with the blade chord to modify the rotor solidity. The changes of the second scenario included the chord length with replacing the aerofoils of the reference model by new ones, which have different lift coefficient compared to the aerofoils of the reference model.

For both types of modification of rotor solidity, it was necessary to adjust the aerodynamic and structural blade properties due to the modification of blade chord length. The aerodynamics of blades were adjusted by using ideal rotor conditions [1], [3], [6]. The scaling with similarity [3], [6], [7], [24] was employed to amend the structural properties of blades.

The modification of rotor solidity has an effect on the aerodynamic damping. Therefore, the changes of aerodynamic damping were overviewed as a result of alteration of rotor solidity in the two scenarios. The two graphs of aerodynamic damping ratio display that the aerodynamic damping is proportional to the rotor solidity and has influence on fore-aft tower base loads.

For both scenarios, steady state and spectral analyses were performed in order to check that modifications did not lead to adverse changes to the wind turbine models. The analysis did not reveal any negative impact from the modifications and proved that the modifications were correctly applied.

The first scenario showed that the extreme and fatigue (lifetime DELs) loads of blade root (edge-wise and flap-wise), low-speed shaft and yaw bearing moment are proportional to the rotor solidity or chord length. The loads become larger at higher solidity and vice versa. Moreover, the loads in the power production condition were scaled with values, which are close to the predicted values of steady loads estimated by the scaling with similarity. The extreme and fatigue loads of start-ups, shut downs and idling conditions scale differently, usually with much higher values than

the predicted ones. The output data of tower base loads showed a different pattern, which is similar to a quadratic shape curve. It is result of increased tower top mass due to the enlarged blade mass from the modifications, which leads to amplification of tower fore-aft base moments due to gravity of the tower top mass, when the tower top is deflected from the nominal position by the thrust force. But the increase of tower base moments for models with low solidity is a consequence of the reduction of aerodynamic damping by the decreasing the rotor solidity or chord length. A more detailed explanation about the causes of the quadratic shape curve for the output data of tower base load can be found in section 8.1.4.3.

The second scenario demonstrated similar patterns of extreme and fatigue load trends in most of the design load cases to the first scenario. However, there are many design load cases of the second scenario which produced almost horizontal trend lines with low values of *R*-squared, as the output data was randomly spread around the original loads output of the reference model. This was a result of the insignificant modifications of the altered models compared with the reference model producing major changes of moments between the reference and altered wind turbine models. Additionally, the simple PI controller was implemented in the modified model instead of sophisticated one as the modifications of rotor solidity require adjusting the controller in order to operate at maximum efficiency. It is obvious that a sophisticated controller is better than simple PI controller in terms of loads alleviation.

The main goal of this chapter was to investigate the effect of the rotor solidity on the extreme and fatigue loads. Both scenarios have shown that the extreme and fatigue loads are a function of rotor solidity. The loads become larger at higher solidity and vice versa. However, the previous statement is not true for tower base loads as shown and explained in section 8.1.4.3, 8.1.6.1.2 and 8.2.5.1.2.

Moreover, the estimated dependency of extreme and fatigue loads from the rotor solidity concurs with the hypothesis of mitigating extreme and fatigue tower top (blade roots, rotor and shaft) loads by the reduction of rotor solidity, which can be used to reduce mass, cost of wind turbine and energy as stated by Blonk *et al.* [80].

Additionally, the extreme and fatigue loads of normal power production conditions scale by the values, which were estimated for steady loads by a method based on the scaling with similarity, because the structural properties of blade in the modified models were adjusted by the method based on the scaling with similarity.

9. Up-scaling of reference model

The main goal of this chapter is to investigate how extreme and fatigue loads scale up if the reference model is scaled up with the similarities [3], [6], [24]. So, the author tries to answer to the following question:

- *How the fatigue and extreme loads change due to the up-scaling with similarities?*

In order to answer the above question, seven up-scaled wind turbine models with rated power 4, 5, 6, 7, 8, 9 and 10 MW are produced from the 3MW reference model. The calculated extreme and fatigue loads of reference and up-scaled models are used to develop a generic power load trend to determine up-scaled exponents to compare with the up-scaled exponents of steady loads, which are calculated by the up-scaling with similarity technique. Thus, the second question of this chapter is

- *Do extreme and fatigue loads scale in the same way as steady state loads?*

This question tries to investigate the performance and accuracy of the up-scaling technique for the prediction of extreme and fatigue loads in an up-scaled wind turbine. Up-scaling with similarity tends to be avoided in commercial designs as the weight of some components can become increasingly problematic at larger scales. However, the value of examining scaling with similarity is that it offers the opportunity to detect the underlying trends of system loads in a clear and systematic way.

Section 9.1 provides a brief overview of the up-scaling procedure for the reference model and highlights its key parameters. Section 9.2 validates the accuracy of the applied modifications of the up-scaling with similarities in terms of steady and dynamics state. In section 9.3, an analysis is provided for the changes in fatigue loads due to the up-scaling. The changes in deterministic and stochastic fatigue edge-wise blade loads are discussed in section 9.4. The alterations of extreme loads in the up-scaled models are presented in section 9.5. Section 9.6 provides a comparison between the scale exponent coefficient of commercial wind turbines and the calculated exponents of up-scaled models generated in this study. In section 9.7, scale impact on turbulence is inspected for the fatigue loads. Section 9.8 investigates the shear effect on up-scaled model loads. The concluding section of this chapter provides a summarised discussion of the results.

9.1. Up-scaling procedure:

Up-scaled wind turbine models with rated power 4, 5, 6, 7, 8, 9 and 10 MW were created from the 3 MW reference model by using the method of up-scaling with similarity [3], [6], [24]. An appropriate rotor diameter was chosen to maintain the power density (which is shown by equation 9.1) of the reference model in the up-scaled wind turbines models. This is a direct consequence of scaling with similarity. Consequently, the up-scaling or modification factor, which depends on the power density and rated power of the up-scaled model, can be calculated as shown in equation 9.2.

$$Pow.den = \frac{P}{A_{rotor}} \tag{9.1}$$

$$F = \left(\sqrt{\frac{4\,P_1}{\pi * Pow.den}} \right) \div D_o \tag{9.2}$$

P_1 is rated power of the up-scaled unit, D_o is radius of the reference model. The calculated scale factor is used to up-scale the reference model by using the method of scaling with similarity [3], [6], [24].

Chapter 3 defined the scaling of wind turbine parameters and some key such parameters are listed in Table 9.1. The parameter variations are detailed in references [3], [6], [7], [24], [26], [87].

Parameters	Symbols	Modification
Dimensions (m)	L	F^1
Mass (kg)	m	F^3
Stiffness (Nm^2)	I	F^4
Mass inertia (kgm^2)	I_{mass}	F^5
Shaft damping (Nm/rad)	$c_{damp\,shaft}$	$F^{3.5}$
Shaft stiffness (Nms/rad)	I_{shaft}	F^4
Torque (Nm)	Q	F^3
Rotational Speed (Hz)	Ω	F^{-1}
Tip speed (m/s)	$w_{rot} * R$	F^0
Bladed twist distribution (°)	β	F^0
Gearbox ratio	N	F^0

Table 9.1: Modification of up-scaling key parameters for a wind turbine.

Figure 9.1 plots the rotor diameter against rated power of up-scaled wind turbine models; the plot was generated by applying up-scaling with similarity and maintaining the original value of power density in the reference model. Additionally, Figure 9.1 includes the power law trend, which is generated from the output data of the reference and up-scaled models and the power law equation of the trend. The exponent of power law equation equals 2, which matches the predicted exponents of rated power estimated by the up-scaling method perfectly. Therefore, it is possible to say that wind turbines were up-scaled correctly in terms of power production. However, an accurate up-scaled power production output is not enough to validate the procedure of up-scaling. Thus, the validation of up-scaling procedure will continue in section 9.2.

The scaling of power to an exponent of 2 is consistent with similarity, although it is violated by wind shear, which, at least if considered as quasi-static and in effect deterministic, would impose an absolute vertical scale independent of turbine parameters.

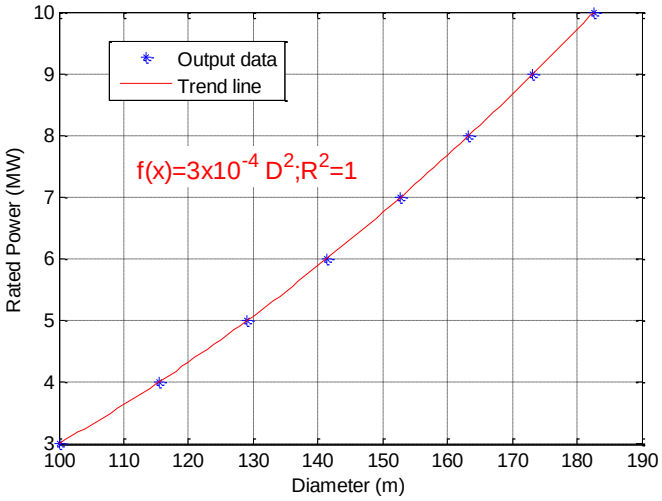

Figure 9.1: Diameter and rated power of up-scaled wind turbines

Additionally, a new controller is necessary for each wind turbine generated from the reference model as the dynamics of the up-scaled wind turbines are different from those of the reference model. The controller of a large wind turbine is tuned for the specific dynamic of the machine and the original controller was naturally developed to suit the dynamics of the reference model. In the up-scaled models, a new simple PI controller was employed for the below rated region to match the new frequencies of up-scaled machines. However, the original controller was used for the above rated region because it includes the tower feedback loop [88], [89], which reduces tower top movements by decreasing pitch activity. The simple PI controller is unstable in the above rated region for the 7, 8, 9 and 10MW up-scaled wind turbines. This instability

characterises the excessive pitch activity, which produces the significant fore-aft movements of the nacelle and a dramatic increase of the thrust force.

The tower is deflected as a consequence of the wind-induced thrust force as shown in Figure 8.11. If the wind speed rises, the blades are pitched to maintain the rated power. Pitching the blades reduces the thrust and the tower top then moves towards to the incoming flow. In this case, the wind turbine rotor experiences an increase in relative wind velocity due to the motion of tower top towards the incoming wind. As a result, the blades are pitched further. And when the tower top reaches the nominal vertical position, the pitch angle is larger than required. This feedback is potentially unstable. A tower feedback loop is therefore used to reduce and stabilise the pitch activity by tracking the motion of the tower top. This removes excessive oscillation of the tower top. Therefore, all up-scaled machines deploy the original controller of the reference model, which includes the tower feedback loop, at the above-rated region.

Appendix F provides a comparison between the controller (with tower feedback loop) of the reference wind turbine and the new simple PI controller (without tower feedback loop) for the up-scaled wind turbine with 8MW rated power.

9.2. Validation

This section validates the accuracy of the up-scaling procedure used in this study. The validation concerns steady and dynamic state analyses, which are presented in sections 9.2.1 and 9.2.2, respectively.

9.2.1. Steady state analysis

The accuracy of the up-scaling procedure is validated by evaluating the steady state performance of up-scaled wind turbines. As it was mentioned in chapter 3 that similarity scaling is based on assumptions which preserve the aerodynamic similarity to the reference model. One assumption is the maintenance of the original TSR from the reference model. Figure 9.2 shows a plot of TSR against the operational range wind speed for both the reference and the up-scaled wind turbine models. The curves of up-scaled models are completely match the curve of reference model as required.

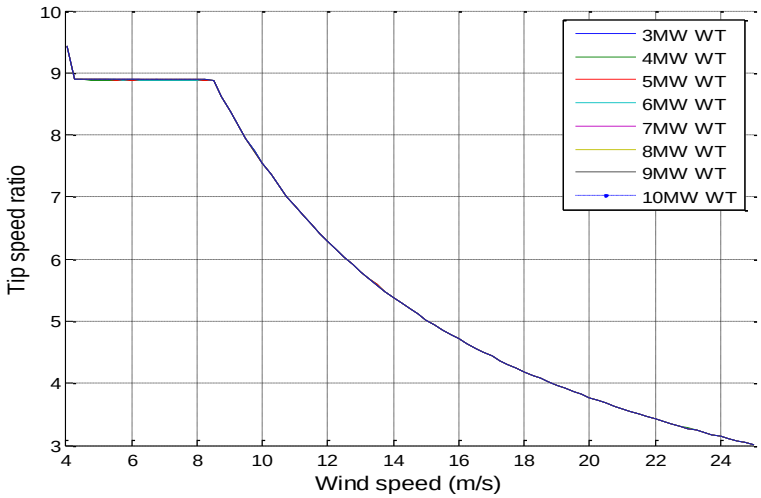

Figure 9.2: TSR of reference and up-scaled models against wind flow speed.

The combination of preserving original TSR with other assumptions such as the maintenance of original aerofoils and the linear alteration of geometry can preserve the aerodynamics of reference model in the up-scaled wind turbine models. Figure 9.3 depicts the power coefficient of the reference and up-scaled models against TSR. Each power coefficient curve of up-scaled models is identical to the power coefficient curve of 3MW reference turbine model. Thus, the Reynolds number of the reference model has been retained in the up-scaled models. Figure 9.2 and 9.3 verify that the aerodynamics of up-scaled wind turbines did not change and maintain the aerodynamics of the reference model. It is additional proof, that the procedure of up-scaling was implemented correctly.

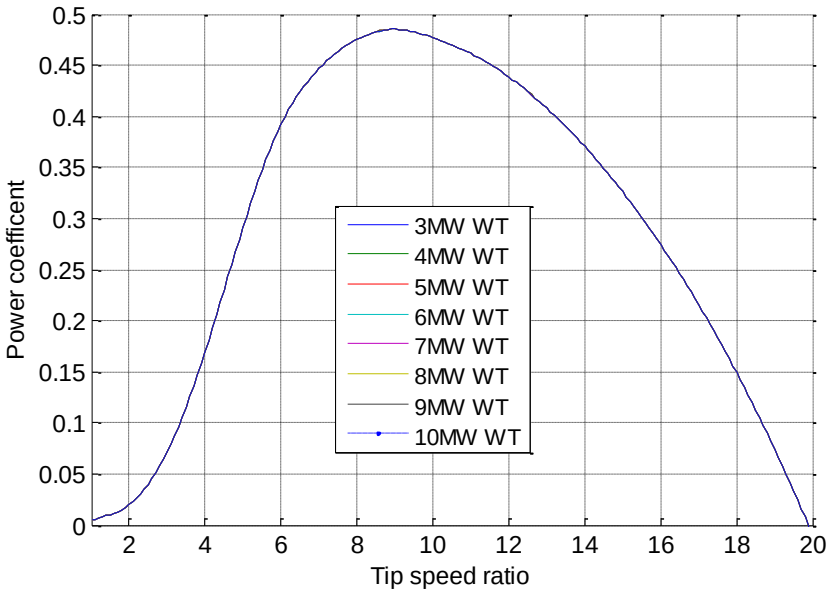

Figure 9.3: Power coefficient of reference and up-scaled models against wind flow speed.

Additionally, it is necessary to ensure that the operational strategy of up-scaled models remains the same as the operational strategy of the base model. In this case Figure 9.4 depicts the power curves of reference and up-scaled models as a function of mean wind speed. Figure 9.4 shows that the cut-in (4 m/s), rated speed (11.5 m/s) and cut-out (25 m/s) are preserved in the up-scaled models. Owing to the preservation of the above mentioned speeds, it is possible to affirm that the operation regions, which are 1st constant speed, maximum *Cp* tracking, 2nd constant speed and pitching, remain unchanged in the up-scaled models. Therefore, the operational strategy of up-scaled models is identical to the operational strategy of the reference model.

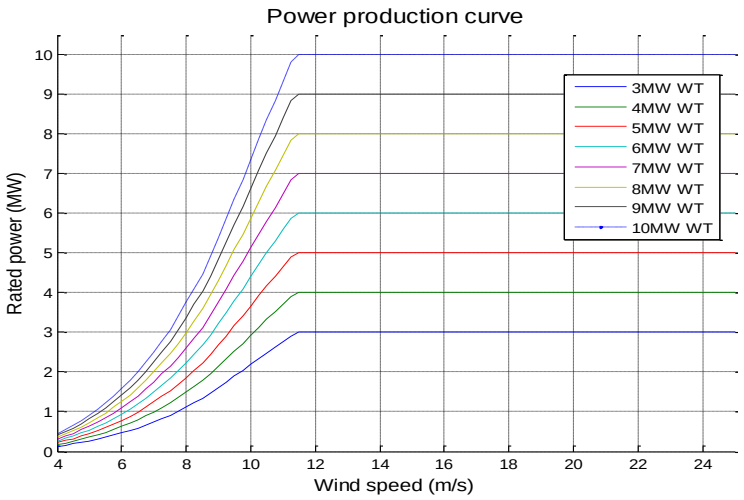

Figure 9.4: Power production curves of reference and up-scaled models against wind flow speed.

These results prove that the original aerodynamics and operational strategy of the reference model are preserved in the up-scaled models. Consequently, the next step is to inspect the accuracy of up-scaling procedure by looking at steady loads. Figure 9.5 shows the three graphs, which include the output data of rotor thrust, blade root flap-wise moment and tower fore-aft base moment, respectively. The steady loads were measured at 8 m/s of wind flow speed for the all three parameters. A power trend line was generated for each load. The exponents of all three power law trend lines are identical to the predicted exponents of the same loads estimated by the technique of up-scaling with similarity, which are R^2 for thrust, R^3 for blade root flap-wise moment and tower fore-aft base moment. The agreement between the measured and predicted exponents indicates that the reference wind turbine model has been up-scaled correctly.

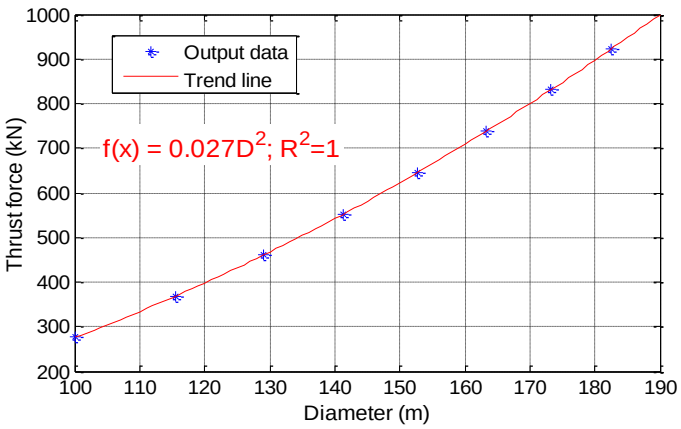

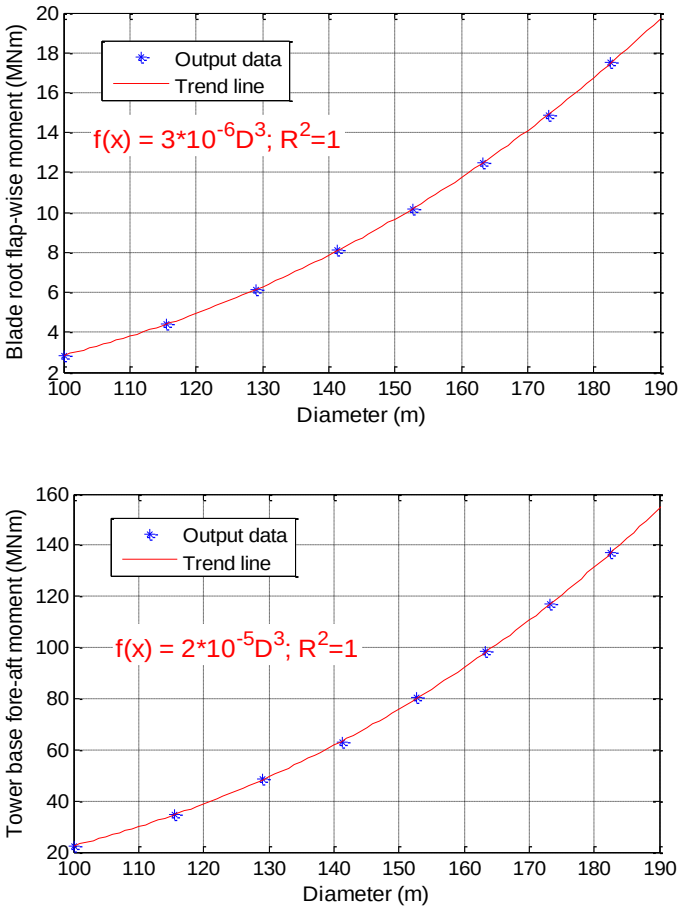

Figure 9.5: The output data with power trend line of rotor thrust force, blade root flap-wise moment and tower fore-aft base moment, which were measured at a wind speed of 8 m/s in steady state conditions.

In the next section, up-scaled models are examined for matching between the rotational frequency of the rotor and natural frequencies of various wind turbine components.

9.2.2. Dynamic state analysis

This section investigates the behaviour of up-scaled models in dynamic conditions by using spectral analysis, which checks the moments of up-scaled models, namely, edge-wise and flap-wise of blade root, low speed shaft, yaw bearing and fore-aft tower base in the frequency domain. Additionally, the moments of up-scaled models are compared with the moments of the reference model. The graphs of spectral analysis include the models (two up-scaled and one reference. The 6MW and 10MW units are used to illustrate the up-scaled models in the graphs as

6 MW represents the middle point in range, which stretches from 3MW to 10MW, while the 10MW unit is the largest up-scaled model in the chosen range.

9.2.2.1. Edge-wise blade root moment:

Figure 9.6 depicts power spectra density (PSD) and cumulative PSD graphs of the blade root edge-wise moment, respectively. The important peaks are labelled on the PSD graph in Figure 9.6. It is noticeable from the PSD graph that compared to the reference model, there is a shift in the peaks of the up-scaled models, which corresponds to the rotor frequency. The frequency reduction of the up-scaled wind turbine was anticipated as one of the assumptions of the linear scaling rule is the maintenance of reference model tip speed. As a result, the angular velocity of rotor has to be scaled down to maintain the original tip speed value, which leads to a reduction in rotor frequency (*1P*) and its harmonics. Moreover, the frequency of blade structural modes decreased with the up-scaling of the reference model, which is a consequence of structural property modification as shown in Table 9.1. If a blade is assumed to be a rectangular, untwisted and homogeneous cantilever beam for simplicity, Its natural frequency can be expressed as described in equation 9.3 [90], [91].

$$w_n = {\Lambda_n}^2 \sqrt{\frac{EI}{m\,R^4}} = {\Lambda_n}^2 \sqrt{\frac{E\,R^4}{R^3 * R^4}} = {\Lambda_n}^2 \sqrt{\frac{E}{R^3}} \qquad 9.3$$

Where, Λ_n is eigenvalues of cantilever beam, E is young modulus, I Second moment of area, m is mass and R is a radius or length of blade. According to the up-scaling procedure, all dimensions change with the scaling factor and the modification of mass is assumed to be equal to F^3 or R^3as stated in [3], [6], [7], [24]. Thus the equation of blade natural frequency can be rewritten in terms of scaling to see how the natural frequency changes.

$$w_n = {\Lambda_n}^2 \sqrt{\frac{E\,R^4}{R^3 * R^4}} = {\Lambda_n}^2 \sqrt{\frac{E}{R^3}} \qquad 9.4$$

Equation 9.4 shows that the natural frequency changes as the inverse of the rotor power diameter, which matches the changes of blade edge-wise structural modes on figure 9.6.

The above mentioned changes do not have a negative impact as there are no un-damped peaks that have the same or higher frequency as the *1P* harmonics and structural blade modes. Furthermore, the curves of the cumulative PSD do not have any significant peaks apart from at *1P*. Therefore, it is possible to conclude that the PSD and cumulative PSD of edge-wise blade root

moment did not show any irregular behaviour in up-scaled wind turbine models. The rest of the moments (flap-wise blade root, low-speed shaft, yaw bearing and fore-aft tower base) did not reveal any irregular behaviour either and the PSD graphs of these moments can be found in Appendix F.

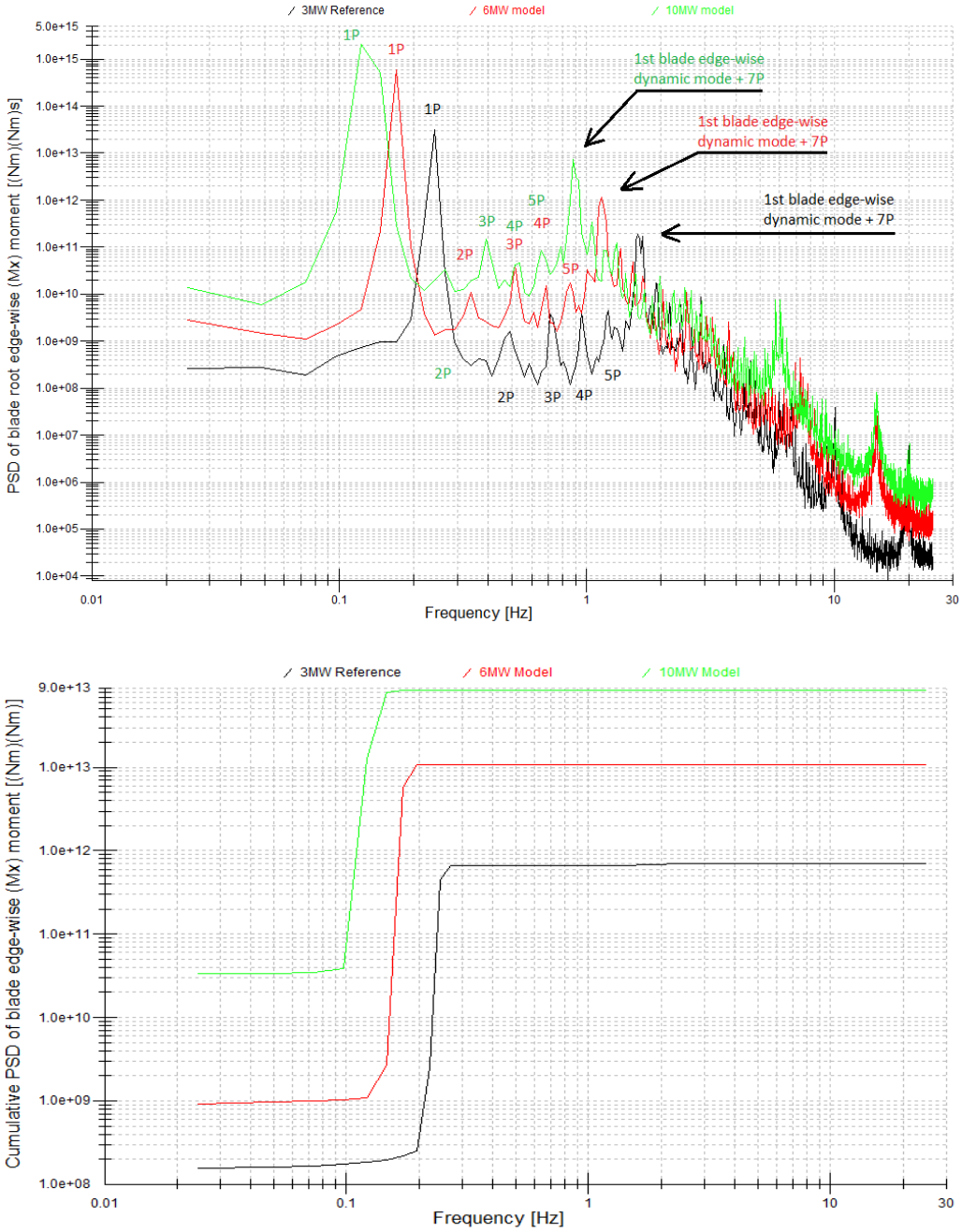

Figure 9.6: PSD and cumulative PSD of blade root edge-wise moment of a reference (3MW) reference and two up-scaled models (6MW and 10MW) at 14 m/s.

9.3. Fatigue loads analysis

This section highlights changes in fatigue loads in terms of lifetime DELs that are caused by the up-scaling of the reference turbine model. As in the previous chapter the lifetime DELs are calculated for DLC 1.2, 3.1/4.1 and 6.4, which are based on IEC standards [5] and correspond to power production range, the number of start-ups and shut-downs and idling conditions of a wind turbine, respectively.

The section is divided into four subsections, each of which cover a moment of interest, namely, blade root, low-speed shaft, yaw bearing and fore-aft tower base. Note, each figure in this section shows the calculated values of lifetime DELs with the power trend lines for Wohler coefficient 4 and 10, which are typical of steel and composite material, respectively.

9.3.1. Blade root moments

Figure 9.7 shows lifetime DELs of edge-wise and flap-wise blade root moment of the three above mentioned DLCs. The left and right columns of the graph correspond to edge-wise and flap-wise blade root moments, respectively.

DLC 1.2 is expressed in the first horizontal pair of graphs on Figure 9.7. The exponents of the power law trend lines demonstrate that the lifetime DELs of DLC 1.2 scale almost the same as the steady edge-wise (D^4) and flap-wise (D^3) blade root moments, which were predicted by the method of up-scaling with similarity. However, the exponent of Wohler coefficient 10 matches steady moments better because the exponent of Wohler coefficient 4 is slightly smaller than the exponents of Wohler coefficient 10 for both moments as shown by the first pair on graphs in Figure 9.7. The difference between the calculated and estimated exponents of lifetime DELs is a result of the turbulence and the constraints on assumptions in the algorithm of GH Bladed. However, the effect of wind shear on the up-scaled models is reviewed in section 9.8.

On Figure 9.7 the second pair of graphs displays the blade root moment of lifetime DELs for DLC 3.1/4.1, which show an even closer agreement with the predicted exponents for steady moments than the estimated exponents of DLC 1.2.

The last horizontal pair of graphs corresponds to Lifetime DELs of DLC 6.4. The edge-wise moment exponents of both Wohler coefficients do not match the predicted exponents of steady moments.

This is possibly a result of the idling operational conditions of the wind turbine, where the rotor does not rotate or slightly rotates. As the method of scaling with similarities is based normal power production operational conditions, but the idling conditions do not correspond to the conditions of power production range. However, the flap-wise lifetime DELs of both Wohler coefficients scale somewhat more than the values of predicted flap-wise blade root moment.

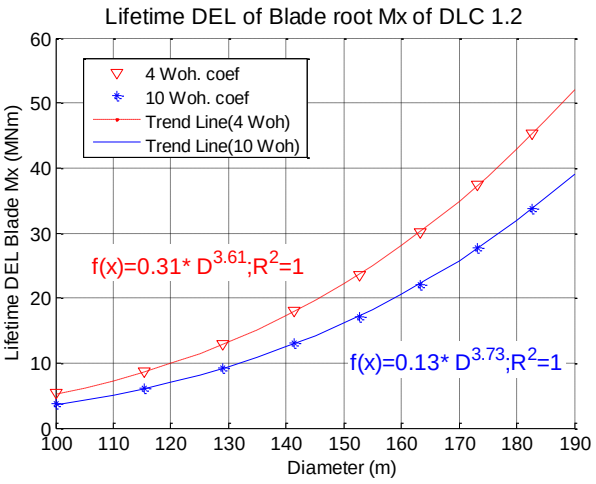

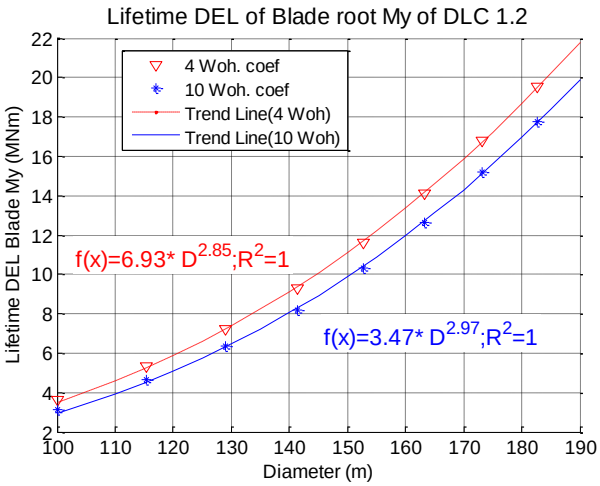

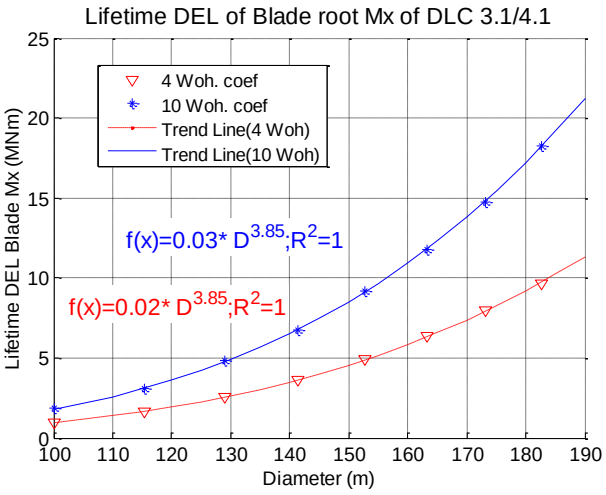

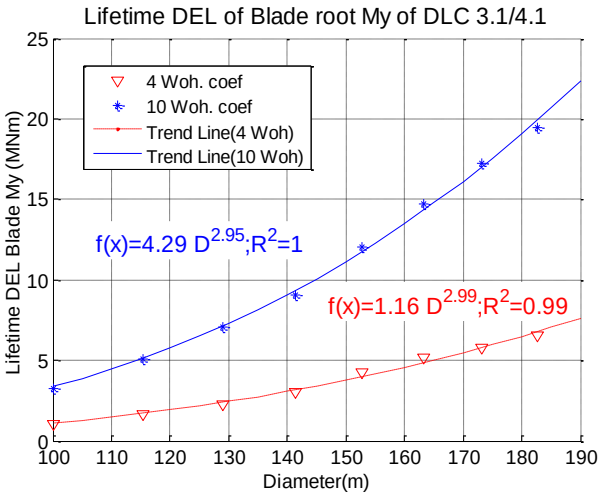

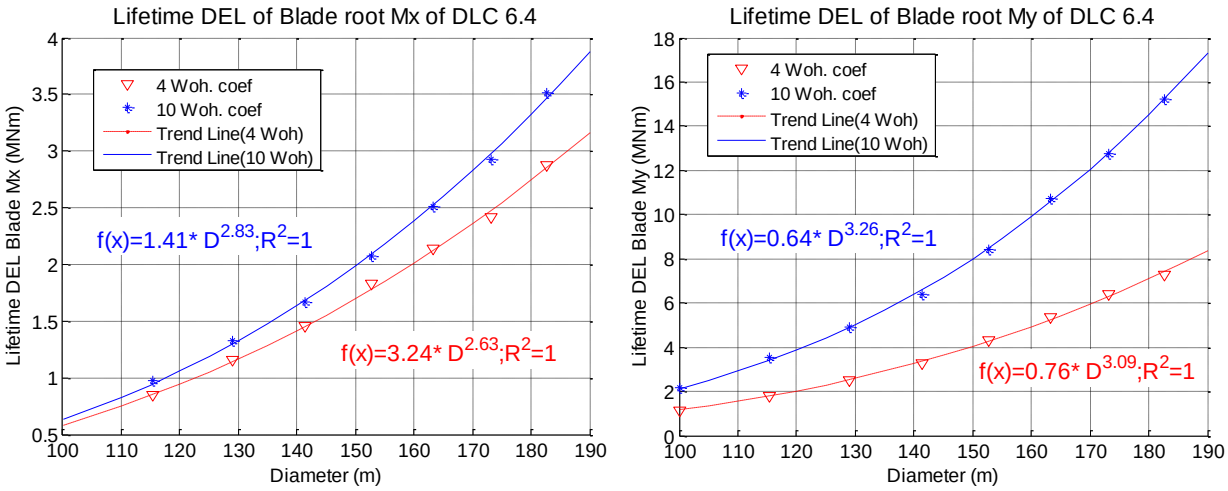

Figure 9.7: DLC 1.2, 3.1/4.1 and 6.4 lifetime DELs of edge-wise and flap-wise blade root bending moments for Wohler coefficients 4 and 10.

9.3.2. Low-Speed shaft moment

The three graphs in Figure 9.8 depict the lifetime DELs of low speed shaft moment for DLC 1.2, 3.1/4.1 and 6.4, respectively. Both Wohler coefficients for these three graphs have the exponents of power trend lines, which are slightly smaller than the anticipated exponent (D^3) of low-speed shaft steady moment. The difference between the calculated and anticipated exponents is caused by turbulence and assumptions of algorithms in GH Blade, as mentioned in section 9.3.1.

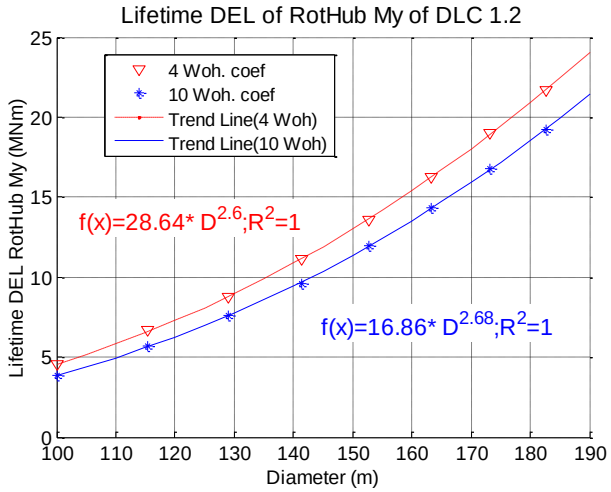

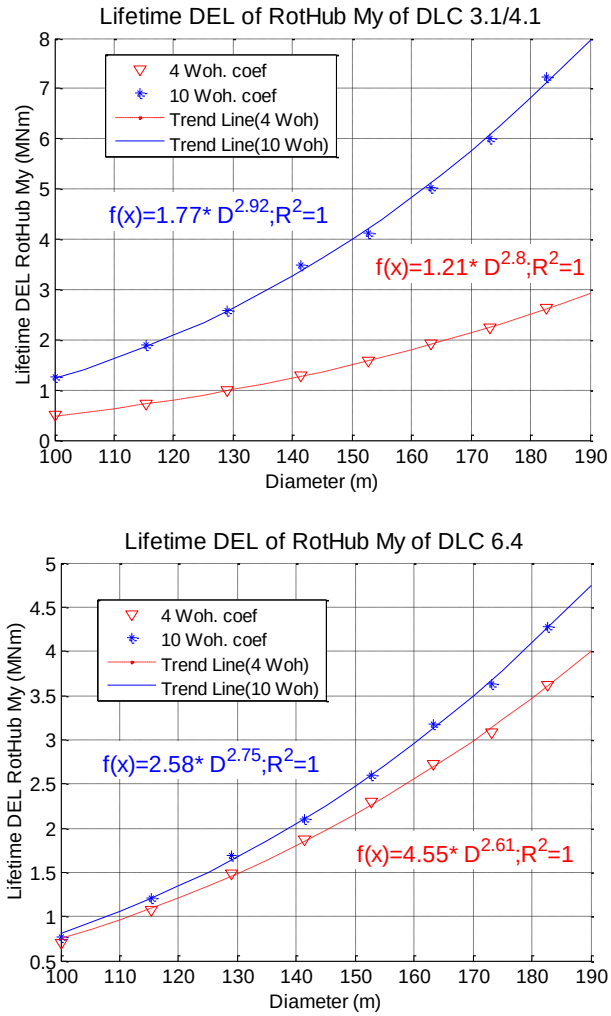

Figure 9.8: DLC 1.2, 3.1/4.1 and 6.4 lifetime DELs of low-speed shaft moment for Wohler coefficient 4 and 10.

9.3.3. Yaw bearing moment

Figure 9.9 shows the three graphs, which as noted previously correspond to three cases of wind turbine operation conditions. Each graph presents the modifications of yaw bearing lifetime DELs in terms of moments. The first (DLC 1.2) and third (DLC 6.4) graph of Figure 9.9 show that the lifetime DEL of yaw bearing moment scales approximately by the same value, which is ~2.5. The yaw moment (Mz) is proportional to torque [1], which scales by a power of 3 as stated in an report on similarity rules for wind turbine up-scaling [24]. In this case the the calculted exponents of DLC 1.2 and 3.1/4.1 are smaller than the predicted exponents by approximately 17%. This is probably a result of dynamic conditions, especially turbulence.

However, the second graph (DLC 3.1/4.1), which corresponds to the number of start-ups and shut-downs of the machine, demonstrates that the calculated exponents are in the range 3.6-3.7 for both Wohler coefficients. They are also approximately 23% larger than the estimated ones.

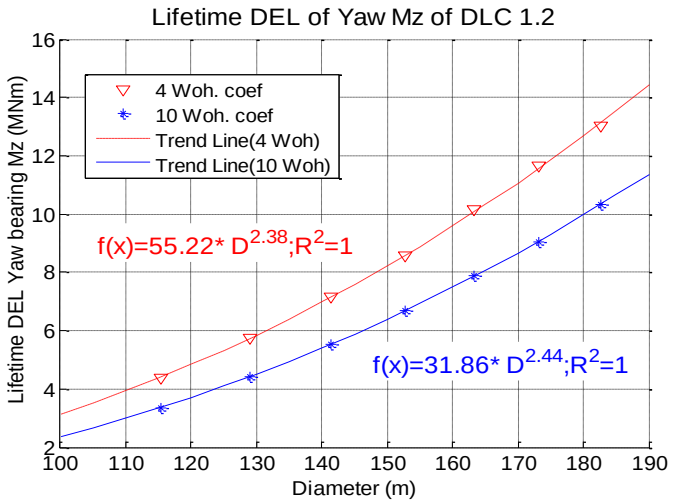

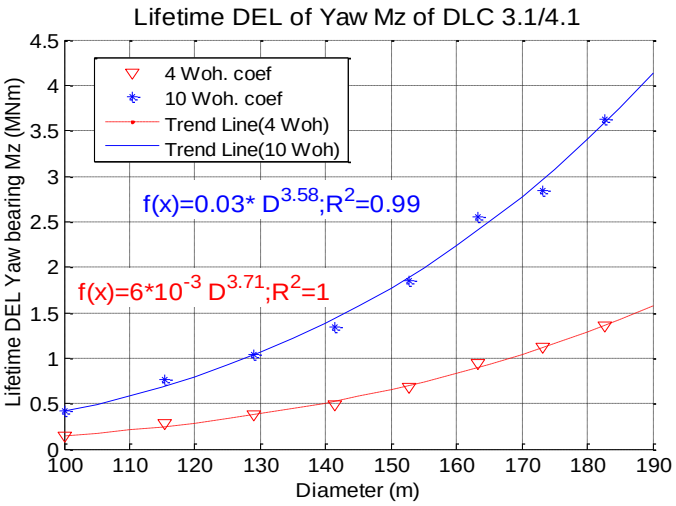

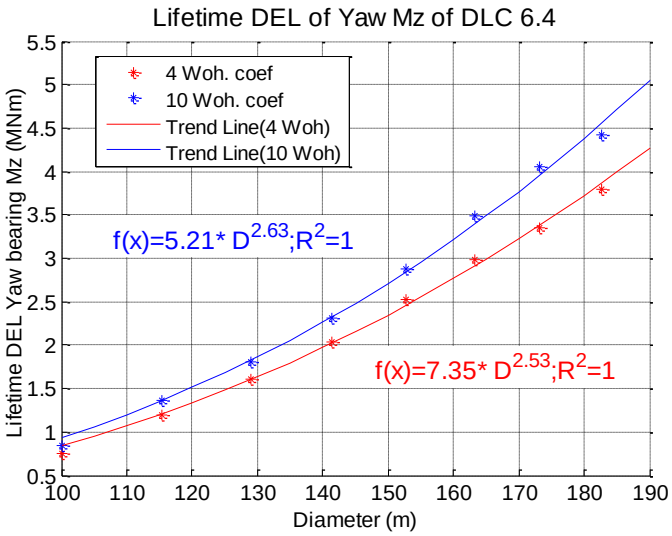

Figure 9.9: DLC 1.2, 3.1/4.1 and 6.4 lifetime DELs of yaw bearing moment for Wohler coefficient 4 and 10.

9.3.4. Tower base fore-aft moment

The three following graphs of Figure 9.10 depict the lifetime DELs of tower base fore-aft for the three DLCs.

The first graph in Figure 9.10, which relates to DLC 1.2, shows that the exponents of both Wohler coefficients are much smaller than the predicted exponent, which equals 3, for the tower fore-aft base steady moment estimated by the method of up-scaling with similarity. This is a result of the implementation of the sophisticated controller with the tower feedback loop, which minimises the pitch activity of blades in order to reduce the tower base loads, as mentioned at the beginning of this chapter.

However, the graphs of DLC 3.1/4.1 and 6.4 show that the lifetime DELs of tower base moment scale roughly by 3 for both Wohler coefficients the lifetime DELs of DLC 3.1/4.1 scale by a factor slightly larger than 3, while the exponents of DLC 6.4 scale by a factor slightly smaller than 3. Nevertheless, it is possible to assume a scaling factor of 3 for both the DLC 3.1/4.1 and 6.4 lifetime DELs of tower fore-aft base moment, which is also the value estimated for steady tower fore-aft base moment loads by the method of up-scaling with similarity.

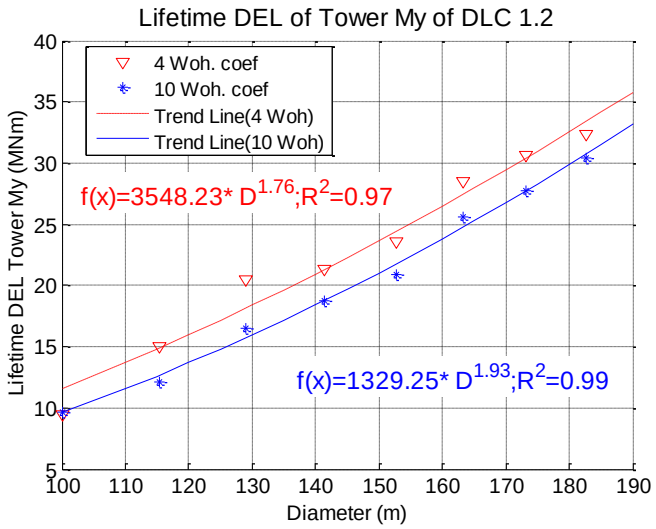

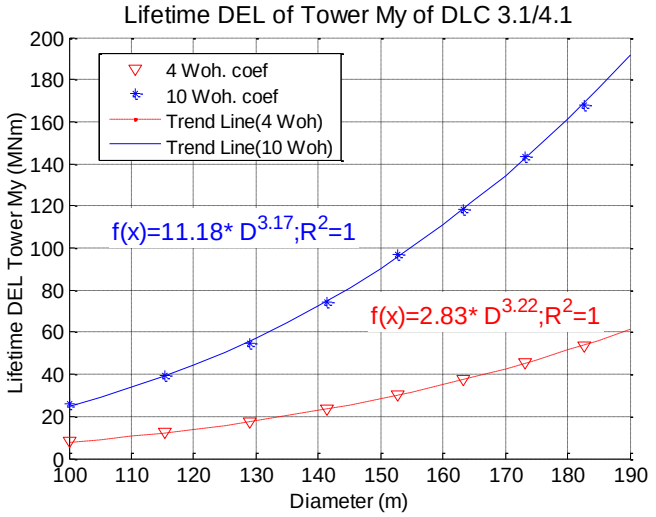

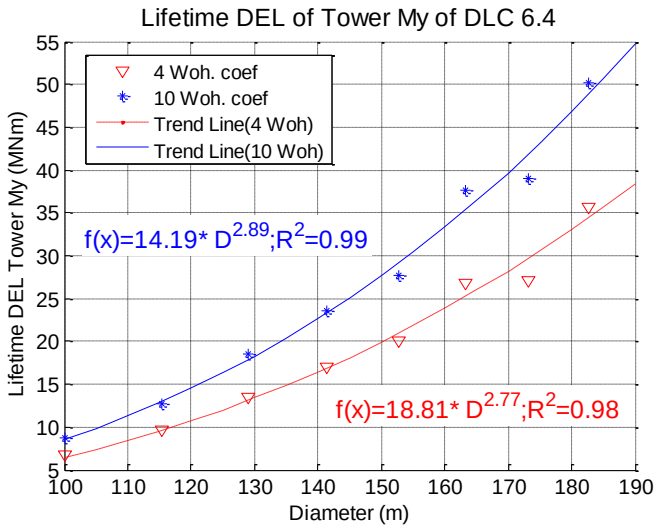

Figure 9.10: DLC 1.2, 3.1/4.1 and 6.4 lifetime DELs of tower base fore-aft moment for Wohler coefficient 4 and 10.

9.4. Deterministic and stochastic fatigue loads

This section displays how lifetime DELs of deterministic and stochastic parts of DLC 1.2 scale up for the edge-wise blade root moment, separately. Wohler coefficient 4 and 10 are used to show the changes of lifetime DELs for the deterministic and stochastic parts.

Figure 9.11 shows the deterministic lifetime DELs of edge-wise blade root moments for both Wohler coefficients. Figure 9.12 depicts the stochastic lifetime DELs of edge-wise blade root moments, where the stochastic part of load is caused by turbulence.

In Figure 9.11 the exponents of deterministic trend lines are larger than the exponents of total (deterministic and stochastic parts) lifetime DELs, which are shown in Figure 9.7. As demonstrated in Chapter 7, edge-wise blade root moment is mainly a function of blade self-weight. The calculated exponents of deterministic lifetime DELs are slightly smaller than the estimated value of 4 (Table 3.2). Therefore, the difference between the deterministic lifetime DELs and estimated exponents is minor and it may be a result of the constraints posed by the underlying assumptions in the algorithm.

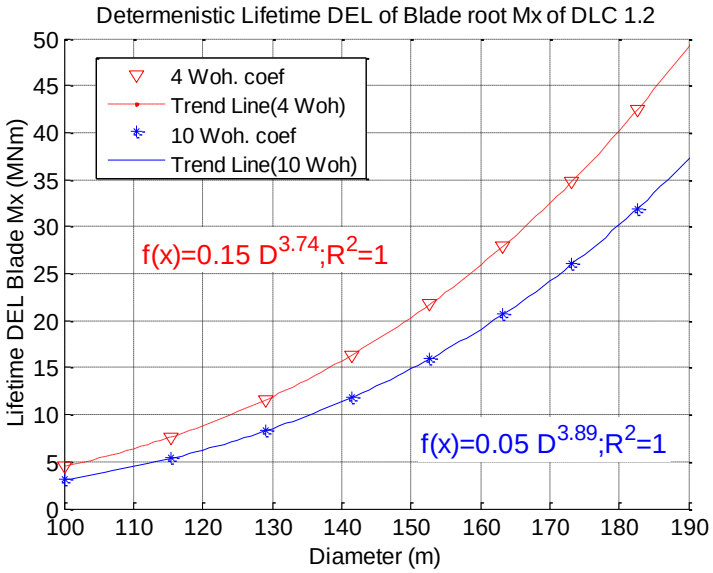

Figure 9.11: DLC 1.2 deterministic lifetime DELs of blade root edge-wise moment for Wohler coefficient 4 and 10.

In Figure 9.12 the exponents of stochastic lifetime DELs are roughly equal to 2, which is half of the exponents of deterministic DELs. The figure shows why the exponents of total load (deterministic and stochastic parts) of DLC 1.2 are smaller than the exponents of deterministic lifetime DELs.

Therefore, the graph of stochastic lifetime DELs demonstrates that turbulence is affected by scaling, because the exponents of the stochastic load part are half those of the deterministic load part. Consequently, the stochastic part of load decreases with increasing size in the up-scaled wind turbines. More detail information of scale effect on turbulence can be found in section 9.7.

Note that the sum of the deterministic and the stochastic parts of lifetime DELs is not equal to total lifetime DELs because lifetime DELs are not calculated linearly.

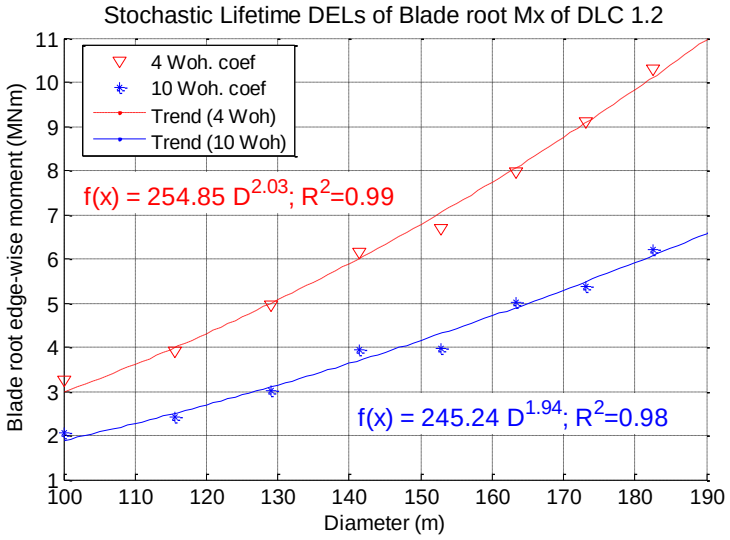

Figure 9.12: DLC 1.2 stochastic lifetime DELs of blade root edge-wise moment for Wohler coefficient 4 and 10.

9.5. Extreme loads analysis

This section presents an overview of the extreme moments for blade root, low speed shaft, yaw bearing and tower base fore-aft in terms of the four DLCs [5]: 1.1, 1.3, 6.1 and 6.4. Each of four DLCs characterise different wind and wind turbine operational conditions. This section is divided into two subsections. The first subsection shows the output data of DLC 1.1. The remaining DLCs (1.3, 6.1 and 6.3) are presented in the second subsection.

9.5.1. Design load case (DLC) 1.1

DLC 1.1 corresponds to the statistical extrapolation technique based on long-term (50 year period) exceedance probability [60]–[62], [86] for the calculation of extreme loads in wind conditions with the normal turbulence model NTM.

9.5.1.1. Blade root moments

The changes in edge-wise and flap-wise blade root extreme moments are shown in the two graphs of Figure 9.13. The calculated exponent of edge-wise blade root moment trend line has a value of 3, which is lower than the predicted value (D^4). The extreme moments of flap-wise blade root scale by 2.65, which is a slightly smaller than the predicted value, D^3.

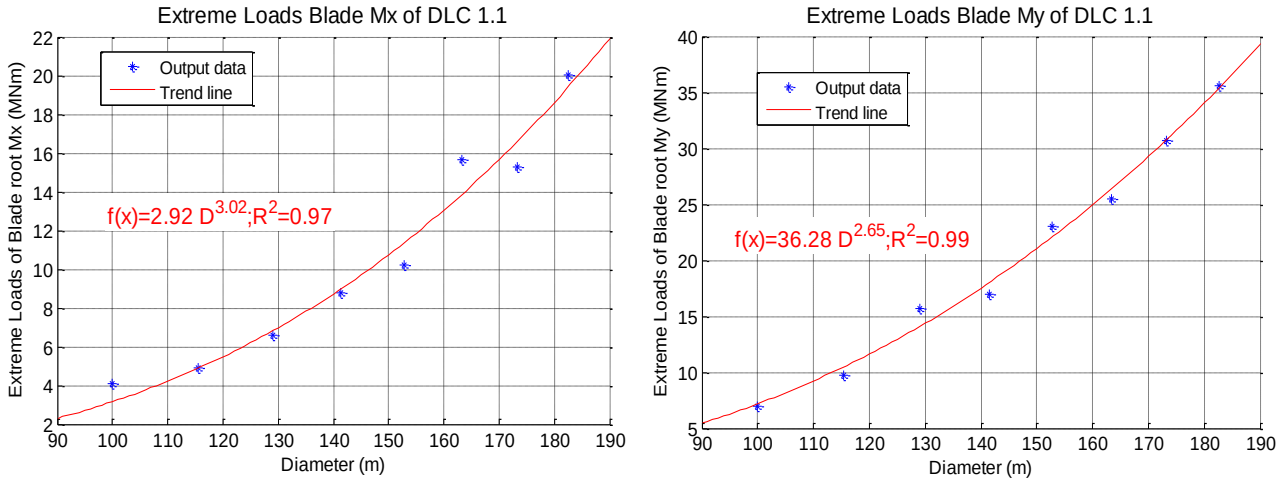

Figure 9.13: DLC 1.1 extreme moments of edge-wise and flap-wise blade root.

9.5.1.2. Low speed shaft, yaw bearing and tower base moments

Figure 9.14 presents three graphs that plot low speed shaft, yaw bearing and tower fore-aft base moments, respectively.

The first graph shows that the extreme low-speed shaft moment scales by 2.68, which is almost identical to the calculated exponents of DLC 1.2 lifetime DELs. The steady moment of low speed shaft scales by a factor of 3 as the up-scaling with similarity method showed in [24]. The difference between the calculated and predicted scale factors is roughly 10 %, which is not significant. It is most likely a consequence of the dynamic conditions in the simulations such as wind shear, tower shadow and turbulence.

The second graph expresses how the DLC 1.1 extreme moment of yaw bearing scales up due to the up-scaling the reference model with similarities. The exponent of DLC 1.1 power trend line equals 2.68, which is not far from the predicted value of exponent (D^3) for steady moment of yaw bearing. Similar to the case of the first graph, the dissimilarity between the predicted and obtained exponents is result of wind shear, tower shadow and turbulence.

DLC 1.1 extreme moment of fore-aft tower base is presented in the last graph of Figure 9.14, which shows that the calculated exponents of power trend line equals 2.82. The anticipated exponents of steady tower base fore-aft moment have a value of 3. The variation between the calculated and predicted exponents is 6%.

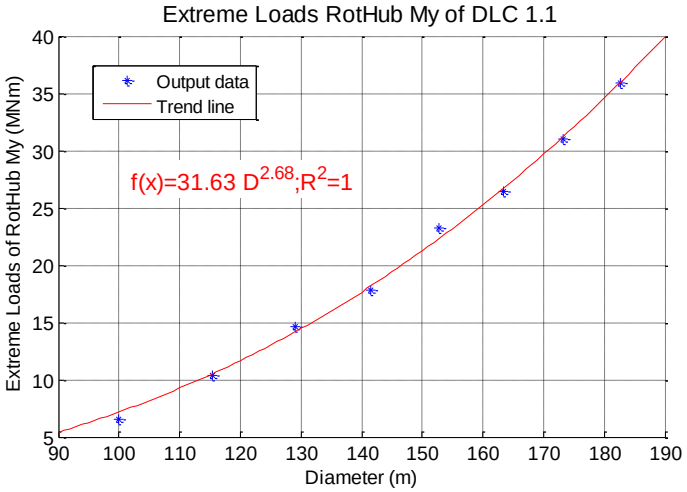

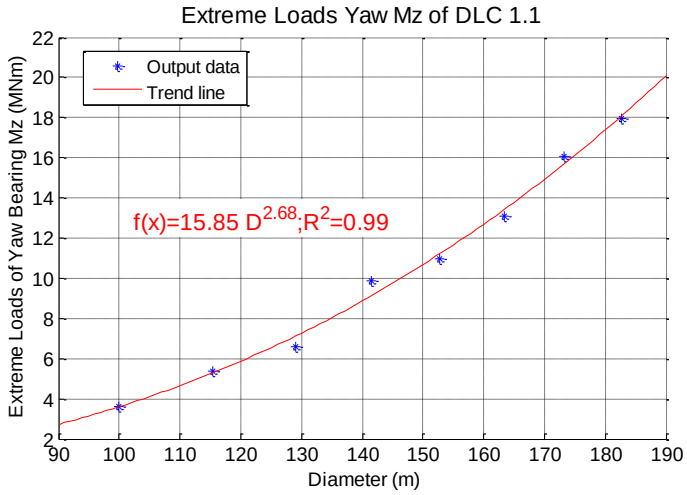

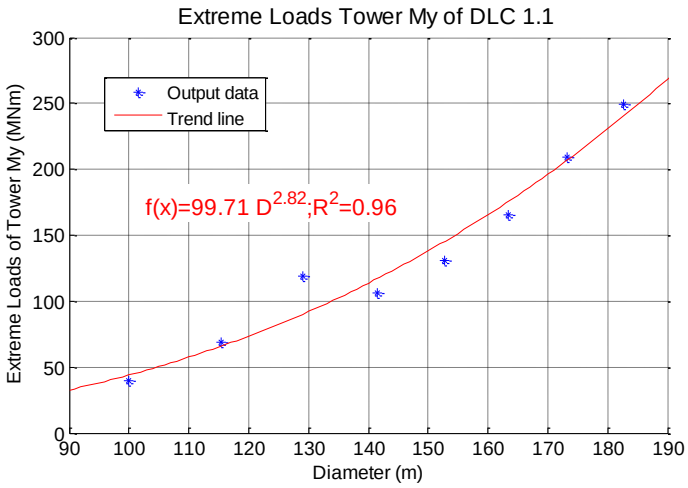

Figure 9.14: DLC 1.1 extreme moments of low speed shaft, yaw bearing and for-aft base of tower.

9.5.2. Design load case (DLC) 1.3, 6.1 6.3

The changes of DLC 1.3, 6.1 and 6.3 extreme loads are presented in this subsection. These DLCs will be presented as a single graph for a given moment. This subsection is divided into the two parts, where the first part relates to blade root extreme moments and the second part covers the other three extreme moments of interest in this study: low speed shaft, yaw bearing and fore-aft of tower base.

9.5.2.1. Blade root moments:

This part of subsection investigates the modifications of blade root extreme moment. Figure 9.15 is made up of two graphs that depict edge-wise and flap-wise blade root extreme moments for DLC 1.3, 6.1 and 6.3.

The graph of the edge-wise extreme moment shows that DLC 1.3 has an exponent of 3.43, which is approximately 14% smaller than the predicted exponent (D^4) for edge-wise blade root moment. As the same time, the exponent of DLC 1.3 is slightly smaller than the exponents of DLC 1.2 lifetime DELs for both Wohler coefficients. The edge-wise exponents of DLC 6.1 and 6.3 are approximately identical, but much smaller than the predicted exponents. As the same time, the values of DLC 6.1 and 6.3 exponents are closer to the values of DLC 6.4 exponents of both Wohler

coefficients, which characterise lifetime DELs of blade root edge-wise moment for the idling operational conditions of wind turbine.

The flap-wise blade root extreme moment is presented in the second graph of Figure 9.15, which reveals that the up-scaling of DLC 1.3 and 6.1 extreme moments nearly matches the estimated value of the up-scaling exponent for steady flap-wise blade root moment. The extreme moment of DCL 6.3 scales by a factor of 3.4, which is larger than the predicted value but matches approximately the exponents of DLC 6.4 lifetime DELs, in particular the scale factor of Wohler coefficient 10, which is related to composite materials.

The two graphs in Figure 9.15 display the variation in exponent values between DLCs. This variation is a result of the operational conditions of the wind turbine (which are power production and idling) and wind flow. In this case it is possible to state that at the power production operational condition the extreme and lifetime DELs scale by factors that are close to the estimated values for steady loads, but the up-scaling with similarities method is less applicable for the idling operational conditions of wind turbine.

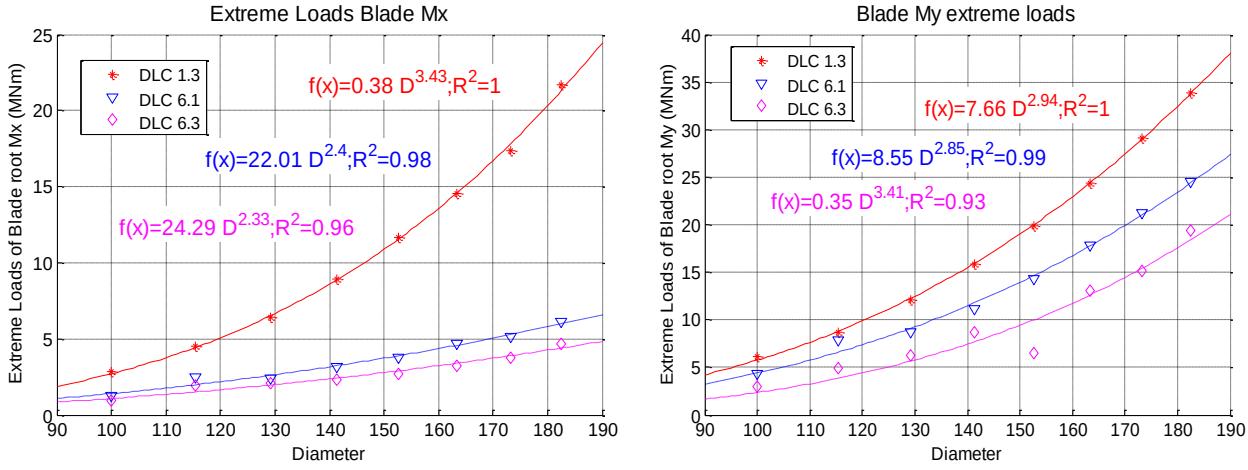

Figure 9.15: DLC 1.3, 6.1 and 6.3 of edge-wise and flap-wise blade root extreme moments.

9.5.2.2. Low speed shaft, yaw bearing and tower base moments

Figure 9.16 is made up of three graphs that depict the extreme moment of low speed shaft, yaw bearing and fore-aft tower base for DLC 1.3, 6.1 and 6.3

The first graph shows the low speed shaft extreme moment and it can be seen that the exponents of DLC 1.3 and 6.3 have almost identical values. However, the values are smaller than the estimated up-scale factor, which has a value of 3. The dissimilarity between the calculated and

predicted up-scaling factors is a result of turbulence and algorithm constraints. Furthermore, the exponent of DLC 1.3 is identical to the exponent of low speed shaft extreme moment DLC 1.1. For both Wohler coefficients, the value of the exponent of DLC 6.3 is very close to that of the exponents of DLC 6.4 lifetime DELs. For DLC 6.1, the calculated and estimated exponents show a good match.

The extreme yaw bearing moment of the three DLCs is displayed in the second graph of Figure 9.16. The exponent of DLC 1.3 is smaller than the estimated exponents by approximately 23%. However, it also happens to be almost identical to the two exponents of DLC 1.2 lifetime DELs, which are shown in the first graph of Figure 9.9. Furthermore, there is no significant difference between extreme moments of DCL 1.3 and 1.1. The exponents of DLC 6.1 and 6.3 are almost identical and smaller than the predicted exponent by approximately 10%. Additionally, the values of both exponents are close to the exponents of DLC 6.4 lifetime DELs, which are depicted in the third graph of Figure 9.9.

The last graph of Figure 9.16 characterises the changes in the extreme fore-aft tower base moment for the three aforementioned DLCs. The exponents of three DLCs are very close to each other and fall in the range 2.67-2.96. Recall that the estimated exponent of fore-aft tower base steady moment had a value of 3. Therefore, the calculated exponents of extreme moments are slightly smaller the predicted value. Moreover, for the extreme tower base moment, the exponent of DLC 1.3 is slightly smaller than that of DLC 1.1 (see the third graph of figure 9.14). The exponents of DLC 6.1 and 6.3 are roughly identical to both exponents of DLC 6.4 lifetime DELs of tower base fore-aft moment, which are discussed in the third graph of Figure 9.10.

For all three DLCs, each generated power trend line has a high *R*-squared value of 1 or slightly less, as seen on the graphs in Figure 9.16. Therefore, the power trend lines and calculated exponents are reliable. Additionally, it is possible to summarise that the extreme moments up-scale by a factor that is slightly smaller than the predicted values for steady moments.

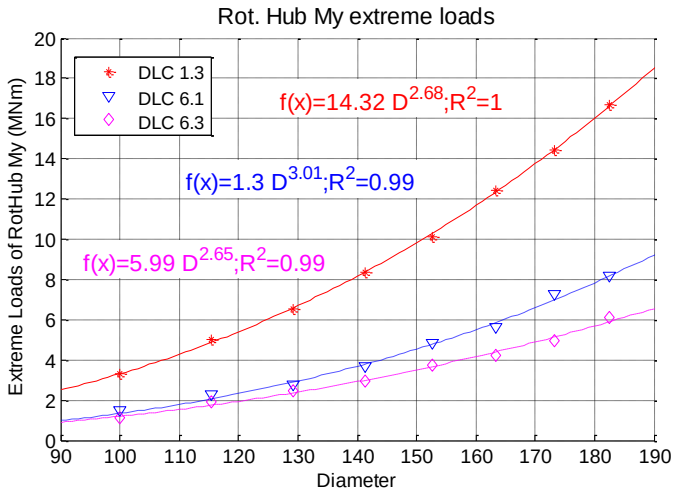

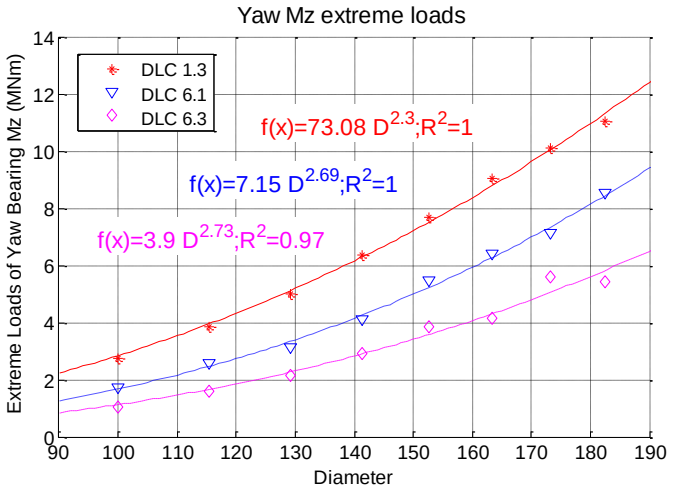

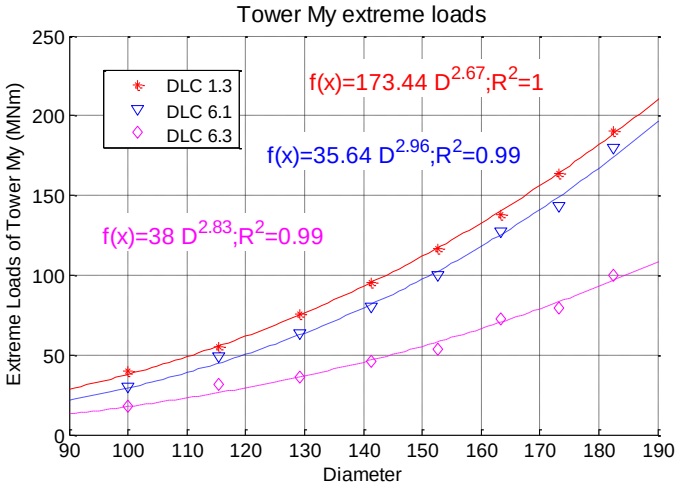

Figure 9.16: DLC 1.3, 6.1 and 6.3 extreme moments of low speed shaft, yaw bearing and for-aft base of tower.

9.6. Comparison of exponents

This section provides a comparison between calculated/generated and commercially available exponents of up-scaled wind turbine models to inspect the accuracy of up-scaling in terms of extreme loads [3], [25], [92], [93]. An overview of the scaling extreme moments for commercial data is provided in chapter 3.

Trend line exponents may be extracted from commercial data in the same way as in the analyses of scaling with similarity. Hence, they usually reflect the on-going efforts to bring technology to newer, larger designs. However, they do not in any significant way reflect the true physics of up-scaling as there are few inherent benefits of up-scaling; tooling of blades, transport and handling all become more challenging at larger scale. The more advanced technology applied to the largest designs in the industry. However, this study has focused the scaling with similarities, because it offers the clearest indication of underlying trends in loads with scale. There are of course some factors which unavoidably violate scaling with similarity. Turbulence scales and wind shear, although highly variable, are unrelated to machine scale and have their own absolute scale factors. The impact of these factors has therefore been addressed as affecting loads on turbines scaled with similarity.

This section is divided into two parts, which compare the exponents of commercial data with those of the measured/simulated data for the cases of fatigue (lifetime DELs) and extreme loads.

9.6.1. Comparison with lifetime DELs

Table 9.2 and 9.3 provide a comparison between exponents of up-scaled commercial wind turbines and the generated exponents of lifetime DELs in this study.

It can be seen form Table 9.2 and 9.3 that the calculated exponents of edge-wise blade moments for DLC 1.2 and 3.1/4.1 are 15% and 18% large, respectively, that the commercially-available coefficients. Up-scaling with similarity requires that the technology employed (materials, structural features etc.) is preserved. However, commercial companies often seek to reduce the blade mass of up-scaled wind turbines by new choices of profile and material [94], which may be a potential cause for the differences seen in this case.

The calculated exponents of the edge-wise blade root moment of DLC 6.4 (2.63) are lower than the commercially available ones (3.25) by 20%. For flap-wise blade root moment, the calculated

exponents of DLC 1.2 3.1/4.1 and 6.4 are higher by 4%, 5% and 14%, respectively than the scale coefficient of commercial data.

A comparison of low speed shaft moment reveals that compared to the commercial exponents, the calculated exponents of DLC 1.2 3.1/4.1 and 6.4 are slightly smaller by 13%, 7% and 13%, respectively.

Moments	Lifetime DELs of Wohler coefficent 4							
	Commercial data		*DLC 1.2*		*DLC 3.1/4.1*		*DLC 6.4*	
	Exponent	*R-squared*	*Exponent*	*R-squared*	*Exponent*	*R-squared*	*Exponent*	*R-squared*
Edge-wise blade root	3.25	0.88	3.61	1	3.85	1	2.63	1
Flap-wise blade root	2.86	0.94	2.85	1	2.99	0.99	3.09	1
Low speed shaft (My)	3.01	0.99	2.6	1	2.8	1	2.61	1
Yaw bearing (Mz)	4.05	0.76	2.38	1	3.71	1	2.53	1
Tower fore-aft base	2.33	0.71	1.76	0.97	3.22	1	2.77	0.98

Table 9.2: Comparison between exponents of commercial data and up-scaled models for Wohler coefficient 4.

For yaw bearing moment, the commercial exponent equals 4.05, but the *R*-squared value is 0.76, which is low to rely on the commercially-available exponent of yaw bearing moment. In the scaling with similarity method, the yaw bearing (Mz) moment scales by the cubed. The measured/calculated exponents of DLC 1.2 and 6.4 have values of around 2.5. Therefore, the calculated exponents are smaller by 40% than the commercial exponent. The exponents of DLC 3.1/4.1 have a value of around 3.65, which is lower than commercial exponent of yaw bearing moment by 9%.

Moments	Lifetime DELs of Wohler coefficent 10							
	Commercial data		*DLC 1.2*		*DLC 3.1/4.1*		*DLC 6.4*	
	Exponent	*R-squared*	*Exponent*	*R-squared*	*Exponent*	*R-squared*	*Exponent*	*R-squared*
Edge-wise blade root	3.25	0.88	3.73	1	3.85	1	2.83	1
Flap-wise blade root	2.86	0.94	2.97	1	2.95	1	3.26	1
Low speed shaft (My)	3.01	0.99	2.68	1	2.92	1	2.75	1
Yaw bearing (Mz)	4.05	0.76	2.44	1	3.58	0.99	2.63	1
Tower fore-aft base	2.33	0.71	1.93	0.99	3.17	1	2.89	1

Table 9.3: Comparison between exponents of commercial data and up-scaled models for Wohler coefficient 10.

The commercial exponent of tower fare-aft base moment has a value of 2.33 as shown in Tables 9.2 and 9.3. The *R*-squared value of commercial tower fare-aft base moment is 0.71, which is not very high. The low *R*-squared value of commercial tower fore-aft base moment is a result of differences in environmental and terrain conditions between sites as mentioned in chapter 3. Nonetheless, the calculated exponents of both Wohler coefficients DLC 1.2 are smaller by 26%

and 17% than the scale coefficient of commercial data. It is a result of the implementation of sophisticated controller in the up-scaled models. The calculated exponents of DLC 3.1/4.1 and 6.4 are approximately 37% and 22% larger, respectively than the commercial scale coefficient for tower base fore-aft extreme moment. Probably, this difference is a penalty of the preserved technology at the up-scaled models by similarity, which is the assumption of the similarity scaling, and the implementation of simple PI controller for DLC 3.1/4.1 and 6.4 compared to commercial wind turbines with the latest optimisations.

9.6.2. Comparison with extreme loads

In this subsection, the exponents for the commercial wind turbines are compared with those obtained in this study. Table 9.4 highlights the exponents and *R*-squared values for five extreme moments.

In terms of DLC 1.1 the calculated scale exponents of edge-wise and flap-wise blade root extreme moments are approximately similar to the commercial scale coefficients, which are 3.25 and 2.86 respectively. The calculated DLC 1.1 exponents of edge-wise and flap-wise moments are smaller by 7% than the commercial scale coefficients. The DLC 1.1 low speed extreme moment scales by a factor of 2.68, which is 11% smaller than the exponent of commercial wind turbines. For DLC 1.1, while the calculated exponent of yaw bearing extreme moment (Mz) is significant smaller (34%) than the value of commercial exponent, the calculated exponent of tower base fore-aft extreme moment 21% larger.

For edge-wise extreme moments, the generated exponent of DLC 1.3 is larger by 6 % than the commercial scale coefficient, but the exponents of DLC 6.1 and 6.3 are smaller by 26% and 28%, respectively.

A comparison of the generated and commercial exponents of flap-wise blade root extreme moment for the three DLCs shows that the up-scaled exponents are 3% and 19% larger for DLC 1.3 and DLC 6.3, respectively. However, there are no differences for DLC 6.1.

A comparison of the generated and commercial (3.01) exponents of low speed shaft extreme moment demonstrates that the up-scaled exponents of DLC 1.3 and 6.3 are 3% and 19% smaller, respectively. For DLC 6.1 there are no differences.

The comparison between the calculated and commercial exponents of yaw bearing extreme moment indicates that the estimated exponents of DLCs 1.3, 6.1 and 6.3 are smaller by 43%, 34% and 33%, respectively than their commercial counterparts.

Moments	Extreme loads									
	Commercial data		*DLC 1.1*		*DLC 1.3*		*DLC 6.1*		*DLC 6.4*	
	Exponent	*R-squared*	*Exponent*	*R-squared*	*Exponent*	*R-squared*	*Exponent*	*R-squared*	*Exponent*	*R-squared*
Edge-wise blade root	3.25	0.88	3.02	0.97	3.43	1	2.4	0.98	2.33	0.96
Flap-wise blade root	2.86	0.94	2.65	0.99	2.94	1	2.85	0.99	3.41	0.93
Low speed shaft (My)	3.01	0.99	2.68	1	2.68	1	3.01	0.99	2.65	0.99
Yaw bearing (Mz)	4.05	0.76	2.68	0.99	2.3	1	2.69	1	2.73	0.97
Tower fore-aft base	2.33	0.71	2.82	0.96	2.67	1	2.96	0.99	2.83	0.99

Table 9.4: Comparison between exponents of commercial data and extreme moments of the up-scaled models.

For the tower fore-aft base extreme moment the obtained exponent of DLC 1.3, 6.1 and 6.3 are larger by 15%, 27% and 21%, respectively than the commercial one. However, the *R*-squared value of commercial exponent is low, 0.71, to rely on. This is a consequence of the different wind turbine design due to dissimilar environmental and terrain conditions of sites among the commercial machines. Nonetheless the low value of *R*-squared value for the commercial exponent, the difference between the commercial and generated coefficients can be due to underlying assumption in similarity up-scaling, which result in the preservation the technologies of reference model in the up-scaled models, as stated in [3], [6], [7].

9.7. Scale impact on turbulence

It is not a secret that turbulence has an adverse effect on wind turbine loads, especially fatigue loads as stated in [71], [95]. Hence, this section tries to investigate the impact of turbulence on up-scaled wind turbines. It is generally believed that the different-sized wind turbines respond differently to same strength level turbulence in terms of turbulence intensity and wind class [5] because the wind spectrum remains same. The spectrum of up-scaled wind turbines shifts to towards to lower frequency as the angular velocity of rotor decreases with the up-scaling according the assumption of the up-scaling with similarity [3], [6], [7]. The structural modes of blades decreased as a result of a reduction in blade natural frequency due to up-scaling as illustrated by equation 9.4. Therefore, the load outputs of up-scaled models have to be compared with the output of the reference model. Obviously, the largest up-scaled wind turbine models

have larger loads compared to smaller up-scaled wind turbine. Therefore, it is necessary to normalise the output data of up-scaled wind turbines to enable a relevant comparison with the output of the reference model. The normalisation procedure needs to include the effect of up-scaling on dimensions and wind shear, which up-scale with wind turbine size as discussed in section 3.1.6. Equation 9.5 represents the procedure of normalisation, which includes the effect of up-scaling and wind shear for flap-wise blade root moment the output data of up-scaled wind turbines.

$$M_{flp\,Norm} = M_{flp} * \left(\frac{D_o}{D}\right)^{3+2\alpha} \qquad 9.5$$

Where, D_o is the diameter of reference wind turbine, D is the diameter of up-scaled wind turbine and α is an exponent of wind shear power law.

Figure 9.17 depicts normalised PSD and cumulative PSD of blade root flap-wise moment for 3, 6 and 10 MW wind turbine models at a wind speed of 14 m/s. Figure 9.17 includes two pairs of horizontal graphs; the first pair corresponds to normalised PSD and cumulative PSD, the second pair relates to the zoom of the first pair of graphs. The graphs of normalised PSD show that while the peaks of *1P* of up-scaled models are wider than those of the reference models, the harmonics (*2P, 3P* and etc.) and structural mode peaks of the up-scaled models are lower and narrower. The cumulative PSD graphs show that the loading is higher in the reference model than the normalised up-scaled models. Therefore, the up-scaled models are less sensitive to turbulence than the reference model.

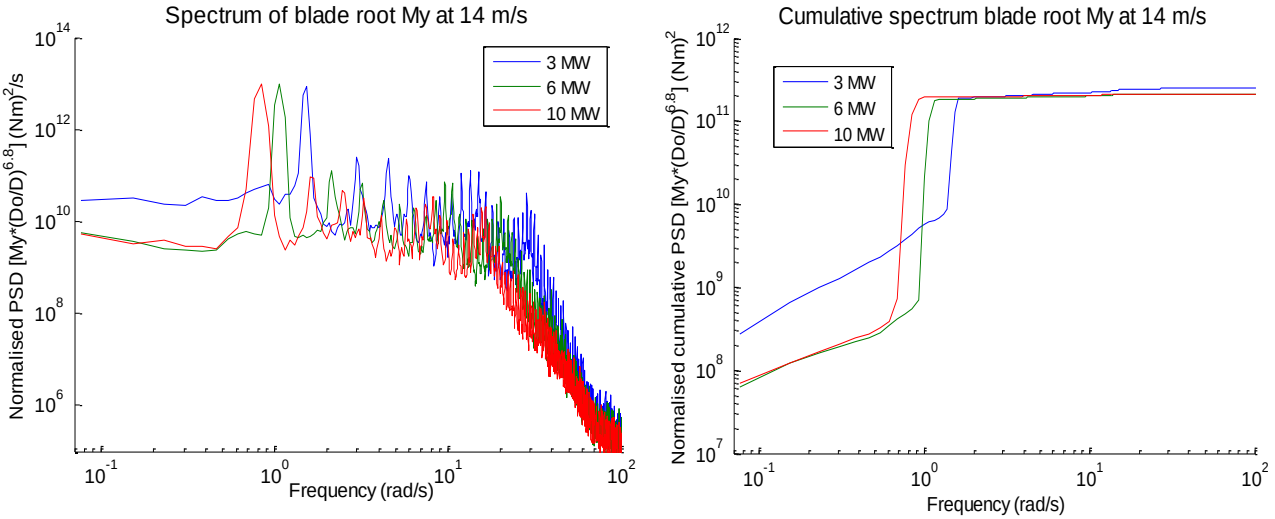

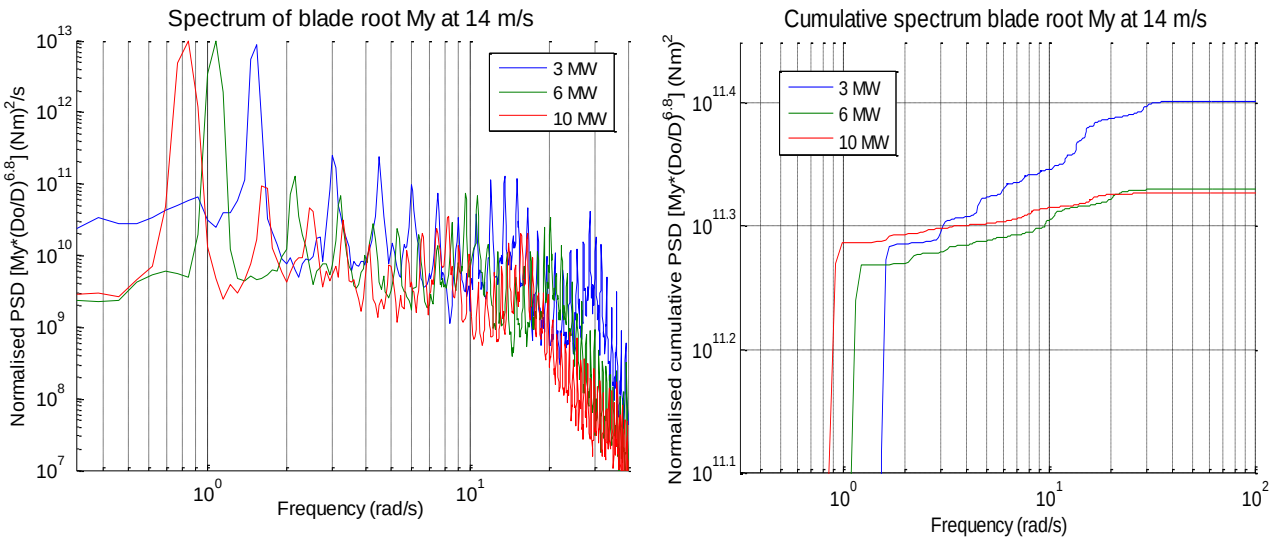

Figure 9.17: Normalised PSD and cumulative PSD of blade root flap-wise moment of 3MW, 6MW and 10MW models at 14 m/s

However, the up-scaled wind turbines experience significantly more unbalance wind distribution along rotor swept area. The uneven aerodynamic of the rotor is mainly a result of turbulence, tower shadow and wind shear. The uneven aerodynamic load distribution of rotor can be mitigated by increasing damping [96]. Figure 9.18 depicts the aerodynamic damping of a blade for both the reference and the up-scaled wind turbine models. It can be noticed that the aerodynamic damping of each blade increased with the size of turbine. Hence, it can be concluded that the reason for reduction in turbulence sensitivity in up-scaled models is increased rotor inertia and aerodynamic damping.

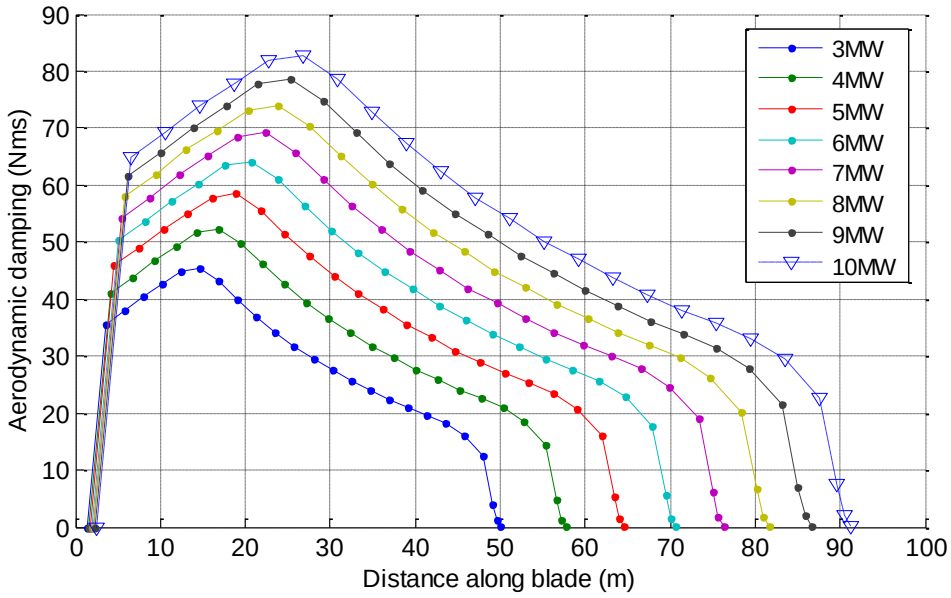

Figure 9.18: Blade aerodynamic damping for the reference and up-scaled wind turbines models at 16 m/s average wind speed.

9.7.1. Turbulence impact on fatigue loads

The uneven aerodynamic load distribution over the swept area of rotor affects the dynamic fluctuations of wind turbine, which are related to fatigue loads [97]. Hence, fatigue loads depend mainly on turbulence, wind shear and tower shadows. This section provides an overview of scale impact on turbulence fatigue loads, which is presented in terms of lifetime DELs, for the blade root flap-wise, low speed shaft and tower base fore-aft moments. According to IEC standards [5], in this study the fatigue loads (lifetime DELs) are examined for DLC 1.2, 3.1, 4.1 and 6.4, which correspond to power production range, number of start-ups, number of shut-downs and idling respectively. DLC 3.1 and 4.1 relate to steady wind condition without turbulence. Thus, these two DLCs are excluded from the examination of the scale impact of turbulence. Figure 9.19 presents the impact of scale on turbulence in terms of fatigue loads, which are represented by DLC 1.2 and 6.4, for blade root flap-wise, low speed shaft and tower base fore-aft moments. The lifetime DELs of the up-scaled wind turbines models are normalised using equation 9.5. Figure 9.19 is composed of six graphs, where the left and right columns represent DLCs 1.2 and 6.4, respectively, while the rows each represent one of the three above-mentioned moments.

It can be seen from the first row that fatigue loads grow smaller as wind turbine gets larger especially at the normal power production conditions, which are characterised by DLC 1.2,

because the exponents of DLC 1.2 are half those of DLC 6.4. Moreover, the reduction is more significant for Wohler coefficient 4 than for Wohler coefficient 10 as seen from a comparison of the exponents of Wohler coefficient 4 and 10.

The second pair of graphs depicts behaviour similar to that seen on the first pair of graphs. Nevertheless, DLC 1.2 exponents of low speed shaft moment are roughly 1/3 or 1/4 those of the exponents of blade root flap-wise moment for DLC 1.2. Additionally, the exponents of DLC 6.3 are around 20% larger than the exponents of low-speed shaft moment for DLC 1.2.

The third row demonstrates that the reduction in fatigue loads is more significant for tower base fore-aft moment than for blade root flap-wise and low speed shaft moments. For lifetime DLC 1.2 the calculated absolute value of exponents is higher by two times for Wohler coefficient 4 and three times for Wohler coefficient 10 than exponents of blade root flap-wise moment in lifetime DLC 1.2. The values of tower moment exponents of DLC 6.4 are similar to the exponents values of low speed shaft for DLC 6.4.

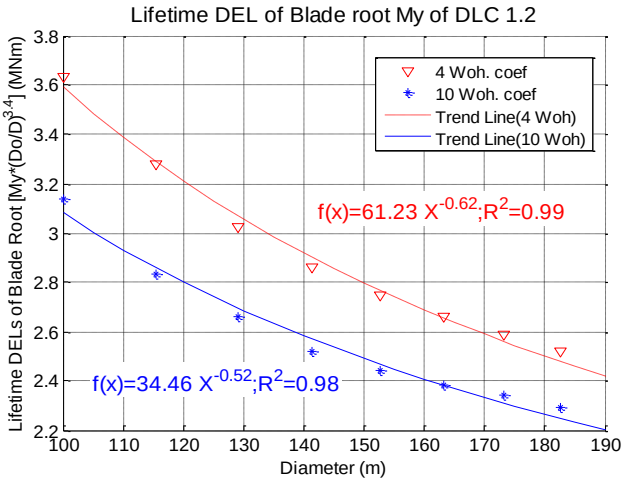

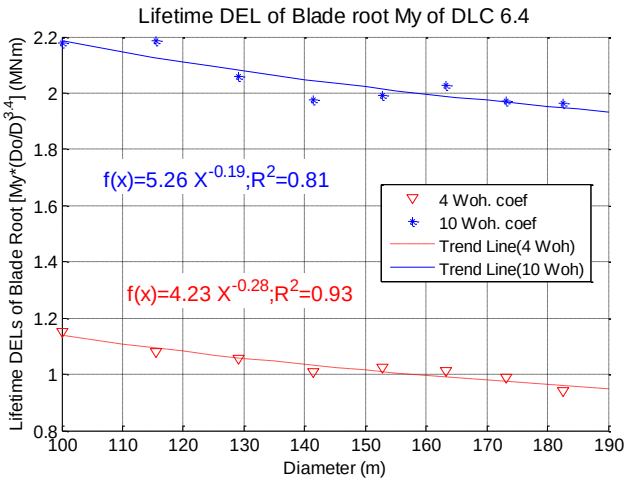

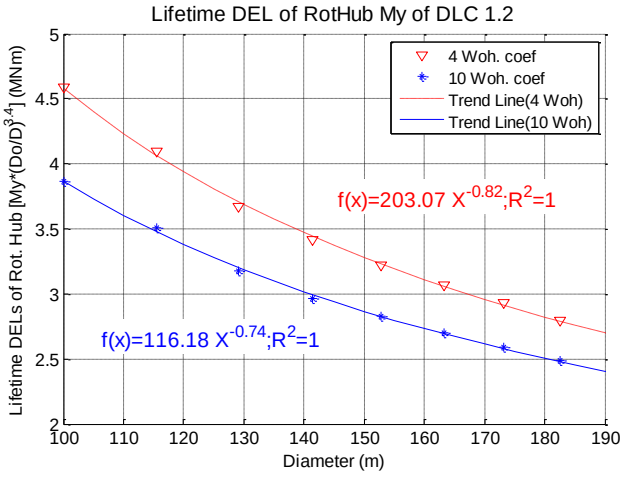

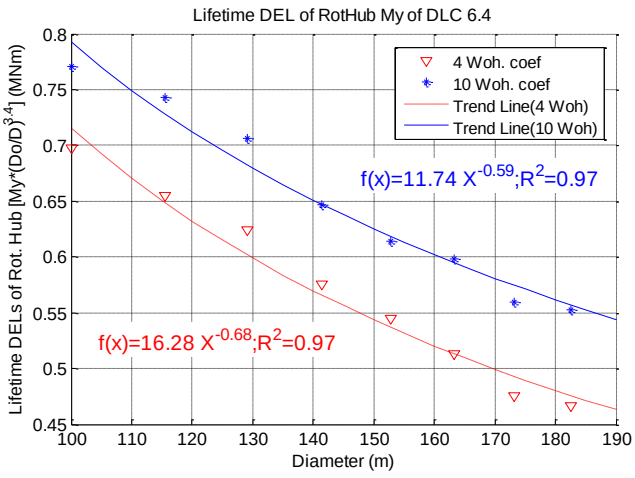

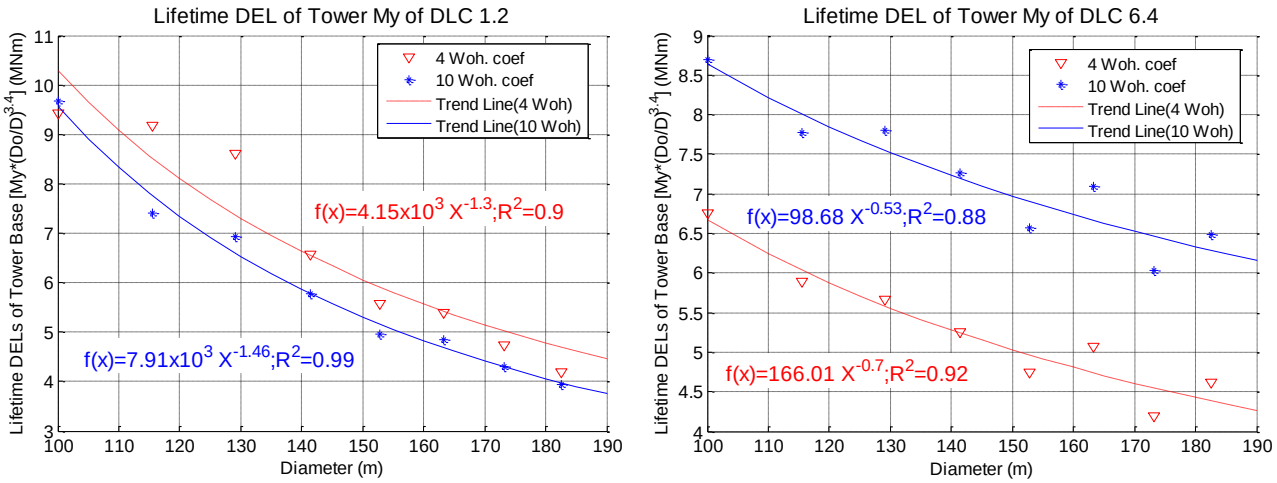

Figure 9.19: Scale impact on turbulence in terms of lifetime DLC 1.2 and 6.4 for blade root edge-wise, low speed shaft and tower base fore-aft moments.

9.8. Shear effect in the up-scaling

This section reviews the effect of wind shear on up-scaled wind turbines. According to the principles of scaling with similarity, the diameter and hub height of the reference wind turbine model scales up with turbine size. The up-scaled wind turbine experiences a different mean wind speed compared to the reference model as shown by equation 9.6.

$$V(z) = V_{hub}\left(\frac{Z}{Z_{hub}}\right)^{0.2} \qquad 9.6$$

Furthermore, for the up-scaled wind turbine models, hub height changes linearly with a diameter of wind turbine. Hence, equation 9.6 can be rewritten in terms of diameter as demonstrated in equation 9.7.

$$V(z) = V_{hub}\left(\frac{D}{D_o}\right)^{0.2} = V_{hub} * Vf \qquad 9.7$$

$Vf\ (= [D/D_o]^{0.2})$ is the velocity modification factor due to the wind shear and up-scaling.

The differences in the velocity modification factor between the up-scaled model and the reference wind turbine model are plotted in Figure 9.20.

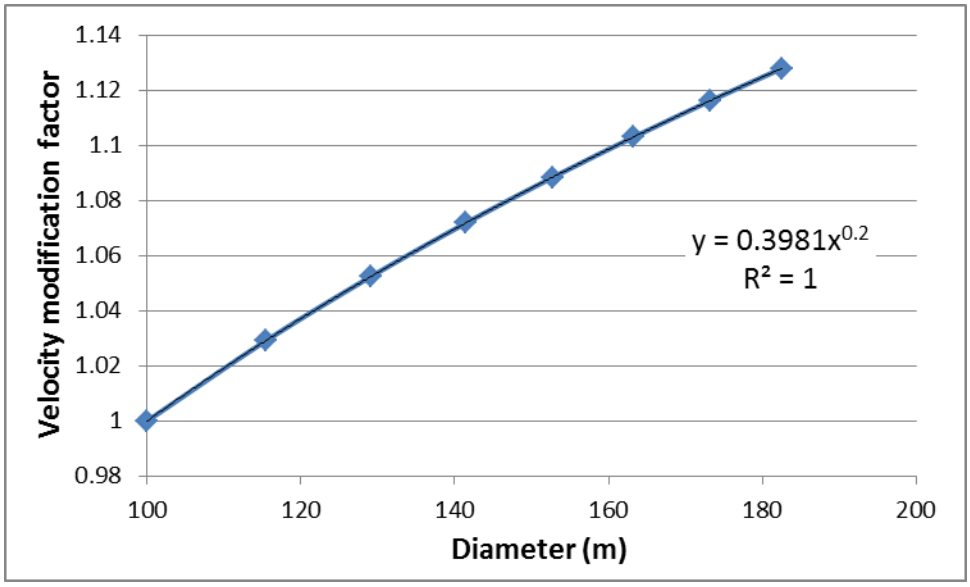

Figure 9.20: Changes in velocity modification factor with up-scaling

It is worth mentioning that the same wind flow acts differently on the reference and up-scaled wind turbine models due to up-scaling and wind shear. The next step is to look at the effect of wind shear on steady loads for up-scaled wind turbine. Therefore, Figure 9.21 shows the changes in steady blade root flap-wise moment with and without wind shear at a mean wind speed of 8 m/s. The steady blade root flap-wise moment was calculated by using equation 3.5. The calculated exponent of steady blade root flap-wise moment with the wind shear is 3.4, which matches the predicted value calculated using equation 3.6 completely. Figure 9.21 shows that the wind shear has to be taken into account in the up-scaling.

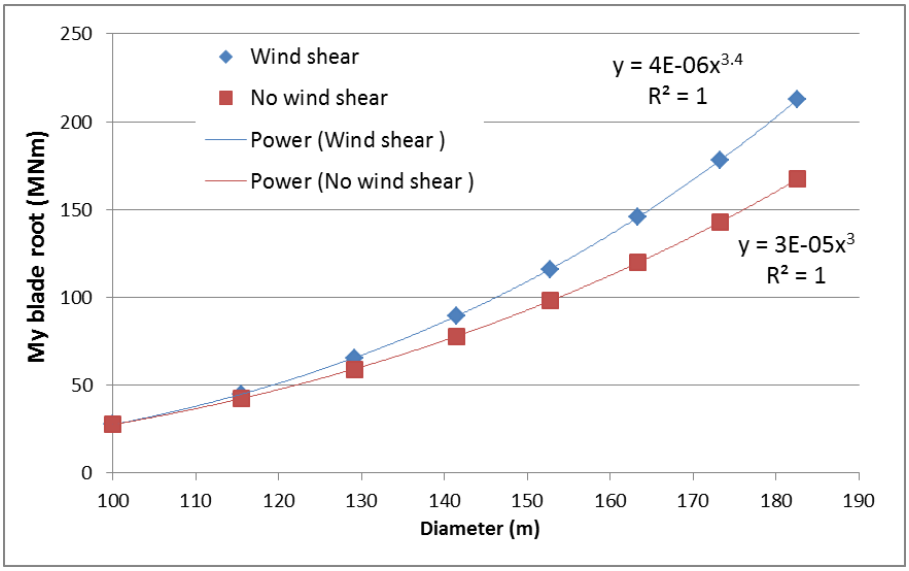

Figure 9.21: The up-scaling of steady blade root flap-wise moment with wind shear at a mean wind speed of 8 m/s

The next step is to examine the effect of wind shear on fatigue loads in terms of lifetime DELs. Figure 9.22 and 9.23 display lifetime DELs with and without wind shear for the four important moments evaluated in this work. Figure 9.22 presents a comparison of lifetime DELs both with (left column) and without (right column) wind shear for edge-wise blade root (first row) and yaw bearing moments (second row). It can be seen from Figure 9.22 that the edge-wise blade root and yaw bearing moment exponent coefficients of lifetime DELs with and without the wind shear are almost identical. These is because these moments mainly do not depend mainly on aerodynamic loads; the edge-wise blade root loads are a function of blade self-weight.

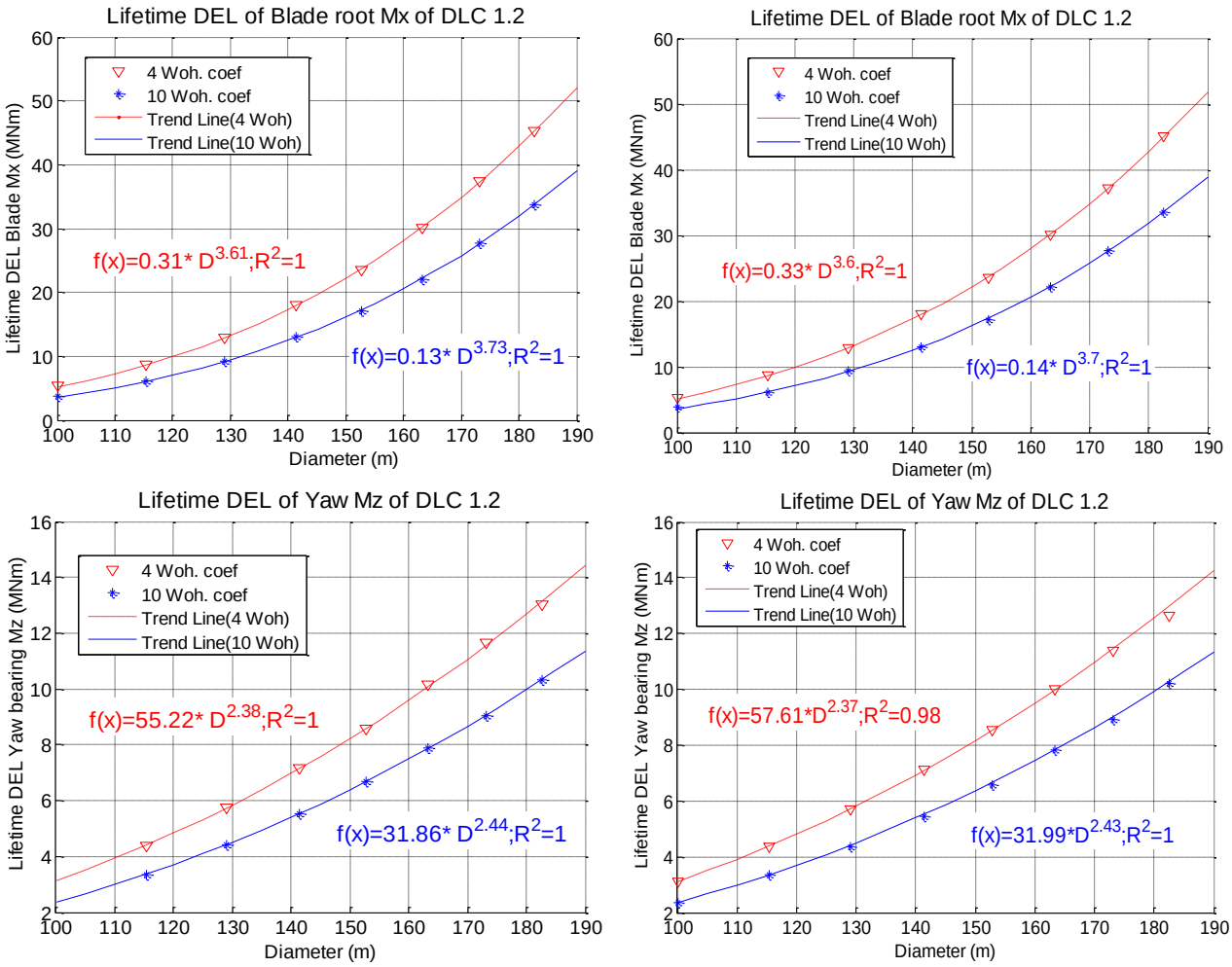

Figure 9.22: Comparison of edge-wise blade root and yaw bearing moments for lifetime DELs with and without the wind shear. Note the wind shear is included on the left column but excluded on the right one.

Figure 9.23 presents a comparison of flap-wise blade root (first row) and low speed shaft (second row) moments for lifetime DELs both with (left column) and without (right column) wind shear. It is clear from the figure that while a noticeable difference does exist for both moments, it is, similar to the case of steady loads presented in Figure 9.21, not very significant. Fatigue loads are

more sensitive to turbulence than to wind shear. Therefore, turbulence plays a crucial role determining the extent of fatigue damage in wind turbine components as stated in [7].

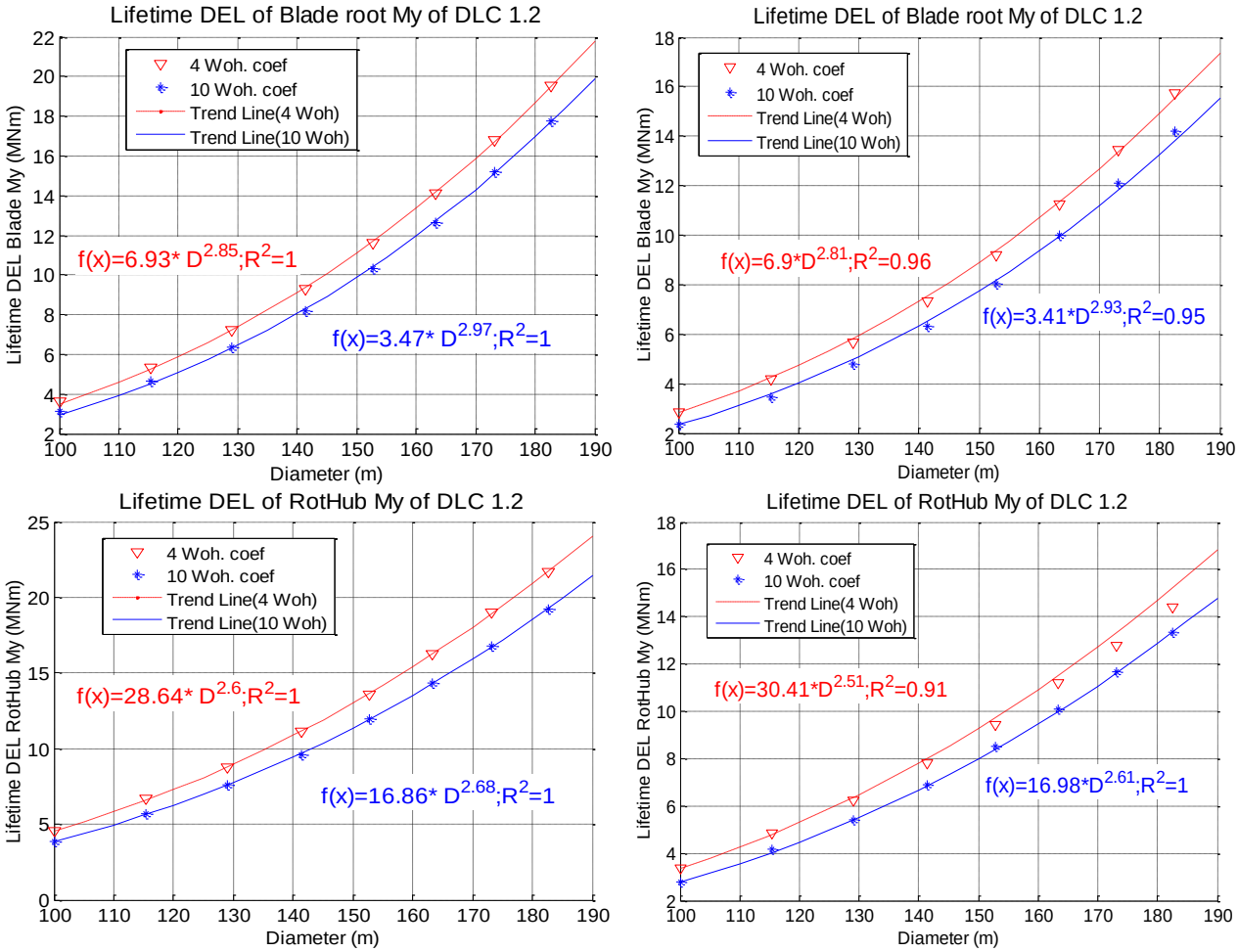

Figure 9.23: Comparison of flap-wise blade root and low speed shaft moments for lifetime DELs with and without wind shear. Note the wind shear is included on the left column but excluded on the right one.

9.9. Summary and discussion

This chapter presents and discusses the changes in extreme and fatigue loads (lifetime DELs) caused by the up-scaling of a reference wind turbine model with the similarity method. The seven up-scaled models were created in such a way as to maintain the power density of the reference model. Up-scaling requires adjusting the controller as the properties (e.g. rotor speed, natural frequencies blades and tower and so on) of up-scaled models are different compared to the reference model. Thus, a simple PI controller was introduced to below rated region and tuned for each up-scaled wind turbine. However, the original controller of the base model was used for the

above rated region in order to better manage the pitch activity of the blades, which moderates tower loads, as the original controller included a tower feedback loop.

The modification of up-scaled wind turbine models was validated using steady state analysis. The original values for the tip speed and the power coefficient of the reference model were preserved in the up-scaled models in order to preserve the original aerodynamics. Additionally, the changes in steady loads were compared to changes in predicted loads. The comparisons showed that the steady loads scaled up by a value that could be predicted by the method of up-scaling with similarity. Hence, this demonstrated that the up-scaling procedure was performed correctly.

Afterwards the spectral analysis was applied to inspect the behaviour of up-scaled model at dynamic conditions. The main focus of the analysis was to ensure that the modified frequency of structural modes of up-scaled models did not coincide with the frequency of rotor speed harmonics and that the controller for the modified models worked correctly. The spectral analysis did not reveal any unexpected behaviour in up-scaled wind turbines.

Fatigue load analysis was performed by using three design load cases that were evaluated in terms of lifetime damage equivalent loads based on IEC standards. The three design load cases were as follows: wind turbine operational conditions of normal power production, summation of start-ups and shut downs, and idling operational condition. Trend-lines were drawn using calculated loads to see how fatigue loads scaled up in order to compare with predicted up-scaling coefficients for steady loads, which were estimated using the up-scaling with similarity method. In most cases the calculated exponents of trend lines were slightly smaller than the predicted values, in particular for the moments of edge-wise and flap-wise blade root, low speed shaft, yaw bearing and fore-aft tower base (DLC 3.1/4.1 and DLC 6.4). In a few cases for DLC 6.4, the calculated exponents of flap-wise blade root and tower base fore-aft base moments were slightly larger than the predicted ones. The relatively small difference between the calculated and predicted values is the result of a variation in the magnitude and direction of vectors generated by turbulence and wind shear at wind flow. However, the coefficients of the calculated fore–aft tower base moment for DLC 1.2 as well as those for the calculated edge-wise blade root moment for DLC 6.4 were significantly smaller than the predicted values. This is possibly a consequence of the choice of controller for above rated region, especially for DLC 1.2 of tower base fore-aft moment as the controller includes a tower feedback loop [88], [89], which significantly minimises tower loads.

Four design load cases were implemented to investigate changes of extreme loads based on IEC standards. The first pair of DLCs corresponded to wind turbine power production with normal and extreme turbulence. The second pair represented the idling condition at extreme wind with ±8 and 20 degrees of yaw misalignment, respectively. The extreme moments of flap-wise blade root, low speed shaft, yaw bearing and fore-aft tower base scale up by the values that are close to, or slightly smaller than, the predicted values of steady moments estimated by the up-scaling with similarity method. The calculated up-scale exponents of edge-wise blade root extreme moments (DLC 1.1, 6.1 and 6.3) were significant lower than the predicted ones. There was only one case, that of the extreme blade root flap-wise moment for DLC 6.3, where the predicted up-scaling coefficient was smaller than the calculated one.

The five different moments of the wind turbine were investigated for changes in extreme and fatigue (Lifetime DELs) loads as a consequence of up-scaling with similarity. Four different design load cases were used to perform the calculations for extreme and fatigue loads. This yielded a total of 40 cases out of which 20 represented extreme load and the remainder corresponded to fatigue loads. One tenth of the calculated extreme and fatigue loads scales up by the scale factor which is larger around by 10 % of the predicted values of steady loads estimated by the up-scaling with similarity. A quarter of the calculated extreme and fatigue loads scales up by least 30% smaller than the predicted values. However, in a majority of cases, the predicted co-efficient did not deviated from their estimated counterparts by more than 10%. Additionally, the calculated exponents of the generated trends were compared with the exponent of commercial extreme moments, which represent the real commercial wind turbine on sites. It was discovered that the obtained exponents of extreme moments were similar ($\pm\,10\%$) to the commercial exponents, especially in the case of flap-wise, edge-wise blade root, low speed shaft and tower base fore-aft moments in the power production range, which is exemplified by DLCs 1.1 and 1.3. The exponents of idling operational conditions (DLC 6.1 and 6.3) are less accurate; their values fall within $\pm\,30\%$ of the exponents of commercial wind turbines. The values of the exponents of lifetime DELs are within $\pm\,15\%$ of the commercial exponents for blade root, low speed and tower base fore-aft moments for DLC 1.2, which characterises normal power production conditions. There is a significant difference between commercial and calculated exponents of yaw or tower torsional moment for extreme and lifetime DELs. As the commercial data for these cases is from 2007, it may be obsolete.

This research has demonstrated that while scaling with similarity can be used to obtain extreme and fatigue loads of up-scaled units, they scale somewhat less well than steady state loads.

Hence, the calculated values of up-scaled extreme and fatigue loads will be conservative. The power trend equations of extreme and fatigue loads, which were generated in this chapter, can give more a more accurate estimation than the method of scaling with similarity. The generated power trend equations are valuable as a check on loads generated by detailed modelling. Any differences identified thus would provide stimuli for investigation of underlying reasons, while very large differences may indicate an error.

Section 9.7 examined the sensitivity of the up-scaled wind turbines to the turbulence in terms of loads. The examination required the normalisation of wind turbine loads in order to enable a comparison between reference and up-scaled models. As the size of the up-scaled wind turbines increased, the normalised fatigue loads grew smaller owing to a decrease in turbulence sensitivity with size. The decrease of turbulence sensitivity is a result of the increase of rotor inertia of up-scaled wind turbines.

Section 9.8 investigated the effect of wind shear on up-scaling fatigue loads. Gravity driven loads, e.g. edge-wise blade root moments, were found to be independent of wind shear, which had an effect on loads that were mainly a function of wind flow, e.g. flap-wise blade, overturning low speed shaft and tower fore-aft base moments. However, the impact of wind shear on fatigue loads is less significant that effect on steady state loads. For flap-wise blade and low-speed shaft moments of lifetime DELs, the difference between the exponents of power trend line equation with and without the wind shear was 0.1. For flap-wise blade root moment, the same figure was 0.4.

Up-scaling with strict similarity has not been evident in commercial designs. This is due to on-going technology development being applied to the newest, largest turbines. However up-scaling with similarity is the basis of understanding load trends and the design changes that may be deliverable. Moreover, as technology matures and the latest development is applied to smaller turbine sizes there will be a return closer to similarity.

10. Conclusion and Recommendations

This chapter is the final part of the thesis, which summarises the work done throughout this research and provides some ideas about work that can be performed in the future. This chapter is divided into several sections. The first section, section 10.1, provides a short summary of the research. A review of the results is then provided in section 10.2. Section 10.3 highlights the limitations of the research. Then the chapter is concluded by section 10.4, which proposes future work building on this research.

10.1. Summary of thesis

At the moment there is lack of systematic parameterised and quantitative characterisation of trends in terms of wind turbine loads. This leads to an absence of systematic understanding of the loading trends and their impact. The main goal of this research is to fill this gap by investigating the changes of extreme and fatigue loads, which are considered as the design driving loads for wind turbines [2], due to applied modifications. The key parameters, which affect the extreme and fatigue loads, are structural properties of the blades, rotor solidity and scaling. Therefore, the main questions of this study were:

- *How do fatigue and extreme loads change due to modification of certain parameters?*

- *Is it possible to develop fatigue and extreme load algorithms using the acquired data from the sensitivity analysis that are a function of the modified parameters?*

This research has demonstrated that the fatigue and extreme loads are sensitive to the modifications of structural properties of blades, rotor solidity and scaling. Additionally, this study proved the possibility to develop an algorithm for fatigue and extreme loads as a function of the modified parameters. These developed algorithms, which predict extreme and fatigue loads due to the blades, rotor solidity and scaling modifications of the wind turbine, are shown in section 10.2.

The thesis has been divided into two parts. The first part provides the overview of theory, methods, software tools and validation of the reference model for this research. The first part of thesis is covered by the first six chapters. The brief description of the first six chapters is below:

1. An introduction, which highlights the key areas of investigation for this study.
2. Provides an overview of the different types of loads and what causes them. It also categorises loads into different groups.
3. Reviews the features of scaling with similarity and highlights the scaling of existing commercial data.
4. Looks at different numerical methods and software to perform aerodynamic and structural calculations for wind turbines, in order to select the primary software to implement the calculations for the research.
5. Is an overview of several wind turbines to select the reference wind turbine for this study.
6. Is the last chapter of the first part, and highlights the methodology of the loads investigation and the different types of calculations, which are implemented in this study. Moreover, the second part of this chapter has an overview of wind flow modelling.

The second part of the thesis consists of the following three chapters, which demonstrate the developed algorithm from the output data, which are based on the modifications to the reference wind turbine model, in order to estimate how the loads, vary for the perspective wind turbines. A brief description of these three chapters is below:

7. This chapter examines the impact of blade structural parameters on the blade root loads.
8. The second of the result chapters investigates the effect of rotor solidity on the aerodynamic damping, extreme and fatigue loads.
9. In the last chapter the scaling impact is inspected, where the reference model is up-scaled by employing up-scaling with similarity. This is done to see how the extreme and fatigue loads up-scale, and to compare with the predicted up-scaling coefficients of loads, which were estimated by the up-scaling with similarity, and the commercial up-scaled coefficients, which were calculated from the real turbines. Additionally, this chapter investigates the impact of up-scaling on turbulence, which demonstrates the sensitivity of up-scaled wind turbines to turbulence. The effect of wind shear on up-scaling is also included in this chapter.

10.2. Summary of results

As mentioned in section 10.1, chapters 7, 8 and 9 look at the output data of modified wind turbine models to generate the trends of loads in order to develop an algorithm, which can systematically parameterise and quantify extreme and fatigue loads. Moreover, these chapters also include additional goals to the main ones. Therefore, this section highlights the performed work and achieved results in this study.

- ***Blade structural properties (Chapter 7)***

This chapter investigates the effect of blade structural properties on the fatigue and extreme loads.

The main goal of this chapter was to answer the main two question of this study, which were highlighted in section 10.1. There were four different modifications to the blade structural properties: the 1st scenario relates to blade mass, 2nd – blade mass and stiffness, 3rd – scaling with similarity and 4th – dimensions, stiffness and blade mass (maintaining the original frequency). The developed algorithms of these four scenarios for edge-wise and flap-wise blade root bending moments are shown in Table 10.1 and Table 10.2. The key achievements of chapter 7 are highlighted below

- The changes of natural frequencies do not have a negative effect on the wind turbine.
- The lifetime DELs demonstrate a consistent pattern among all the scenarios, especially for the scenarios with preserved natural frequency.
- The lifetime DELs of the deterministic part of the edge-wise blade is mainly a function of gravity loads.
- The possibility to generate trends for fatigue and extreme loads was proved.

Design load case	Scenarios	Wohler Coefficients	
		4	***10***
1.2	***1***	$f(x) = 5 * 10^6 x^{0.55};\ R^2 = 0.95$	$f(x) = 4 * 10^6 x^{0.44};\ R^2 = 0.88$
	2	$f(x) = 5 * 10^6 x^{0.9};\ R^2 = 1$	$f(x) = 4 * 10^6 x^{0.89};\ R^2 = 1$
	3	$f(x) = 5 * 10^6 x^{1.12};\ R^2 = 0.98$	$f(x) = 4 * 10^6 x^{0.94};\ R^2 = 0.95$
	4	$f(x) = 5 * 10^6 x^{1.4};\ R^2 = 0.95$	$f(x) = 4 * 10^6 x^{1.33};\ R^2 = 0.97$
3.1/4.1	***1***	$f(x) = 10 * 10^5 x^{0.9};\ R^2 = 1$	$f(x) = 2 * 10^6 x^{0.55};\ R^2 = 0.96$
	2	$f(x) = 10 * 10^5 x^{0.94};\ R^2 = 1$	$f(x) = 2 * 10^6 x^{0.7};\ R^2 = 1$
	3	$f(x) = 10 * 10^5 x^{1.58};\ R^2 = 1$	$f(x) = 2 * 10^6 x^{1.33};\ R^2 = 1$
	4	$f(x) = 10 * 10^5 x^{1.59};\ R^2 = 1$	$f(x) = 2 * 10^6 x^{1.38};\ R^2 = 1$
6.4	***1***	$f(x) = 6 * 10^5 x^{0.32};\ R^2 = 0.97$	$f(x) = 6 * 10^5 x^{0.37};\ R^2 = 0.97$
	2	$f(x) = 6 * 10^5 x^{0.24};\ R^2 = 0.99$	$f(x) = 6 * 10^5 x^{0.22};\ R^2 = 0.95$
	3	$f(x) = 6 * 10^5 x^{1.07};\ R^2 = 0.99$	$f(x) = 6 * 10^5 x^{1.12};\ R^2 = 0.99$
	4	$f(x) = 6 * 10^5 x^{1.01};\ R^2 = 1$	$f(x) = 6 * 10^5 x^{1.01};\ R^2 = 1$

Table 10.1: Power law algorithms (blade structural properties) of edge-wise blade root moment for DLC 1.2, 3.1/4.1 and 6.4. Scenarios: 1-Blade mass, 2-Blade mass and stiffness , 3-Scaling with similarities and 4-Dimension, mass and stiffness of blade (maintaining the original natural frequency).

Design load case	Scenarios	Wohler Coefficients	
		4	***10***
1.2	***1***	$f(x) = 4 * 10^6 x^{0.16};\ R^2 = 0.98$	$f(x) = 3 * 10^6 x^{0.14};\ R^2 = 0.99$
	2	$f(x) = 4 * 10^6 x^{0.31};\ R^2 = 1$	$f(x) = 3 * 10^6 x^{0.29};\ R^2 = 1$
	3	$f(x) = 4 * 10^6 x^{1.34};\ R^2 = 1$	$f(x) = 3 * 10^6 x^{1.28};\ R^2 = 1$
	4	$f(x) = 4 * 10^6 x^{1.52};\ R^2 = 1$	$f(x) = 3 * 10^6 x^{1.46};\ R^2 = 1$
3.1/4.1	***1***	$f(x) = 10 * 10^5 x^{-0.01};\ R^2 = 0.25$	$f(x) = 3 * 10^6 x^{-0.03};\ R^2 = 0.37$
	2	$f(x) = 10 * 10^5 x^{0.03};\ R^2 = 0.87$	$f(x) = 3 * 10^6 x^{0.01};\ R^2 = 0.01$
	3	$f(x) = 10 * 10^5 x^{0.93};\ R^2 = 0.94$	$f(x) = 3 * 10^6 x^{0.88};\ R^2 = 0.9$
	4	$f(x) = 10 * 10^5 x^{0.99};\ R^2 = 0.94$	$f(x) = 3 * 10^6 x^{0.94};\ R^2 = 0.9$
6.4	***1***	$f(x) = 1 * 10^6 x^{0.32};\ R^2 = 0.99$	$f(x) = 2 * 10^6 x^{0.19};\ R^2 = 0.98$
	2	$f(x) = 1 * 10^6 x^{0.37};\ R^2 = 0.99$	$f(x) = 2 * 10^6 x^{0.25};\ R^2 = 0.98$
	3	$f(x) = 1 * 10^6 x^{1.02};\ R^2 = 1$	$f(x) = 2 * 10^6 x^{1.05};\ R^2 = 1$
	4	$f(x) = 1 * 10^6 x^{1.07};\ R^2 = 1$	$f(x) = 2 * 10^6 x^{1.1};\ R^2 = 1$

Table 10.2: Power law algorithms (blade structural properties) of flap-wise blade root moment for DLC 1.2, 3.1/4.1 and 6.4. Scenarios: 1-Blade mass, 2-Blade mass and stiffness, 3-Scaling with similarities and 4-Dimension, mass and stiffness of blade (maintaining the original natural frequency).

- ***Effect of rotor solidity (Chapter 8)***

This chapter investigates the impact of rotor solidity modifications on extreme and fatigue loads. In this chapter the two ways of changing the rotor solidity were considered. The first way is based on the modification of TSR or tip speed and chord length of aerofoils. The second method maintains the original TSR by varying the chord length and using aerofoils with a different design lift coefficient. Table 10.3 and Table 10.4 depict the developed algorithms of the rotor solidity effect for fatigue loads. The algorithms for extreme loads are displayed in Table 10.5 and Table 10.6.

Design load case	Moment	Wohler Coefficients	
		4	***10***
1.2	***Edge-wise blade root***	$f(x) = 5 * 10^6 x^{2.13};\ R^2 = 0.95$	$f(x) = 4 * 10^6 x^{2.13};\ R^2 = 0.92$
3.1/4.1		$f(x) = 10 * 10^5 x^{1.34};\ R^2 = 0.99$	$f(x) = 2 * 10^6 x^{0.58};\ R^2 = 0.88$
6.4		$f(x) = 7 * 10^5 x^{1.07};\ R^2 = 0.92$	$f(x) = 1 * 10^6 x^{0.88};\ R^2 = 0.84$
1.2	***Flap-wise blade root***	$f(x) = 4 * 10^6 x^{1.3};\ R^2 = 0.99$	$f(x) = 3 * 10^6 x^{1.23};\ R^2 = 0.97$
3.1/4.1		$f(x) = 1 * 10^6 x^{0.58};\ R^2 = 0.91$	$f(x) = 3 * 10^6 x^{0.29};\ R^2 = 0.65$
6.4		$f(x) = 1 * 10^6 x^{1.08};\ R^2 = 0.98$	$f(x) = 2 * 10^6 x^{0.89};\ R^2 = 0.89$

Table 10.3: Power law algorithms (rotor solidity) of flap-wise and edge-wise blade root moments for fatigue loads: DLC 1.2, 3.1/4.1 and 6.4.

Design load case	Moment	Wohler Coefficients
		4
1.2	***Low – speed shaft***	$f(x) = 5 * 10^6 x^{1.13};\ R^2 = 0.97$
3.1/4.1		$f(x) = 5 * 10^5 x^{0.54};\ R^2 = 0.62$
6.4		$f(x) = 7 * 10^5 x^{1.08};\ R^2 = 0.81$
1.2	***Yaw bearing***	$f(x) = 3 * 10^6 x^{1.89};\ R^2 = 0.98$
3.1/4.1		$f(x) = 5 * 10^5 x^{-0.98};\ R^2 = 0.38$
6.4		$f(x) = 8 * 10^5 x^{1.53};\ R^2 = 0.78$
1.2	***Tower fore-aft base***	$f(x) = 49.49 * 10^6 x^2 - 137.73 * 10^6 x + 101.93 * 10^6;\ R^2 = 0.56$
3.1/4.1		$f(x) = 7.38 * 10^5 x^2 - 20.49 * 10^5 x + 101.93 * 10^6;\ R^2 = 0.56$
6.4		$f(x) = 8.3 * 10^6 x^{1.83};\ R^2 = 0.93$

Table 10.4: Power law algorithms (rotor solidity) of low-speed shaft, yaw bearing and tower fore-aft base root moments for fatigue loads: DLC 1.2, 3.1/4.1 and 6.4.

The following bullet points highlight additional key results of chapter 8.

- The developed algorithms of the sensitivity of extreme and fatigue loads have proved the hypothesis of Blonk *et al*. [80] that says reducing solidity tends to mitigate the tower top

loads, which are blade root, rotor and drivetrain loads. The reduction of tower top loads can be implemented to decrease the mass of wind turbine components, which leads to a reduced cost to the wind turbine and so cost of energy.

- The rotor solidity affects the aerodynamic damping of a wind turbine. Therefore, the reduction in rotor solidity decreases the aerodynamic damping of the rotor, which is crucial for fore-aft loads on the tower base.
- Tower base loads therefore need attention during the reduction of rotor solidity. As the tower base loads increase because of the reduced aerodynamic damping. However, the effect of the rise of tower loads due decreasing aerodynamic damping can be mitigated by introducing a more sophisticated controller.

Design load case	Moment	Power trend line equation	Moment	Power trend line equation
1.1	***Edge-wise blade root***	$f(x) = 4 * 10^6 x^{1.5};\ R^2 = 0.98$	***Flap-wise blade root***	$f(x) = 7 * 10^6 x^{0.78};\ R^2 = 0.97$
1.3		$f(x) = 3 * 10^6 x^{1.56};\ R^2 = 0.99$		$f(x) = 6 * 10^6 x^{1};\ R^2 = 0.99$
6.1		$f(x) = 3 * 10^5 x^{5.66};\ R^2 = 0.97$		$f(x) = 4 * 10^6 x^{1.2};\ R^2 = 0.99$
6.3		$f(x) = 6 * 10^5 x^{4.08};\ R^2 = 0.92$		$f(x) = 3 * 10^6 x^{1.44};\ R^2 = 0.99$
	Low-speed shaft	$f(x) = 6 * 10^6 x^{1.03};\ R^2 = 0.88$	**Yaw Mz bearing**	$f(x) = 4 * 10^6 x^{1.55};\ R^2 = 0.99$
1.3		$f(x) = 3 * 10^6 x^{1.36};\ R^2 = 0.99$		$f(x) = 3 * 10^6 x^{1.59};\ R^2 = 1$
6.1		$f(x) = 5 * 10^5 x^{4.73};\ R^2 = 0.98$		$f(x) = 5 * 10^5 x^{4.51};\ R^2 = 0.98$
6.3		$f(x) = 3 * 10^6 x^{2.27};\ R^2 = 0.91$		$f(x) = 3 * 10^6 x^{2.37};\ R^2 = 0.91$

Table 10.5: Power law algorithms (rotor solidity) of blade roots, low-speed shaft and yaw bearing extreme: DLC 1.1, 1.3, 6.1 and 6.3.

Design load case	Moment	Power trend line equation
1.1	***Tower fore-aft base***	$f(x) = 21.56 * 10^6 x^2 - 59.51 * 10^6 x\ + 89.37 * 10^6;\ R^2 = 0.46$
1.3		$f(x) = 4 * 10^7 x^{-0.41};\ R^2 = 0.66$
6.1		$f(x) = 3 * 10^7 x^{0.56};\ R^2 = 0.74$
6.3		$f(x) = 2 * 10^7 x^{0.72};\ R^2 = 0.73$

Table 10.6: Power law algorithms (rotor solidity) of tower fore-aft base extreme moment: DLC 1.1, 1.3, 6.1 and 6.3.

- ***Up-scaling with similarity (Chapter 9)***

This chapter investigates the changes of extreme and fatigue (lifetime DELs) loads as a result of up-scaling the reference wind turbine model with similarity. The seven up-scaled models (4, 5, 6, 7, 8, 9 and 10 MW rated power) were created in such way as to maintain the original value of power density of the reference model (3 MW rated power). Table 10.7 and Table 10.8 demonstrate how the fatigue loads up-scale. The scaling of extreme loads is shown in Table 10.9 and Table 10.10.

Design load case	Moment	Wohler Coefficients	
		4	***10***
1.2	***Edge-wise blade root***	$f(x) = 0.34\ D^{3.61};\ R^2 = 1$	$f(x) = 0.13\ D^{3.73};\ R^2 = 1$
3.1/4.1		$f(x) = 0.02\ D^{3.85};\ R^2 = 1$	$f(x) = 0.03\ D^{3.85};\ R^2 = 1$
6.4		$f(x) = 3.24\ D^{2.63};\ R^2 = 1$	$f(x) = 1.41\ D^{2.83};\ R^2 = 1$
1.2	***Flap-wise blade root***	$f(x) = 6.93\ D^{2.85};\ R^2 = 1$	$f(x) = 3.47\ D^{2.97};\ R^2 = 1$
3.1/4.1		$f(x) = 1.16\ D^{2.99};\ R^2 = 0.99$	$f(x) = 4.29\ D^{2.95};\ R^2 = 1$
6.4		$f(x) = 0.76\ D^{3.09};\ R^2 = 1$	$f(x) = 0.64\ D^{3.26};\ R^2 = 1$

Table 10.7: Power law algorithms (scaling with similarities) of flap-wise and edge-wise blade root moments for fatigue loads: DLC 1.2, 3.1/4.1 and 6.4.

Design load case	Moment	Wohler Coefficients
		4
1.2	***Low – speed shaft***	$f(x) = 28.64\ D^{2.6};\ R^2 = 1$
3.1/4.1		$f(x) = 1.21\ D^{2.8};\ R^2 = 1$
6.4		$f(x) = 4.55\ D^{2.61};\ R^2 = 1$
1.2	***Yaw bearing***	$f(x) = 55.22\ D^{2.38};\ R^2 = 1$
3.1/4.1		$f(x) = 6 * 10^{-3} D^{3.71};\ R^2 = 1$
6.4		$f(x) = 7.35\ D^{2.53};\ R^2 = 1$
1.2	***Tower fore-aft base***	$f(x) = 3548.23\ D^{1.76};\ R^2 = 0.97$
3.1/4.1		$f(x) = 2.83\ D^{3.22};\ R^2 = 1$
6.4		$f(x) = 18.81\ D^{2.77};\ R^2 = 0.98$

Table 10.8: Power law algorithms (scaling with similarities) of low-speed shaft, yaw bearing and tower fore-aft base root moments for fatigue loads: DLC 1.2, 3.1/4.1 and 6.4.

This chapter has shown that the extreme and fatigue loads, especially power production loads, scale slightly smaller than the steady state loads in the scaling with similarity. Therefore, the method of scaling with similarity can be used to obtain extreme and fatigue loads of up-scaled wind turbines. However, the calculated values of up-scaled extreme and fatigue loads will be conservative. The developed algorithms of extreme (Table 10.9 and Table 10.10) and fatigue (Table 10.7 and Table 10.8) loads, which were generated in this chapter, can give more an

accurate estimation than the method of scaling with similarity. The additional achievements of chapter 9 are listed below

- This chapter has shown that the up-scaled wind turbines are less sensitive to turbulence than the reference model. Therefore, the impact of turbulence decreases with the size of the wind turbine. The decrease of turbulence sensitivity is a result of the increase of rotor inertia for up-scaled wind turbines.

- The wind shear has smaller impact on the fatigue loads compared to steady state loads. The difference between the exponents of up-scaled fatigue flap-wise blade root and low-speed shaft loads with wind shear and without is 0.1. The difference between the exponents of up-scaled flap-wise steady moment with and without the wind shear is 0.4.

Design load case	Moment	Power trend line equation	Moment	Power trend line equation
1.1	***Edge-wise blade root***	$f(x) = 2.92\ D^{3.02};\ R^2 = 0.97$	***Flap-wise blade root***	$f(x) = 36.28\ D^{2.65};\ R^2 = 0.99$
1.3		$f(x) = 0.38\ D^{3.48};\ R^2 = 1$		$f(x) = 7.66\ D^{2.94};\ R^2 = 0.99$
6.1		$f(x) = 22.01\ D^{2.4};\ R^2 = 0.98$		$f(x) = 8.55\ D^{2.85};\ R^2 = 0.99$
6.3		$f(x) = 24.29\ D^{2.33};\ R^2 = 0.99$		$f(x) = 0.35\ D^{3.41};\ R^2 = 0.93$
1.1	***Low-speed shaft***	$f(x) = 31.63\ D^{2.68};\ R^2 = 1$	**Yaw Mz bearing**	$f(x) = 15.85\ D^{2.68};\ R^2 = 0.99$
1.3		$f(x) = 14.32\ D^{2.68};\ R^2 = 1$		$f(x) = 73.08\ D^{2.3};\ R^2 = 1$
6.1		$f(x) = 1.3\ D^{3.01};\ R^2 = 0.99$		$f(x) = 7.15\ D^{2.69};\ R^2 = 1$
6.3		$f(x) = 5.99\ D^{2.65};\ R^2 = 0.99$		$f(x) = 3.9\ D^{2.73};\ R^2 = 0.97$

Table 10.9: Power law algorithms (scaling with similarities) of blade roots, low-speed shaft and yaw bearing extreme: DLC 1.1, 1.3, 6.1 and 6.3.

Design load case	Moment	Power trend line equation
1.1	***Tower fore-aft base***	$f(x) = 99.71\ D^{2.82};\ R^2 = 0.96$
1.3		$f(x) = 173.44\ D^{2.67};\ R^2 = 1$
6.1		$f(x) = 35.64\ D^{2.96};\ R^2 = 0.99$
6.3		$f(x) = 38\ D^{2.83};\ R^2 = 0.99$

Table 10.10: Power law algorithms (scaling with similarities) of tower fore-aft base extreme moment: DLC 1.1, 1.3, 6.1 and 6.3.

10.3. Limitations

This study has several limitations or boundaries, which are summed up in this section. Some of these limitations were mentioned in the text of the previous chapters.

- The first limitation is in the design parameters of the reference wind turbine model, which are up-wind, three bladed, variable speed, pitch regulated and 3MW rated power. There are a variety of 3MW wind turbines with different design parameters e.g. diameter, hub height, operational strategy etc.
- Considering principally scaling with similarity may be thought of as limitation. However as commercial designs depart from similarity in a rather variable way, considering similarity is the best way to search for underlying trends in loads.
- The up-scaling with similarity was employed to up-scale the reference wind turbine model in chapter 9, which investigates the scaling impact on the extreme and fatigue loads. The up-scaling with similarity is based on assumptions: geometry changes linearly, material and technology of reference model is preserved. Often the commercial design seeks the way to reduce the weight to minimise mass penalties from the up-scaling.
- The simple PI controller was applied for the modified wind turbine for below rated region. Generally, more sophisticated controllers are used with large wind turbines in order to alleviate loads and increase the efficiency of the wind turbine.
- The performed studies of this research did not cover the total number of states which a wind turbine experiences, such as: fault conditions and emergency shut downs. Furthermore, the transient wind conditions were not taken into account in this study. For this study it was assumed that there are no faults with the wind turbine. Therefore, the investigation of extreme and fatigue loads covers the calculations of power production range (4-25m/s), number of start-ups and shut downs and idling conditions based on IEC standards [5]. These above mentioned calculations applied the three different turbulence wind models, these are: the normal turbulence model, extreme turbulence model and extreme wind speed model. Future work can focus on performing calculations for the rest of design load cases of IEC standards, which take into account faults, grid losses and transient wind conditions.

10.4. Future work

There are several points, which are suggested for the future, building on this study. The list of suggested points is provided below:

- Repeat the same analysis for 3MW wind turbines with different characteristics, e.g. different operational strategy and dimensions, as the diameter of 3MW machines vary from 90 m up to 137 m depending on manufacturers and the location of a site [98]–[102]. Ideally, it would be nice to perform the same calculations for a unit with different operational conditions and dimensions in order to compare the variation among developed algorithms.
- Perform an entire analysis of extreme and fatigue loads, which includes the rest of the design load cases, which were not considered in this study, based on IEC standards [5].
- Introduce new sophisticated controllers for each modified wind turbine of this study and repeat the analysis of this research. Compare the gained data with the data of this study.
- Link the developed algorithms for predicting extreme and fatigue loads with a cost model to foresee the changes in cost of prospective wind turbines.

Bibliography:

[1] T. Burton, N. Jenkins, D. Sharpe, B. Ervin, and D. Sharpe, *Wind Energy Handbook*. John Wiley & Sons, Inc., 2011.

[2] M. O. L. Hansen, *Aerodynamics of wind turbines*, 2nd ed. London: Earthscan, 2008.

[3] P. Jamieson, *Innovation in Wind Turbine Design*. John Wiley & Sons, 2011.

[4] B. Maples, G. Saur, and M. Hand, "Installation, operation, and maintenance strategies to reduce the cost of offshore wind energy," *NREL, Denver*, 2013.

[5] I. E. Commission, "Wind Turbine—Part 1: Design Requirements, IEC 61400-1," Geneva, 2005.

[6] J. F. Manwell, J. G. McGowan, and A. L. Rogers, *Wind Energy Explained: Theory, Design and Application*. 2002.

[7] R. Gasch and T. Jochen, *Wind Power Plants: Fundamentals, Design, Construction and Operation*, Second. Springer, 2012.

[8] R. T. Jose Zayas, Michael Derby, Patrick Gilman, Shreyas Ananthan, Eric Lantz Jason Cotrell, Fredric Beck, "Enabling Wind Power Nationwide," 2015.

[9] P. Madsen, K. Pierce, and M. Buhl, "Predicting ultimate loads for wind turbine design," 1998.

[10] E. Bossanyi, "GH Bladed–Theory Manual, Version 4.4," *Garrad Hassan and Partners*, 2013.

[11] E. Bossanyi, "GH Bladed-User Manual, Version 4.4," *Garrad Hassan Bl.*, 2013.

[12] L. Bergami, "Adaptive Trailing Edge Flaps for Active Load Alleviation in a Smart," Technical University of Denmark, 2013.

[13] H. Veldkamp, "Chances in wind energy: a probalistic approach to wind turbine fatigue design," Delft University, 2006.

[14] M. Miner, "Cumulative damage in fatigue," *Appl. Mech.*, vol. 12, no. 3, pp. 159–164, 1945.

[15] P. Ragan and L. Manuel, "Estimation of Wind Turbine Fatigue Loads Using Time-Ragan, P., & Manuel, L. (2007). Estimation of Wind Turbine Fatigue Loads Using Time-Domain and Spectral Methods. 45th AIAA Aerospace Sciences Meeting and. Retrieved from http://arc.aiaa.org/doi/pdf/10.25," *45th AIAA Aerosp. Sci. Meet.*, 2007.

[16] P. Ragan and L. Manuel, "Comparing Estimates of Wind Turbine Fatigue Loads using Time-Domain and Spectral Methods," *Wind Eng.*, vol. 31, no. 2, pp. 83–99, 2009.

[17] F. Campbell, *Elements of metallurgy and engineering alloys*, vol. #05224G. 2008.

[18] S. Downing and D. Socie, "Simple rainflow counting algorithms," *Int. J. Fatigue*, vol. 4, no. 1, pp. 31–40, 1982.

[19] G. Glinka and J. Kam, "Rainflow counting algorithm for very long stress histories," *Int. J. Fatigue*, vol. 9, no. 4, pp. 223–228, 1987.

[20] ASTM E1049-85(2011)e1, "Standard Practices for Cycle Counting in Fatigue Analysis," West Conshohocken, PA, 2011.

[21] M. Junginger, A. Faaij, and W. Turkenburg, "Cost reduction prospects for offshore wind farms," *Wind Eng.*, vol. 28, no. 1, pp. 97–118, 2004.

[22] E. Lantz, M. Hand, and R. Wiser, "The Past and Future Cost of Wind Energy," *World Renewables Energy Forum 2012*, no. August, pp. 1–10, 2012.

[23] Ö. Ceyhan, “Towards 20MW Wind Turbine: High Reynolds Number Effects on Rotor Design,” *50th AIAA Aerosp. Sci. Meet.*, no. January, pp. 1–15, 2012.

[24] K. Chaviaropoulos, P. van Langen, and P. Jamieson, “Similarity rules for W/T up-scaling,” *UpWind Report, WP 1B4*, pp. 1–8, 2007.

[25] P. Jamieson, “Loading and cost trends using certification calculation,” 2007.

[26] T. Ashuri, “Beyond Classical Upscaling : Integrated Aeroservoelastic Design and Optimization of Large Offshore Wind Turbines,” Delft University of Technology, 2012.

[27] P. Gardner, P. Jamieson, H. Snodin, and A. Tindal, “WIND ENERGY - THE FACTS VOLUME 1 TECHNOLOGY,” 2009.

[28] A. Chehouri, R. Younes, and A. Ilinca, “Optimal Design for a Composite Wind Turbine Blade With Fatigue and Failure Constraints,” *Trans. Can. Soc. Mech. Eng.*, vol. 39, no. 2, pp. 171–186, 2015.

[29] J. McArthur, “Aerodynamics of wings at low reynolds numbers,” UNIVERSITY OF SOUTHERN CALIFORNIA, 2007.

[30] N. Fichaux, J. Beurskens, P. H. Jensen, and J. Wilkes, “Design limits and solutions for very large wind turbines: A 20 MW turbine is feasible,” *UpWind*, no. March, pp. 1–108, 2011.

[31] T. Van Zandt, “FAST User’s Guide,” *Acta Psychiatr. Scand.*, vol. 123, no. 6, pp. 407–8, 2007.

[32] P. J. Moriarty and a C. Hansen, “AeroDyn Theory Manual,” *Renew. Energy*, vol. 15, no. January, pp. 500–36313, 2005.

[33] A. Manjock, “Design Codes FAST and ADAMS® for Load Calculations of Onshore Wind Turbines,” *Ger. Lloyd Wind. GmbH*, p. 18, 2005.

[34] R. E. Wilson, S. N. Walker, and P. Heh, “Technical and User’s Manual for the FAST_AD Advanced Dynamics Code,” Denver, 1999.

[35] T. Larsen and A. Hansen, *How 2 HAWC2, the user’s manual*. 2007.

[36] T. J. Larsen, a M. Hansen, and T. Buhl, “Aeroelastic effects of large blade deflections for wind turbines,” *Sci. Mak. torque from Wind*, pp. 238–246, 2004.

[37] N. Stuurman and R. D. Vale, *Impact of new camera technologies on discoveries in cell biology*, 2nd ed., vol. 231, no. 1. Cambridge University Press, 2016.

[38] J. G. Snel, H.; Schepers, “Joint investigation of dynamic inflow effects and implementation of an engineering method,” Energy Research Centre of the Netherlands, 1995.

[39] H. Glauert, “The analysis of experimental results in the windmill brake and vortex ring states of an airscrew,” *Gt. Britain Aeronaut. Res. Comm.*, vol. 1026, p. 8, 1926.

[40] J. G. Leishman and T. S. Beddoes, “A Semi-Empirical Model for Dynamic Stall,” *Am. Helicopter Soc.*, vol. 34, no. 3, pp. 3–17, 1989.

[41] K. G. Pierce, *Wind Turbine Load Prediction Using the Beddoes-Leishman Model for Unsteady Aerodynamics and Dynamic Stall*. Department of Mechanical Engineering, University of Utah, 1996.

[42] J. E. Minnema, *Pitching Moment Predictions on Wind Turbine Blades Using the Beddoes-Leishman Model for Unsteady Aerodynamics and Dynamic Stall*. Department of Mechanical Engineering, University of Utah, 1998.

[43] J. W. Larsen, S. R. K. Nielsen, and S. Krenk, “Dynamic stall model for wind turbine airfoils,” *J. Fluids Struct.*, vol. 23, no. 7, pp. 959–982, Oct. 2007.

[44] Germanischer Lloyd, “Rules and Guidelines Industrial Services: Guideline for the Certification of Offshore Wind Turbines,” Hamburg, 2005.

[45] Germanischer Lloyd, “Rules and Guidelines IV Industrial Services 2 Guideline for the Certification of Offshore Wind Turbines,” Hamburg, 2005.

[46] E. Bossanyi, D. Witcher, and T. Mercer, “Project UpWind: Controller for 5MW reference turbine,” Bristol, 2009.

[47] P. S. Veers, “Three-Dimensional Wind Simulation,” *J. Geophys. Res.*, vol. 92, no. A3, p. 2289, 1987.

[48] N. Thompson, “Characteristics of Atmospheric Turbulence Near the Ground,” 1983.

[49] T. von Karman, “Progress in the statistical theory of turbulence,” *Proc. Natl. Acad. Sci. U. S. A.*, vol. 34, no. 11, pp. 530–539, 1948.

[50] J. Mann, “Wind field simulation,” *Probabilistic Eng. Mech.*, vol. 13, no. 4, pp. 269–282, 1998.

[51] J. Mann, “The spatial structure of neutral atmospheric surface-layer turbulence,” *J. Fluid Mech.*, vol. 273, no. 1, p. 141, 1994.

[52] H. B. Pedersen, “Investigation and implementation of turbulent wind in a specialized software tool for offshore wind turbines,” Norwegian University of Science and Technology, 2014.

[53] A. Kolmogorov, “The local structure of turbulence in incompressible viscous fluid for very large Reynolds numbers,” *Dokl. Akad. Nauk SSSR*, 1941.

[54] C. Plumley, “The Smart Rotor Wind Turbine,” Strathclyde University, 2015.

[55] J. D. Sørensen, “Fatigue reliability and effective turbulence models in wind farms,” *Probabilistic Eng. Mech.*, pp. 1–8, 2007.

[56] K. Thomsen Sorenson, P., “Fatigue sloads for wind turbines operating in wakes,” *J. Wind Eng. Ind. Aerodyn.*, vol. 80, pp. 121–136, 1999.

[57] A. Sathe and W. Bierbooms, “Influence of different wind profiles due to varying atmospheric stability on the fatigue life of wind turbines,” *J. Phys. Conf. Ser.*, 2007.

[58] P. S. Veers, L. Manuel, P. S. Veers, and S. R. Winterstein, “Parametric Models for Estimating Wind Turbine Fatigue Loads for Design,” 2001.

[59] P. Stoica and R. Moses, *Spectral Analysis of Signals*. London: PRENTICE HALL, 2004.

[60] P. Agarwal and L. Manuel, “Extreme loads for an offshore wind turbine using statistical extrapolation from limited field data,” *Wind Energy*, vol. 11, no. 6, pp. 673–684, 2008.

[61] A. Natarajan and W. E. Holley, “Statistical Extreme Load Extrapolation With Quadratic Distortions for Wind Turbines,” *J. Sol. Energy Eng.*, vol. 130, no. 3, pp. 31017-1–7, 2008.

[62] P. J. Moriarty, W. E. Holley, and S. P. Butterfield, “Extrapolation of Extreme and Fatigue Loads Using Probabilistic Methods Extrapolation of Extreme and Fatigue Loads Using Probabilistic Methods,” Denver, 2004.

[63] K. Stroud and D. Booth, *Advanced engineering mathematics*, 4th ed. Palgrave MacMillan, 2011.

[64] K. A. Stroud and D. Booth, *Advanced engineering mathematics*, 9th ed. John Wiley & Sons, 2003.

[65] D. J. Malcolm and A. C. Hansen, “WindPACT Turbine Rotor Design Study WindPACT Turbine Rotor Design Study,” 2006.

[66] J. Jonkman, S. Butterfield, W. Musial, and G. Scott, “Definition of a 5-MW reference wind turbine for offshore system development,” 2009.

[67] H. Kooijman and C. Lindenburg, “DOWEC 6 MW PRE-DESIGN, Aeroelastic modelling of the DOWEC 6 MW pre-design in PHATAS,” 2003.

[68] C. Bak *et al.*, “Description of the DTU 10 MW Reference Wind Turbine,” 2013.

[69] H. D. Gans and W. J. Andersont, “Structural Optimization Incorporating Centrifugal and Coriolis Effects,” Air Force Institute of Technology, 1988.

[70] R. W. Thresher, L. P. Mirandy, T. G. Carne, D. W. Lobitz, and G. H. James, “Structural Dynamic Behaviour of Wind Turbines,” *Wind Turbine Technol. Fundam. Concepts Wind Turbine Eng.*, pp. 607–665, 2009.

[71] S. Lee, M. Churchfield, P. Moriarty, and J. Jonkman, “Atmospheric and wake turbulence impacts on wind turbine fatigue loadings,” in *Proc. of the 50th AIAA Aerospace Sciences Meeting*, 2012, no. NREL/CP-5000-53567, pp. 1–15.

[72] I. P. Girsang, J. S. Dhupia, and L. Y. Pao, “Gearbox and Drivetrain Models to Study Dynamic Effects of Modern Wind Turbines Eduard Muljadi Mohit Singh,” *IEEE Power Syst.*, vol. 9994, no. c, pp. 874–881, 2014.

[73] D. J. Trudnowski, A. Gentile, J. M. Khan, and E. M. Petritz, “Fixed-speed wind-generator and wind-park modeling for transient stability studies,” *IEEE Trans. Power Syst.*, vol. 19, no. 4, pp. 1911–1917, 2004.

[74] H. Li, B. Zhao, C. Yang, H. W. Chen, and Z. Chen, “Analysis and estimation of transient stability for a grid-connected wind turbine with induction generator,” *Renew. Energy*, vol. 36, no. 5, pp. 1469–1476, May 2011.

[75] B. Srikant, *Mechanical Vibrations: Theory and Practice*. Pearson Education India, 2010.

[76] J. Hannah and M. Hillier, *Mechanical engineering science*, 3rd ed. Prentice Hall, 1999.

[77] J. . Ward, *Solid Mechanics*. 1992.

[78] A. Nussbaumer, L. Borges, and L. Davaine, *Fatigue Design of Steel and Composite Structures: Eurocode 3: Design of Steel Structures, Part 1-9 Fatigue; Eurocode 4: Design of Composite Steel and Concrete Structures*. 2012.

[79] I. Stephens, Ralph, A. Fatemi, R. Stephens, Robert, and O. Fuchs, Henry, *Metal Fatigue in Engineering*. 2001.

[80] L. Blonk, P. Rainey, D. a J. Langston, and F. Vanni, “Quantifying the benefits of a slender, high tip speed blade for large offshore wind turbiness,” *J. Phys. Conf. Ser.*, vol. 524, p. 12014, 2014.

[81] MIT, “Area and Bending Inertia of Airfoil Sections,” vol. 1, no. 6. pp. 6–7, 2006.

[82] M. M. Rodriguez, “Analysis of structural damping,” 2006.

[83] S. Adhikari, “Damping Models for Structural Vibration,” p. 228, 2001.

[84] D. J. C. Salzmann and J. van der Tempel, “Aerodynamic damping in the design of support structures for offshore wind turbines,” *Proc. Offshore Wind Energy Conf.*, pp. 1–9, 2005.

[85] J. Köller, W. Peters, and J. Köppel, “Offshore Wind Energy. Research on Environmental Impacts,” in *Offshore Wind Energy. Research on Environmental Impacts*, J. Köller, W. Peters, and J. Köppel, Eds. Springer-Verlag, 2006.

[86] J. Fogle, P. Agarwal, and L. Manuel, “Towards an improved understanding of statistical extrapolation for wind turbine extreme loads,” *Wind Energy*, vol. 11, no. 6, pp. 613–635, 2008.

[87] G. Sieros, P. Chaviaropoulos, J. D. Sørensen, B. H. Bulder, and P. Jamieson, “Upscaling wind turbines: theoretical and practical aspects and their impact on the cost of energy,” *Wind*

Energy, vol. 15, no. 1, pp. 3–17, 2012.

[88] E. Bossanyi, "Wind turbine control for load reduction," *Wind Energy*, vol. 6, no. 3, pp. 229–244, 2003.

[89] W. Leithead, S. Dominguez, and C. Spruce, "Analysis of Tower / Blade interaction in the cancellation of the tower fore-aft mode via control," *Eur. Wind Energy Conf. EWEA*, pp. 1–10, 2004.

[90] R. Gasch and K. Knothe, *Strukturdynamik. Band 1: Diskrete Systeme*, vol. 1. 1987.

[91] R. Gasch and K. Knothe, "Strukturdynamik: Band 2: Kontinua und ihre Diskretisierung (German Edition)," p. 356, 2008.

[92] P. Jamieson, "Loading trends from certification calculations," *UpWind Report, WP 1B4*, 2007.

[93] J. D. Sørensen, T. Chaviaropoulos, P. Jamieson, B. B.H., and S. T. Frandsen, "Setting the frame for up-scaled off-shore wind turbines," *Design*, pp. 145–152, 2010.

[94] R. H. Barnes, E. V. Morozov, and K. Shankar, "Improved methodology for design of low wind speed specific wind turbine blades," *Compos. Struct.*, vol. 119, pp. 677–684, Jan. 2015.

[95] F. Porté-Agel, H. Lu, and Y.-T. Wu, "Interaction between Large Wind Farms and the Atmospheric Boundary Layer," *Procedia IUTAM*, vol. 10, pp. 307–318, 2014.

[96] H. Liu, Q. Tang, and Y. Chi, "Vibration reduction strategy for wind turbine based on individual pitch control and torque damping control," *Trans. Electr.*, 2016.

[97] S. Frandsen, "Turbulence and turbulence-generated structural loading in wind turbine clusters," Technical University of Denmark, 2007.

[98] Siemens AG, "Siemens D3 platform – 3.0MW, 3.2MW, 3.3MW, and 3.4MW direct drive turbines," 2015.

[99] GE Renewable Energy, "GE'S 3 MW Platform -," 2015.

[100] Gamesa, "Gamesa G132-3.3 MW Platform Brochure," 2016.

[101] Nordex, "Nordex N100/3300, N117/3000, N131/3000 Platforms brochure: DELTA GENERATION PROVEN TECHNOLOGY – AT A NEW STAGE OF EVOLUTION," 2014.

[102] Vestas, "Vestas V90-3.0MW Wind Turbine brochure," 2013.

[103] M. Monfared, H. Madadi Kojabadi, and H. Rastegar, "Static and dynamic wind turbine simulator using a converter controlled dc motor," *Renew. Energy*, vol. 33, no. 5, pp. 906–913, 2008.

[104] S. Bhattacharya, "Challenges in Design of Foundations for Offshore Wind Turbines," *Eng. Technol. Ref.*, 2014.

[105] S. Bhattacharya, D. Lombardi, and D. Muir Wood, "Similitude relationships for physical modelling of monopile-supported offshore wind turbines," *Int. J. Phys. Model. Geotech.*, vol. 11, no. 2, pp. 58–68, 2011.

Appendix A: Parameters of reference wind turbine

The Appendix demonstrates the extraction of bladed report, which shows parameters of reference wind turbine model.

GENERAL CHARACTERISTICS OF ROTOR AND TURBINE

Rotor diameter	100	m
Number of blades	3	
Teeter hinge	No	
Hub height	81.11	m
Offset of hub to side of tower centre	0	m
Tower height	79	m
Tilt angle of rotor to horizontal	6	deg
Cone angle of rotor	0	deg
Blade set angle	0	deg
Rotor overhang	4.33	m
Rotational sense of rotor, viewed from upwind	Clockwise	
Position of rotor relative to tower	Upwind	
Transmission	Gearbox	
Aerodynamic control surfaces	Pitch	
Fixed / Variable speed	Variable	
Diameter of spinner	4.444	m
Radial position of root station	1.33	m
Extension piece diameter	2.684	m
Extension piece drag coefficient	1	
Cut in windspeed	4	m/s
Cut out windspeed	25	m/s

BLADE GEOMETRY

Blade name	LM43.8P	
Blade length	48.7382	m
Pre-bend at tip	1.66711	m
Pitch control	Full span	

Distance along blade (m)	Distance along pitch axis (m)	Chord (m)	Aerodynamic Twist (deg)	Thickness (%)	Neutral axis (x) (m)	Neutral axis (y) (m)	Neutral axis, local (x) (%)	Neutral axis, local (y) (%)
0	0	2.68	5	100	0.056269	-0.026845	2.09958	48.9983
2.22001	2.22	2.76	5.38	96.412	0.060373	-0.021329	2.18744	48.2272
4.44051	4.44	2.94	6.695	80.537	0.070465	-0.06739	2.43078	45.7078
6.67065	6.67	3.13	8.093	65.08	0.077956	-0.091146	2.71424	44.088
8.89065	8.89	3.31	9.37	51.689	0.079103	-0.094513	2.99406	43.1446
11.1115	11.11	3.48	10.215	40.327	0.06748	-0.032951	3.43335	44.0531
13.3317	13.33	3.52	9.39	32.55	0.043671	-0.029798	3.00203	43.1535
15.5624	15.56	3.33	7.17	28.4	0.032398	0.025309	2.23416	42.76
17.7826	17.78	3.1	5.42	25.62	0.005051	0.010436	1.55002	41.3366
20.0034	20	2.86	4.326	23.769	-0.039403	-0.026685	1.13977	40.067
22.2241	22.22	2.65	3.499	22.248	-0.09308	-0.006296	0.90265	39.7624
24.445	24.44	2.46	2.859	20.99	-0.154577	-0.020115	0.708271	39.1823
26.6759	26.67	2.29	2.31	20.034	-0.215275	-0.003254	0.599352	39.8579
28.8982	28.89	2.13	1.762	19.405	-0.311283	-0.036131	0.409254	38.3037
31.1203	31.11	2	1.281	19.027	-0.406825	-0.023869	0.308733	38.8066
33.3431	33.33	1.86	0.893	18.785	-0.516762	-0.007101	0.227855	39.6182
35.5766	35.56	1.73	0.559	18.642	-0.639254	0.021958	0.158734	41.2692
37.8011	37.78	1.62	0.3	18.61	-0.777477	0.047786	0.093985	42.9498
40.0265	40	1.52	0.12	18.52	-0.928341	0.086639	0.043354	45.7
42.2531	42.22	1.41	-0.04	18.36	-1.09623	0.118299	0.016329	48.39
44.4806	44.44	1.25	-0.22	18.17	-1.27814	0.109998	0.091385	48.7998
46.7198	46.67	0.96	-0.334	17.39	-1.47723	0.06614	0.127605	46.8896
47.8383	47.78	0.63	0.591	16.309	-1.5783	-0.026905	0.110677	35.7294
48.282	48.22	0.44	2.043	15.605	-1.62288	-0.062658	0.027094	25.7595
48.7382	48.67	0.01	5.8	14.84	-1.66711	-0.002566	-1.08231	14.3448

Distance along blade (m)	Aerofoil section	Aerodynamic control
0	1	Moving
2.22001	2	Moving
4.44051	2	Moving
6.67065	2	Moving
8.89065	3	Moving
11.1115	3	Moving
13.3317	3	Moving
15.5624	3	Moving
17.7826	3	Moving
20.0034	3	Moving
22.2241	3	Moving
24.445	4	Moving
26.6759	4	Moving
28.8982	5	Moving
31.1203	5	Moving
33.3431	5	Moving
35.5766	5	Moving
37.8011	5	Moving
40.0265	5	Moving
42.2531	5	Moving
44.4806	5	Moving
46.7198	6	Moving
47.8383	6	Moving
48.282	6	Moving
48.7382	7	Moving

BLADE MASS DISTRIBUTION

Centre of mass (x) (%)	Centre of mass (y) (%)	Mass/unit length (kg/m)	Polar intertia/unit length (kgm)	Radii of gyration ratio	Mass axis orientation (deg)
2.09958	48.9983	707	0	1	5
2.18744	48.2272	689.491	0	0.96412	5.38
2.43078	45.7078	361.708	0	0.80537	6.695
2.71424	44.088	208.512	0	0.6508	8.093
2.99406	43.1446	162.817	0	0.51689	9.37
3.43335	44.0531	158.281	0	0.40327	10.215
3.00203	43.1535	156.764	0	0.3255	9.39
2.23416	42.76	155.234	0	0.284	7.17
1.55002	41.3366	153.717	0	0.2562	5.42
1.13977	40.067	152.195	0	0.23769	4.326
0.90265	39.7624	150.673	0	0.22248	3.499
0.708271	39.1823	149.152	0	0.2099	2.859
0.599352	39.8579	134.224	0	0.20034	2.31
0.409254	38.3037	121.83	0	0.19405	1.762
0.308733	38.8066	109.438	0	0.19027	1.281
0.227855	39.6182	97.0454	0	0.18785	0.893
0.158734	41.2692	84.5978	0	0.18642	0.559
0.093985	42.9498	72.2068	0	0.1861	0.3
0.043354	45.7	59.8171	0	0.1852	0.12
-0.016329	48.39	57.2016	0	0.1836	-0.04
-0.091385	48.7998	50.9254	0	0.1817	-0.22
-0.127605	46.8896	44.6216	0	0.1739	-0.334
0.110677	35.7294	41.4814	0	0.16309	0.591
0.027094	25.7595	37.0501	0	0.15605	2.043
-1.08231	14.3448	31.5348	0	0.1484	5.8

Blade 1 Mass Integrals (No ice)

Blade Mass	8221.47	kg
First Mass Moment	121425	kgm
Second Mass Moment	3.211E+06	kgm²
Blade inertia about shaft	3.547E+06	kgm²

BLADE STIFFNESS DISTRIBUTION

Bending Stiffness about yp (Nm^2)	Bending Stiffness about xp (Nm^2)	Principal Axis Orientation (deg)
9.66E+09	9.66E+09	5
4.83E+09	7.51E+09	5.38
2.7E+09	4.83E+09	6.695
1.9E+09	4.51E+09	8.093
1.45E+09	3.69E+09	9.37
1.1E+09	3.25E+09	10.215
8.5E+08	2.85E+09	9.39
6.6E+08	2.39E+09	7.17
4.93E+08	1.8E+09	5.42
3.83E+08	1.4E+09	4.326
3.01E+08	1.44E+09	3.499
2.3E+08	1.27E+09	2.859
1.72E+08	1.05E+09	2.31
1.24E+08	1.02E+09	1.762
8.69E+07	7.94E+08	1.281
5.89E+07	6.1E+08	0.893
3.79E+07	3.9E+08	0.559
2.29E+07	2.36E+08	0.3
1.27E+07	1.46E+08	0.12
6.23E+06	1.14E+08	-0.04
2.47E+06	6.19E+07	-0.22
664000	2.5E+07	-0.334
73600	3.37E+06	0.591
2840	1.83E+06	2.043
1.23	152	5.8

HUB MASS AND INERTIA

Mass of hub	45267.5	kg
Mass centre of hub	-0.1	m
Hub inertia: about shaft	60966.3	kgm^2
perpendicular to shaft	60966.3	kgm^2
Total Rotor Mass	69931.9	kg
Total Rotor Inertia	1.07E+07	kgm^2

TOWER DETAILS

Station Number	Height (m)	Diameter (m)	Wall thickness (mm)	Material	Mass/unit length (kg/m)	Stiffness (Nm²)
1	-33.333	5.111	55.556	steel	6926.44	5.92E+11
2	-27.778	5.111	55.556	steel	6926.44	5.92E+11
3	-22.222	5.111	55.556	steel	6926.44	5.92E+11
4	-16.667	5.111	55.556	steel	6926.44	5.92E+11
5	-11.111	5.111	55.556	steel	6926.44	5.92E+11
6	-8.333	5.111	55.556	steel	6926.44	5.92E+11
7	-5.556	5.111	55.556	steel	6926.44	5.92E+11
8	-2.778	5.111	55.556	steel	6926.44	5.92E+11
9	-2.608E-11	5.111	55.556	steel	6926.44	5.92E+11
10	2.778	5.111	55.556	steel	6926.44	5.92E+11
11	5.556	5.111	55.556	steel	6926.44	5.92E+11
12	8.333	5.111	54.085	steel	6745	5.768E+11
13	11.111	5.111	52.614	steel	6563.45	5.616E+11
14	16.667	4.947	49.672	steel	5999.14	4.812E+11
15	27.778	4.62	43.789	steel	4941.85	3.461E+11
16	38.889	4.293	37.906	steel	3977.73	2.409E+11
17	50	3.965	32.022	steel	3105.91	1.607E+11
18	61.111	3.638	26.139	steel	2328.3	1.016E+11
19	79	3.111	16.667	steel	1271.87	4.072E+10

steel: density	7850	kg/m³
steel: Young's modulus	2.1E+11	N/m²

Total Tower Mass	553810	kg
Total Turbine Mass	760915	kg

Drag coefficient for tower	0.6	
Environment	Offshore	
Mean sea depth	30	m
Marine growth density	0	kg/m³
Hydrodynamic drag coefficient	1	
Hydrodynamic mass coefficient	2	

Movement of tower foundation

Tower base translational motion?	No	
Tower base rotational motion?	Yes	
Moment of inertia of foundation	4.12E+07	kgm²
Rotational stiffness of foundation	1.23E+11	Nm/rad

NACELLE GEOMETRY

Nacelle width	3.89	m
Nacelle length	11.11	m
Nacelle height	3.89	m
Nacelle drag coefficient	1.2	

NACELLE MASS

Nacelle mass	137174	kg
Nacelle centre of mass lateral offset	0	m
Nacelle centre of mass above tower top	1.44	m
Nacelle centre of mass in front of tower axis	-0.666	m
Yaw inertia (about tower axis)	643533	kgm²
Nodding inertia (about CoG)	0	kgm²
Rolling inertia (about CoG)	0	kgm²
Total Tower-head Mass	207106	kg
Total Yaw Inertia: 0° azimuth	7.266E+06	kgm²
Total Yaw Inertia: 90° azimuth	7.266E+06	kgm²

DRIVE TRAIN

Gearbox ratio	46.667	
Position of shaft brake	High speed shaft	(Gearbox End)
Generator inertia	600	kgm²
High speed shaft inertia:	0	kgm²
Gearbox inertia	0	kgm²
Low speed shaft	Flexible	
High speed shaft	Stiff	

GENERATOR CHARACTERISTICS

Generator model	Variable Speed	
Power electronics time constant	0	s
Maximum generator torque	60000	Nm
Minimum generator torque	0	Nm
Phase Angle	0	deg

MECHANICAL LOSS TORQUE (kNm, referred to low speed shaft)
interpolated on low speed shaft torque and speed

LSS speed (rpm)	0 kNm	1896 kNm	3792 kNm
0	0	0	0
16	0	31	31
32	0	31	62

ELECTRICAL LOSSES

Shaft power (kW)	Power loss (kW)
6	3
45	10
113	13
224	17
389	21
618	27
923	33
1314	43
1803	57
2400	79
3115	114

POWER PRODUCTION CONTROL

Variable Speed Pitch Regulated Controller	Dynamic	
Minimum generator speed	336	rpm
Optimal mode quadratic speed-torque gain	3.93997	Nms²/rad²

Optimal mode maximum generator speed	672	rpm
Generator torque set point	44251	Nm
Above-rated generator speed set-point	672	rpm
Minimum pitch angle	-1	deg
Maximum pitch angle	90	deg
Pitch direction	to Feather	
Speed transducer time constant	0.04	s
Power transducer time constant	0.04	s
Maximum negative pitch rate	-8	deg/s
Maximum positive pitch rate	8	deg/s
Torque controller	Discrete	
Pitch controller	Discrete	

Discrete Controller: d:\users\gfb11177.ds\desktop\bladed\project\discon.dll

Communication interval	0.01	s
Maximum logging variables	70	
Power production control:	Pitch,	
Torque,		
Yaw		

External Controller data:

NORMAL STOP CALCULATION

Pitch rate for stopping	2	deg/s
Final pitch angle	90	deg
Rotor speed for parking brake application	5.76	rpm

SHAFT BRAKE CHARACTERISTICS
Brake Number: 1

Maximum brake torque	60000	Nm
Shaft brake ramp time	30	s

PITCH ACTUATOR
Input Demand

Input Demand	Position	
Setpoint Trajectory Planning	SetpointTrajectoryPlanning	
Setpoint Trajectory Planning - Rate Limits	True	
Setpoint Trajectory Planning - Minimum	-7.999999	deg/s
Setpoint Trajectory Planning - Maximum	7.999999	deg/s
Setpoint Trajectory Planning - Acceleration Limits	False	
Setpoint Trajectory Planning - Minimum	0	deg/s²
Setpoint Trajectory Planning - Maximum	0	deg/s²
Individual Pitch Control	False	

External

External DLL	False	
Track External Hardware	False	

Actuator dynamic response

Response to Position Demand	2nd order passive	
Response to Position Demand - Frequency (f)	0.9999992	Hz
Response to Position Demand - Damping factor (?)	0.8	-

Position Limits

Limit Switches	True	
+ Positions	Min: -5, Max: 90	deg
End Stops	False	

Actuator Details

Bearing Friction	False	
Actuator Drive Details	None	
Single Actuator Pitch System	False	
Safety System Definition	Rate Demand	
Safety System Definition - Actuator Torque/Force Limits	None	
Safety System Definition - Rate calculated according to	Constant rate	
Safety System Definition - Rate Demand	0	deg/s

TOWER SHADOW

Tower shadow model	Potential Flow	
Fraction of tower diameter to use	1	

VERTICAL WIND SHEAR

Wind shear model	Exponential	
Wind shear exponent	0.2	
Vertical Direction Shear	0	deg/m

PHYSICAL CONSTANTS

Air density	1.225	kg/m^3
Air viscosity	1.82E-05	kg/ms
Gravitational acceleration	9.81	m/s^2
Density of water	1030	kg/m^3

IDLING SIMULATION

Pitch angle for idling	90	deg
External controller	No	

Appendix B: Aerodynamic properties of aerofoil

The Appendix demonstrates the extraction of bladed report, which shows the lift and drag coefficient of aerofoils at the reference wind turbine model.

Aerofoil dataset: Profile 1

Angle of Attack (deg)	Lift coefficient	Drag coefficient	Pitch moment coefficient
-180	0	0.1	0
-170	0.8	0.24	0.4
-150	0.8	0.58	0.325
-120	0.49	1.06	0.325
-90	-0.114	1.3	0.325
-60	-0.755	1.06	0.325
-30	-1.2	0.45	0.22
-20	-1.2	0.2	0.05
-15	-1.1	0.04	0
-10	-0.72	0.0105	-0.11
-6	-0.265	0.008	-0.11
-2	0.1857	0.0057	-0.11
2	0.6461	0.0059	-0.115
4	0.8763	0.0067	-0.11
6	1.095	0.01	-0.11
8	1.27	0.0165	-0.11
10	1.335	0.019	-0.11
12	1.335	0.0235	-0.11
14	1.275	0.047	-0.11
16	1.2383	0.082	-0.11
18	1.2066	0.1295	-0.11
20	1.175	0.177	-0.11
25	1.1	0.32	-0.12
30	1.09	0.51	-0.14
40	1.06	0.69	-0.18
50	0.93	0.9	-0.22
60	0.755	1.06	-0.26
70	0.555	1.18	-0.2925
80	0.34	1.26	-0.325
90	0.114	1.3	-0.325
100	-0.11	1.27	-0.325
120	-0.49	1.06	-0.325
150	-0.8	0.58	-0.325
170	-0.8	0.24	-0.4
180	0	0.1	0

Aerofoil dataset: Profile 2

Angle of Attack (deg)	Lift coefficient	Drag coefficient	Pitch moment coefficient
-180	0	0.1	0
-170	0.8	0.24	0.4
-150	0.8	0.58	0.325
-120	0.49	1.06	0.325
-90	-0.114	1.3	0.325
-60	-0.755	1.06	0.325
-30	-1.2	0.45	0.22
-20	-1.2	0.2	0.05
-15	-1.05	0.1	0
-10	-0.72	0.013	-0.1
-6	-0.265	0.01	-0.1
-2	0.1814	0.006	-0.1
2	0.6471	0.006	-0.1
4	0.88	0.007	-0.1
6	1.09	0.009	-0.1
8	1.26	0.012	-0.1
10	1.33	0.015	-0.1
12	1.33	0.024	-0.1
14	1.31	0.048	-0.1
16	1.2767	0.082	-0.1
18	1.2433	0.123	-0.1
20	1.21	0.164	-0.11
25	1.18	0.32	-0.12
30	1.12	0.5	-0.14
40	1.06	0.69	-0.18
50	0.93	0.9	-0.22
60	0.755	1.06	-0.26
70	0.555	1.18	-0.2925
80	0.34	1.26	-0.325
90	0.114	1.3	-0.325
100	-0.11	1.27	-0.325
120	-0.49	1.06	-0.325
150	-0.8	0.58	-0.325
170	-0.8	0.24	-0.4
180	0	0.1	0

Aerofoil dataset: Profile 4

Angle of Attack (deg)	Lift coefficient	Drag coefficient	Pitch moment coefficient
-180	0	0.1	0
-170	0.8	0.24	0.4
-150	0.8	0.58	0.325
-120	0.49	1.06	0.325
-90	-0.114	1.3	0.325
-60	-0.755	1.06	0.325
-30	-1.2	0.45	0.22
-20	-1.2	0.2	0.05
-15	-1.05	0.1	0
-10	-0.72	0.013	-0.11
-6	-0.265	0.01	-0.11
-2	0.1814	0.006	-0.11
2	0.6471	0.0061	-0.115
4	0.88	0.0071	-0.11
6	1.09	0.01	-0.11
8	1.26	0.014	-0.11
10	1.4	0.018	-0.11
12	1.49	0.023	-0.11
14	1.5233	0.037	-0.11
16	1.5067	0.063	-0.11
18	1.48	0.09	-0.11
20	1.4367	0.134	-0.11
25	1.3133	0.282	-0.12
30	1.24	0.48	-0.14
40	1.06	0.69	-0.18
50	0.93	0.9	-0.22
60	0.755	1.06	-0.26
70	0.555	1.18	-0.2925
80	0.34	1.26	-0.325
90	0.114	1.3	-0.325
100	-0.11	1.27	-0.325
120	-0.49	1.06	-0.325
150	-0.8	0.58	-0.325
170	-0.8	0.24	-0.4
180	0	0.1	0

Aerofoil dataset: Profile 5

Angle of Attack (deg)	Lift coefficient	Drag coefficient	Pitch moment coefficient
-180	0	0.1	0
-170	0.8	0.24	0.4
-150	0.8	0.58	0.325
-120	0.49	1.06	0.325
-90	-0.114	1.3	0.325
-60	-0.755	1.06	0.325
-30	-1.2	0.45	0.22
-20	-1.2	0.2	0.05
-15	-1.05	0.1	0
-10	-0.72	0.013	-0.11
-6	-0.265	0.01	-0.11
-2	0.1814	0.011	-0.11
2	0.6471	0.0123	-0.115
4	0.88	0.0132	-0.11
6	1.05	0.014	-0.11
8	1.2	0.014	-0.11
10	1.3	0.016	-0.11
12	1.36	0.0248	-0.11
14	1.41	0.047	-0.11
16	1.41	0.074	-0.11
18	1.37	0.106	-0.11
20	1.3333	0.148	-0.11
25	1.2217	0.3	-0.12
30	1.15	0.45	-0.14
40	1.06	0.69	-0.18
50	0.93	0.9	-0.22
60	0.755	1.06	-0.26
70	0.555	1.18	-0.2925
80	0.34	1.26	-0.325
90	0.114	1.3	-0.325
100	-0.11	1.27	-0.325
120	-0.49	1.06	-0.325
150	-0.8	0.58	-0.325
170	-0.8	0.24	-0.4
180	0	0.1	0

Aerofoil dataset: LM37ROOT

Angle of Attack (deg)	Lift coefficient	Drag coefficient	Pitch moment coefficient
-180	0	0.6	0
-175	0	0.6	0
-170	0	0.6	0
-167	0	0.6	0
-160	0	0.6	0
-145	0	0.6	0
-120	0	0.6	0
-90	0	0.6	0
-60	0	0.6	0
-30	0	0.6	0
-20	0	0.6	0
-15	0	0.6	0
-10	0	0.6	0
-6	0	0.6	0
-2	0	0.6	0
2	0	0.6	0
4	0	0.6	0
6	0	0.6	0
8	0	0.6	0
10	0	0.6	0
12	0	0.6	0
14	0	0.6	0
16	0	0.6	0
18	0	0.6	0
20	0	0.6	0
25	0	0.6	0
30	0	0.6	0
40	0	0.6	0
50	0	0.6	0
60	0	0.6	0
70	0	0.6	0
80	0	0.6	0
90	0	0.6	0
100	0	0.6	0
120	0	0.6	0
150	0	0.6	0
160	0	0.6	0
165	0	0.6	0
170	0	0.6	0
175	0	0.6	0
180	0	0.6	0

Aerofoil dataset: Profile 3

Angle of Attack (deg)	Lift coefficient	Drag coefficient	Pitch moment coefficient
-180	0	0.1	0
-170	0.8	0.24	0.4
-150	0.8	0.58	0.325
-120	0.49	1.06	0.325
-90	-0.114	1.3	0.325
-60	-0.755	1.06	0.325
-30	-1.2	0.45	0.22
-20	-1.2	0.2	0.05
-15	-1.05	0.1	0
-10	-0.72	0.013	-0.11
-6	-0.265	0.01	-0.11
-2	0.1814	0.006	-0.11
2	0.6471	0.0061	-0.115
4	0.88	0.0071	-0.11
6	1.09	0.009	-0.11
8	1.26	0.012	-0.11
10	1.33	0.015	-0.11
12	1.33	0.034	-0.11
14	1.3233	0.069	-0.11
16	1.3067	0.1	-0.11
18	1.29	0.14	-0.11
20	1.2567	0.18	-0.11
25	1.1833	0.3	-0.12
30	1.14	0.48	-0.14
40	1.06	0.69	-0.18
50	0.93	0.9	-0.22
60	0.755	1.06	-0.26
70	0.555	1.18	-0.2925
80	0.34	1.26	-0.325
90	0.114	1.3	-0.325
100	-0.11	1.27	-0.325
120	-0.49	1.06	-0.325
150	-0.8	0.58	-0.325
170	-0.8	0.24	-0.4
180	0	0.1	0

Appendix C: MATLAB codes

This Appendix shows MATLAB codes for the loads calculation for 50 years loads extrapolation and deterministic lifetime damage equivalent loads.

C.1. Extreme load extrapolation

```
function [ExtremeLoad,Pe,x] = ExtrapolationOfDLC1p1(ReaData,Vel)
% The statistical extrapolation technique based on by long-term
% (50 year period) exceedance probability for the calculation extreme
loads.

% Initial conditions
b=0;
x = 0 : max(ReaData(:,6)) /100:5*max(ReaData(:,6));
Pe = 0 ;
Pve = 0 ;
g=0;

for k=1:length(Vel);

    g=g+1;

    % Find a load for specific wind speed as there are 6 seeds
    % per each wind speed
    [i,j]=find(ReaData==Vel(k));
    imin=min(i);
    imax=max(i);
    ReadataSec(:,:)=ReaData(imin:imax,:);
    % Calculate seeds number per wind speed
    windseed(1)=imax-imin+1;

    % Select the extreme load values, which is higher than the
threshold.
    % The value of threshold minimises the statistical uncertainties at
    % the low level of turbulence and increases accuracy of the generated
    % trend of extreme loads
    for n=1:windseed;

        b=b+1;

        % Specify a threshold for the extreme load values, which is equal
        % to the mean plus 1.4 times the standard deviation
        if ReadataSec(n,6)> ReadataSec(n,3)+1.4*ReadataSec(n,5)
           a(b)=1;
           MaximaData(k,n)=ReadataSec(n,6);

        else
            a(n)=0;
        end
    end
```

```
    MaximaDataSort(k,:) = sort(MaximaData(k,:)) ;

   % Estimation of the extreme value parameters,
   % The minus sign in frond of X is for evalution of maximum(+X for
minima )
   parameters = evfit (-MaximaDataSort(k,:));

   % Calculate short-term probability. Returns the cumulative
distribution
   % function (cdf) for the type 1 extreme value distribution
   % (Gumbel distribution),
   GumbelDist = evcdf (-x , parameters(1),parameters(2));

   % Define the number of maximum per 10 minute run. Divide by 6 as there
are
   % 6 seeds per each wind speed simulation
   N = length(MaximaDataSort)/6 ;

   % V(ave)=0.2*V(ref), Where, Vref (= 50 m/s) is the reference wind
speed
   % average over 10 min,
   Vave = 0.2*50 ;

   % Calculate long-term extreme loads extrapolation per each wind speed
   P_FVj = exp(-pi*((Vel(k)-1)/(2*Vave)).^2)-exp(-
pi*((Vel(k)+1)/(2*Vave)).^2);

   % Long-term extreme loads extrapolation equation
   Pe = Pe+(1-(1-GumbelDist).^N).*P_FVj;
   Pve = Pve + P_FVj;

end
% Calculate the extremes from the 50-year exceedance probability by using
% 50 year recurrence value ( = 3.8*10^(-7)) of the reference 10 minute
period.

a=(Pe<10^(-5) & Pe>10^(-9));
ExtremeLoad = interp1(Pe(a), x(a),(3.8*10^-7),'spline');

end
```

C.2. Deterministic lifetime damage equivalent loads

```
function [ L_lifeTimeDEL ] = PeriodicLifetimeDELs(Px, m, ReaData)
% Calculation of deterministic lifetime DELs

% Px - Weibull Distribution probability
% m - Wohler coefficient
% ReaData - load calculation per a specific wind speed

% Initial conditions:
% Velocity array for dlc 1.2
Vel=4:2:24;
% Number of cycles per 20 years
N=1E+7;
```

```
% Frequency of each cycle No.cycles per year over time of 20 years in
seconds
freq=N/(20*365*24*60^2);

% Time of each simulation
t_sim=600;


  for n=1:length(Vel);

        PowProd(n)=Px(2+n);
        % Find the load corresponded to specific speed
        [i,~]=find(ReaData(:,1)==Vel(n));
         imin=min(i);
         imax=max(i);
         ReadataSec(:,:)=ReaData(imin:imax,:);
         % Obtain a number simulations for a specific wind velocity
         NumWindSeed=imax-imin+1;
         PowProdVar(n)=PowProd(n)/(NumWindSeed);

        for k = 1:NumWindSeed;

            % Determine a number of cycles
            Cyc(n,k)=ReadataSec(k,6)/(2*pi)*t_sim;

            % Fatigue damage per cycle
            Li_Cyc(k)=(ReadataSec(k,7)^m)*Cyc(n,k);

        end

        % The total fatigue damage per wind speed in terms of DELs
        Ldel(n)=((sum(Li_Cyc))/(t_sim*freq))^(1/m);

        % Lifetime DELs at the particular wind speed for specific
Wohler coefficient
        Ldel_weig(n)=((Ldel(n)^m)*PowProdVar(n))^(1/m);

  end

    % The Lifetime DELs of particular Wohler coefficient
    L_lifeTimeDEL=(sum(Ldel_weig(:).^m))^(1/m);

end
```

Appendix D: Modifications of blade properties

This Appendix provides the figures of chapter 7 (blade structural properties), which exclude from the main body of the thesis. The first section corresponds to graphs of Lifetime DELs. The second section shows the graphs of extreme loads.

D.1. Lifetime DELs of edge-wise flap-wise blade root moments

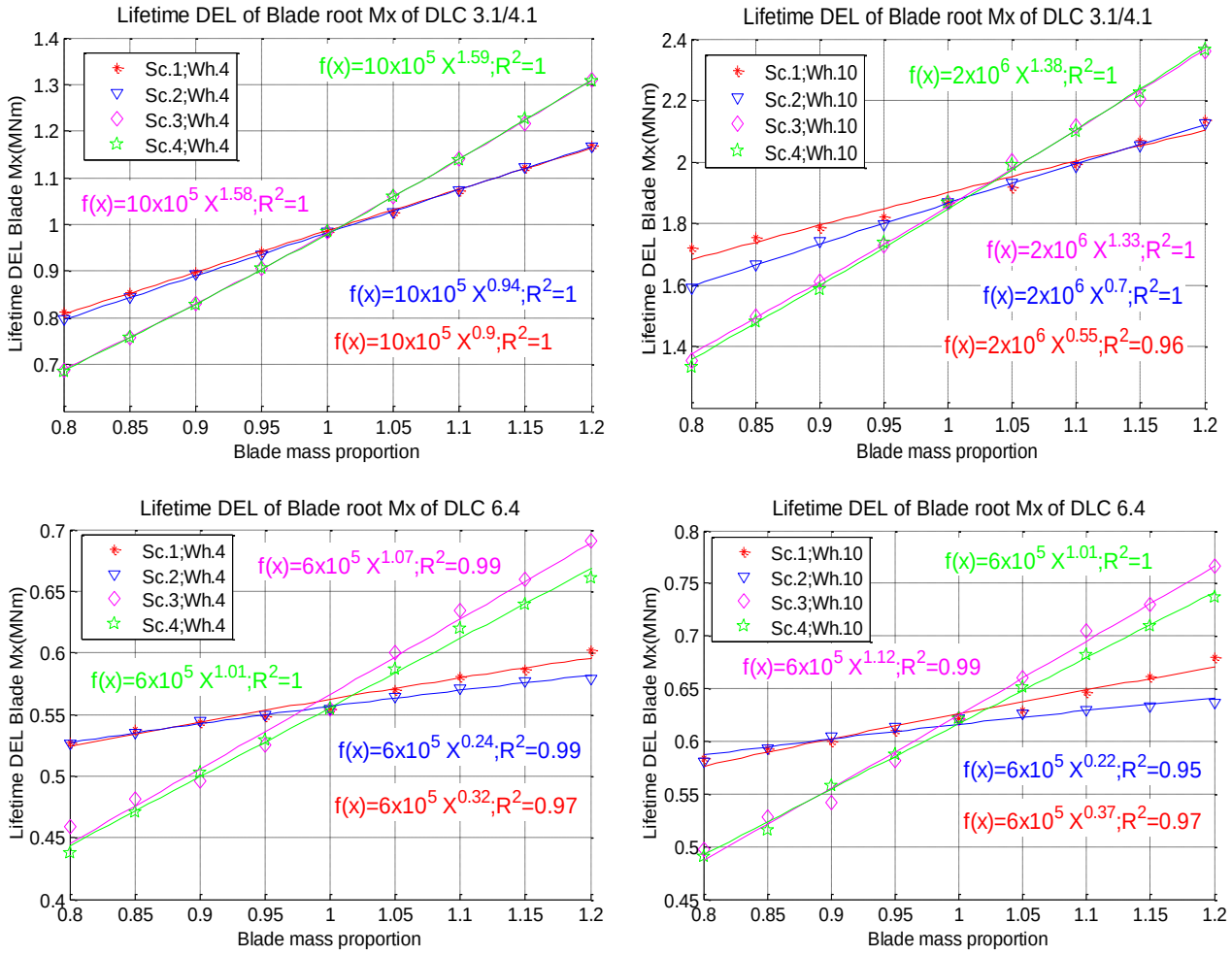

Figure 1: DLC 3.1/4.1 and 6.4 lifetime DELs of **edge-wise blade root bending moment** of four scenarios of different blade modifications for Wohler coefficient 4 and 10.

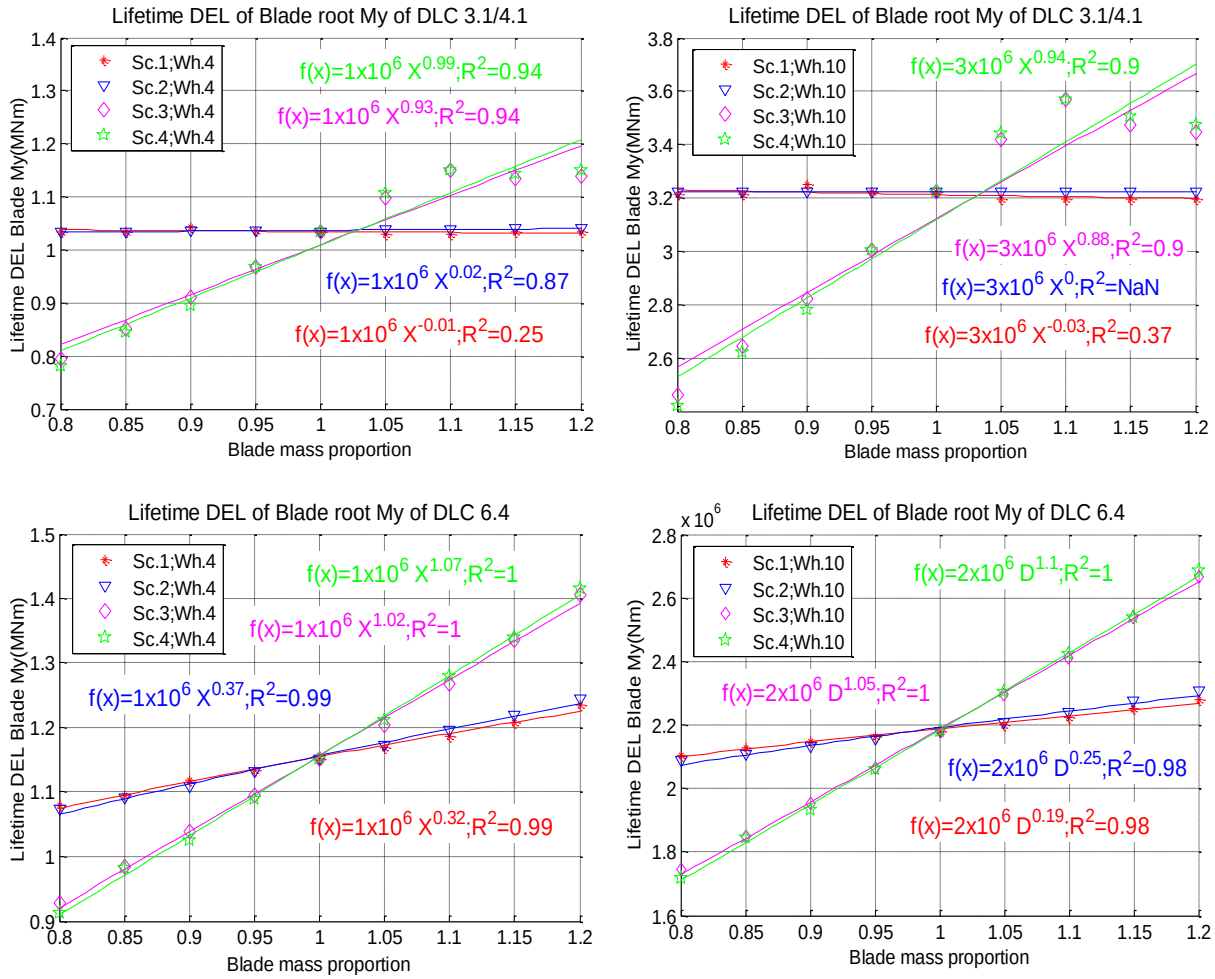

Figure 2: DLC 3.1/4.1 and 6.4 lifetime DELs of **flap-wise blade root bending moment** of four scenarios of different blade modifications for Wohler coefficient 4 and 10.

D.2. Extreme loads of edge-wise flap-wise blade root moments:

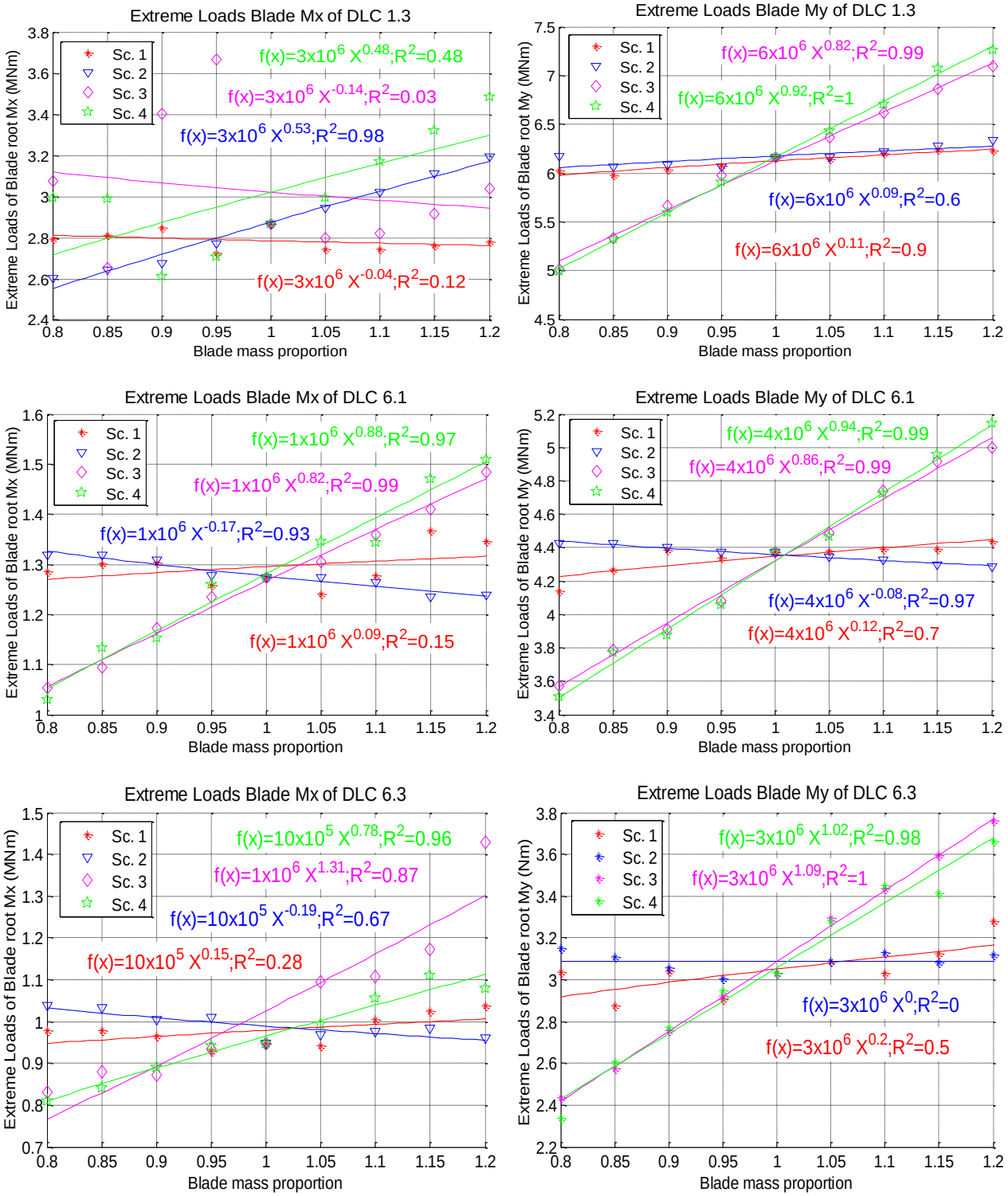

Figure 3: Edge-wise and flap-wise blade root extreme moments of DLC 1.3, 6.1 and 6.3 for the four scenarios of the blades modifications

Appendix E: Rotor solidity

This Appendix has the related information of chapter 8 (Rotor solidity). There are two parts of the Appendix, which correspond to the two methods of modifications for the rotor solidity, as chapter 8. The first part relates to the method of tip speed ratio impact and the second one is for the method of chord impact.

E.1. Tip speed ratio impact

This section consists of three subsections, which correspond to validation of applied modifications, lifetime DELs and extreme loads.

E.1.1. Validation of performed changes

In this study one of validation methods is the spectral analysis. This subsection displays the graph of power spectral density and cumulative spectral density, which were not placed in the main body of the thesis. Additionally, the description for the graphs is provided.

E.1.1.1. Blade root flap-wise moment:

Figure E.1 depicts the two graphs of PSD and cumulative PSD of flap-wise blade root moment, respectively. The curves of Figure E.1 show similar characteristics as the PSD curves of edge-wise blade root moment in Figure E.1 from the previous subsection. The values of the rotor frequency and its harmonics of each curve are completely identical to the values of the edge-wise blade root curves. Nevertheless, the frequency values of structural modes are dissimilar between the edge-wise and flap-wise blade moments due to the shape of blade. Therefore, the frequency of structural flap-wise modes is lower than the frequency of edge-wise modes in the modified and reference models. It confirms that the reference wind turbine model was designed correctly as it was mentioned before. It also points that the modified models were modified properly. Figure E.1 shows there are no un-damped peaks, which are higher than 1P for each curve. Hence, the

modification of rotor solidity did not generate any negative effects according to flap-wise blade root moment.

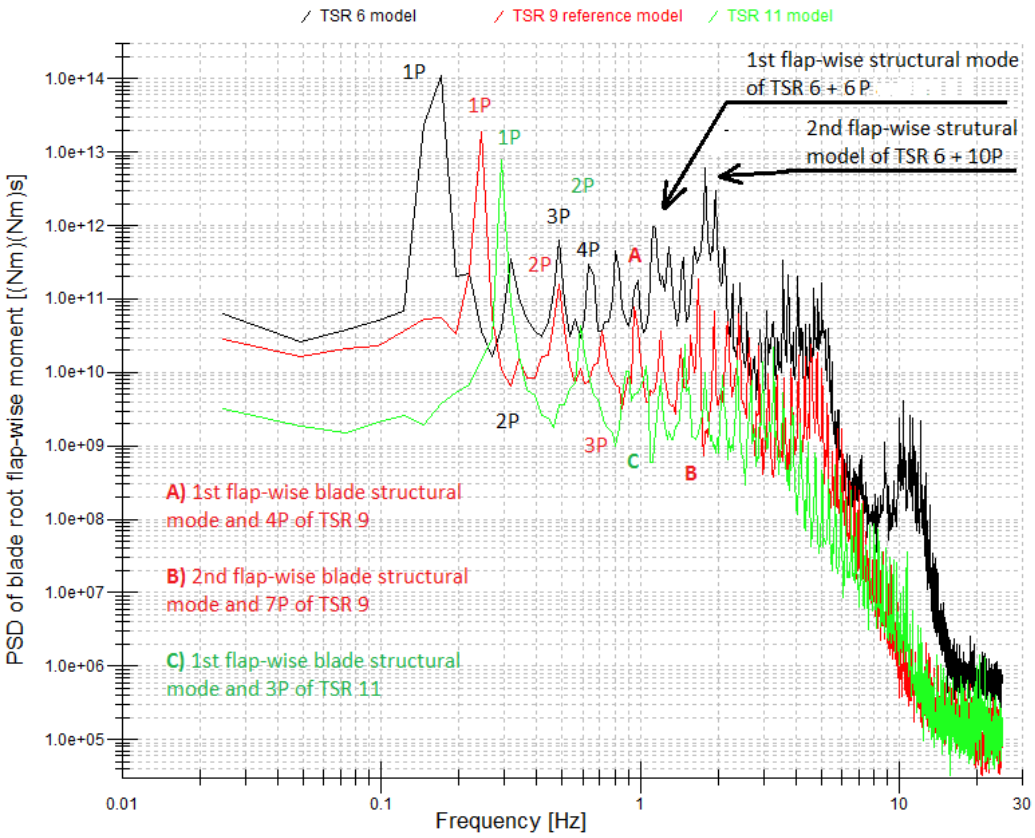

Figure E.1: PSD of blade root flap-wise moment of TSR 6, 9 and 11 at 16 m/s mean wind speed.

E.1.1.2. Low-Speed shaft moment:

This section provides the overview of changes for low-speed shaft moment. The two graphs of PSD and cumulative PSD curves of low speed shaft moment are depicted by Figure E.2.

The most part of peaks are labelled as shown in the first graph of Figure E.2. The graph of cumulative PSD shows that the harmonics peaks of 1P and structural modes are adequate damped for TSR 9 and 11 models as the cumulative PSD curves of TSR 9 and 11 do not have significant rises apart from *1P*. However, the curve TSR 6 model does not follow by the same description because the cumulative PSD graph shows the significant upsurges of the curve of TSR 6 model, which affect the fatigue loads. Moreover, it looks like peak A of TSR 6 model is not damped because it is very narrow (e.g. has a shape of spike) and has same height as 1P of TSR 6 model. In the PSD cumulative

graph peak A is characterised by large rise. Possibly this peak represents the coupling of the coincident frequency between the 2nd flap-wise structural mode and *11P* harmonic of rotor frequency. It is obvious that this peak produces the significant impact on low speed shaft moment, which will be shown in section E.1.2 and E.1.3 corresponded to the analysis of fatigue and extreme loads.

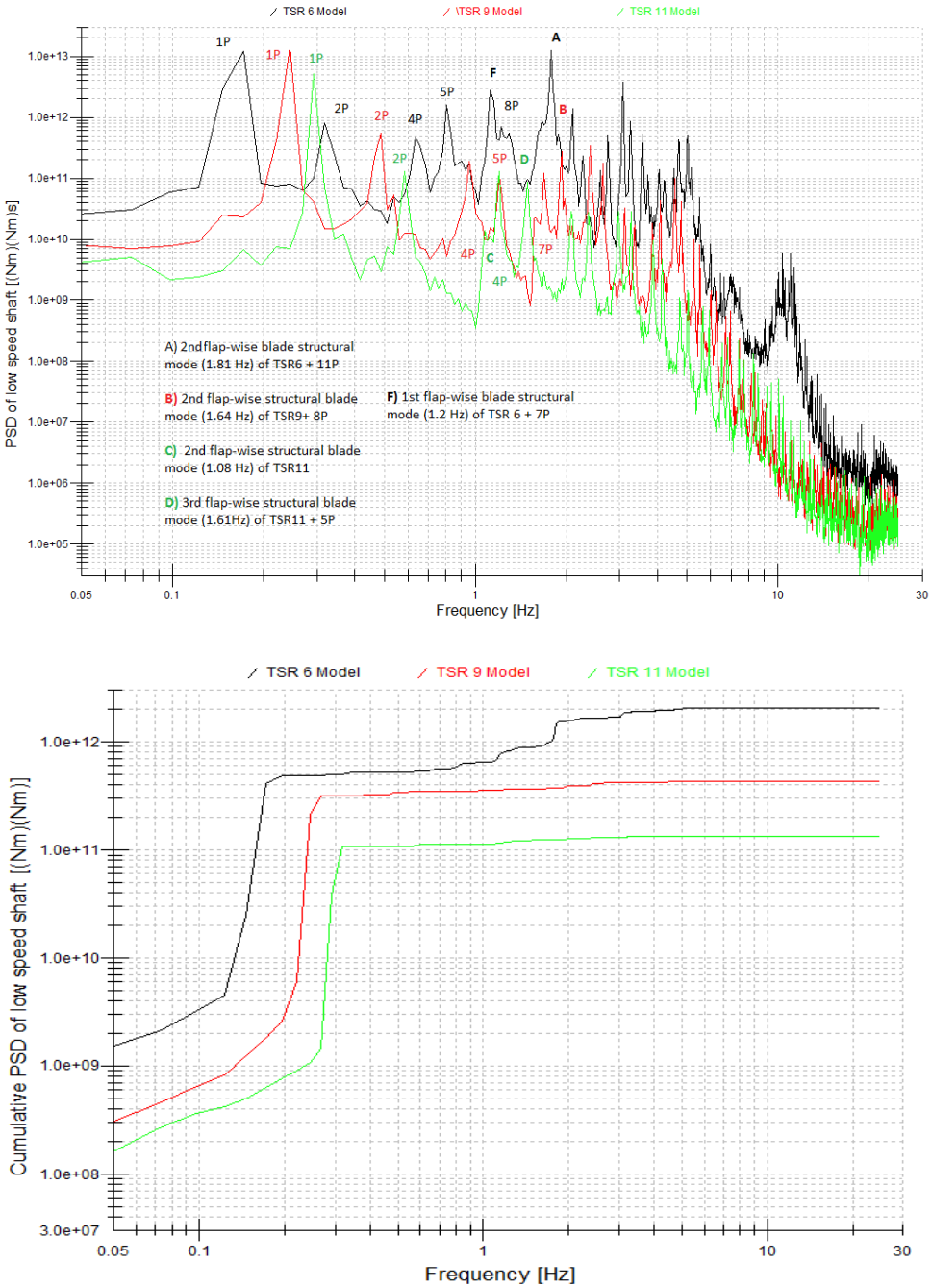

Figure E.2: PSD and cumulative PSD of low-speed shaft moment of TSR 6,9 and 11 at 16 m/s mean wind speed, respectively.

E.1.1.3. Yaw bearing moment

The changes of yaw bearing loads in the modified models are shown by Figure E.3, which depicts the PSD and cumulative PSD of yaw bearing moments. The labels of the peaks are provided in the graph. The PSD curves of TSR 9 and 11 models do not demonstrate any unusual behaviour as harmonics peaks of *3P* are not higher *3P* peak itself. However, the height of 3P harmonics is almost similar to the height of *3P*, which shows the significant amount of energy carried by these peaks. The energy is a source of significant fatigue loads as shown by the rises in the cumulative PSD curves of TSR 9 and 11 models in Figure E.4. The PSD curve of TSR 6 model demonstrates the behaviour, where the harmonics peaks are higher than *3P*, especially *12P* harmonic. It is most likely the frequency of *12P* harmonic peak locates in the vicinity to the frequency of the 2nd flap-wise structural mode because *12P* peak is not damped as revealed by the shape and height of this peak. The cumulative PSD curve of TSR 6 has larger rises than the curve of TSR 9. So TSR 6 model will have much larger fatigue loads than the reference model.

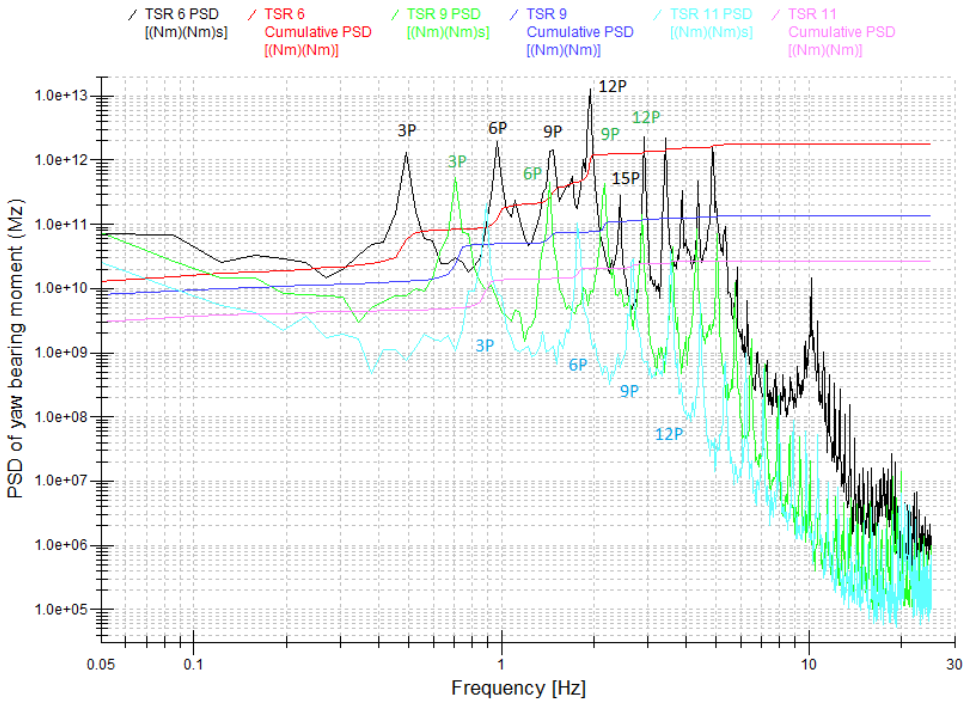

Figure E.5: PSD and cumulative PSD of yaw bearing moment of TSR 6, 9 and 11 at 16 m/s mean wind speed.

E.1.2. Fatigue loads analysis

This subsection presents lifetime DELs of low-speed shaft and yaw bearing moments for design load cases (DLCs): 1.2, 3.1/4.1 and 6.4. These DLCs characterise the normal power production, summation of start-ups and shut downs and idling operational conditions, respectively. Figure E.6 and E.7 depict graphs of Lifetime DELs of low-speed shaft and yaw bearing moments.

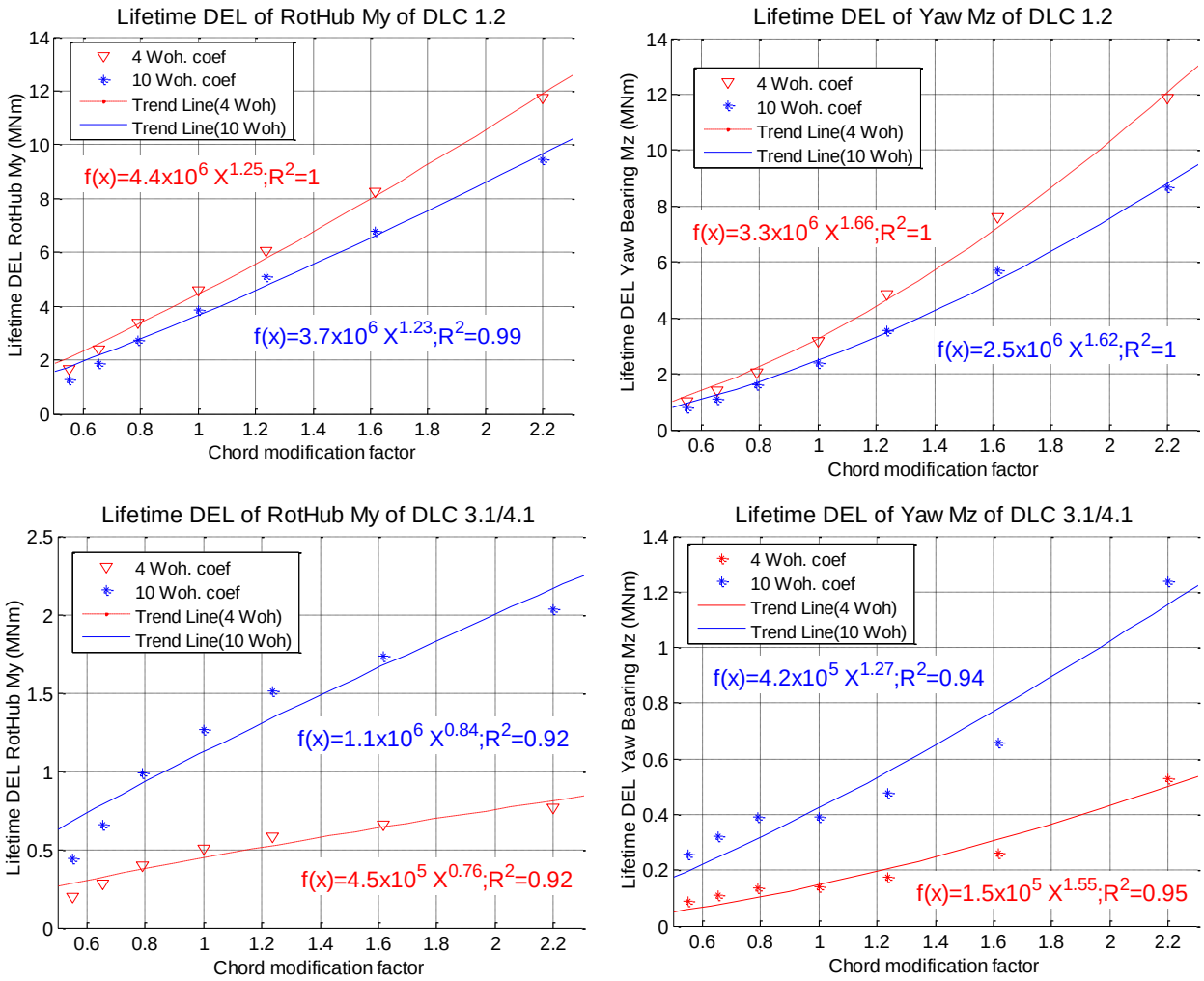

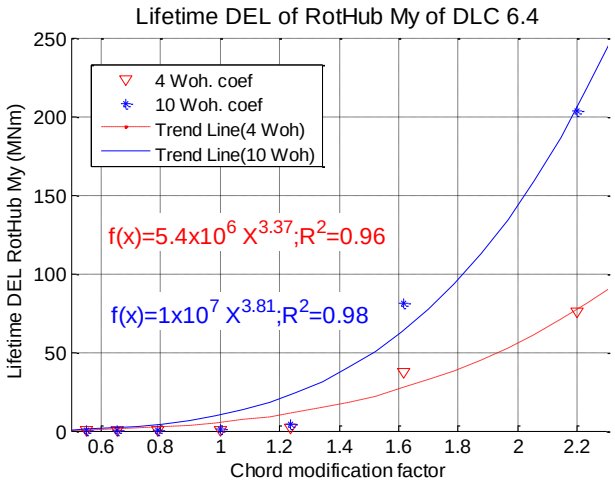

Figure E.6: DLC 1.2, 3.1/4.1 and 6.4 lifetime DELs of low-speed shaft moments for Wohler coefficient 4 and 10.

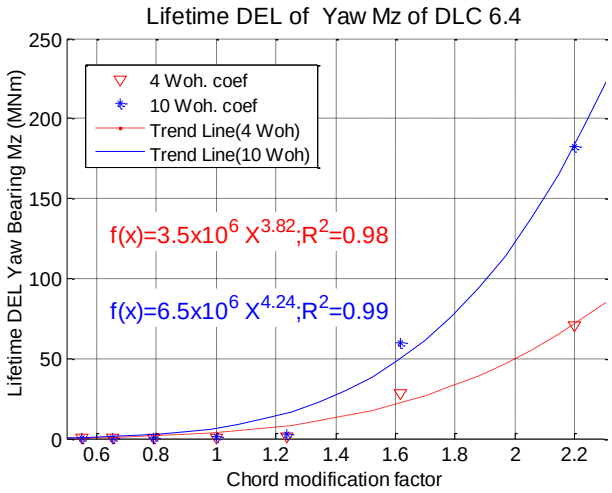

Figure E.7: DLC 1.2, 3.1/4.1 and 6.4 lifetime DELs of yaw bearing moments for Wohler coefficient 4 and 10.

E.1.3. Extreme loads

This subsection shows the changes of extreme moments of blade root, low-speed shaft, yaw bearing and tower base for design load cases 1.3, 6.1 and 6.3. DLC 1.3 corresponds to normal power production conditions with the extreme turbulence conditions. DLC 6.1 and 6.3 refer to idling condition of a wind turbine with extreme 50 year wind speed, which are 50 and 40 m/s for DLCs 6.1 and 6.3 respectively. Additionally, DLC 6.3 corresponds to the extreme yaw misalignment.

Figure E.8 depicts the extreme moments of edge-wise and flap-wise blade root for the above mentioned DLCs.

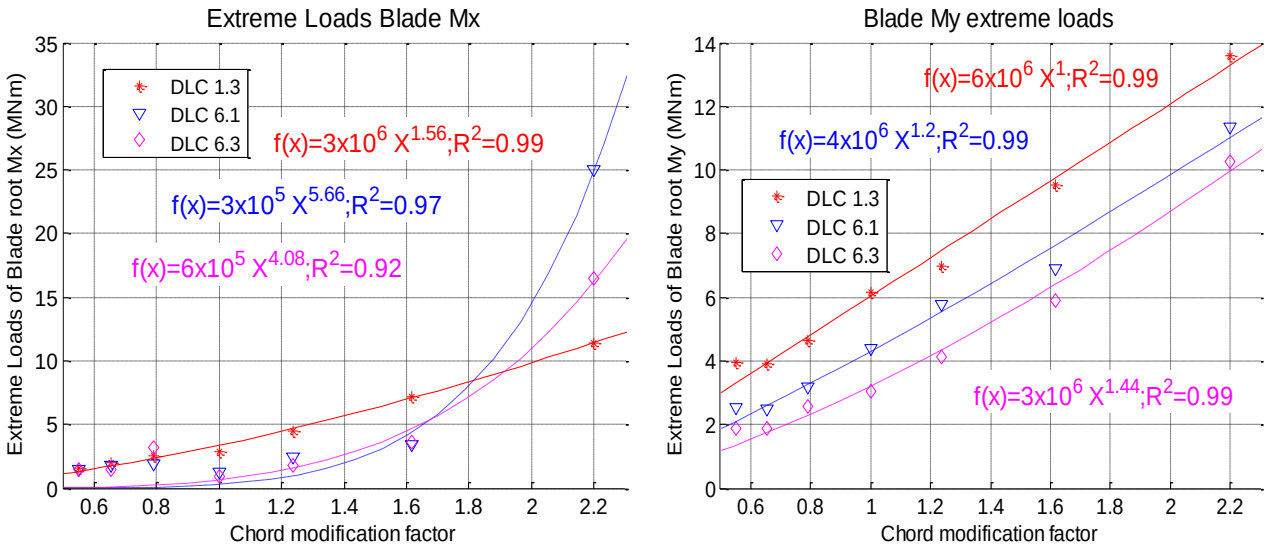

Figure E.8: DLC 1.3, 6.1 and 6.3 extreme moments of edge-wise and flap-wise blade root.

The extreme moments of low-speed shaft, yaw bearing and tower fore-aft base are demonstrated by Figure E.9. The three DLCs are

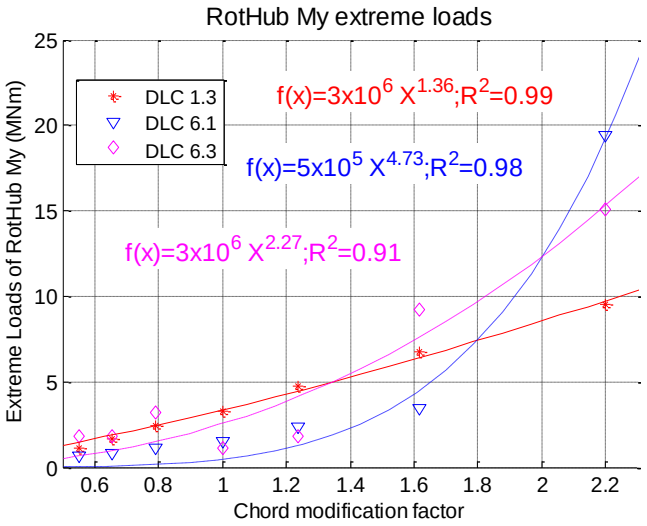

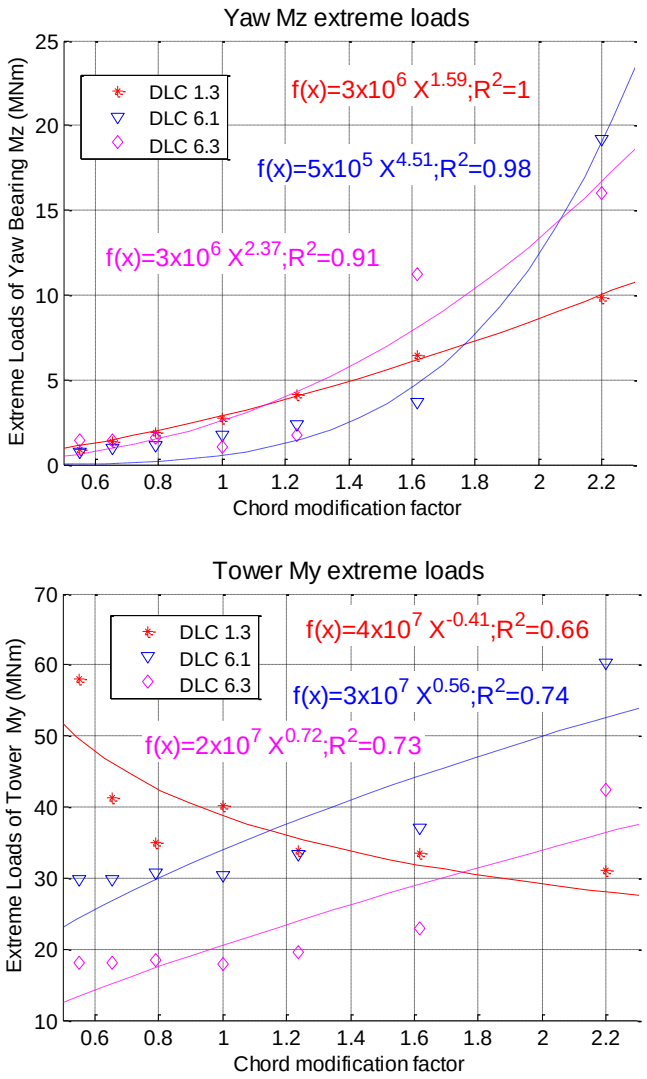

Figure E.9: DLC 1.3, 6.1 and 6.3 extreme loads of low speed shaft, yaw bearing and fore-aft tower base moment.

E.2. Chord impact

This section consists of three subsections, which correspond to validation of applied modifications, lifetime DELs and extreme loads.

E.2.1. Validation of performed changes

This section displays the graph of power spectral density and cumulative spectral density, which were not placed in the main body of the thesis, with the description. This section includes four subsections, which correspond to flap-wise blade root, overturning low speed shaft, yaw bearing and tower base fore-aft moments.

E.2.1.1. Blade root flap-wise moment

Figure E.10 shows the PSD and cumulative PSD graph of flap-wise blade root moment of the above mentioned three models. The flap-wise curves of the modified models resemble the characteristics of the edge-wise moments, which ware explained in section 8.2.2.2.1. The two graphs of flap-wise blade root moment do not show any excessive loads as a consequence of the introduced modifications of rotor solidity. Thus, the controller of modified wind turbines works adequately to suppress the side effect of the changes of natural frequency of blades.

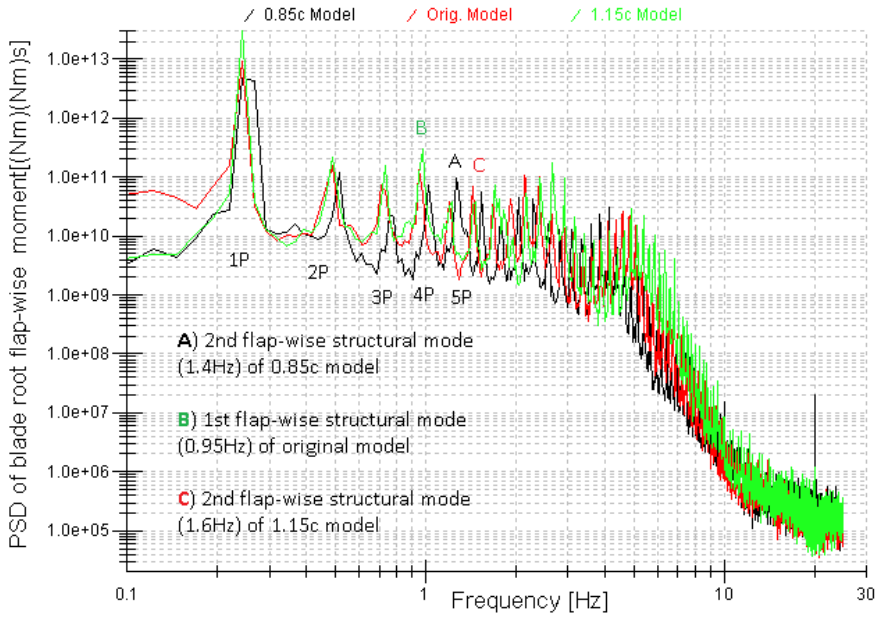

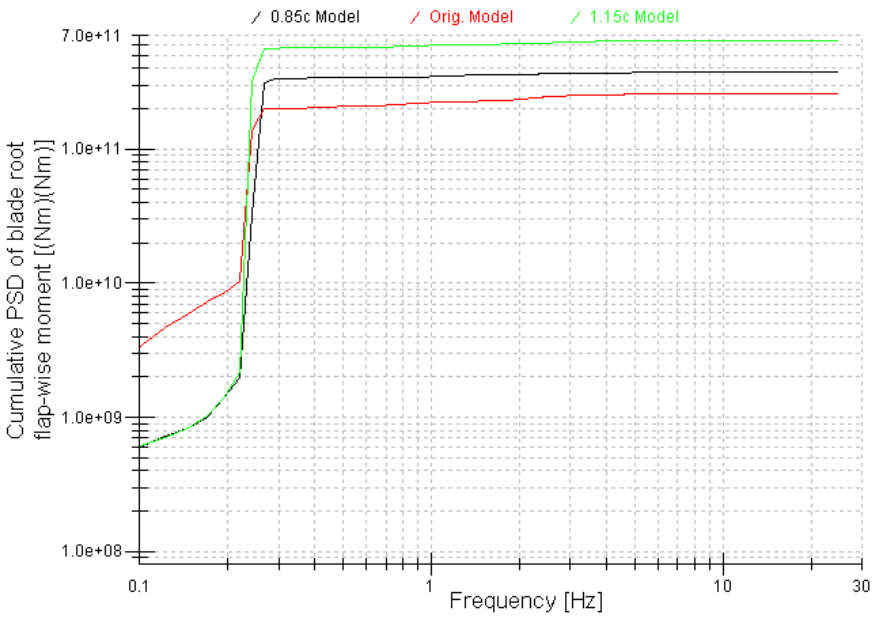

Figure E.10: PSD and cumulative PSD of blade root flap-wise moment of 0.85c, original and 1.15c models at 16 m/s mean wind speed.

E.2.1.2. Low-Speed shaft moment

Figure E.11 provides the overview of low-speed shaft moment. There are PSD and cumulative PSD curves are located at the same graph. There is the similar behaviour of the mismatching the frequency of *1P* and its harmonic peaks between the *0.85c* model and reference model, which was explained in section 8.2.2.2.1. The PSD curve of 1.15 model shows that the flap-wise blade structural modes have an impact onto low speed shaft moment as the frequency of these modes is located at the vicinity to harmonic peaks of 1P. The vicinity between two frequencies generates the unplanned loads, which labelled by A and C as shown in Figure E.11. However, these generated loads of A and C peaks are damped because these peaks are not characterised by significant rises at the cumulative PSD curve of *1.15c* model as depicted in Figure E.11.

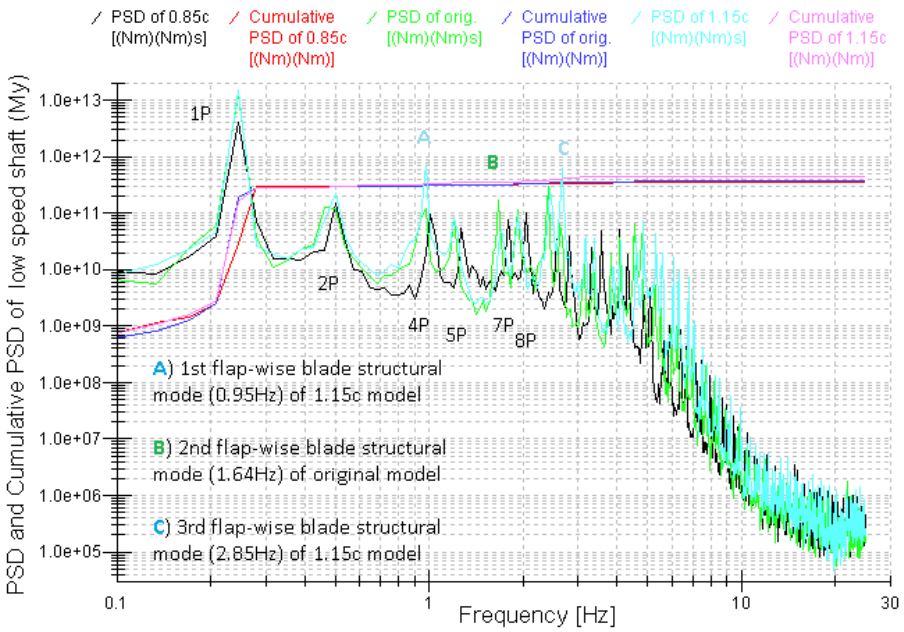

Figure E.11: PSD and cumulative PSD of low speed shaft moment of 0.85c, original and 1.15c models at 16 m/s mean wind speed.

E.2.1.3. Yaw bearing moment

Figure E.12 illustrates the PSD and cumulative PSD of yaw bearing moment in single graph to notice any changes in yaw bearing moment as a result of the applied modifications. There is a mismatch of frequency of *3P, 6P, 9P, 12P* and etc. between the *0.85c* and reference models as a result of shifted *1P* frequency of *0.85c* model. Peaks of *3P, 6P, 9P* and *12P* generate significant impacts onto fatigue loads for all three models as shown by the rises of cumulative PSD curves, which correspond to the abovementioned peaks.

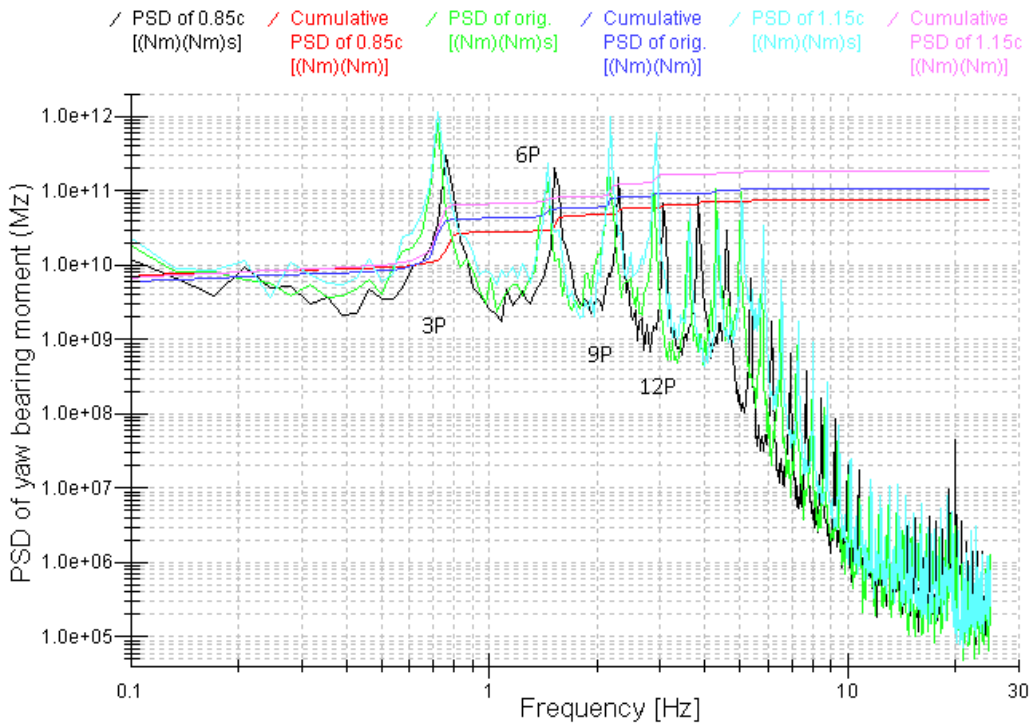

Figure E.12: PSD and cumulative PSD of yaw bearing moment of 0.85c, original and 1.15c models at 16 m/s mean wind speed.

E.2.1.4. Tower base moment

The PSD and cumulative PSD curves of fore-aft tower base moment are illustrated in Figure E.13 to investigate the changes of the modified models compared to the original model. There is mismatch of *3P* between the *0.85c* and reference model due to rotor speed alterations to maintain the original power curve of reference model. The cumulative PSD curves demonstrate that the all peaks are damped as the cumulative PSD curves do not show any sharp rises, apart from the peak tower fore-aft translational mode at low frequency. Therefore it is possible to state that there are no unexpected loads, which emerged from the modifications, at the tower fore-aft base loads.

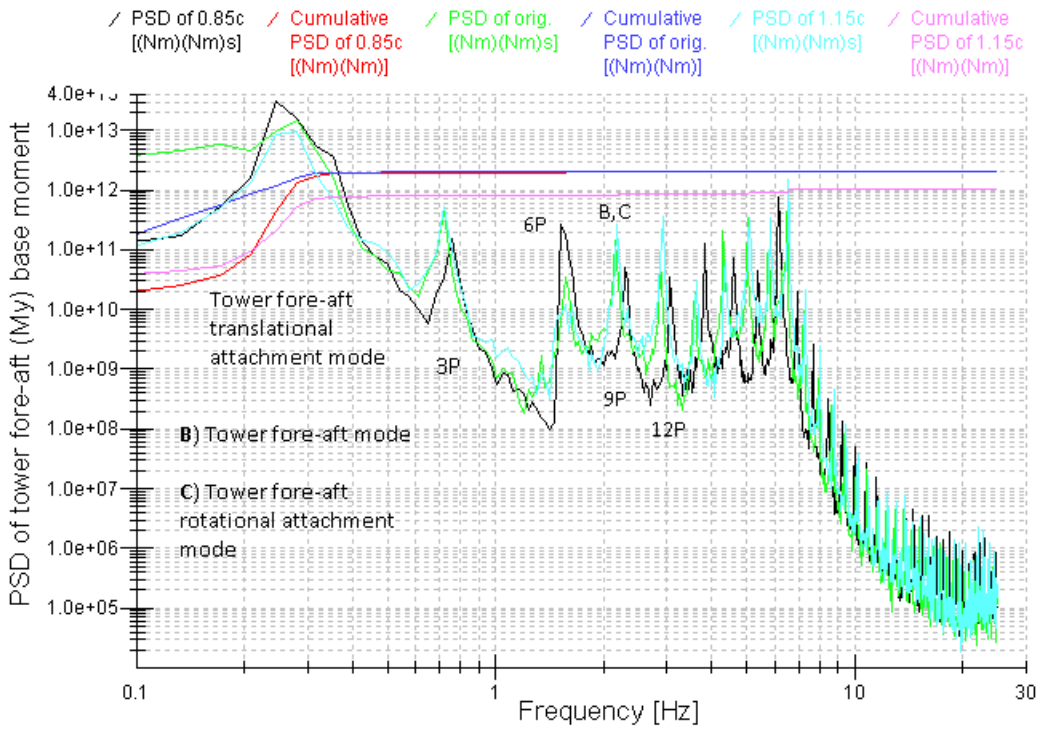

Figure E.13: PSD and cumulative PSD of fore-aft tower base moment of 0.85c, original and 1.15c models at 16 m/s mean wind speed.

E.2.2. Fatigue loads analysis

This subsection presents lifetime DELs of low-speed shaft and yaw bearing moments for design load cases (DLCs): 1.2, 3.1/4.1 and 6.4. Figure E.14 and E.15 depict graphs of Lifetime DELs of low-speed shaft and yaw bearing moments.

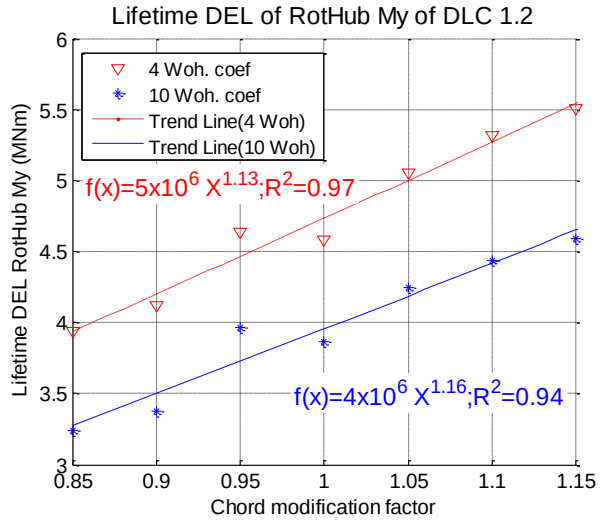

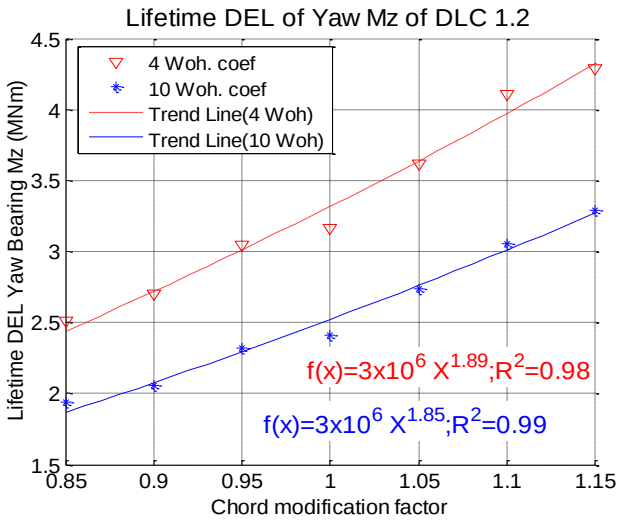

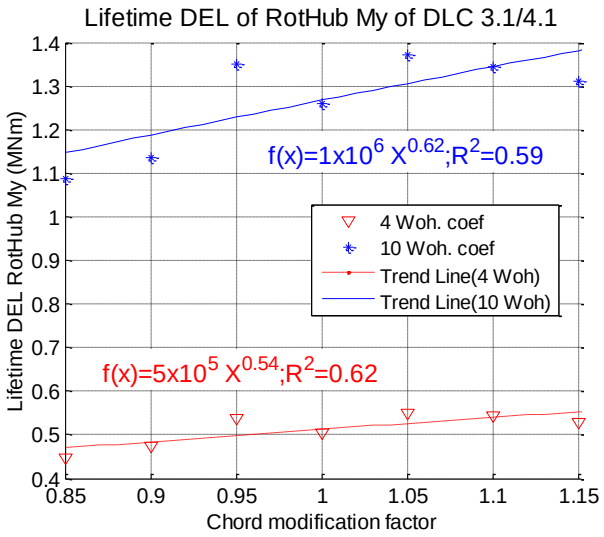

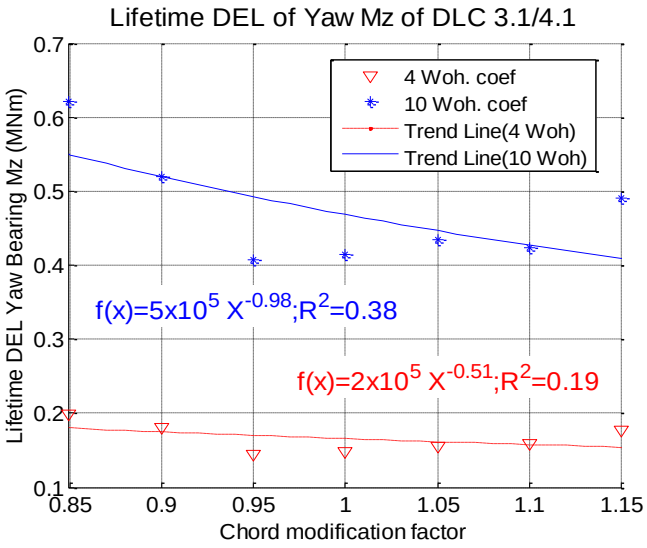

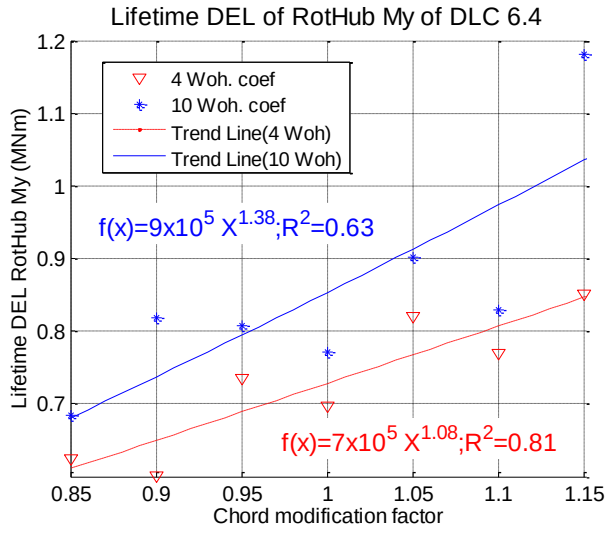

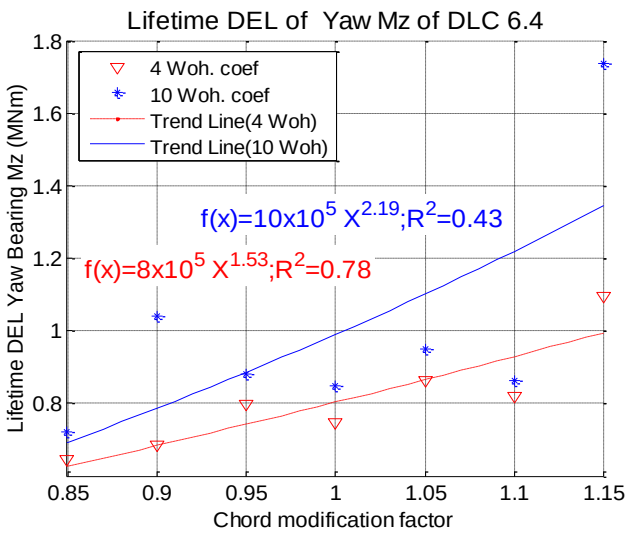

Figure E.14: DLC 1.2, 3.1/4.1 and 6.4 lifetime DELs of low-speed shaft moments for Wohler coefficient 4 and 10.

Figure E.15: DLC 1.2, 3.1/4.1 and 6.4 lifetime DELs of yaw bearing moments for Wohler coefficient 4 and 10.

E.2.3. Extreme loads

This subsection shows the changes of extreme moments of blade root, low-speed shaft, yaw bearing and tower base for design load cases 1.1, 1.3, 6.1 and 6.3. DLC 1.1 referrers to the statistical extrapolation technique based on by long-term (50 year period) exceedance probability for the calculation of extreme loads at a wind flow with normal turbulence model. This section is divided into two parts, where the first part displays the changes of the above mentioned extreme moments in respect of DLC 1.1. The second part shows the changes in terms of DLC 1.3, 6.1 and 6.3.

E.2.3.1. Design load case (DLC) 1.1

Figure E.16 depicts the changes of edge and flap wise bladed root extreme moments in respect of DLC 1.1. The changes of rotating hub and yaw bearing extreme moments are shown in Figure E.17.

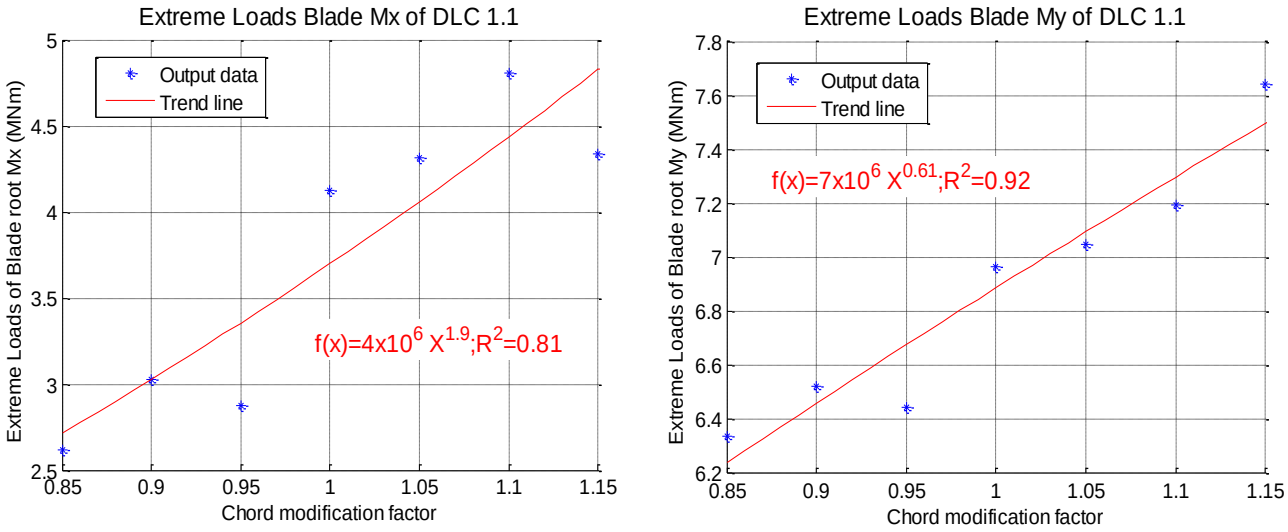

Figure E.16: DLC 1.1 extreme loads of edge-wise and flap-wise blade root moments.

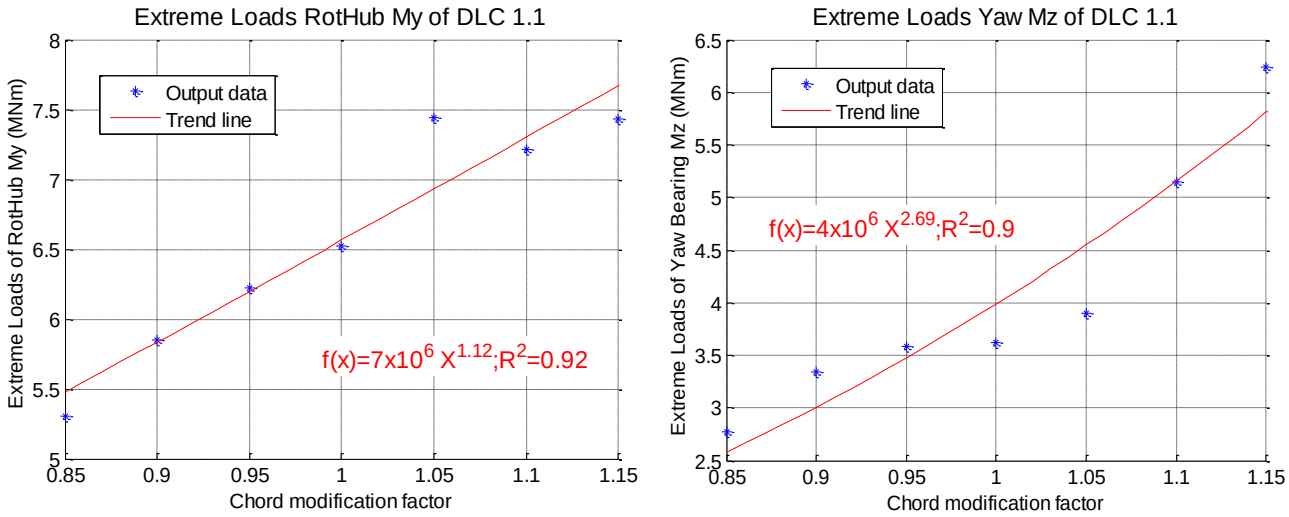

Figure E.17: DLC 1.1 extreme loads of low speed shaft, and yaw bearing moment, when the original value of TSR is maintained.

E.2.3.2. Design load cases (DLCs) 1.3, 6.1 and 6.3

Figure E.18 depicts the changes of low-shaft, yaw bearing and tower base fore-aft extreme moments in terms of DLC 1.3, 6.1 and 6.3.

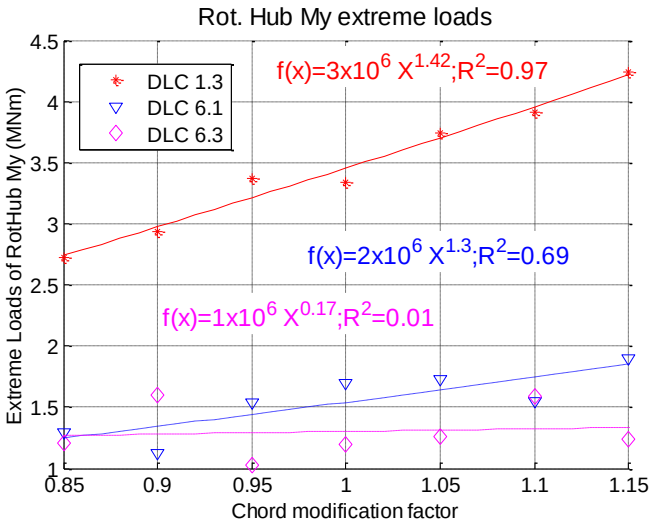

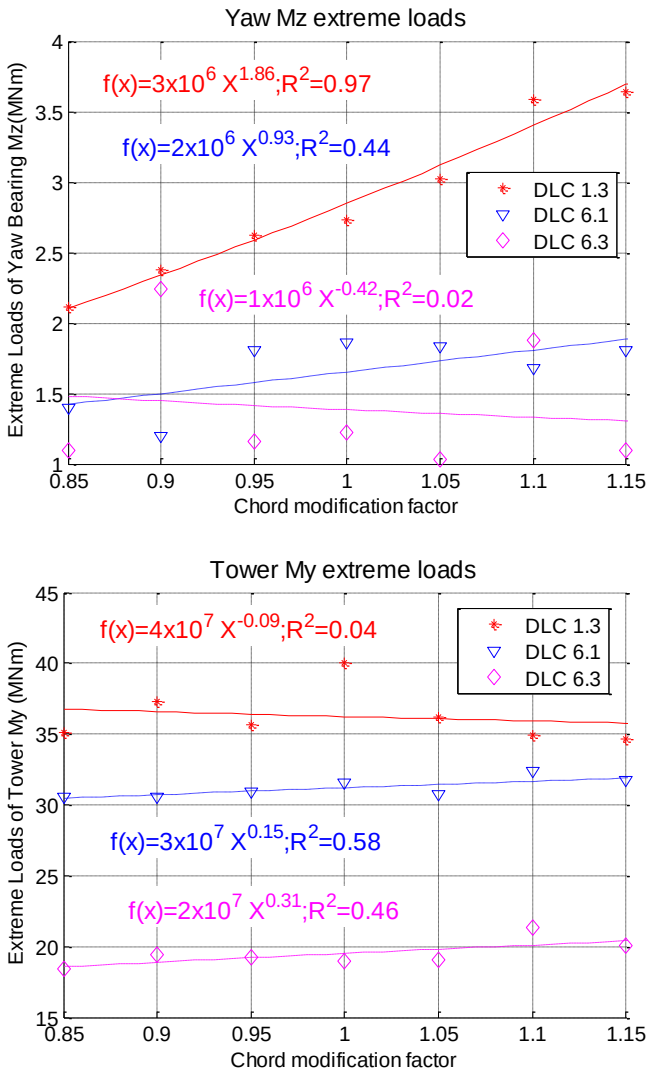

Figure E.18: DLC 1.3, 6.1 and 6.3 extreme loads of low speed shaft moment.

Appendix F: Additional calculations

This Appendix consists of two sections. The first section or F.1 provides comparison between simple PI and sophisticated controllers. Section F.2 presents the power spectral analysis for flap-wise blade root, low-speed shaft, yaw bearing and tower fore-aft base moments

F.1. Comparison of controllers

This section demonstrates the comparison between the simple PI controller without the tower feedback look and sophisticated controller of the reference model, which includes the tower feedback loop. The goal of tower feedback loop reduces the pitch activity of blades. Figure F.1 shows the pitch activity of up-scaled wind turbine model, which is has 8 MW rated power, to compare the pitch activity of both controllers. Each of controllers is tested by the identical turbine model (8 MW rated power), which was developed by the using the scaling with similarity, at 14 m/s mean wind speed.

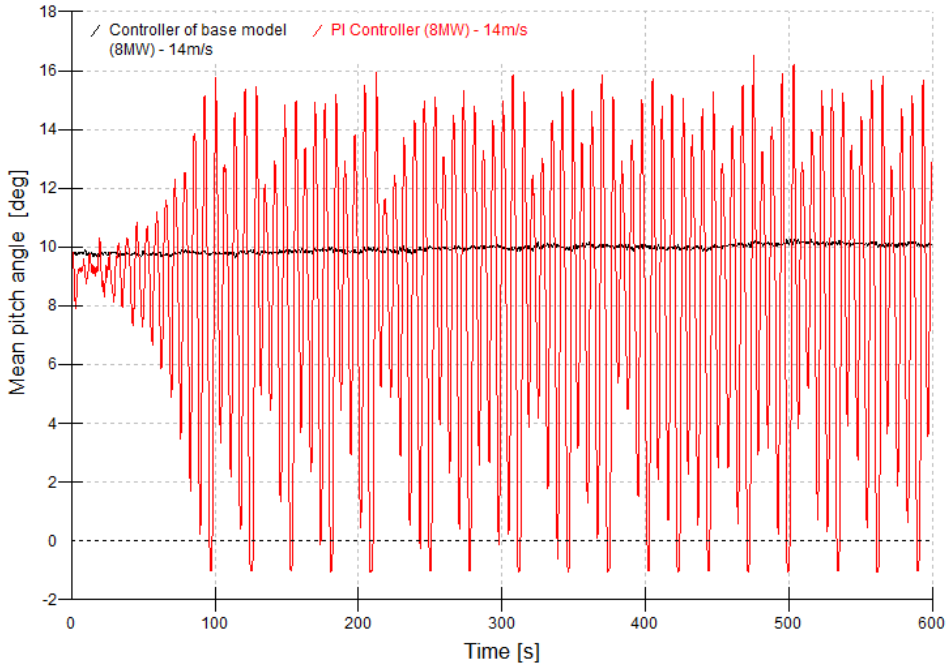

Figure F.1: Pitch activity of sophisticated and simple PI controllers

Figure F.1 demonstrates the significant difference between the pitch activities of the two wind turbine models. The pitch angle of model with the sophisticated controller varies between 9.65

and 10.25°. For the wind turbine model with simple PI controller the variation of mean pitch angle is from -1 till 16° as shown in Figure F.1.

The figure of pitch activity reveals the major dissimilarity between the two controllers. It is necessary to look at the tower top fore-aft movement for each wind turbine model with the sophisticated and simple PI controller. Hence, Figure F.2 depicts the tower top fore-aft displacement of both models to compare the controllers in terms of the nacelle movement. Figure F.2 demonstrates the same characteristics between the two controllers as Figure F.1. The nacelle fore-aft displacement of the wind turbine model with the original controller varies from 0.37 up to 0.44 meters, but the nacelle displacement of model with the PI controller is from -0.8 till 1.7 meters.

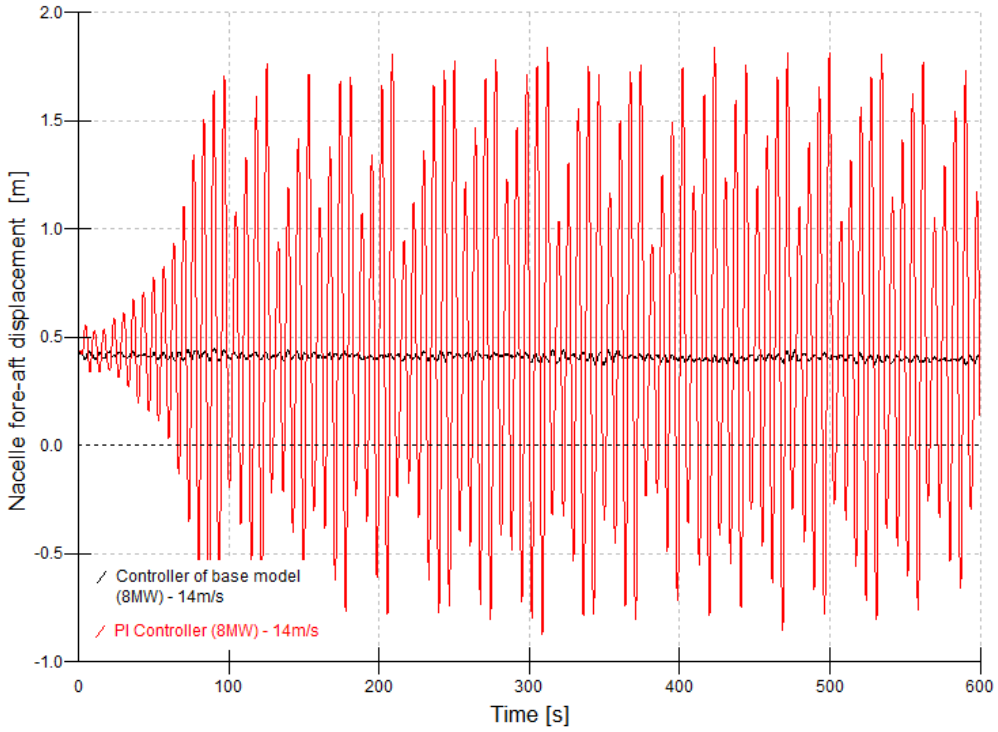

Figure F.2: Nacelle fore-aft displacement of wind turbines with sophisticated and simple PI controller

The excessive tower top fore-aft displacement of the simply PI controller produces the large trust on the wind turbine model. Consequently, this large thrust leads to significant impact onto the fatigue loads. Figure F.3 and F.4 show the comparison between the two controllers for blade root flap-wise and tower base fore-aft fatigue moments, which will be expressed in terms of the lifetime DELs. Each Figure of F.3 and F.4 consists of two graphs, which correspond to the simply PI controller and original controller of the reference model, respectively. The each of these graphs

depicts the output data with the power trend lines and its equations for the Wohler coefficient 4 and 10, which characterise steel and composite materials.

The comparison of Figure F.3 demonstrates that the output data of 7, 8, 9 and 10MW models with the simple PI controller are shifted up compared to the same wind turbine models with the original controller. Consequently, both exponents of power trend line for wind turbine models with the simple PI controller are significantly higher than the exponents of trend line for the wind turbines with original controller, which are almost match to estimated exponents by the scaling with similarity.

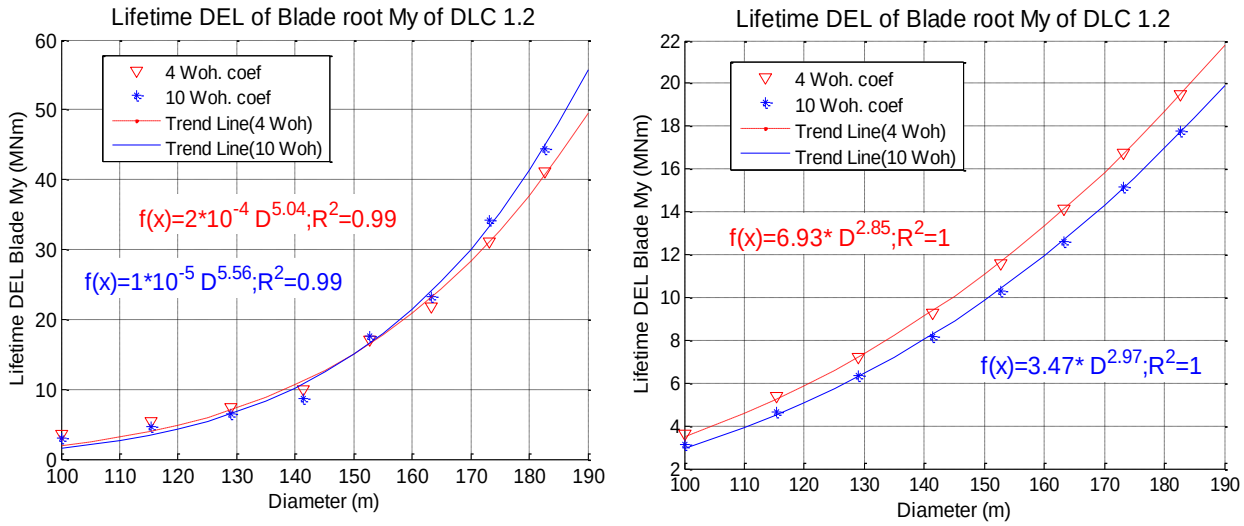

Figure F.3: DLC 1.2 lifetime DELs of flap-wise blade root bending moments between the PI and sophisticated controller**.**

The comparison of Figure F.4 displays the same characteristics for the tower base fore-aft fatigue moment as for blade root flap-wise fatigue moments. However, the exponents of the power trend line for models with PI controllers are much larger than the exponents of trend line for the machines with the original controller, because the nacelle fore-aft motion has more severe impact onto the tower base than the blade roots when the machines fitted by the simple PI controller.

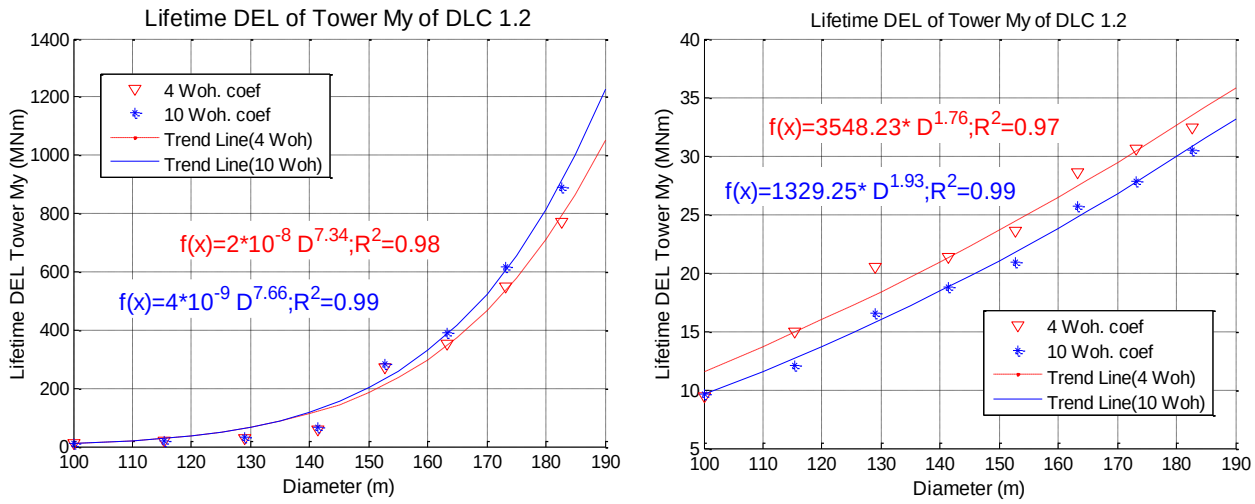

Figure F.4: Comparison of outputs DLC 1.2 lifetime DELs of tower base fore-aft bending moments between the PI and sophisticated controller.

The four figures have showed that the simple PI controller generates excessive pitch activity, which leads to the significant loads for 7, 8, 9 and 10 MW wind turbine models. Consequently, the controller system cannot employ the PI simple controller for above rated strategy as the produced excessive loads. As a result the original controller of reference wind turbine model, which includes the tower feedback, is applied as the above rated controller for the all up-scaled models in order to reduce the pitch activity and produced the output data of loads without excessive thrust force.

F.2. Dynamic state analysis

The dynamic state analysis is a part of the validation for the scaling procedure which was employed in this study. The dynamic state analysis applies spectral analysis investigates the behaviour of up-scaled models in terms dynamic conditions. This section includes the overview of such moment as: flap-wise of blade root, low-speed shaft, yaw bearing and fore-aft tower base.

F.2.1. Flap-wise blade root moment

The graphs of PSD and cumulative PSD of blade root flap-wise moment are presented in figure F.5. The curves of the up-scaled models demonstrate the similar characteristics as the edge-wise curves of up-scaled machines at section 9.2.2.1 in terms of the shifted peaks. The graphs of PSD and cumulative PSD do not reveal any undesirable effects at the up-scaled wind turbine models.

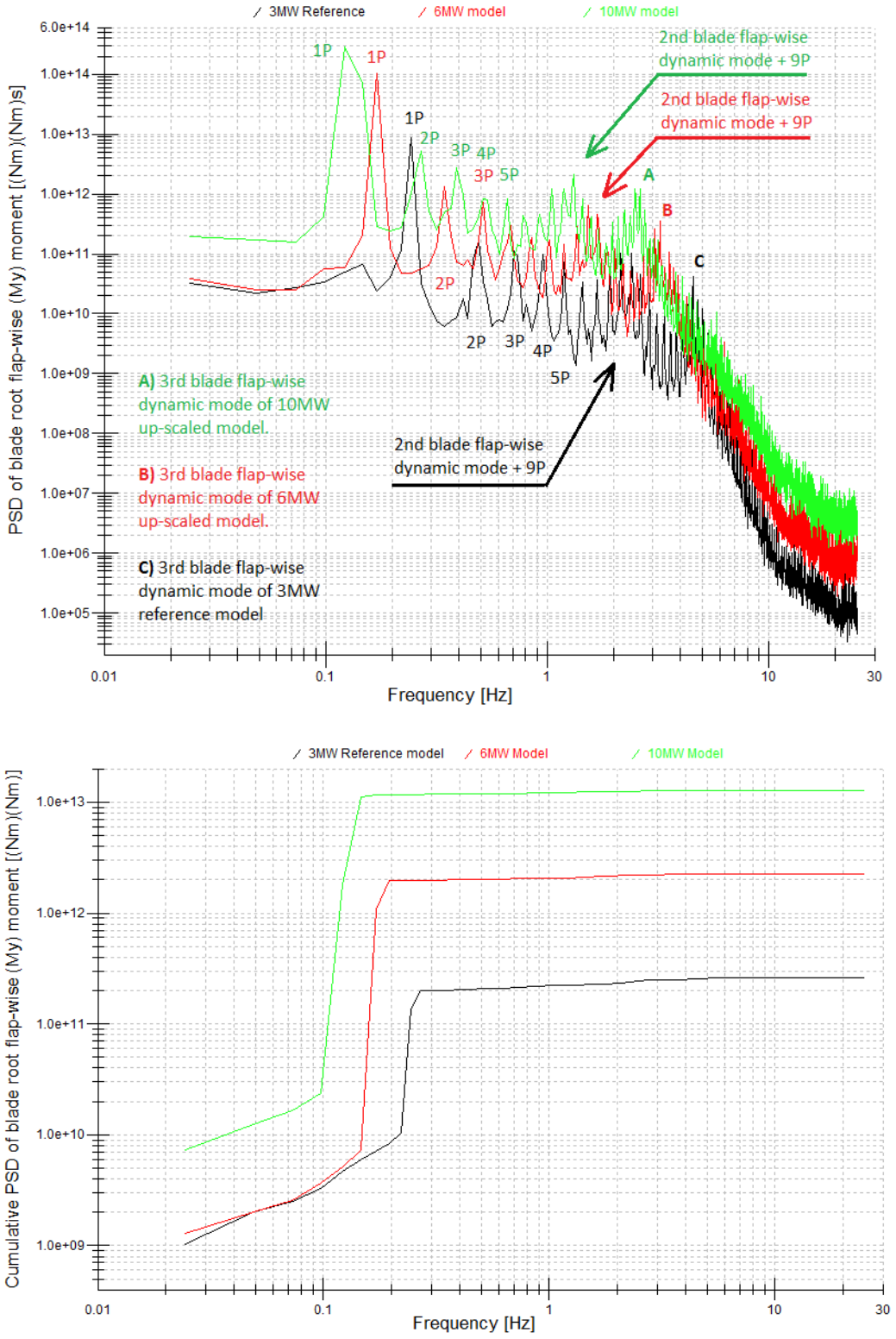

Figure F.5: PSD and Cumulative PSD of blade root flap-wise moment of 3MW reference, two 6MW and 10MW up-scaled models at 14 m/s

F.2.2. Low-Speed shaft moment

Figure F.6 displays the two graphs, which correspond to the PSD and cumulative PSD of low speed shaft moment of the three wind turbine model (3, 6 and 10MW). The curves of the up-scaled units repeat the curve of the base model. However, the curves of up-scaled models are shifted compared to the base model, as a result of the modifications of properties (especially the reduction of rotor frequency) due to the up-scaling modifications. Both graphs did not show any suspicion behaviour of the modified models. Hence, it is possible to conclude there is no any negative impact due to the up-scaling in terms of low-speed shaft moment.

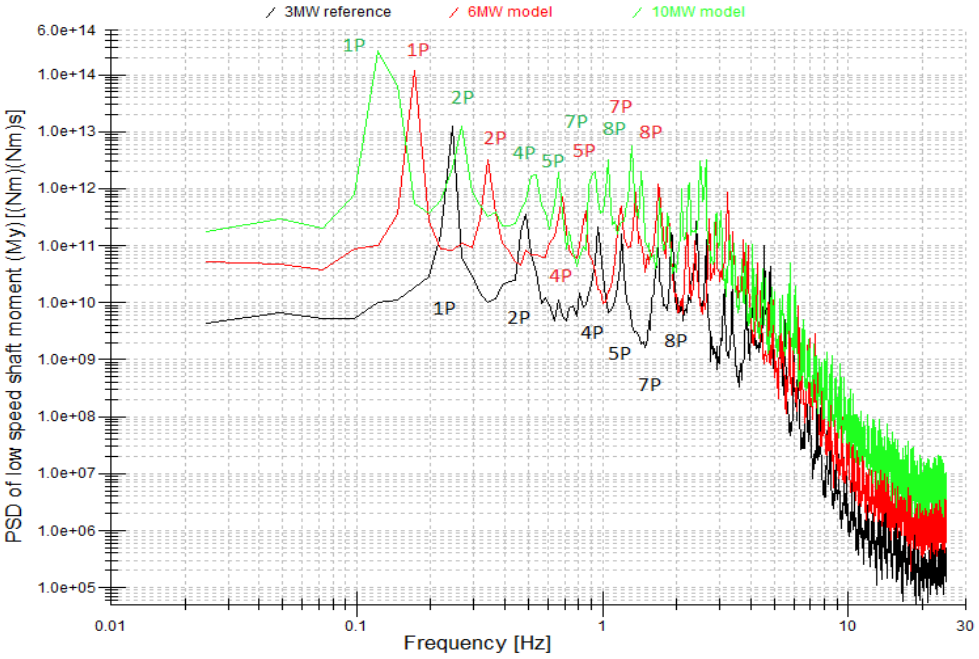

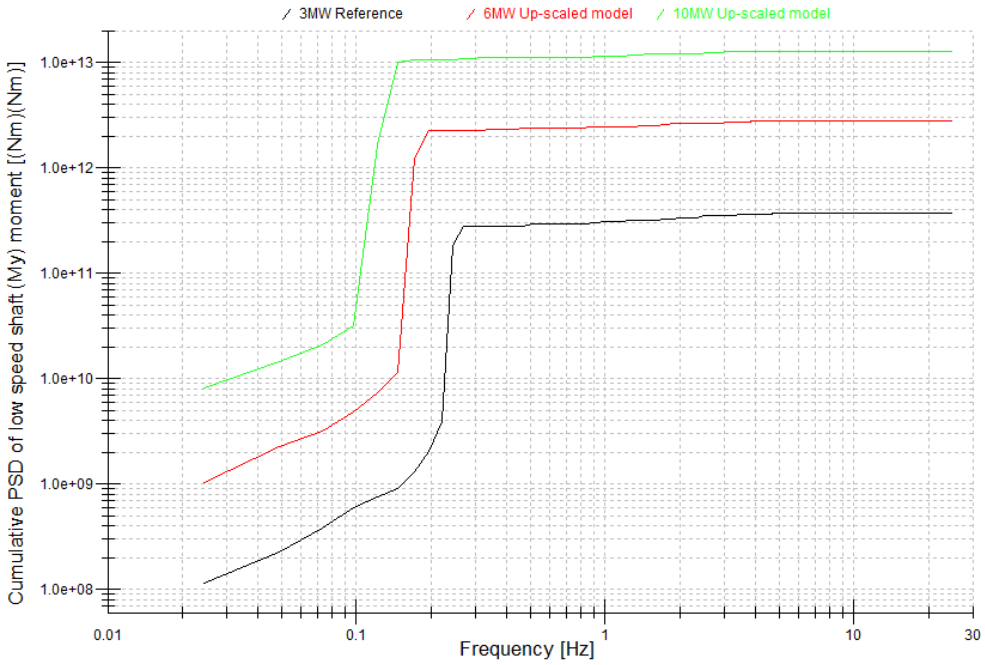

Figure F.6: PSD of low speed shaft moment of 3MW reference, two 6MW and 10MW up-scaled models at 14 m/s

F.2.3. Yaw bearing moment

The graphs of PSD and cumulative PSD of yaw bearing moment are showed by the two graphs of Figure F.7. The two graphs demonstrate that the peaks of *3P, 6P,* and *9P* generate significant impacts onto loads for all three models as shown by the rises of cumulative PSD curves, which correspond to the abovementioned peaks. Nevertheless, the up-scaled models will have larger impacts onto fatigue than the reference model due to up-scaling, which is obvious. Apart from that there is no negative effect as a consequence of the up-scaling because the curves of up-scaled machines are shifted but still repeat the curve shape of reference model.

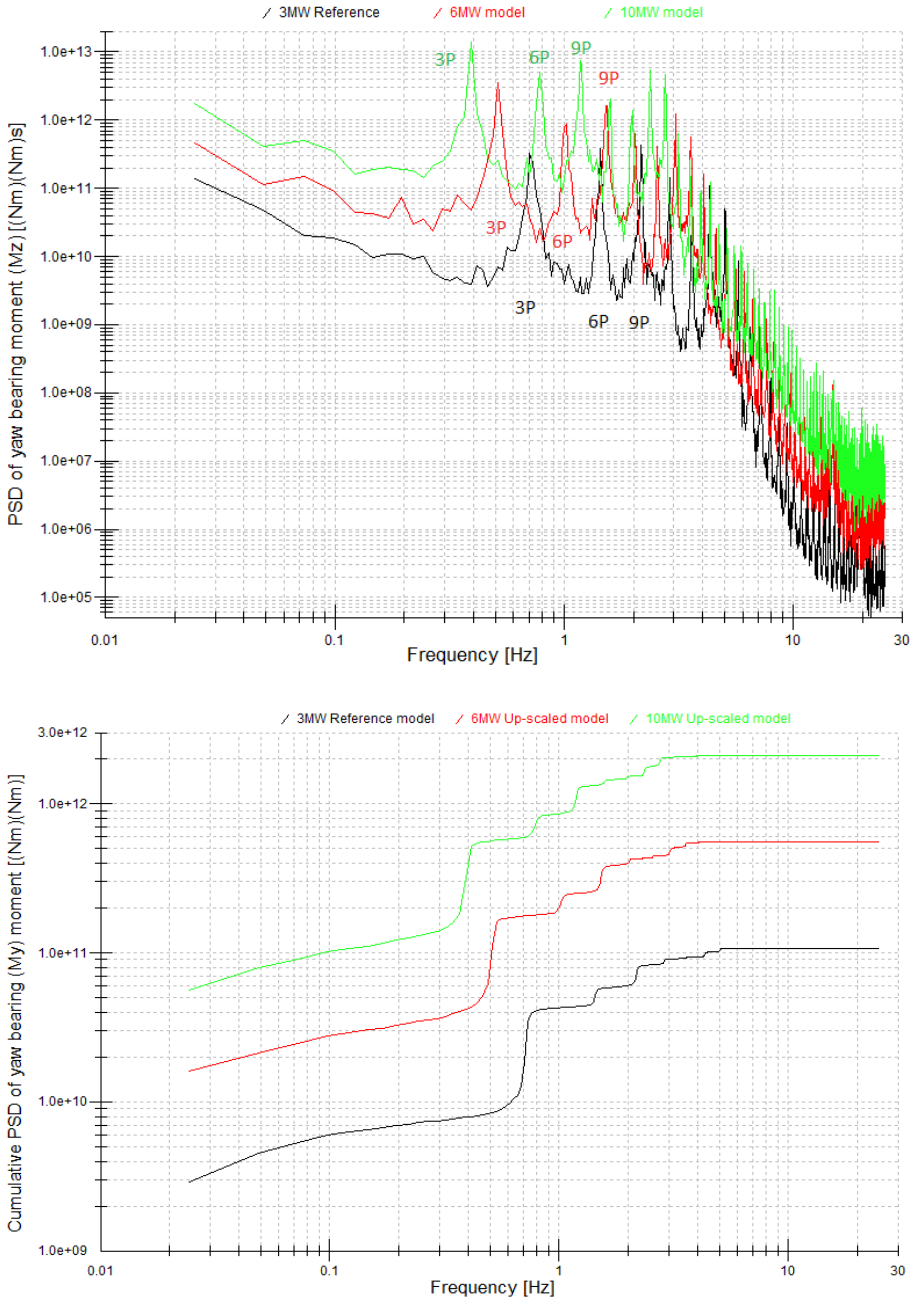

Figure F.7: PSD and Cumulative PSD of yaw bearing moment of 3MW reference, two 6MW and 10MW up-scaled models at 14 m/s

F.2.4. Tower base moment

The next two graphs of Figure F.8 depict the PSD and cumulative PSD of tower base fore-aft moment. The up-scaled models show unusual behaviour, which is represented by the large swell, which labelled by *D*. The cause of the swell is the 2nd structural tower fore-aft normal mode for both up-scaled models. Each swell couples with the *15P* peak of *3P* harmonics, which correspond

the rotational speed oscillations of each blade caused by tower shadow and wind shear effect as stated in [103]–[105]. These oscillations of rotor speed generate tower loads. A result of the coupling is high and un-damped peaks, which carry a lot of energy in terms of fatigue loads. The amount of energy carried by the un-damped peaks can be seen by the rise of cumulative PSD curves of the up-scaled models in the PSD cumulative graph of Figure F.8.

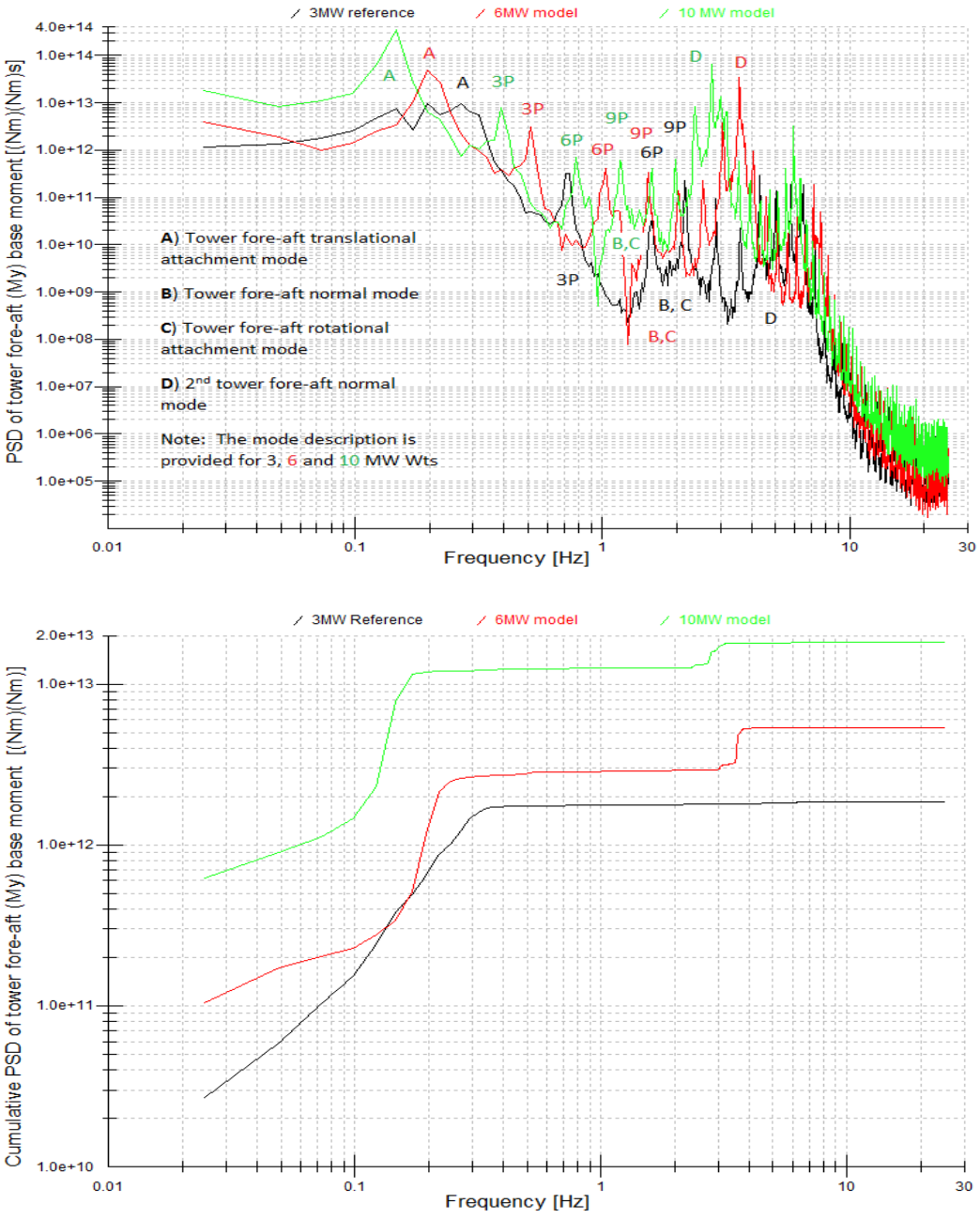

Figure F.8: PSD and cumulative PSD of tower fare-aft (My) base moment for 3MW reference, two 6MW and 10MW up-scaled models at 14 m/s